

BAUSCHINGER EFFECT
IN Nb AND V MICROALLOYED LINE PIPE STEELS

by

Andrii Gennadiovych Kostryzhev

A thesis
submitted to The University of Birmingham
for the degree of DOCTOR OF PHILOSOPHY

School of Metallurgy and Materials
College of Engineering and Physical Sciences
The University of Birmingham
April 2009

UNIVERSITY OF
BIRMINGHAM

University of Birmingham Research Archive

e-theses repository

This unpublished thesis/dissertation is copyright of the author and/or third parties. The intellectual property rights of the author or third parties in respect of this work are as defined by The Copyright Designs and Patents Act 1988 or as modified by any successor legislation.

Any use made of information contained in this thesis/dissertation must be in accordance with that legislation and must be properly acknowledged. Further distribution or reproduction in any format is prohibited without the permission of the copyright holder.

Abstract

Structural steels with a ferrite-pearlite microstructure are widely used in civil, mechanical and chemical engineering. Increased working loads, reliability requirements, extreme temperature and chemically aggressive environments lead to an increased demand for high strength, combined with high toughness, in these steels. The use of welding as a joining method requires good weldability, for which the carbon content in a steel composition should be decreased. A decrease in carbon content results in strength decrease, due to a decrease in the amount of the second phase (pearlite). To overcome this strength drop, additions of titanium, niobium and vanadium microalloying elements, in amounts no more than 0.15 wt%, have been used to provide precipitation strengthening and grain size refinement. Thus, during the last thirty years high strength low alloy (HSLA) structural steels have found widespread use in automotive, construction and pipe-line transportation industries.

Manufacture of large diameter (more than 16", 406.4 mm) welded pipes for oil, gas and water transportation systems is a specific sphere of HSLA steel application. The pipe lines work in severe environmental conditions from Arctic marine waters to African and Arabian deserts and the steels for them should be of very high weldability as well as high strength and toughness. To ensure this combination of properties, thermo-mechanical controlled rolling (TMCR) has been widely implemented in plate processing technology and the mechanical properties are carefully controlled during plate rolling and pipe cold forming.

The main deformation feature of the UOE pipe forming process is the reverse cold deformation in the pipe cross section. Depending on position through wall thickness and around the circumference, it is possible to distinguish several deformation zones with different strain direction sequences. It is well known that reverse cold deformation may lead to a reduction in strength, the Bauschinger effect. Earlier research has shown that the strength change from plate to pipe depends on the pipe geometry, strain levels during forming and

steel grade. The microalloying element carbonitrides influence the mechanical property development during forward-reverse deformation via dislocation-particle interaction, but quantitative data about this influence are scarce. The aim of the present project is to study the influence of steel chemistry, namely Nb and V content, on strength development during reverse cold deformation. This has been carried out via correlation of experimentally measured dislocation-particle interaction parameters and the yield stress change during forward-reverse deformation.

Microstructure of two microalloyed steels has been studied with optical, scanning electron (SEM) and transmission electron microscopy (TEM). The (Ti, Nb, V)- and Cu-rich particle diameter, volume fraction and number density were measured in these steels for the as-rolled and annealed (for 30 min. at 400 °C and 550 °C) conditions at the plate sub-surface and mid-thickness positions. The average particle volume fractions showed good agreement with the Thermo-Calc theoretical predictions. TEM measurements of dislocation density were carried out for both steels in as-rolled and annealed conditions at the plate mid-thickness position. Observed dislocation structure types and measured values of dislocation density correspond to the literature data for bcc structures and strains. The Bauschinger effect was measured during compression-tension testing of the two studied steels in the as-rolled and annealed conditions. The yield stress drop due to the Bauschinger effect has been found to increase with an increase in forward pre-strain, dislocation density and particle number density. The main reason of strength change during reverse deformation in these systems (C-Nb and C-Nb-V steels) is dislocation-particle interaction; with an increase in dislocation-particle interaction sites the yield stress drop increases, which supports the back stress and Orowan theories of the Bauschinger effect. On the basis of the obtained results, a quantitative model of work-hardening behaviour dependence on particle number density and dislocation density has been derived for reverse deformation of the studied steel grades. The model validity should be

restricted to particle number density values (for 12-50 nm diameter particle size) in the range of $70 - 900 \mu\text{m}^{-3}$ and dislocation density values in the range of $(1.1 \dots 4.0) \times 10^{14} \text{ m}^{-2}$. In addition, the obtained model can only be used for the forward-reverse deformation scheme. During more complex deformation schemes, such as forward-reverse-forward and forward-reverse-forward-reverse, it is possible to expect a different quantitative dependence of strength on particle number density and dislocation density, which needs further investigation. However, the obtained model allowed a reasonably accurate prediction of the yield stress change during the UOE pipe forming process.

Acknowledgment

Financial support for this project has come from the “Universities UK” and the Department of Metallurgy and Materials, University of Birmingham in the form of Overseas Research Student Award, for which I am very thankful. Materials for investigation were produced and provided by Corus, plc.

Personal gratitude I would like to express to Prof. P. Bowen, for the provision of laboratory equipment and mechanical testing facilities at the Department of Metallurgy and Materials and Interdisciplinary Research Centre, and Prof. I.P. Jones, for the provision of microscopy facilities at the Centre for Electron Microscopy.

My endless thanks are to my supervisors Dr. Martin Strangwood and Dr. Claire Davis for the everyday encouragement, professional support and human attention.

Through the duration of this project I was having much help and advice from the staff members of the Department:

Mr. Paul Stanley – scanning electron microscopy,

Ms. Ming Chu – transmission electron microscopy,

Mr. Dave Price – mechanical testing equipment,

Mr. Frank Biddlestone – differential scanning calorimetry,

to whom I am also thankful.

I would not be able to carry out this project without a significant impulse from my mama Larisa and dad Gennady.

CONTENTS

page

1. HIGH STRENGTH LOW ALLOY (HSLA) STEELS FOR WELDED PIPE	
FORMING.....	1
1.1 Deformation by slip and dislocation theory of work-hardening.....	1
1.1.1 Deformation by slip.....	1
1.1.2 Burgers vector.....	3
1.1.3 Dislocation density.....	4
1.1.4 Mobility of dislocations.....	5
1.1.5 Dislocation-obstacle interaction.....	6
1.1.6 Dislocation structure dependence on strain.....	11
1.1.7 Yield strength and theory of work-hardening.....	24
1.2 Work-softening due to the Bauschinger effect.....	32
1.2.1 Evaluation of the magnitude of the Bauschinger effect parameters.....	32
1.2.2 Causes of the Bauschinger effect.....	34
1.2.3 Main features of the Bauschinger effect.....	36
1.2.4 Bauschinger effect in HSLA steels.....	41
1.3 Precipitation of alloying elements in HSLA steels.....	47
1.4 Strengthening mechanisms in carbon steels.....	54
1.4.1 Grain refinement.....	55
1.4.2 Solid solution strengthening.....	57
1.4.3 Phase balance strengthening.....	58
1.4.4 Precipitation strengthening.....	61
1.4.5 Work hardening.....	65
1.5 Thermo-mechanical controlled processing (TMCP) of HSLA steel plate.....	66
1.5.1 Plate rolling technology.....	67
1.5.2 Plate property development.....	68
1.6 Large diameter pipe forming.....	76
1.6.1 The UOE forming process.....	76
1.6.2 Strain distribution during pipe forming.....	79
1.6.3 Pipe property evaluation.....	84
1.6.4 Plate to pipe property change	92
1.7 Aims and objectives of the project.....	94

2. MATERIALS AND EXPERIMENTAL TECHNIQUES.....	96
2.1 Materials.....	96
2.2 Experimental techniques.....	97
2.2.1 Thermodynamic modelling	97
2.2.2 Optical microscopy and image analysis	97
2.2.3 Scanning electron microscopy (SEM).....	97
2.2.4 Transmission electron microscopy (TEM).....	98
2.2.5 Energy dispersive X-ray spectroscopy (EDS).....	99
2.2.6 Hardness testing.....	99
2.2.7 Mechanical testing.....	99
2.2.8 Differential scanning calorimetry (DSC).....	101
3. MICROSTRUCTURE AND MECHANICAL PROPERTIES OF PLATE STEELS	102
3.1 Thermodynamic modelling of microstructure with Thermo-Calc.....	102
3.2 Ferrite grain size distributions.....	107
3.3 Second phase content	113
3.4 Mn-, Al- and Si-rich phases (optical and SEM analysis).....	115
3.5 Alloying element content distribution	117
3.6 Ti-Nb-rich phases (SEM analysis)	119
3.7 Nb-, V- and Cu-rich phases (TEM analysis).....	128
3.8 Dislocation structures and dislocation density (TEM analysis)	135
3.9 Dislocation-particle interaction (TEM analysis).....	139
3.10 Hardness and yield stress dependence on microstructure.....	146
4. MECHANICAL PROPERTY CHANGE WITH COLD DEFORMATION.....	154
4.1 Mechanical properties during unidirectional deformation	154
4.2 Mechanical properties during reverse deformation.....	161
4.3 Theoretical assessment of property development during UOE pipe-forming.....	172
5. CONCLUSIONS.....	181
6. FUTURE PLAN OF RESEARCH.....	185
REFERENCES.....	187

1. HIGH STRENGTH LOW ALLOY (HSLA) STEELS FOR WELDED PIPE FORMING

1.1 Deformation by slip and dislocation theory of work-hardening

The concept of crystal defects, such as dislocations, was introduced in physics by Taylor, Orowan and others in the 1930s to describe crystal behaviour during deformation of matter. Later work on crystalline materials, especially metals, showed the strong dependence of mechanical properties on the presence of dislocations. On the basis of dislocation interaction with obstacles in the microstructure (such as grain boundaries, precipitates and other dislocations) the yield and work hardening theories were developed. The present work has investigated the mechanical property behaviour during reverse deformation in microalloyed steels: in particular the yield strength change has been quantitatively related to dislocation-dislocation and dislocation-precipitate interactions, requiring an understanding of dislocation behaviour, which is reviewed in this section.

1.1.1 Deformation by slip

Crystal deformation, by means of translational slip, is shown schematically in Figure 1.1, a, where one part of the crystal slides upon the adjacent part. Relative movement of the crystal parts in an ideal case is pure translation and the crystal orientations of the parts remain the same. In real crystals partial slip occurs, when only one part of the crystal moves along the slip plane over another part (Figure 1.1, b). As a result of partial slip crystal distortion or the *dislocation* can be observed, where atoms of the lattice are improperly surrounded by their neighbours (Figure 1.1, c). With continued external loading, propagation of slip occurs via a

wave of atom displacement and the dislocation starts *moving* through the crystal in the direction of slip (Figure 1.2). Thus in the polycrystalline material macroscopic deformation is related to structural imperfections in a single crystal, namely dislocations and their movement.



Figure 1.1 (a) Translational slip, (b) partial slip related to the dislocation of edge type, and (c) approximate atom arrangement around the edge dislocation, dislocation is denoted by the ⊥-sign

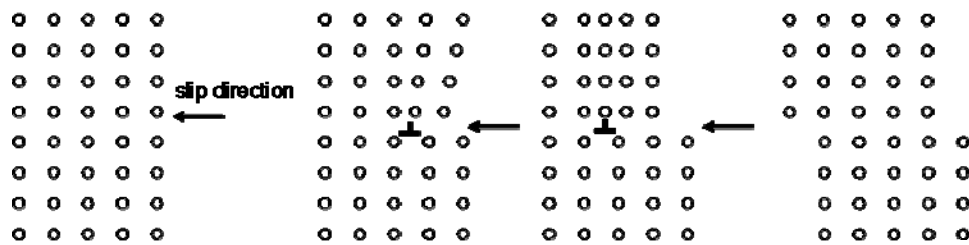


Figure 1.2 Slip propagation by movement of a dislocation

Slip planes and slip directions are not determined by chance. Within a crystal of any type there are one or several families of planes along which the atoms are more densely packed. In these planes there are also definite directions along which interatomic spacing is a minimum. Slip mainly occurs parallel to these densely packed planes and directions. In a polycrystalline material, where individual crystals are oriented at different angles to the load direction, slip starts in those crystal planes which are oriented most closely to 45° to the stress axis (direction of maximum shear stress) along those directions that happen to be most nearly parallel to the direction of maximum resolved shear stress.

In the face-centred cubic structure (fcc), for example, close-packed planes are the $\{111\}$ (octahedral set of planes) and closed-packed directions are the $\langle 110 \rangle$ (cube face diagonals) (Figure 1.3) [1]. In the body-centred cubic structure (bcc) mostly closed-packed planes are the

$\{110\}$ and the directions $\langle 111 \rangle$ (cube diagonals). As the packing density on the $\{110\}$ planes in the bcc structure is not much greater than for other sets of planes, slip in the bcc structure may also occur on the $\{112\}$ and $\{123\}$ planes, which also contain the $\langle 111 \rangle$ direction. In fact slip in this structure can start and proceed on any or all of the three slip system types. As the bcc structure does not have a close packed plane it requires higher stresses to initiate slip and withstands lower plastic deformation to failure than the fcc structure.

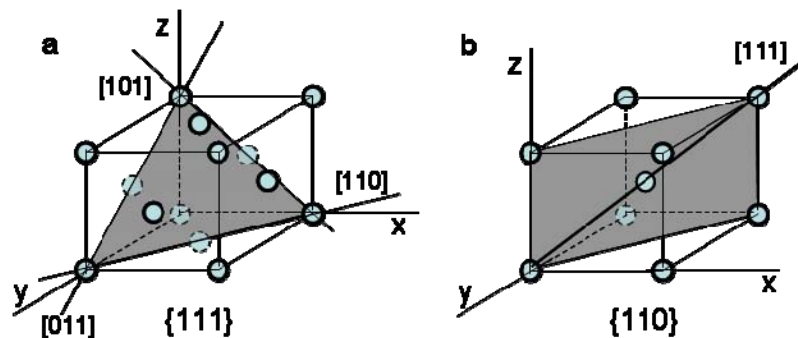


Figure 1.3 Slip planes and directions in the (a) fcc and (b) bcc cubic structure

1.1.2 Burgers vector

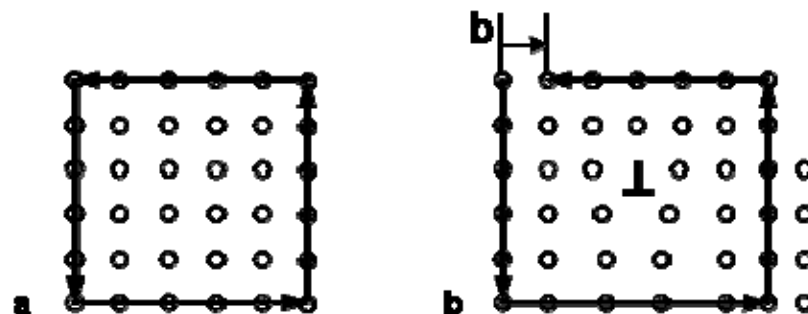


Figure 1.4 (a) Closed Burgers circuit in perfectly arranged cubic lattice and (b) not closed, due to dislocation within the circuit

A dislocation can be uniquely characterised by the Burgers vector \mathbf{b} (Figure 1.4). A Burgers vector is the closure failure of a loop called a Burgers circuit. A Burgers circuit is made by the path of atom-to-atom steps in any one plane of a crystal lattice turning the same direction (clockwise or counter-clockwise) after an equal number of steps. If a Burgers circuit

surrounds perfectly arranged crystal structure it will be closed, but if it surrounds a dislocation it will not close and the closure failure, called the Burgers vector, will characterise the dislocation. It is possible to distinguish dislocations of edge, screw and mixed type. An edge dislocation will occur when a part of an extra crystal plane occupies the space between adjacent crystal planes, Figure 1.5, a, i.e. $\mathbf{b} \perp \mathbf{l}$, and a screw dislocation occurs when a part of a crystal plane is shifted by the Burgers vector parallel to itself, Figure 1.5, b, i.e. $\mathbf{b} \parallel \mathbf{l}$, where \mathbf{l} is dislocation line.

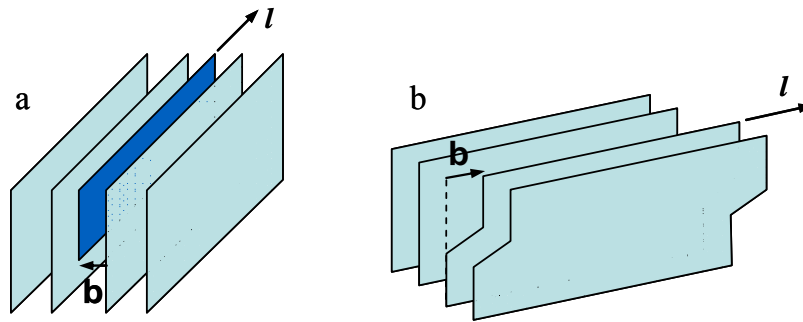


Figure 1.5 Schematic diagrams of (a) an edge and (b) a screw dislocation

1.1.3 Dislocation density

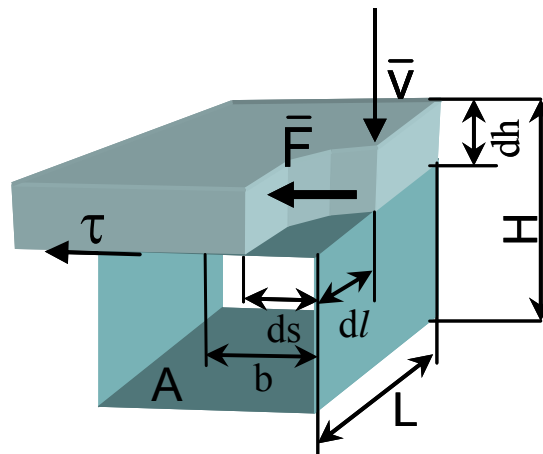


Figure 1.6 Schematic diagram of a crystal shearing

Consider an elementary segment of a dislocation line dl (Figure 1.6). During an element of time dt the segment moves by the distance ds and contributes to the slip of the upper half-

crystal an amount $ds \, dl/A$, where A is the area of the slip plane. The corresponding increment of ordinary shear strain will be given by multiplying this by dh/H , i.e. $\frac{ds \, dl}{A} \cdot \frac{dh}{H}$. In the general case of plastic deformation many dislocations are involved in the shear process. Thus an increment of plastic shear strain during time dt will be a definite integral with respect to the total length of dislocations L and the Burgers vector \mathbf{b} :

$$d\gamma = \int_0^L \int_0^b \frac{ds \, dl \, dh}{AH} = \frac{|\mathbf{b}|L}{V} dh,$$

where $V = AH$ is the total volume of the crystals involved in plastic deformation.

Dividing $d\gamma$ by dt we will get the strain-rate of shear:

$$\dot{\gamma} = b\rho v,$$

where v is the velocity of shear.

The parameter $\rho = L/V$, total length of dislocations per unit volume, is called the dislocation density. It has dimensions of inverse area and shows the number of dislocation lines intersected by a plane of unit area normal to their length, L .

1.1.4 Mobility of a dislocation

When a crystal is subjected to an applied force (external or internal) a dislocation will try to move in the direction of maximum shear stress to lower the potential energy of the system. Therefore, to calculate the force on a dislocation let us consider Figure 1.6. If τ is the maximum shear stress on the slip plane of area A acting in the direction of slip, the shear force will be τA . When an element of dislocation line dl moves in the direction of slip by ds and causes the displacement of the crystal, of $ds \, dl / A$, then the increment of the work, produced by the shear force, is as follows:

$$dw_{\tau} = \int_0^L \int_0^b A \tau \frac{ds dl}{A} \cdot ds = \tau L b \cdot ds$$

If \mathbf{F} is an equally distributed force on the dislocation line its work during the displacement of the dislocation increment dl in the direction of slip by ds is as follows:

$$dw_F = \int_0^L F dl \cdot ds = FL \cdot ds$$

As the dislocation is in equilibrium under the action of the force \mathbf{F} and crystal shear force the increments of work are equal $dw_{\tau} = dw_F$, and

$$\mathbf{F} = \tau \mathbf{b}.$$

Since the Burgers vector is the same for all the segments of a dislocation line, this force has the same magnitude everywhere along the line and lies in the slip plane perpendicular to the dislocation line.

In the process of dislocation motion atoms on each crystal plane that lie perpendicular to the dislocation line far ahead or far behind the dislocation occupy equilibrium positions with respect to their neighbours. Atoms near the dislocation are in a metastable state. Atoms ahead of the dislocation try to pull it backwards in the reverse direction of slip and atoms behind the dislocation, which already occupied new positions, push the dislocation forwards in the direction of slip. Thus the dislocation moves not as a whole but by segments. Because of that, the force, \mathbf{F} , needed to start and propagate the dislocation motion, periodically varies along the dislocation line and is several orders of magnitude lower than the shear modulus.

1.1.5 Dislocation-obstacle interaction

As real crystals are not perfect in their structure and possess numerous defects dislocation motion does not proceed unimpeded. The defects act as obstacles to the moving dislocations

and may fully stop or slow their further propagation. The most important obstacles in the context of this work are grain boundaries, solute atoms, precipitates of alloying elements and other dislocations (mobile or sessile). Qualitative principles of dislocation-obstacle interactions are described below, for a more quantitative approach see section 1.4.

Under the action of external loading newly produced and existing dislocations move along the slip planes until they reach a grain boundary. As individual crystals are situated at rather high angles to each other, dislocations normally cannot cross the boundary and a pile-up occurs by the boundary. Within a small grain the pile-up occurs at lower strains, compared to a large grain, as there is little space for free dislocation motion from a boundary to the opposite boundary. So external forces (the yield stress), required to continue deformation (dislocation motion, new dislocation formation), increase with decreasing grain size. That is the principle of grain refinement strengthening.

The presence of solute element atoms causes distortion of the matrix lattice. Stress fields around the solute atoms (substitutional or interstitial) interact with dislocations retarding dislocation propagation. Stress fields associated with dislocations (mainly of edge type) attract solute atoms (mainly interstitial) and Cottrell atmospheres are formed [2]. These lock the dislocations and hinder their motion. To continue deformation by slip either the dislocations should be torn away from their atmospheres or the atmospheres should be moved together with the dislocations. This requires higher stresses than to move unlocked dislocations. Thus the yield stress increases with alloying due to solid solution strengthening.

Alloying elements tend to form chemical compounds with each other or non-metallic elements (such as carbon, nitrogen and sulphur in steels). Interaction between particles and moving dislocations depends on precipitate size, particle coherency with the matrix and interparticle spacing (Figure 1.7). Small coherent particles may be easily passed by moving

dislocations. Dislocation interaction with large incoherent particles depends on interparticle spacing. If an interparticle spacing is less than $\lambda = \alpha Gb/\tau$ (where α is constant, G is shear modulus, b – magnitude of the Burgers vector and τ - applied shear stress) [2], a dislocation will tend to move through the particles and finally bisect them. If an interparticle spacing is above λ , a dislocation will tend to bend between the particles and bypass them having left the particles surrounded by dislocation loops. Particle cutting will require increasing stresses with particle strength increase due to composition effect on interatomic bond strength and lattice type; and particle size increase, as particle coherency with the matrix generally decreases as particle size increases. In both cases the defect energy of crystal structure increases, either by increase in particle-matrix surface or total dislocation length. In terms of macroscopic deformation – to increase the internal energy greater external loading is needed. Thus the yield stress increases due to precipitation of alloying elements.

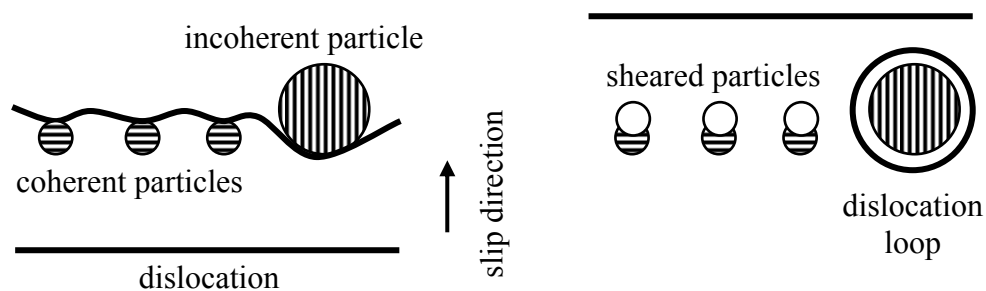


Figure 1.7 Schematic diagram of dislocation-particle interaction

Interaction of moving dislocations with other dislocations (mobile or sessile) present in the crystal structure depends on the dislocation sign, slip plane and direction. If the same-signed dislocations move towards each other on the same slip plane they will repel and block each other (Figure 1.8, a, b). If oppositely-signed dislocations move on the same slip plane in opposite directions they will attract each other and annihilate, as half of the crystallographic plane of the first dislocation will be complemented by the other half of the second dislocation (Figure 1.8, c, d). However, if the different-signed dislocations move on parallel slip planes their stress fields

will attract each other, but the annihilation will not take place (Figure 1.8, e, f). Between the dislocations a vacancy will appear and the two dislocations will form a sessile dislocation, which is strongly immobile due to the oppositely-signed stress fields. Sessile dislocations become strong obstacles for the mobile dislocations. Moving in the same direction on the same slip plane dislocations may not interact with each other if their length is also the same. For dislocations with different lengths, dislocation velocity in the slip direction will be different (a shorter dislocation has a higher speed). For example, a shorter dislocation running after a longer one may “catch” it up after some time, and, if they are of different signs, part of the longer dislocation and the shorter one will cancel each other. If the dislocations are of the same sign, repelling stress fields will retard their motion. Same-signed dislocations moving on the same slip plane may pile-up at an obstacle to glide (such as a grain boundary or a large inclusion); the resulting pile-up can also be a significant obstacle for further dislocation motion (Figure 1.9).

If dislocations move in different directions on different slip planes after intersection each of them will develop a jog; a sudden change in dislocation axis (Figure 1.10). The jog of each dislocation is equal in magnitude and direction to the other dislocation’s Burgers vector. As the length of each dislocation increases as a result of their interaction, the total energy of the crystal structure also increases proportional to the number of dislocation-dislocation interaction sites. In addition, a jog, moving on a different slip plane to its dislocation plane, causes a drag on the dislocation and significantly slows down the dislocation velocity. Dislocations, moving on different slip planes in different directions, can also form a variety of dislocation nodes (Figure 1.11). Such nodes become nucleation sites for dislocation tangles, which are, together with pile-ups, potentially strong obstacles for the mobile dislocations.

In all the cases of dislocation-obstacle interaction mentioned above, to continue macroscopic deformation higher external loading is needed. Thus the yield stress increases with an increase in number density of dislocation-obstacle interaction sites.

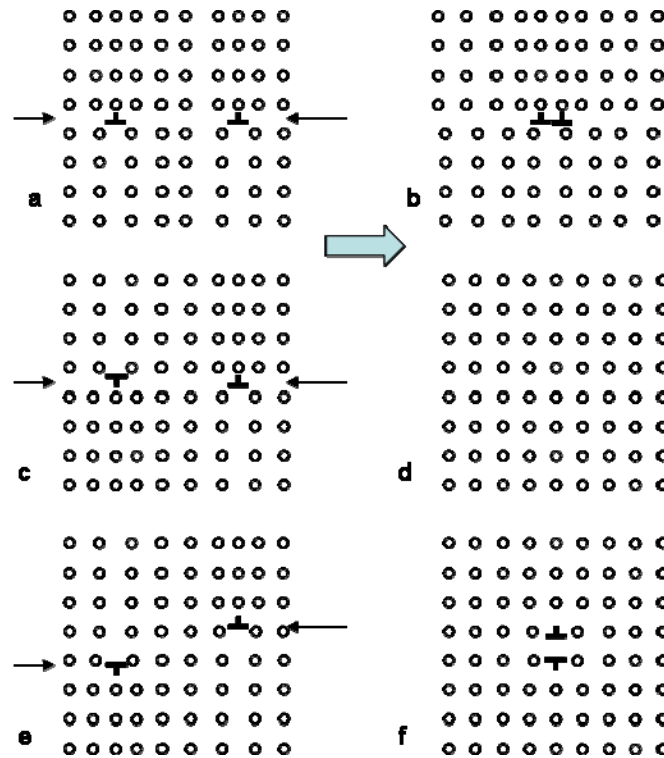


Figure 1.8 (a) Two one-signed dislocations approach each other, (b) dislocation accumulation, (c) two opposite-signed dislocations approach each other on the same slip plane, (d) dislocation annihilation, (e) two opposite-signed dislocations approach each other on parallel slip planes, (f) formation of a sessile dislocation

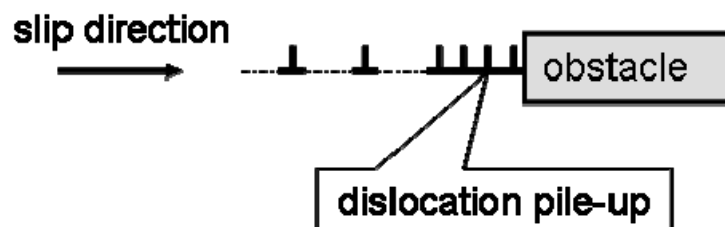


Figure 1.9 Schematic presentation of a dislocation pile-up by the obstacle to slip

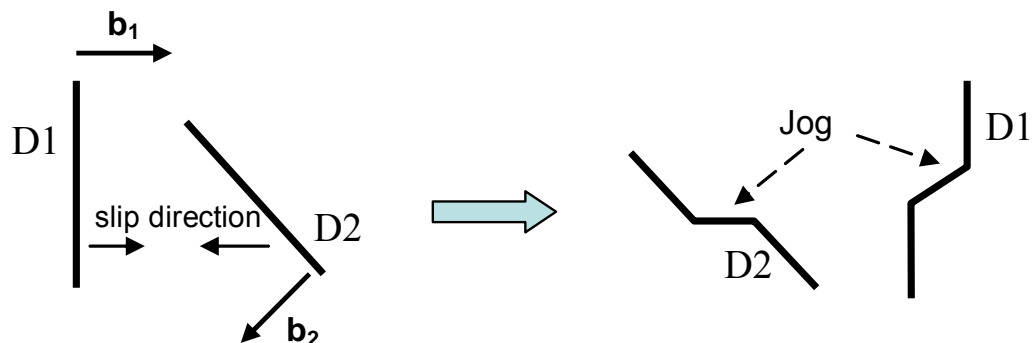


Figure 1.10 Dislocation-dislocation interaction in case of different dislocation slip planes, slip directions and Burgers vectors

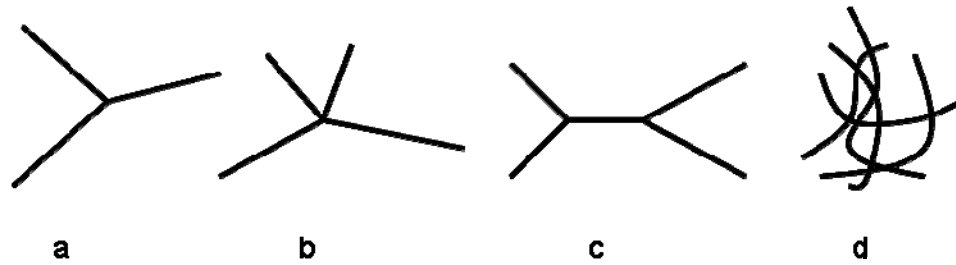


Figure 1.11 Dislocation-dislocation interaction in the form of a (a) three-fold node, (b) four-fold node, (c) four-fold node decomposed into two three-fold nodes, (d) tangle

1.1.6 Dislocation structure dependence on strain

Unidirectional deformation

The average dislocation density increases with an increase in plastic strain, but the dislocation generation rate dependence on strain changes with lattice type (Figure 1.12).

In bcc structures the dislocation generation rate decreases with increasing strain due to pile-ups on favourable slip planes (Figure 1.12, a) [3]. It is higher in the dynamic strain-ageing temperature region 100-350 °C, where values of carbon diffusion rate and dislocation velocity are similar leading to immobilisation of moving dislocations and increased production of new ones under external loading [4]. The dislocation density has been observed to be higher in a fine grained material than in a coarse grained material [3]. This can be explained by shorter distances of free dislocation motion before immobilisation by grain boundaries, leading to an increased number of new dislocations generated to continue slip. In ferritic steels the dislocation density after the same processing schedule has been observed to increase with carbon content increase in steel composition, due to an increased number density of precipitates leading to an increase in the number of potential dislocation sources [5]. This corresponds to the dislocation generation mechanisms described in the literature [6-10], according to which a dislocation locked by precipitates from one or both ends can become a dislocation generation source (Frank-Read mechanism).

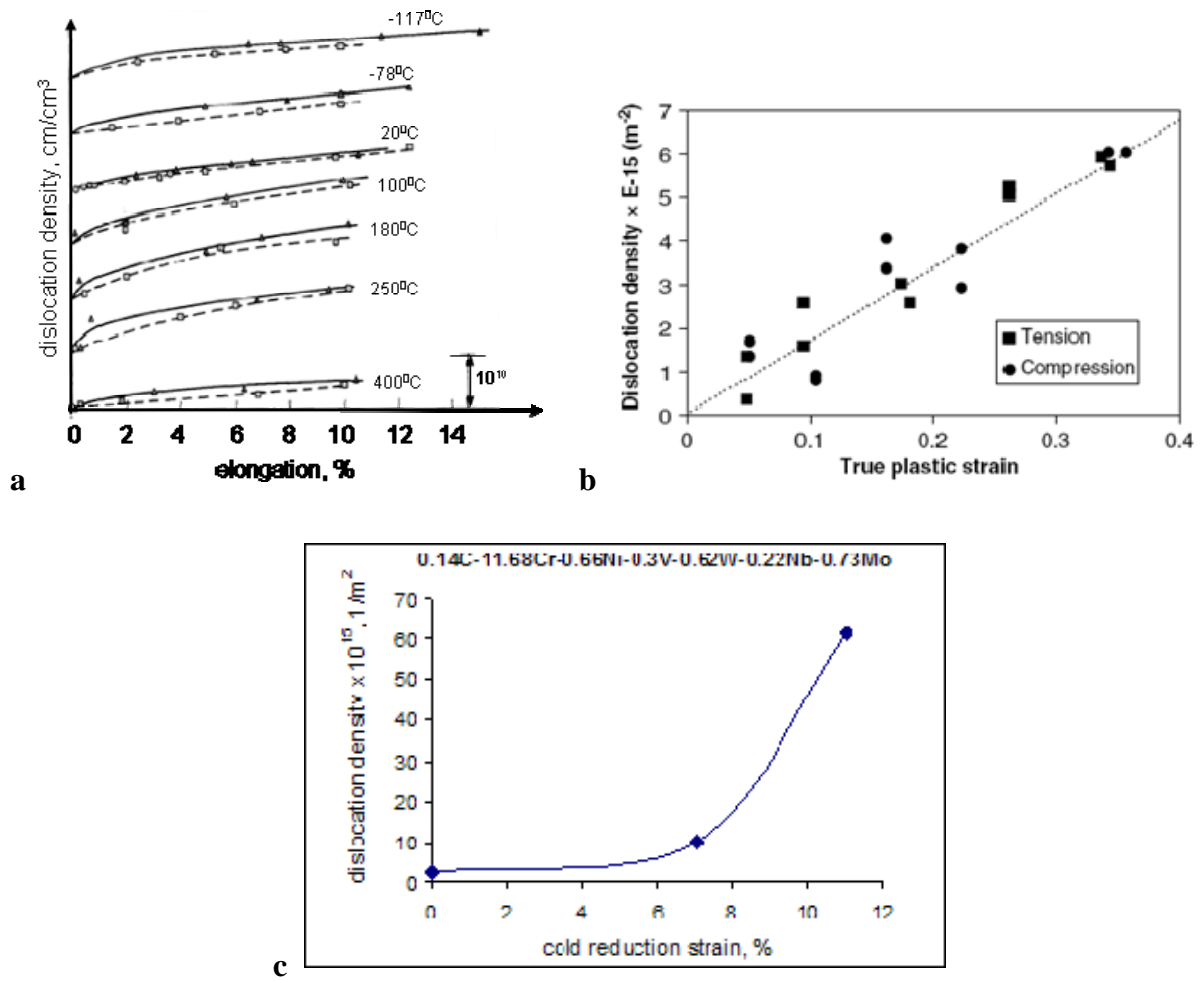


Figure 1.12 Dislocation density dependence on strain during cold deformation of (a) iron (bcc structure) [3], (b) Hadfield steel (fcc) [11] and (c) a martensitic steel (bct) [12]

In the fcc structure absolute values of dislocation density are higher compared to those in the bcc structure, due to the larger number of possible easy slip systems. The dislocation generation rate remains almost constant with increasing strain, Figure 1.12, b, so that the dislocation density dependence on strain can be approximated by a straight line relationship [11]:

$$\rho = k \times 10^{15} \times \epsilon,$$

where ρ is dislocation density; ϵ is strain; and k , the dislocation generation rate, is in the range $k = 1.5 \dots 3.1$ for aluminium and copper and $k = 17$ for the Hadfield steel.

An almost 10 times increase in the dislocation generation rate from pure fcc metals to steel can be related to an increased number of obstacles to slip, due to solute atoms and

precipitates present in steel, which leads to dislocation immobilisation and intensification of new dislocation generation.

The significantly larger dislocation density in martensite can be explained by the lattice distortion accompanying martensitic transformation (Figure 1.12, c).

In contemporary literature it is possible to distinguish four main dislocation structure types (Figure 1.13). The “straight line” structure is characterised by a regularly spaced arrangement of straight dislocations with uniform dislocation density (Figure 1.13, a). The “irregular” structure is distinguished by numerous dislocations running in different directions without any specific spatial arrangement, but maintaining a rather uniform dislocation density (Figure 1.13, b). The “cluster” structure has areas of higher and lower dislocation density, usually dislocations are not straight with numerous curves and nodes are present in clusters (Figure 1.13, c). The “cell” structure is named as it is possible to differentiate between wide areas of low dislocation density (cell interior) and narrow lines of high dislocation density (walls) surrounding them (Figure 1.13, d). Differences in dislocation density between the cells and the walls may reach 15-20 times [13, 14]. In addition to their high number density, dislocations in the cell walls are numerous interconnected and tied in bunches and knots. Adjacent cells, even belonging to the same grain, may have a spatial misorientation, and, because of that, dislocations from one cell cannot cross the wall to another cell [15]. The “cell” structure is intermediate to a sub-grain structure formation. The dislocation structure type changes with strain increase from the “straight line” to the cell type. However, due to inhomogeneity of deformation in different parts of material, all the structure types may be present at the same time in different grains.

In the bcc crystal structure, Figure 1.14, during room temperature deformation below 3-4 % plastic strain a straight line dislocation structure develops into the irregular structure with uniform dislocation density. With strain increase the dislocation density inhomogeneity

increases, and by 4.8 % clusters were observed (Figure 1.14, c). With further strain increase the cell structure appears visible at above 11 % strain (Figure 1.14, d).

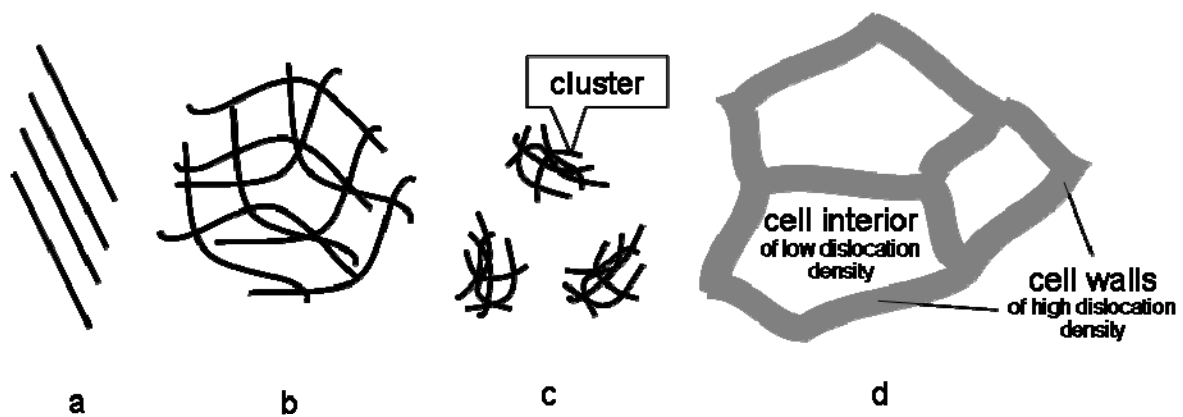


Figure 1.13 Schematic presentations of the dislocation structure types: (a) straight lined, (b) irregular with uniform dislocation density, (b) cluster, (c) cell structure

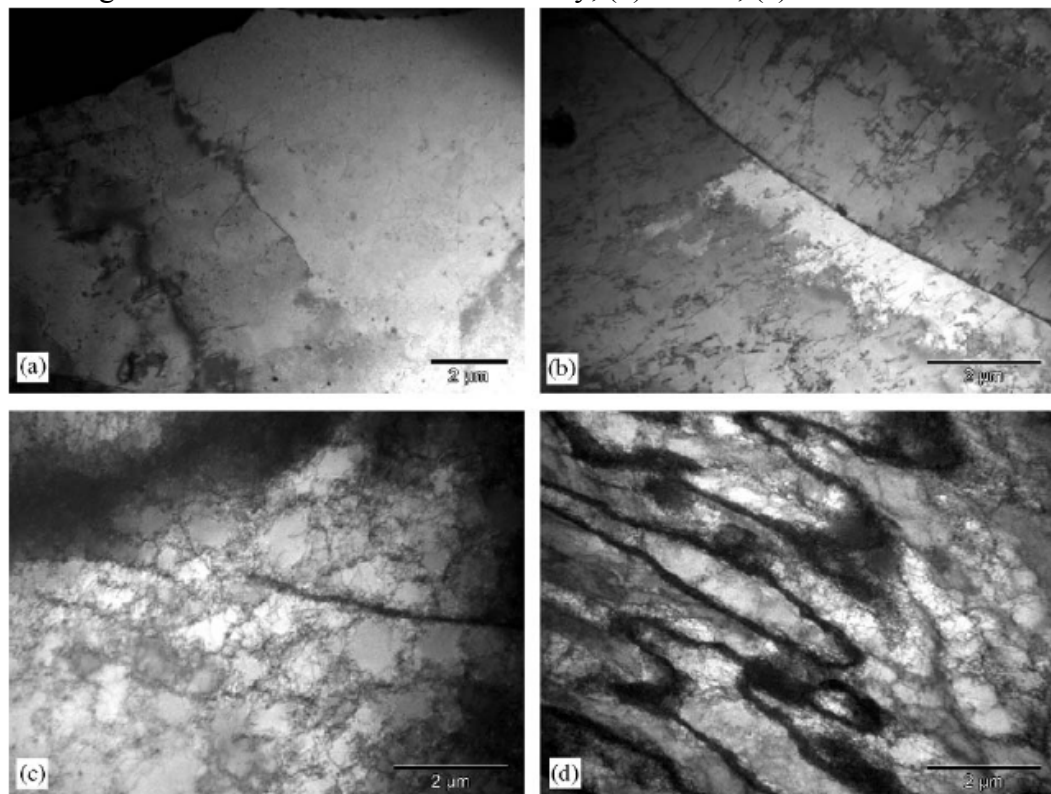


Figure 1.14 Dislocation structures in a ferritic steel deformed at room temperature [16]: (a) – 0% strain, undeformed state with occasional dislocations, (b) – 2.3%, beginning of irregular structure formation, (c) – 4.8%, clusters, (d) – 11.2%, cell structure

The dislocation structure development is not uniform through the strained volume. In some areas, even after 11 % deformation, the straight line structure with uniform dislocation

density may be present, due to lower than average local strain (Figure 1.15, a). Other areas may contain the cell structure and cell structure with rotated laths of different orientation, due to higher than average local strain (Figures 1.15, b and c).

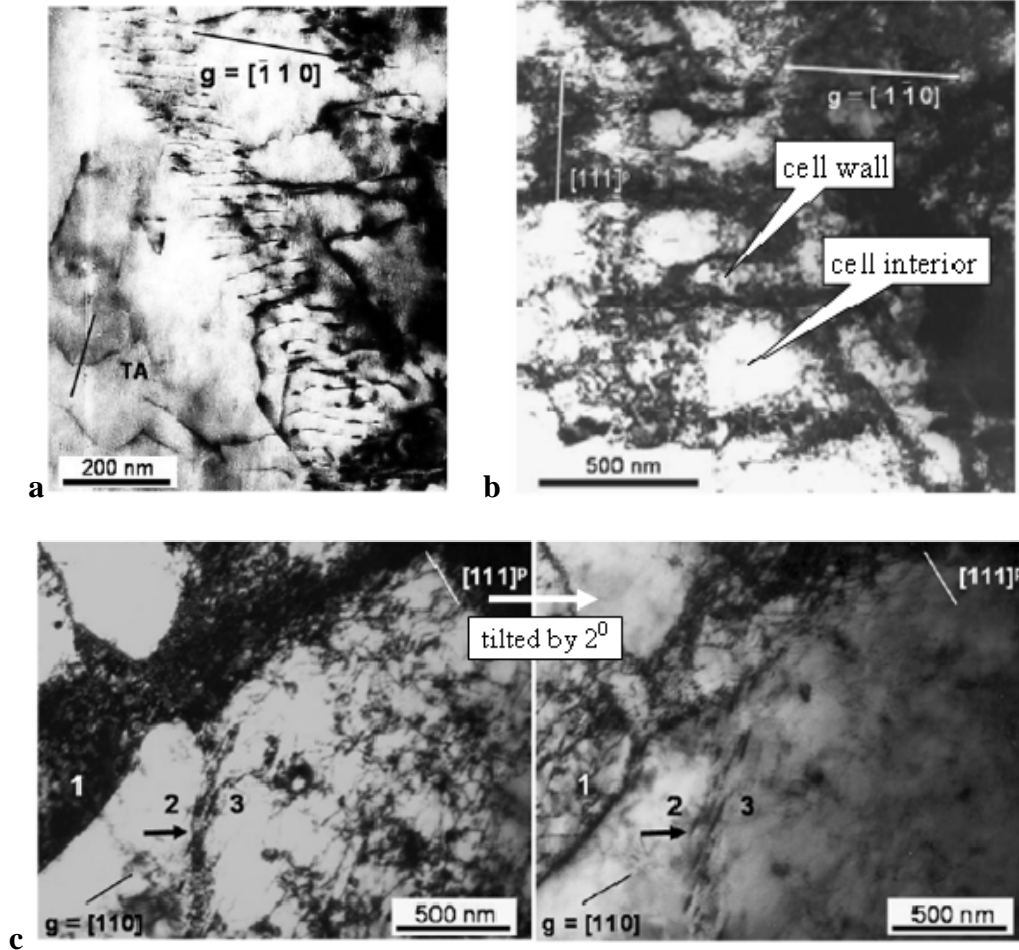


Figure 1.15 Dislocation structures of a ferritic steel tested at room temperature after 11 % strain [17]: (a) – straight line structure with the uniform dislocation density, (b) – cell structure, (c) – cell structure with rotated adjacent laths

Dislocation structure development with strain also depends on temperature and the amount of the second phase (e.g. pearlite) present. Thus in a ferritic steel tested at -196°C the straight line structure “survived” to 2.5 % strain and clusters appeared after 8 % (Figure 1.16, a compared with Figure 1.14, b and Figure 1.16, b compared with Figure 1.14, c). In pure iron deformed at -117°C the straight line structure was present at strains up to 12 % [3]. So, a decrease in temperature led to the formation of the cell structure at higher strains. Presence of

the second phase in steel, compared to single phase pure iron, results in the formation of different types of dislocation structures in different areas. This can be explained by inhomogeneity of deformation related to the difference in phase plasticity [18].

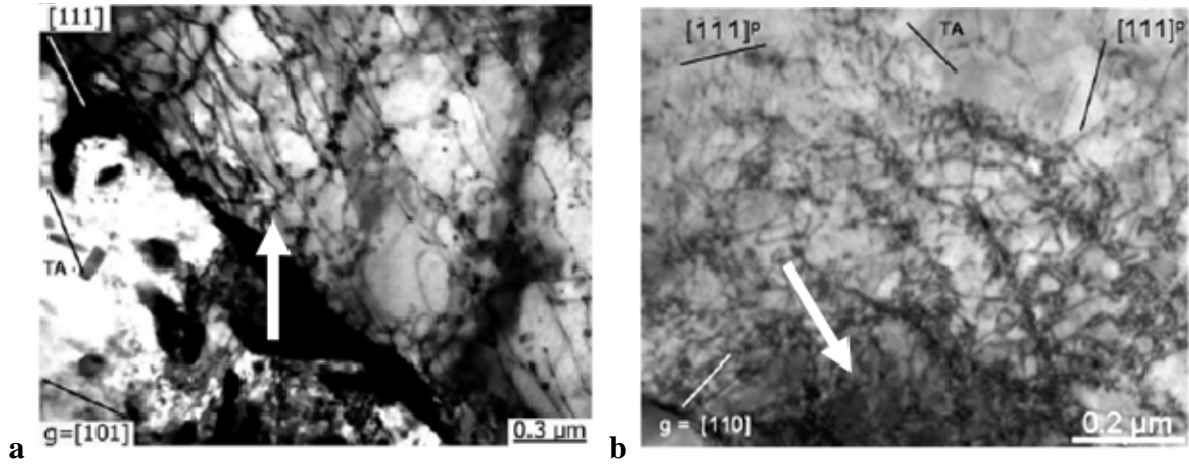


Figure 1.16 Dislocation structure of a ferritic steel tested at -196°C after (a) 2.5 % strain (an arrow marks dislocation straight lines) and (b) after 8 % (an arrow marks a cluster) [17]

With an increase in temperature, dislocation annihilation, leading to the dislocation density decrease, influences the dislocation structure development. Minimum temperature for the thermally activated processes depends on the nature of a metal. In pure iron dislocation climb and grain boundary motion, resulting in the dislocation structure change, starts above 350°C [6]. In alloyed steels this temperature will go up due to dislocation immobilisation by solute atoms and microalloy precipitates. Hot deformation temperatures, above 0.5 of melting point or approximately 700°C for steel, lead to significant grain recrystallisation and dislocation annihilation. This results in a retardation of dislocation structure development with strain, i.e. cluster and cell structure formation at higher temperature requires higher strains than for room temperature deformation. After rolling of a ferritic steel within the $1100-900^{\circ}\text{C}$ temperature range, the dislocation density has been observed to be 10 times less than after room temperature deformation (Figure 1.17). Irregular dislocation structure appeared after 30 % deformation, clusters – after 55 %, Figure 1.18, b,c, which is much higher than during room temperature deformation (compare to Figures 1.14 and 1.15). During hot deformation to the

same strain level the dislocation density decreases with deformation temperature increase, due to annihilation (Figure 1.19).

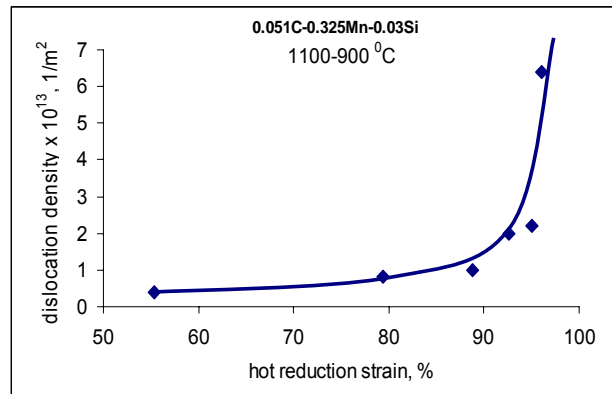


Figure 1.17 Dislocation density dependence on strain during hot deformation of a ferritic steel (derived from [19]); sharp dislocation density increase at 96 % strain can be related to the temperature decrease

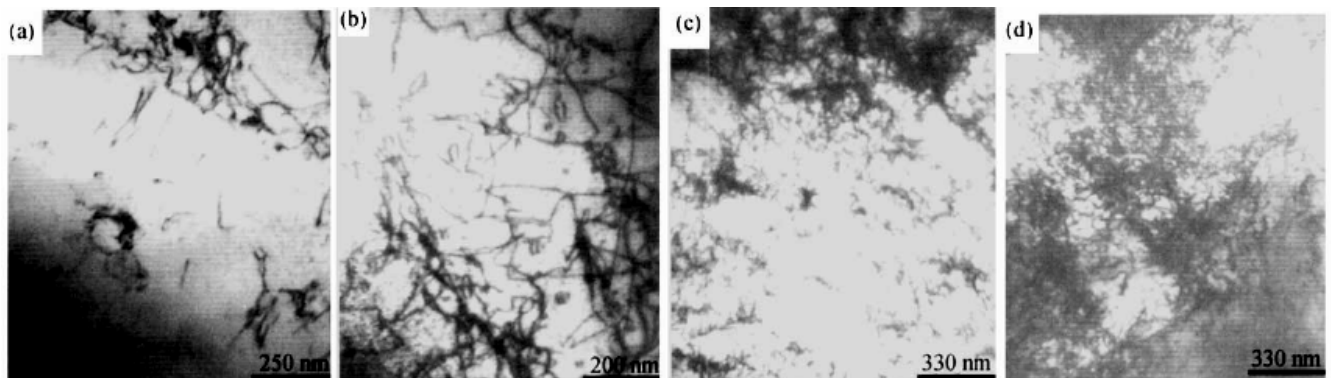


Figure 1.18 Dislocation structure development in a ferritic steel during hot deformation in the range 1100 °-900 °C: (a) – 10 % strain, random dislocations, (b) – 30 %, irregular structure, (c) – 55 %, clusters, (d) – 96 %, cell structure [19]

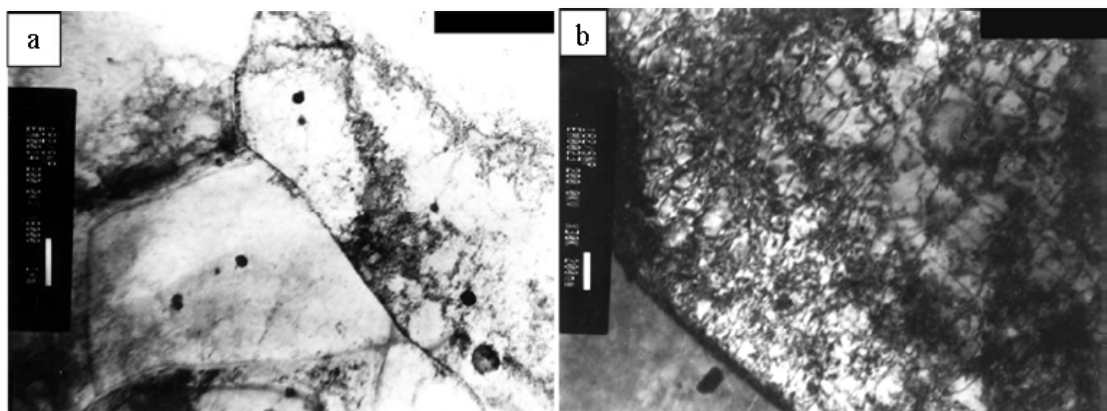


Figure 1.19 Dislocation structure of the 0.11C-0.47Cr-0.47Cu-0.024Nb steel after 50% deformation at (a) 900 °C and (b) 800 °C [20]

Apart from temperature, the dislocation structure development during hot deformation is influenced by (micro) alloy additions. After processing with the same rolling schedule, a more highly alloyed steel had a larger dislocation density than a lower alloyed steel [21], which corresponds to the dislocation density increase with carbon content increase in steel composition found during room temperature deformation [5]. Irregular dislocation structure in the more highly alloyed steel exhibited numerous curved dislocations, although dislocations in the lower alloyed steel were mainly straight-line (Figure 1.20). Precipitates and solute atoms lock the dislocations, increasing the number of dislocation sources and stimulating new dislocation generation.

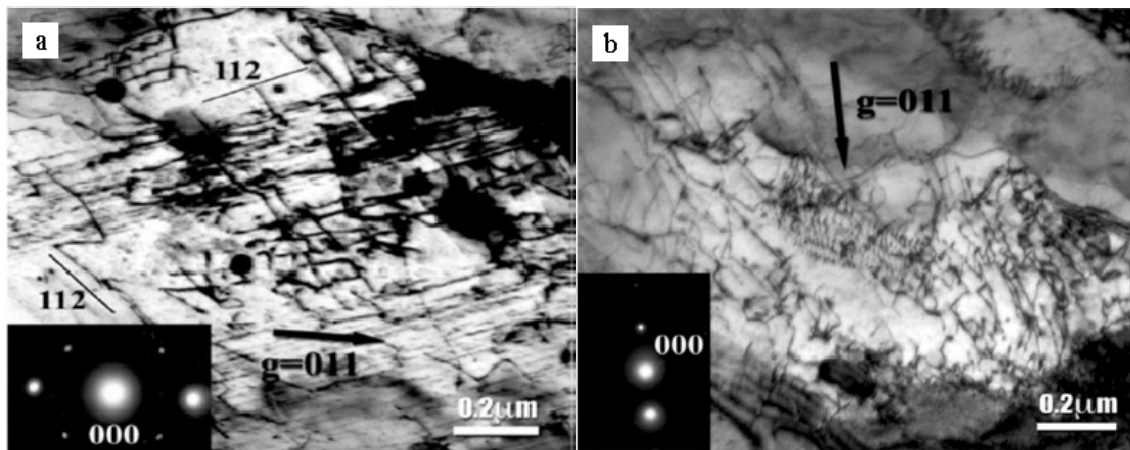


Figure 1.20 Irregular type dislocation structures in the (a) 0.15C steel, dislocation density $0.86 \times 10^{14} \text{ m}^{-2}$, and (b) 0.15 C - 0.1 P steel, dislocation density $2.34 \times 10^{14} \text{ m}^{-2}$ after rolling at 720 – 750 °C to equal strains of 85 % [21]

The dislocation structures after hot deformation may be not equal in different areas. In high strength low alloyed steels some authors have observed grains almost without dislocations and grains with a dislocation density of about 10^{14} m^{-2} in the same material [22, 23], although other authors did not mention such a great difference [24] (Figure 1.21). This can be explained by the unequal distribution of local strains compared to the macroscopic deformation of bulk material.

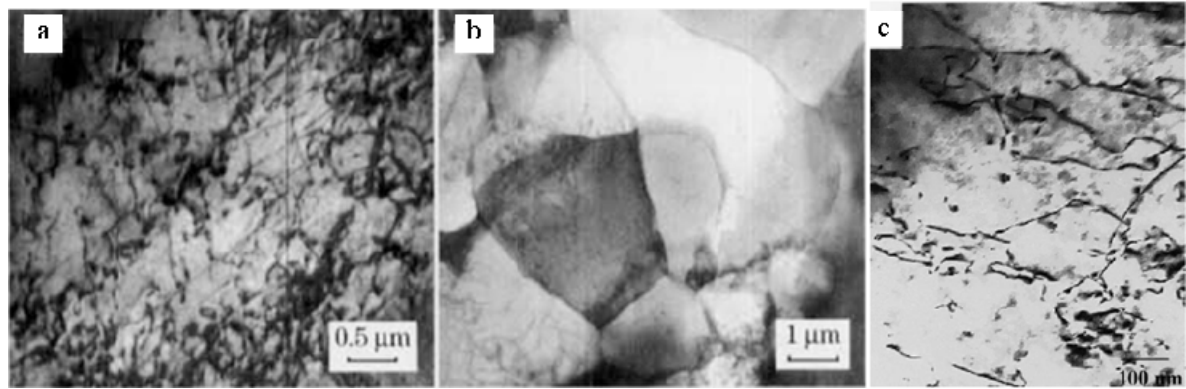


Figure 1.21 Irregular type dislocation structures in the (a), (b) 0.08 C-1.7 Mn-0.08 Nb-0.08 Ti - 0.08 V steel after rolling at 1200 – 900 °C and coiling at 550 °C [22]; and (c) 0.06 C-1.5 Mn-0.07 Nb-0.02 Ti-0.1 V steel after rolling at 1325-900 °C and coiling at 650 °C [24]

In fcc materials it is possible to observe the same dislocation structure types as in the bcc materials, Figure 1.13, but twinning significantly influences the dislocation structure development [25]. Recent investigations of fcc single crystals showed twinning to be the major deformation mechanism in $\langle \bar{1} 11 \rangle$ and $\langle 001 \rangle$ directions and slip in $\langle \bar{1} 23 \rangle$ directions (Figure 1.22). In polycrystalline material both mechanisms operate at the same time, as the grain orientation to the loading direction is more random (Figure 1.23).

Reverse deformation

During reverse deformation the dislocation density has been found to decrease compared to that in the initial stage of straining both in bcc [28], Figure 1.24, a, and fcc structures [29], Figure 1.24, c. Further increase in reverse strain results in a dislocation density increase.

The cell structure, if formed after pre-straining, disappears during the initial stage of the reverse deformation both in bcc [30,31], Figure 1.25, and fcc [31], Figure 1.26, structures. This leads to a rather uniform dislocation density just after the onset of reverse straining. Further reverse strain brings back the cell structure. With an increase in forward pre-strain the cell structure dissolution strain during reverse deformation increases [32].

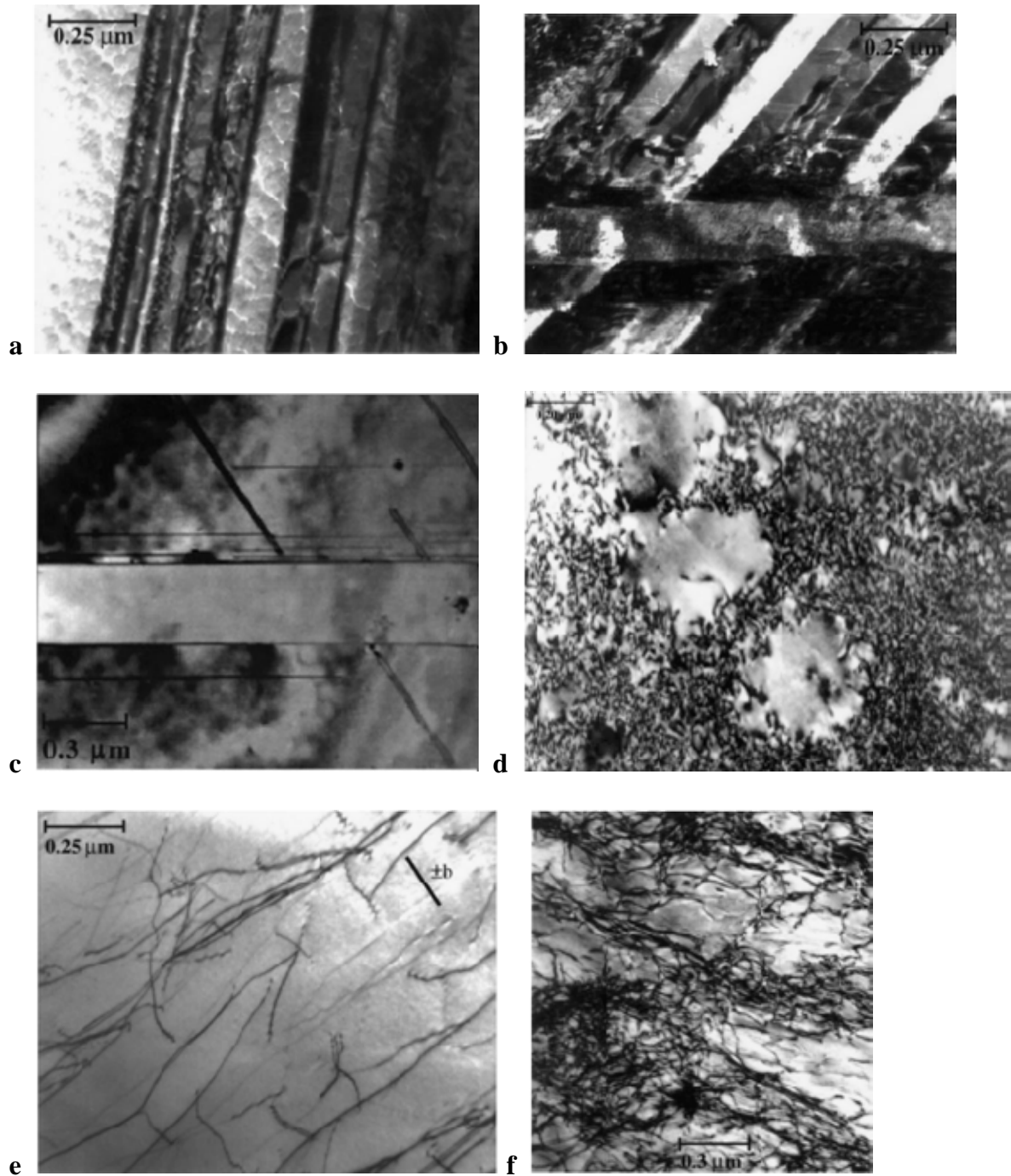


Figure 1.22 TEM micrographs of a fcc single crystal deformed at room temperature in (a), (b) - $\langle \bar{1}11 \rangle$ direction after 3% strain (one twin system) and 35% (two twin systems); (c), (d) - $\langle 001 \rangle$ direction after 3% (one twin system) and 40% (dislocation cell structure); (e), (f) - $\langle \bar{1}23 \rangle$ direction after 3% (start of the irregular dislocation structure formation) and 50% (irregular dislocation structure fully developed) [26]

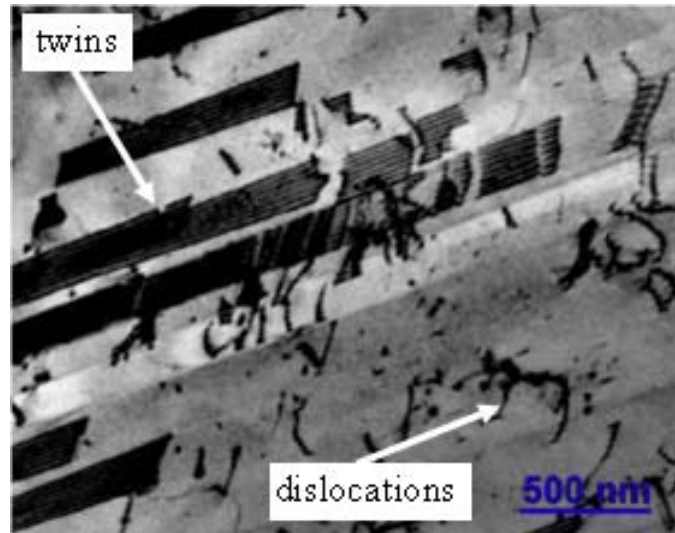


Figure 1.23 TEM micrograph of the 316LN austenitic steel after 5 % deformation at room temperature [27]

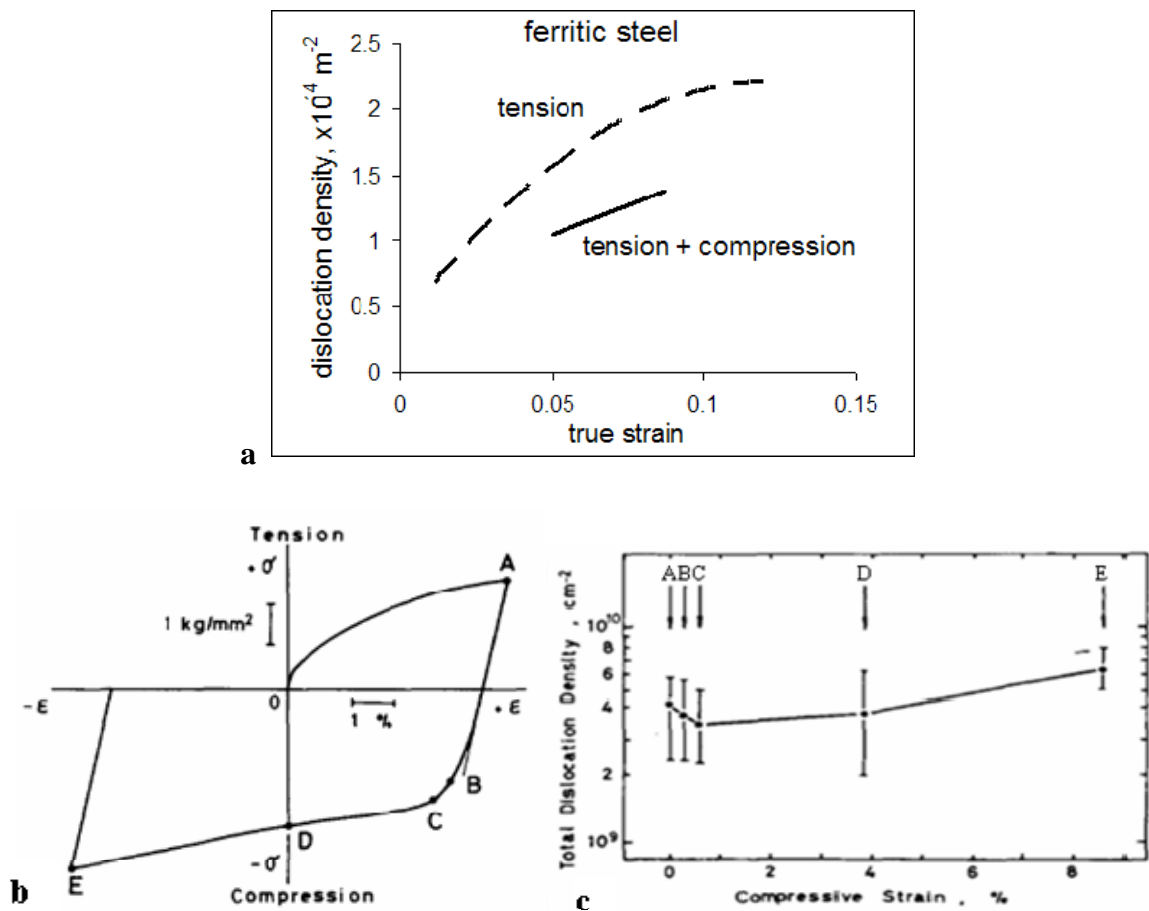


Figure 1.24 (a) Dislocation density change during tension and subsequent compression of a ferritic steel 0.16 C-1.43 Mn-0.41 Si (bcc) [28], (b) tension-compression stress-strain curve of aluminium (fcc) and (c) dislocation density in aluminium during compression half circle after 4.5 % pre-strain in tension, points A-E according to (b) [29]

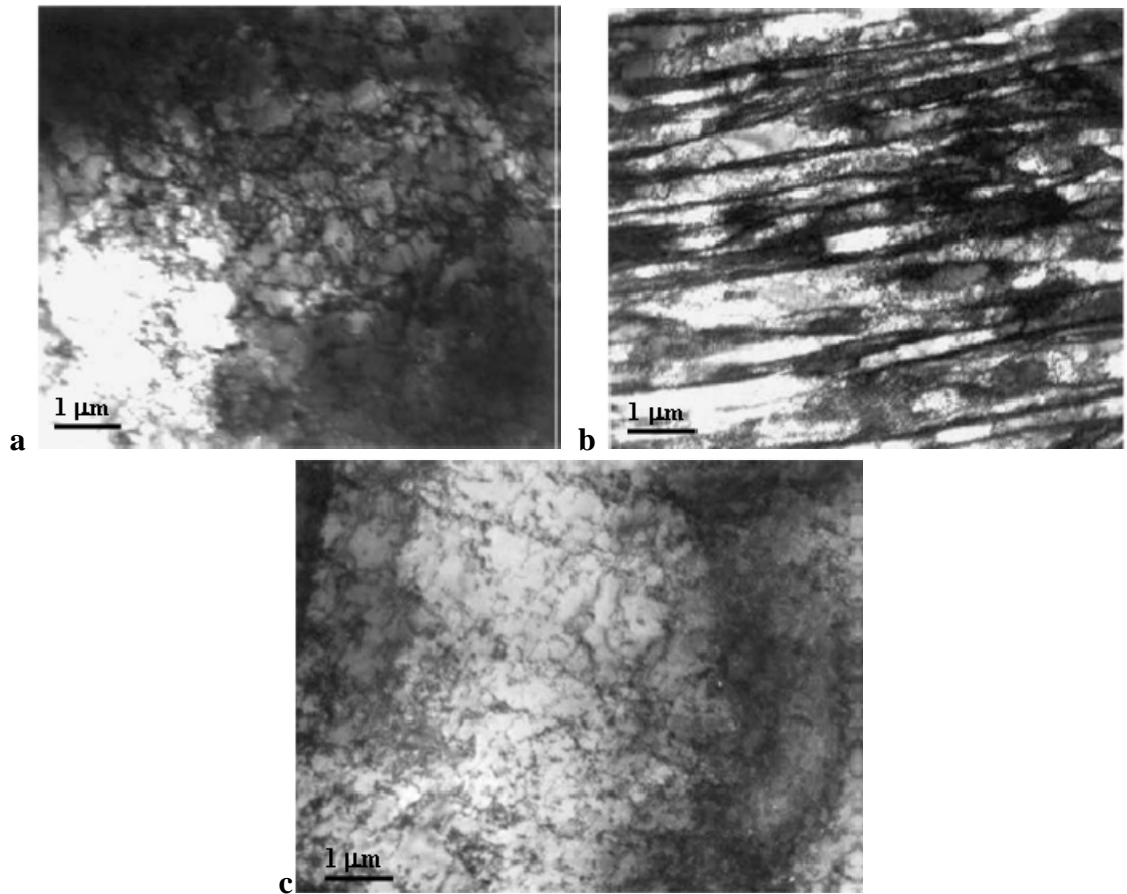


Figure 1.25 Dislocation structures of the interstitial free steel (bcc) deformed at -120°C : (a) the irregular structure after $\epsilon = 0.26$ shear pre-strain, (b) the cell structure after $\epsilon = 1$ shear pre-strain and (c) the irregular structure after $\epsilon = 0.26$ shear reverse strain [31]

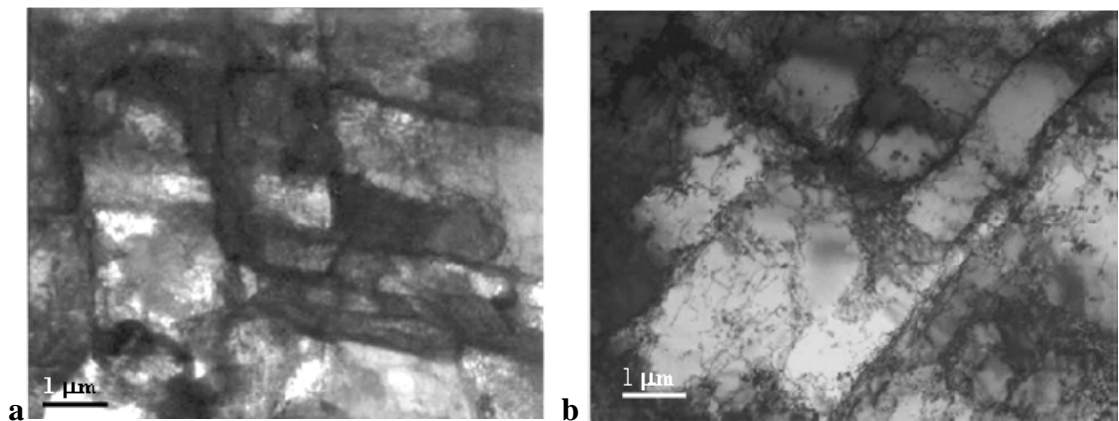


Figure 1.26 Dislocation structures of pure aluminium (fcc) deformed at -120°C : (a) the cell structure after $\epsilon = 0.26$ shear pre-strain and (b) dissolution of the cell walls after $\epsilon = 0.26$ shear reverse strain [31]

Investigation of the dislocation structure change during strain path change of less than 180° also showed dissolution of the cell walls in both bcc [33] and fcc [34], Figure 1.27,

materials. However, in highly alloyed materials dislocation structure change with strain path change has not been observed, which was related to dislocation immobilisation by precipitates after pre-straining [34] (Figure 1.28).

In addition to the yield lowering effect, observed in pure Bauschinger test (strain path change is 180°), strain path changes of less than 180° also leads to yield lowering (see section 1.2). This may have a rather high industrial importance, as pure Bauschinger conditions are observed less frequently than strain path changes of less than 180° . The latter should be taken into account during mechanical property development in cold forming technologies.

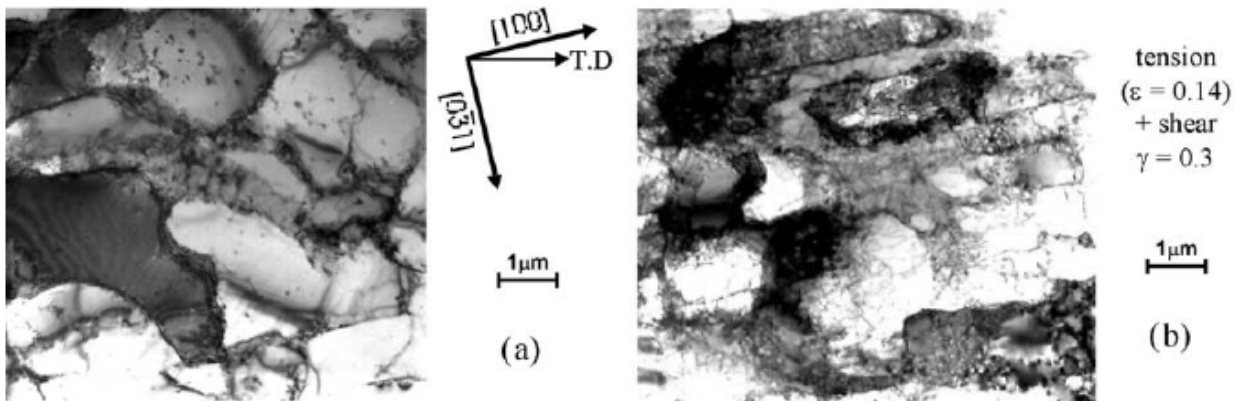


Figure 1.27 Dislocation structures of pure aluminium (fcc) deformed at room temperature: (a) the cell structure after $\epsilon = 0.14$ tension pre-strain and (b) dissolution of the cell walls after $\gamma = 0.3$ shear strain (strain path change is 135°) [34]

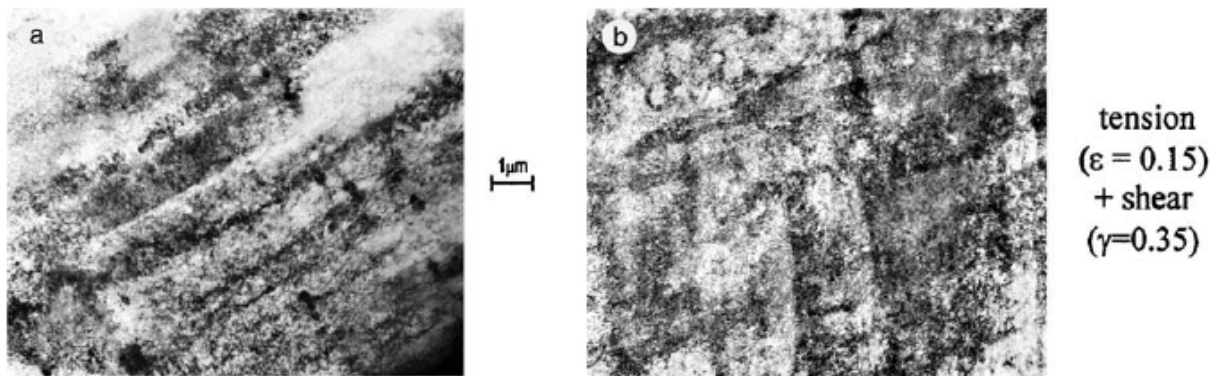


Figure 1.28 Dislocation structures of Al-Mg-Si alloy (fcc) deformed at room temperature: (a) the irregular dislocation structure after $\epsilon = 0.15$ tension pre-strain and (b) the irregular dislocation structure after $\gamma = 0.35$ shear strain (strain path change is 135°) [34]

1.1.7 Yield strength and theory of work-hardening

To start deformation by slip, either existing dislocations should be moved or new dislocations generated and then moved [8]. Dislocations present in the unworked material become anchored by obstacles (such as Cottrell atmospheres of solute atoms, precipitates and other dislocations). To release them from the obstacles a certain stress is required – the upper yield point (UYP, Figure 1.29, a). However, after dislocations start their glide, the stresses needed to continue free dislocation motion become lower – the lower yield point (LYP, Figure 1.29, a). Having started their glide, dislocations move freely without stress increase during some period of straining. When they meet new obstacles on their way the stress required for continued motion increases again. If, shortly after unloading so as not to allow thermal activation of solute diffusion, re-loading is continued in the same direction dislocations start moving from their new positions forward and the yield point is not observed (Figure 1.29, a). Alternatively, some authors have reported a small yield point after unloading and reloading in the same direction, which was not observed when loading was stopped and then resumed from the same position on the stress-strain curve [35]. A possible explanation suggested was that the dislocations, during unloading, move backwards under the action of the back stress from the obstacles and rearrange themselves into a lower energy state. Thus during next stage of forward deformation a small degree of overstressing is needed to break away from this lower energy state and resume the stress-strain behaviour established prior to unloading (Figure 1.29, b).

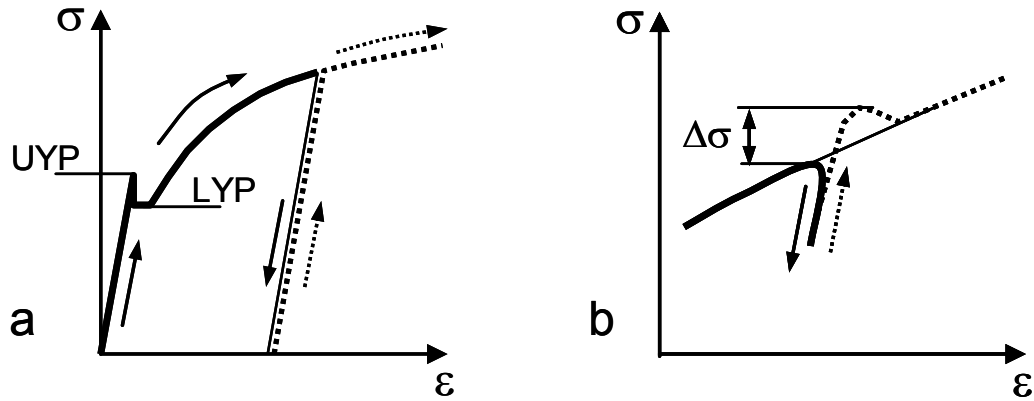


Figure 1.29 (a) Typical stress-strain curve: solid line for the unworked and dot-line for the strain-hardened material, (b) the yield point after unloading and further reloading in the same direction (after [35])

Deformation of a single crystal

The form of the stress-strain curve depends on the crystal lattice type as dislocation movement is determined by the most favourable slip planes and slip directions. In the general case, it is possible to distinguish three main stages of work-hardening, more commonly observed in fcc structures but also applicable to the bcc lattice (Figure 1.30) [6].

According to the *long range work-hardening theory*, during stage I easy glide of dislocations occurs. Here the number of dislocation sources is considered to be constant, the slip planes are not piled-up with dislocations and the spacing between the moving dislocations is large. As the number of dislocation-dislocation interactions is small in this stage, the stress increases slowly. Stage II starts when the dislocation density increases more significantly. Under the increasing external loading new dislocation sources produce more dislocations which then pile-up in groups and lock each other. As the most favourable slip planes become occupied by pile-ups, multiple slip starts on all the possible slip planes for a given crystal type. Interaction of dislocations, moving on intersecting slip planes, significantly retards their further motion. Thus, to continue deformation, in stage II the yield stress also increases dramatically. Stage III starts when the stress reaches the high value needed for cross-slip,

when screw dislocations, instead of gliding along their slip planes, “climb” perpendicularly to other slip planes. This reduces the stress field of pile-ups and consequently the slope of the stress-strain curve.

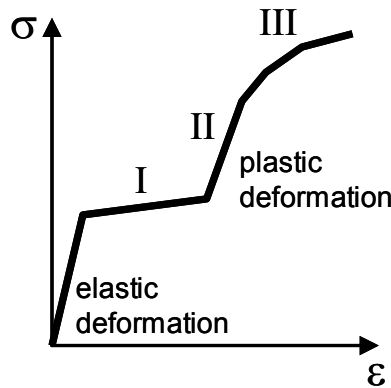


Figure 1.30 Schematic stress-strain curve showing three stages of work-hardening

According to the *short range work-hardening theory*, during stage I dislocation pile-ups (or irregular patterns called dislocation tangles) appear locally within a given grain and retard the dislocation motion in some areas of this grain. The dislocation density is inhomogeneous, and new dislocations are produced constantly to fill free space within that given crystal. Stage II starts when the dislocation density becomes uniform. During the second stage, dislocation density remains uniform but the spacing between the pile-ups and tangles decreases. As less free space remains, shorter length dislocations bow to produce new ones (Frank-Read mechanism [7]). To bow a short dislocation in a loop requires high stresses, therefore the yield stress increases. Stage III in the short range theory is also related to cross-slip.

Stages IV and V of work-hardening were reported quite early [36] (Figure 1.31). Recent investigations explain them by the formation of a cell structure [37-39]. Thus the cell structure, with significant dislocation density in the cell walls and negligible density in the cell interior, appears during stage II. By the end of this stage dislocation density in the walls reaches significant values, up to 10^{16} m^{-2} [38]. A decrease in the work-hardening rate during stage III

occurs due to dislocation annihilation in the cell walls, cross-slip within the walls and additional slip in the cells along the secondary slip planes. With further deformation the crystal lattice misorientation between adjacent cells increases, which leads to formation of a sub-grain structure [40,41]. This prevents dislocations crossing from one cell to another and the work-hardening rate increases during stage IV.

The decrease in hardening rate during stage V is related to multiple twinning instead of gliding [40], although some authors reported work-hardening rate increase due to twinning [11,26]. With increasing temperature sub-grain growth becomes the major cause of the hardening rate decrease. In general, quantitative parameters describing stages IV and V depend on temperature and strain-rate.

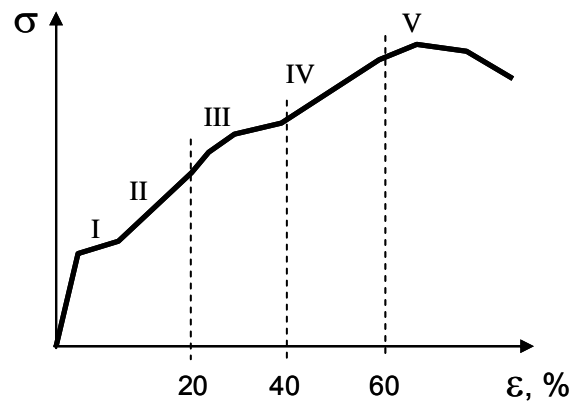


Figure 1.31 Five stages of work-hardening in fcc single crystals (after [37])

Deformation of a polycrystalline material

A bcc material, which is less plastic than an fcc material due to a smaller number of most favourable slip planes, does not normally show distinct differences between stages II, III and IV, Figure 1.32, a, and the work-hardening exponent decreases with increasing strain. The stress-strain curve of an fcc polycrystalline material resembles the shape for the fcc single crystal, but occurs at higher stresses [26] (Figure 1.32, b). Work-hardening exponents for an fcc material may increase or remain stable with increasing strain.

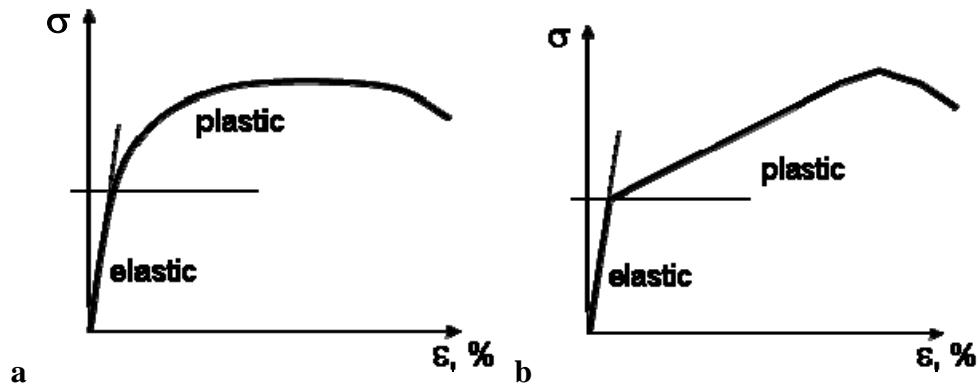


Figure 1.32 Typical view of the stress-strain curve of a (a) bcc material and (b) fcc material

During deformation of polycrystals, grains become separated into domains or cell-blocks within which different slip systems operate [15]. The boundaries between the cell-blocks accommodate the lattice misorientations between blocks which result from different glide systems and cell-block rotation. With increasing strain these block boundaries with high dislocation density develop first into walls and then into sub-grain boundaries. Thus the original grain structure becomes divided into a sub-grain structure. The sub-grains, of much smaller size than the initial grains, follow the Hall-Petch relationship with respect to the yield stress and so the yield stress increases due to “grain refinement”. In a polycrystalline material, which contains a second phase or precipitated particles, slip is non-uniform through the volume, as different phases have different plasticity. This leads to the localisation of deformation in the softer matrix and the appearance of dislocation arrays, or microbands [18]. Localisation of deformation results in significant dislocation density growth in the microbands and the yield stress increases. Accumulation of dislocations after some strain leads to the formation of microcracks within the microbands, which then transform into macrocracks leading to fracture [42].

The stress-strain curve depends on test temperature and strain rate (Figures 1.33 and 1.34). With temperature increase and strain rate decrease the yield stress and the work-hardening

rate decrease [27, 43-45]. This corresponds to the dislocation structure development with strain (see section 1.1.6)

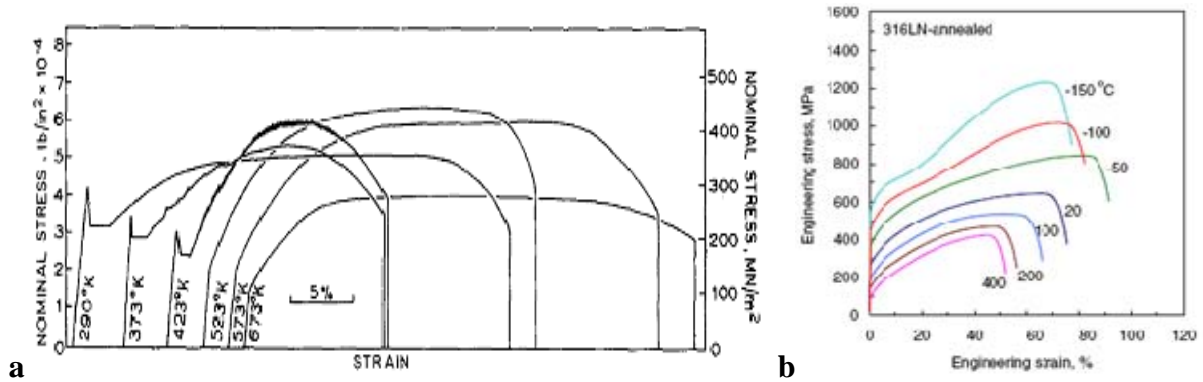


Figure 1.33 Stress-strain curve dependence on test temperature in a (a) ferritic steel (bcc) [43], and (b) austenitic steel (fcc) [27]

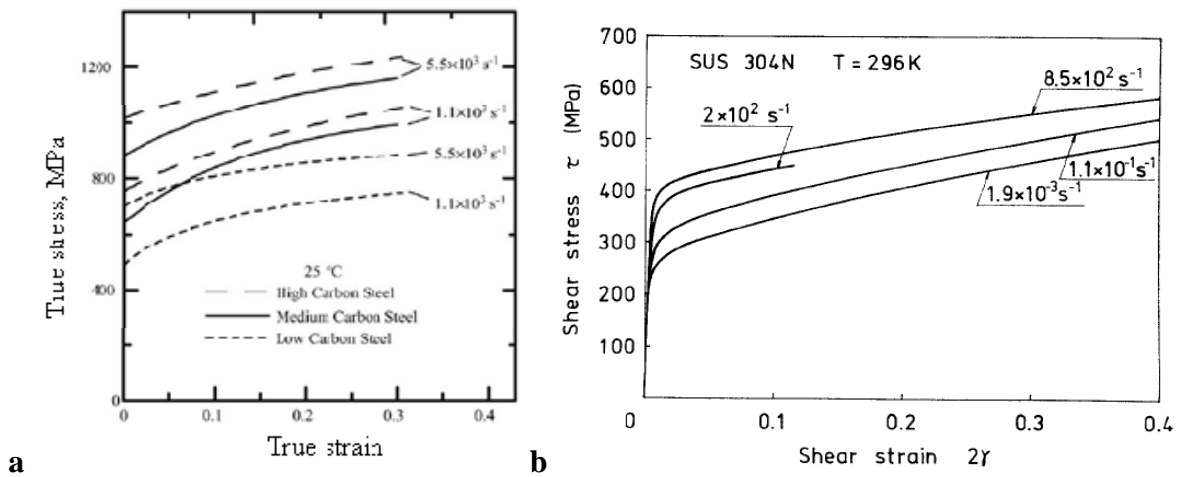


Figure 1.34 Stress-strain curve dependence on strain rate in (a) ferritic steels (bcc) [5], and (b) an austenitic steel (fcc) [44]

In steels the stress-strain curve depends on chemical composition. With an increase in carbon content the yield stress and the work-hardening exponent increase (Figure 1.35). The presence of spheroidised cementite particles in medium- and high-carbon steels prolongs Lüders strain and leads to work-hardening rate decrease [46]. Alloying results in an upward shift of the stress-strain curve along the stress axis, which may happen due to phase balance change, grain refinement, solid solution and precipitation strengthening (see more in section

1.4). The work-hardening exponent in carbon steels has been observed to be in the range 0.07 - 0.30 and decreases with an increase in strength (Figure 1.37).

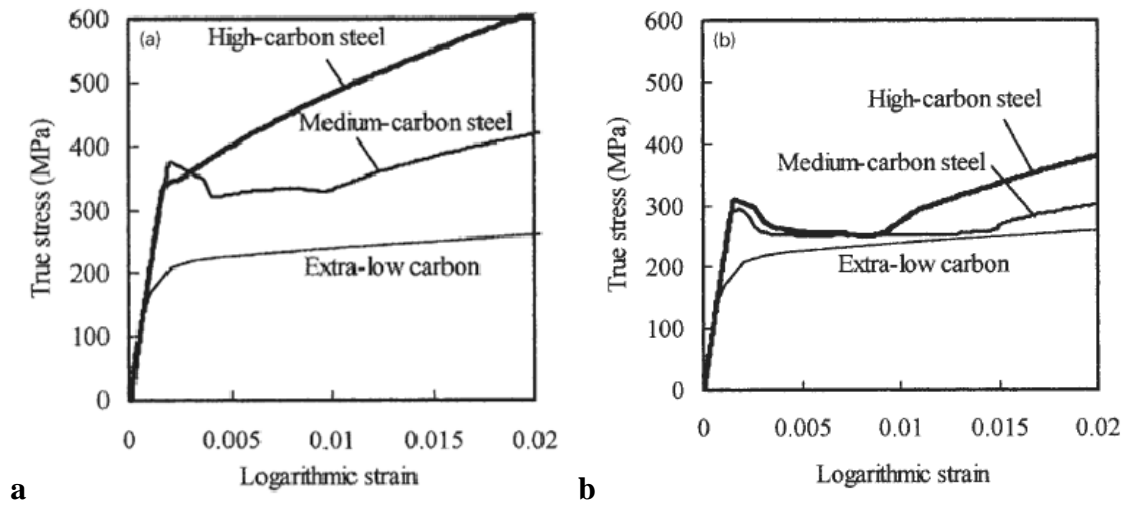


Figure 1.35 Stress-strain curve dependence on carbon content in ferritic steels for (a) rod shape and (b) spheroidised shape carbide morphology [46]

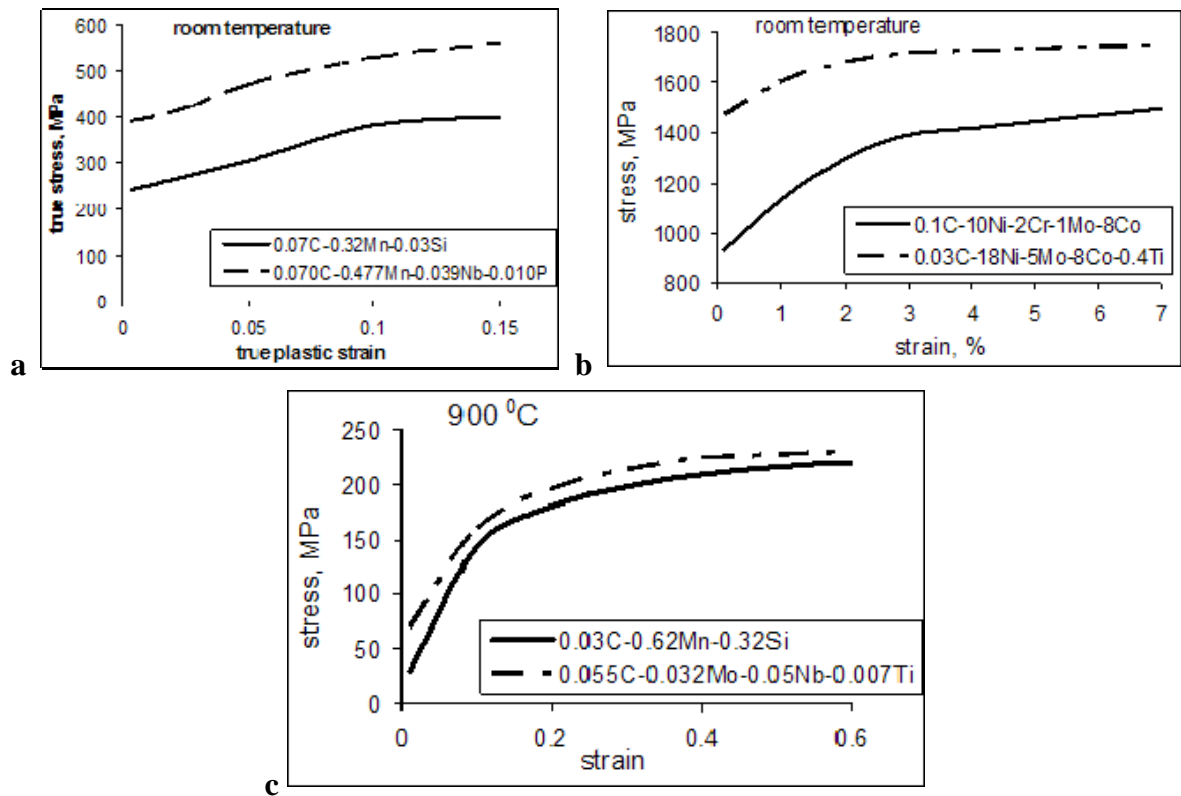


Figure 1.36 Influence of alloying on the stress-strain curve during cold deformation of (a) ferritic steels (solid line after [30], dash line after [47]) and (b) austenitic steels [48]; (c) during hot deformation of ferritic steels [49]

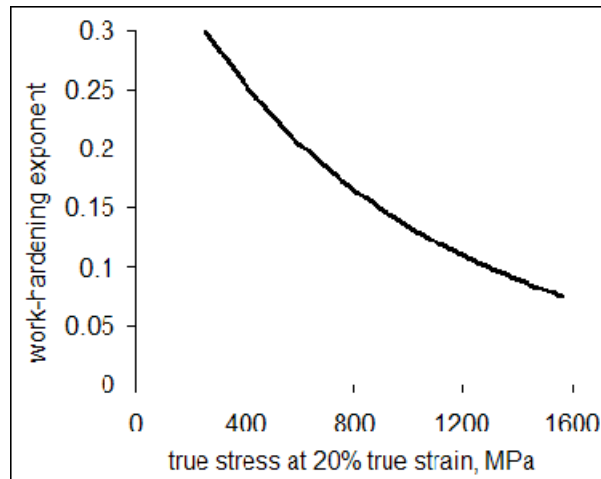


Figure 1.37 Work-hardening exponent dependence on steel strength [50]

The increment of yield stress due to work-hardening shows a linear dependence on the square root of dislocation density (Figure 1.38, a). However, the absolute values of the slope depend on temperature, carbon content and presence of strengthening solute atoms (Figure 1.38, b). The last can be explained by significant pinning of dislocations by solute atoms [51].

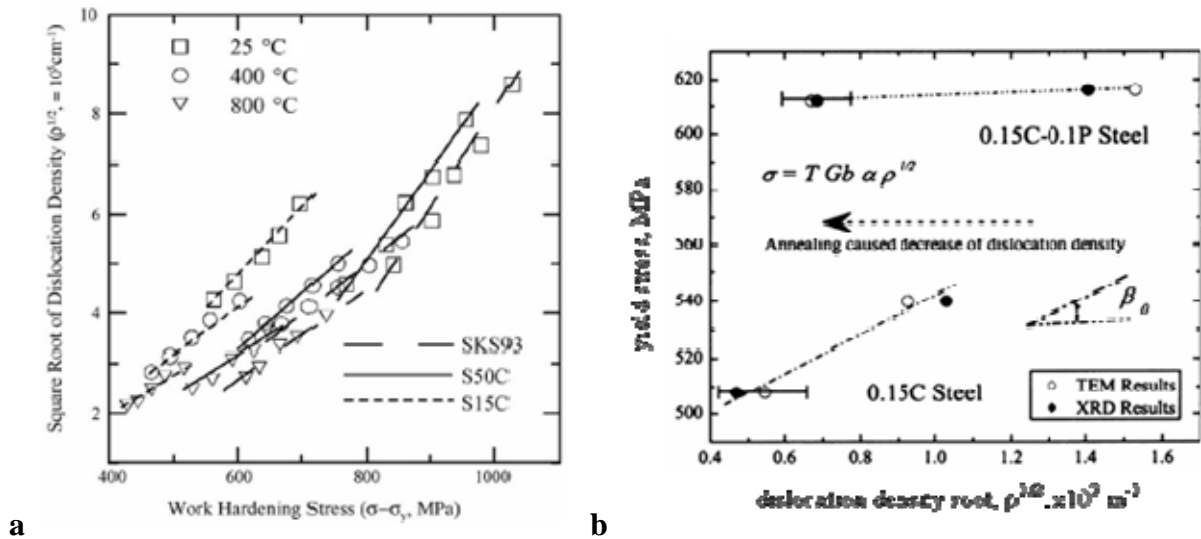


Figure 1.38 Dislocation density-yield stress dependence for (a) carbon steels [5] and (b) phosphorus alloyed steel [21]; steel SKS93 contains 1.16% C, S50C – 0.48% C, S15C – 0.15% C

1.2 Work-softening due to the Bauschinger effect

Reduction in the yield stress of polycrystalline metal specimens following pre-strain in the opposite direction was reported by Bauschinger in 1881 (Figure 1.39).

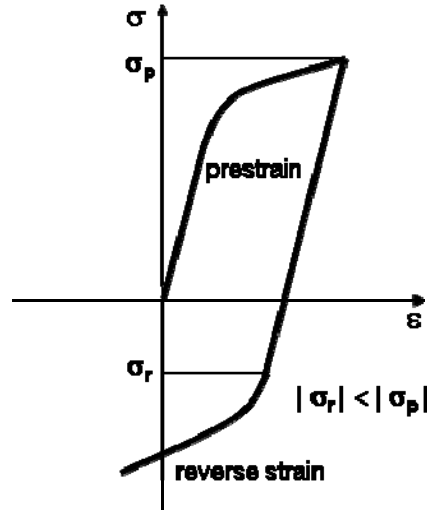


Figure 1.39 Schematic illustration of the Bauschinger effect:
 σ_p – maximum pre-stress, σ_r – the yield stress in the reverse direction

Further work revealed the effect to be more complex and several parameters were developed to assess this affect [52-55] (Figure 1.40).

1.2.1 Evaluation of the magnitude of the Bauschinger effect parameters

There are three established parameters used to assess the absolute values of the Bauschinger effect: the stress, strain and energy parameters (Figure 1.40).

In the literature there are a minimum of four different mathematical expressions of the stress parameter. These are related to different points on the forward-reverse stress-strain curve (Figure 1.40, a). The stress parameter $\beta_{\sigma 1}$ describes the relative decrease in the yield stress from forward to reverse deformation:

$$\beta_{\sigma 1} = \frac{\sigma_p - \sigma_r}{\sigma_p},$$

where σ_p is maximum pre-stress and σ_r is the yield stress in the direction of reverse strain (point of the stress-strain curve deviation from the straight line, normally around 0.1% reverse strain).

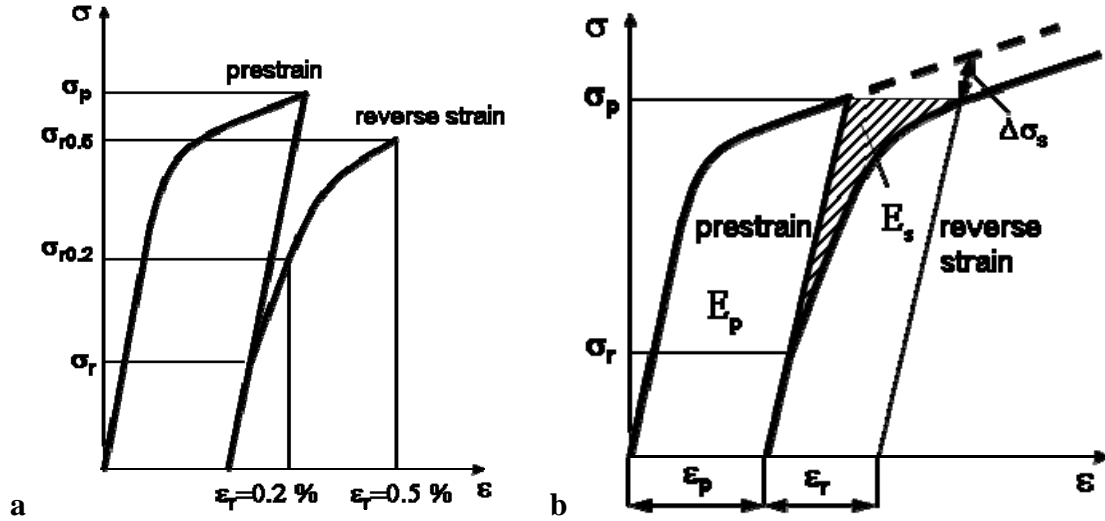


Figure 1.40 Stress-strain curves for (a) the Bauschinger effect stress-parameter and (b) the Bauschinger effect strain and energy parameters: $\sigma_{r0.2}$ and $\sigma_{r0.5}$ – the yield stress at 0.2% and 0.5% reverse strain, $\Delta\sigma_s$ – permanent work-softening, ϵ_p – pre-strain, ϵ_r – “Bauschinger strain”, the strain in the reverse direction corresponding to the point of reverse stress equal to the maximum pre-stress σ_p , E_p – energy spent during pre-strain, E_s – energy saved during reverse straining due to the Bauschinger effect, shown by the shaded area

The stress parameters $\beta_{\sigma 2}$, $\beta_{\sigma 3}$ and $\beta_{\sigma 4}$, calculated using stress values at 0.2 % and 0.5 % reverse strain, show the rate of property restoration during reverse straining after the yield drop:

$$\beta_{\sigma 2} = \frac{\sigma_p - \sigma_{r0.2}}{\sigma_p}, \quad \beta_{\sigma 3} = \frac{\sigma_p - \sigma_{r0.5}}{\sigma_p}, \quad \beta_{\sigma 4} = \frac{\sigma_{r0.5}}{\sigma_p},$$

where $\sigma_{r0.2}$ and $\sigma_{r0.5}$ are stresses at 0.2 % and 0.5 % reverse strain.

As the yield stress represents the start of dislocation slip (with acting back stress from the obstacles, in the case of reverse deformation) parameter $\beta_{\sigma 1}$ describes the “short range” work-softening. As the work-hardening rate depends on material chemistry (carbon content and

alloying) and microstructure (phases, precipitates and dislocation density), the parameters $\beta_{\sigma 2}$, $\beta_{\sigma 3}$ and $\beta_{\sigma 4}$ represent “long range” work-softening and show how permanent the Bauschinger effect is when deformation increases in the reverse direction.

The Bauschinger strain parameter describes the amount of deformation in the reverse direction needed to reach the pre-stress level of stress (Figure 1.40, b):

$$\beta_{\varepsilon} = \frac{\varepsilon_r}{\varepsilon_p},$$

where ε_p is plastic pre-strain and ε_r is plastic strain in the reverse direction for the point of equal stress value to the pre-stress.

The Bauschinger energy parameter describes the amount of energy needed during the reverse deformation to reach the pre-stress level of stress:

$$\beta_E = \frac{E_s}{E_p}$$

where E_p is the energy spent during pre-strain and E_s is energy saved during reverse straining due to the Bauschinger effect (Figure 1.40, b).

In addition to stress parameters $\beta_{\sigma 2}$, $\beta_{\sigma 3}$ and $\beta_{\sigma 4}$ the Bauschinger strain and energy parameters assess how long lasting the Bauschinger effect is and thus also support the “long range” work-softening approach.

1.2.2 Causes of the Bauschinger effect

There are two principal Bauschinger effect theories (Figure 1.41); back stress and Orowan theory [52, 56]. During forward plastic deformation moving dislocations interact with different obstacles (other dislocations, grain boundaries and precipitates) preventing their further propagation. This generates a back stress around the contact point resisting further progress of similarly signed dislocations. During the reverse deformation this back stress

repels the dislocations from the obstacles in the opposite direction, namely in the direction of reverse strain. Thus the stress field helps to move the dislocation in the direction of reverse strain and the reverse yield stress drops by the level of the back stress (Figure 1.41,a). According to the back stress theory an increase in dislocation density increases the number density of dislocation-dislocation interaction sites and consequently the level of back stress. Thus the Bauschinger effect should be larger in a material with a higher dislocation density. But with an increase in initial dislocation density (and/or pre-strain) the number of mobile dislocations can decrease. This occurs due to immobilisation of moving dislocations by pile-ups and possible formation of cell-structures, where mobile dislocations in the cell interior are many times lower in density than the total number accumulated in the cell walls. Thus with an increase in dislocation density it is possible to expect a maximum in the Bauschinger effect and then a decrease after some level of pre-strain. However, this maximum has not been observed so far in the reported literature, due to pre-strains used being below 8 %.

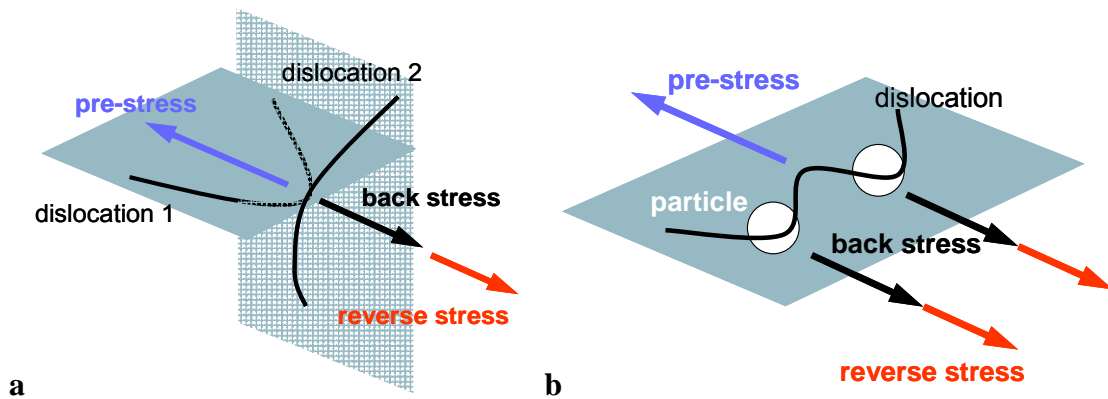


Figure 1.41 Schematic diagram of the (a) dislocation-dislocation and (b) dislocation-particle interaction

In an alloyed material, precipitated particles also act as interaction sites increasing the level of back stress (Figure 1.41, b). Thus, increasing the particle volume fraction and their number density will increase the number of interactions between dislocations and particles and hence the back stress. However, not all the particles equally contribute to dislocation pinning. When particles are coherent with the matrix the cutting mechanism operates. In this case the

dislocation retardation force will depend on particle chemistry, as particle composition influences its mechanical strength. When particles are incoherent the bowing mechanism operates. In this case the dislocation retardation will depend on interparticle spacing, as, with a decrease in interparticle spacing, the dislocation curvature energy needed for a dislocation to pass increases. Predominance of one or another mechanism depends on the average particle size, as, with an increase in particle size, the particles lose coherency with the matrix lattice. Thus particle number density is not enough to assess the influence of precipitates on the Bauschinger effect. Particle chemistry, size and distribution should also be taken into account.

1.2.3 Main features of the Bauschinger effect

With an increase in pre-strain the stress parameter $\beta_{\sigma 1}$ increases and the strain and energy parameters decrease (Figure 1.42). This may be related to the total dislocation density increase, leading to an increased yield lowering effect, but mobile dislocation density decrease, leading to a faster return of strength, with increase in pre-strain. Some authors reported yielding during unloading, and consequently the stress parameter $\beta_{\sigma 1} > 1$ [52]. This was explained by relaxation of the elastic back stresses in some grains leading to plastic deformation in other grains.

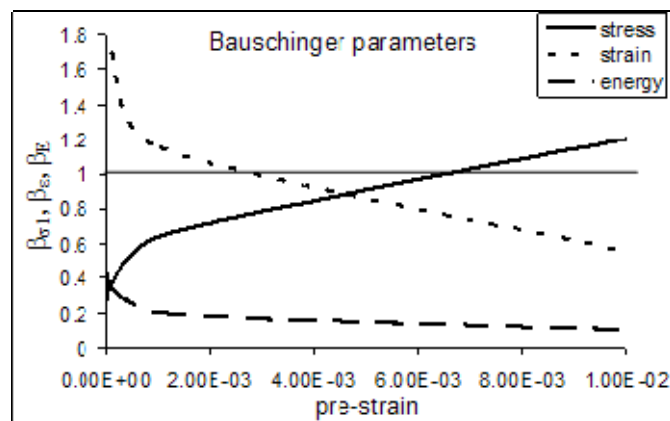


Figure 1.42 The Bauschinger effect parameters dependence on pre-strain for 0.17% C steel (derived from [52])

The appearance of a plateau on the reverse stress-strain curve is related to the dislocation density decrease and the cell structure dissolution during the initial stage of reverse loading both in bcc and fcc materials (Figure 1.43). With an increase in reverse strain the dislocation density increases and the reverse stress-strain curve goes up. With an increase in test temperature the forward-reverse stress-strain curve goes down and the work-hardening rate in the reverse direction decreases, Figure 1.44, which corresponds to a decrease in dislocation density due to annihilation at higher temperatures.

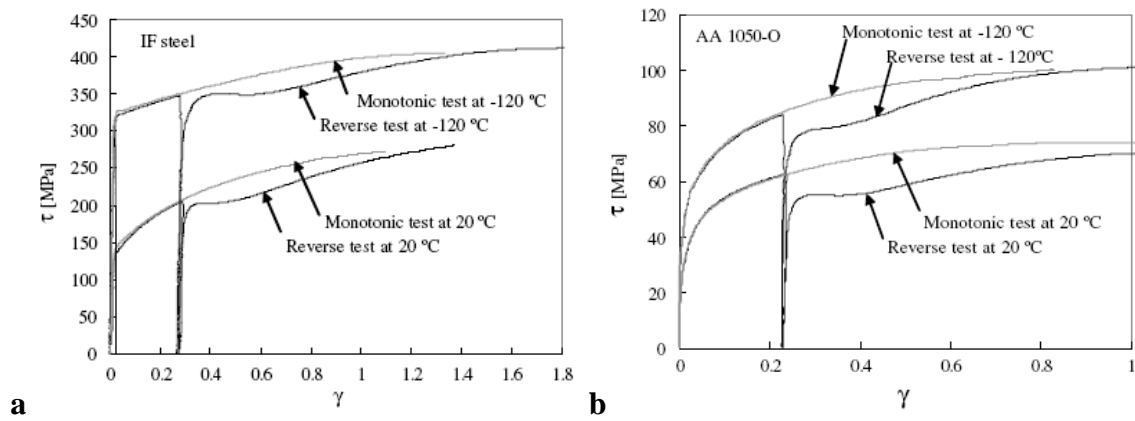


Figure 1.43 Forward-reverse stress-strain curves of (a) IF steel (bcc) and (b) aluminium (fcc) [31]

After reverse loading the work-hardening rate is higher than in the forward direction, but decreases rapidly with an increase in reverse strain both in bcc [31, 57] and fcc [32, 58] materials (Figure 1.45, a). The work-hardening rate does not show significant dependence on strain-rate at relatively low strain rates, i.e. 5×10^{-5} - $5 \times 10^{-3} \text{ s}^{-1}$ (Figure 1.45, b).

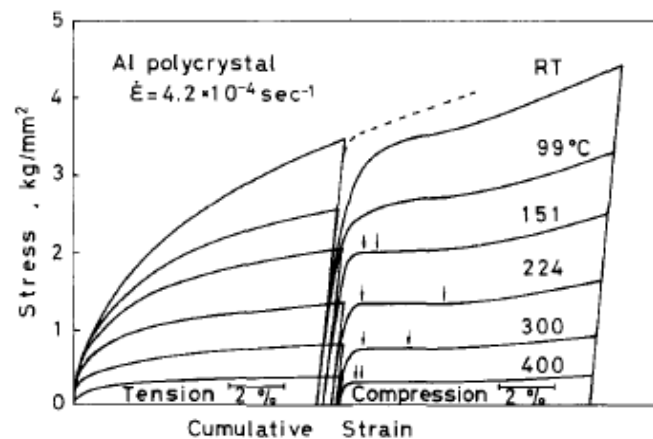


Figure 1.44 Forward-reverse stress-strain curve dependence on temperature [29]

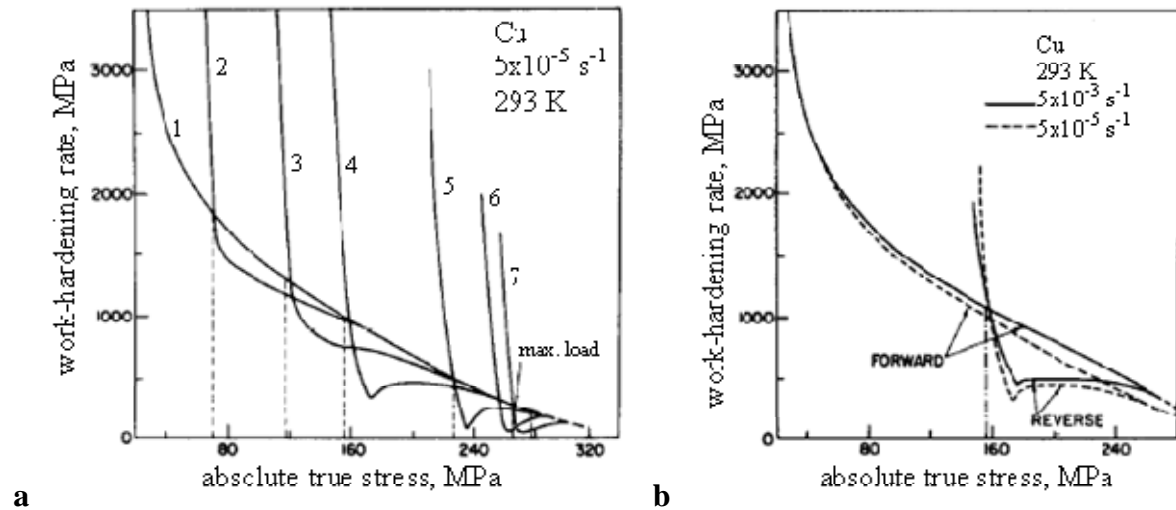


Figure 1.45 (a) Work-hardening rate dependence on stress for forward (curve 1) and reverse deformation after pre-strains of 0.02 (2), 0.04 (3), 0.08 (4) in compression and 0.18 (5), 0.28 (6), 0.33 (7) in tension; (b) work-hardening rate dependence on strain rate [32]

With an increase in carbon content in steels the yield lowering effect and the work-hardening rate in the reverse direction increase (Figure 1.46, a). Steels with plate-like cementite morphology (pearlite), compared to spheroidised shape, show a larger Bauschinger effect (Figure 1.46, b). Permanent softening due to the Bauschinger effect increases with an increase in volume fraction of spheroidised cementite, due to an increase in number density of dislocation-particle interaction sites (Figure 1.46,c).

With an increase in alloying by solute strengthening and precipitation strengthening elements the plateau on the reverse stress-strain curve disappears, Figure 1.47, a, due to retardation of dislocation structure dissolution, and the Bauschinger effect increases, due to an increase in the number of interactions between dislocations and obstacles, namely solute atoms and precipitates (Figure 1.47, b, c).

Ageing after pre-straining decreases the Bauschinger effect due to immobilisation of dislocations by Cottrell atmospheres of interstitial solutes (Figure 1.48).

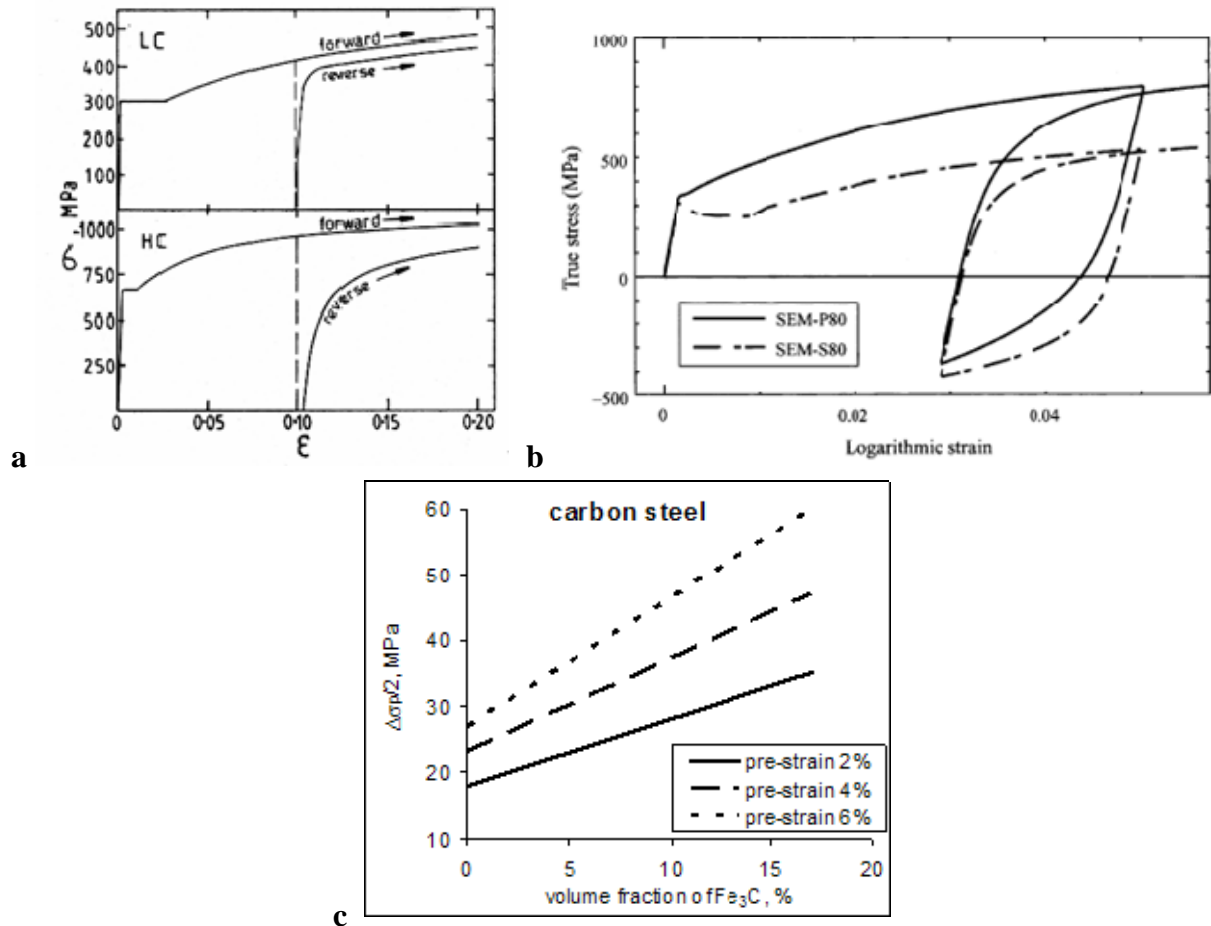


Figure 1.46 (a) Typical forward-reverse deformation stress-strain curves of ferritic steels (bcc), containing LC – 0.043% C and HC – 1.08% C [59]; (b) stress-strain curves of steel 1080 with plate-shape, SEM-P80, and spheroidised, SEM-S80, cementite morphology [60], and (c) permanent softening dependence on spheroidised Fe_3C particle volume fraction (derived from [61])

The forward-reverse stress-strain curves observed for rolled plate material depended on test direction, which has been related to the planar anisotropy of mechanical properties [63] (Figure 1.49, a). In rolled plate the dislocation structure can have a preferable orientation in the rolling direction and a number of dislocation-obstacle interaction sites can form prior to testing. With the loading angle change during testing, the back stress projection on the direction of reverse strain also changes its magnitude (Figure 1.49, b). Thus the yield stress drop during testing due to action of the back stress, increases with an increase in angle between rolling direction and test direction (decrease in angle between the back stress and strain direction during testing).

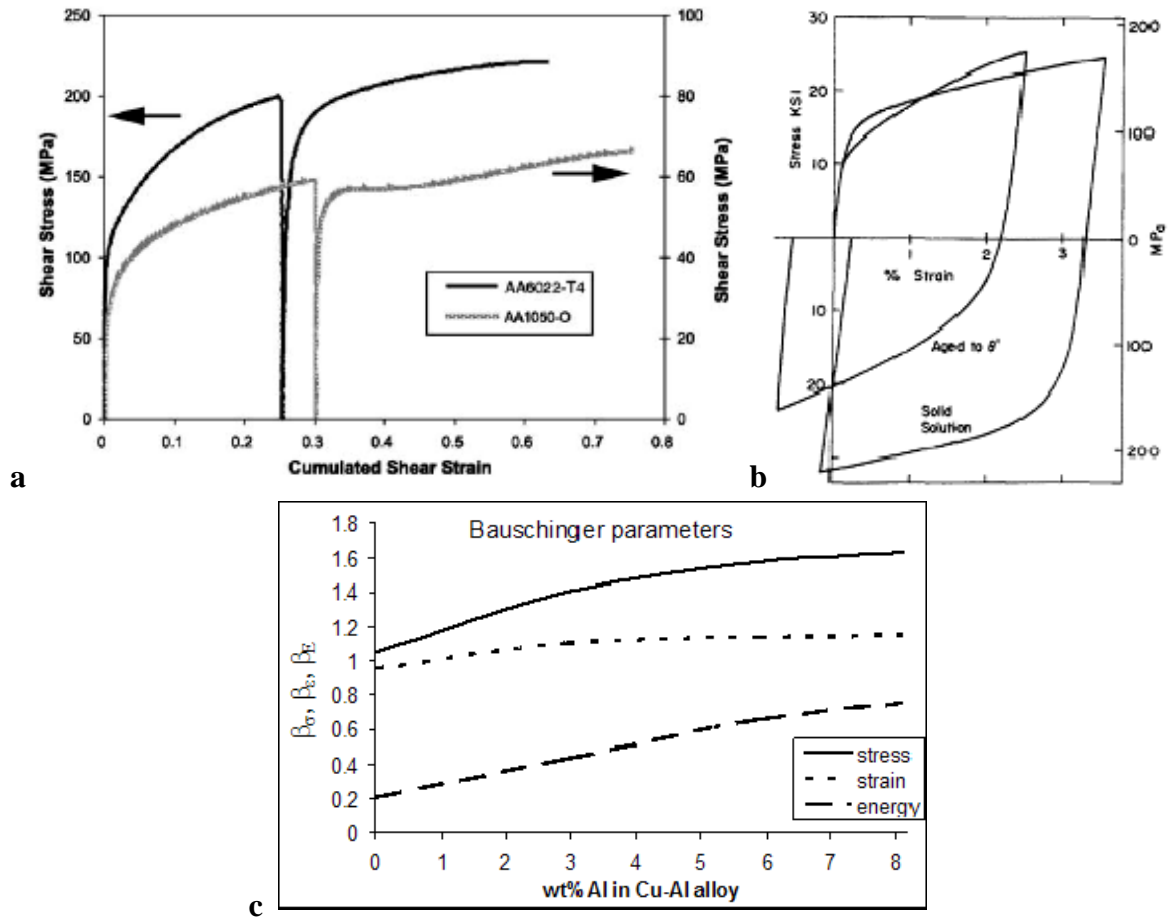


Figure 1.47 (a) Stress-strain curves of aluminium (fcc) and an Al-Mg-Si alloy [34], (b) stress-strain curves of a Cu-Al alloy containing hard particles, “aged to θ' ”, and without particles, “solid solution” [62]; (c) The Bauschinger parameters dependence on Cu-Al alloy composition (derived from [54])

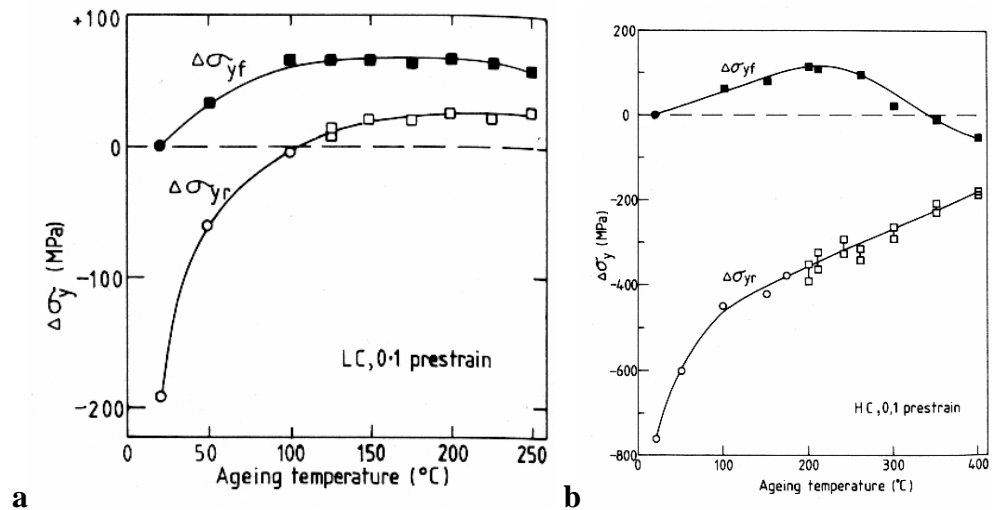


Figure 1.48 Influence of ageing on difference between forward strain and forward pre-strain yield stress $\Delta\sigma_{yf}$, and reverse strain and forward pre-strain yield stress $\Delta\sigma_{yr}$ for (a) low carbon and (b) high carbon steels [59]

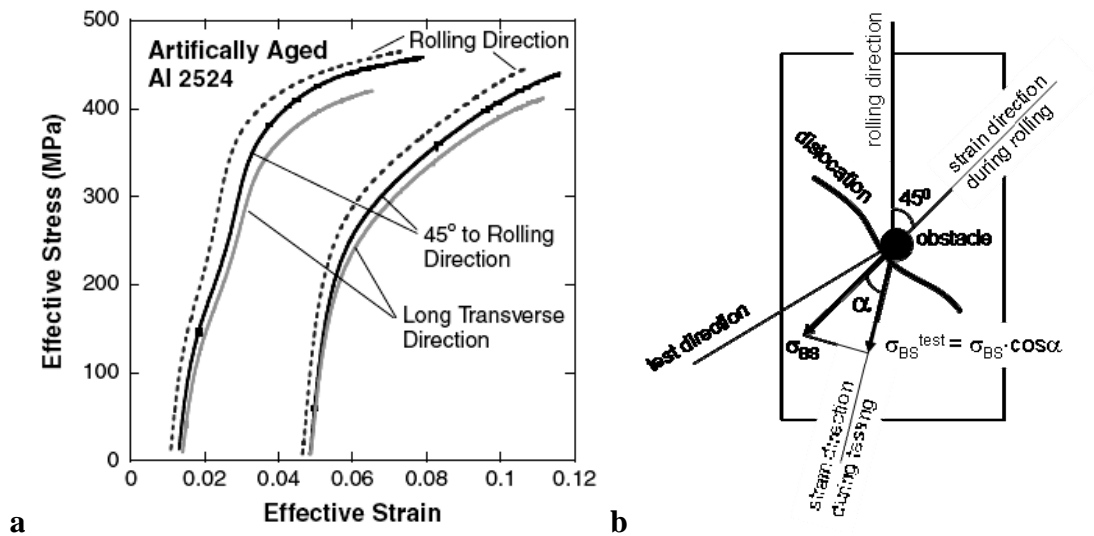


Figure 1.49 (a) Reverse stress-strain curves of rolled aluminium plate tested in different directions [63] and (b) schematic presentation of the back stress projection during testing

1.2.4 The Bauschinger effect in HSLA steels

The Bauschinger effect in HSLA steels has been previously studied with respect to line-pipe production by the UOE forming. The Bauschinger effect influences pipe properties in two ways: during pipe testing where tensile coupons need to be flattened prior to testing, and when comparing the pipe and plate tensile properties. According to the API 5L standard, pipe testing can be carried out by flattening of a pipe wall-piece and tensile testing of the flattened part or by hydraulic expansion of a pipe ring. During flattening the inner side of the pipe wall is subjected to tension and outer side to compression, hence flattening adds a half cycle to the reverse deformation sequence already experienced by the pipe material. Consequently a large difference in pipe mechanical properties can be observed due to the method of testing (20% difference in the yield stress between flattened specimens and ring expansion [64]). The difference in the test data also depends on steel chemistry [65]. Recent investigations of HSLA steels have found that the Bauschinger effect depends on chemistry even for the same method of testing [66, 67]. At the moment, the Bauschinger effect dependence on the

dislocation structure and microalloy particle distributions (related to a steel chemistry and processing parameters) is only known qualitatively and only a limited amount of data are available.

With an increase in pre-strain the drop in yield strength of HSLA steels on reverse loading increases, due to an increase in dislocation density and consequent increase in number density of dislocation-particle interaction sites (Figure 1.50). More highly alloyed steels show a larger yield drop at the beginning of reverse deformation, due to a larger particle number density (parameter $\beta_{\sigma 1}$ is higher for the higher alloyed steel on Figure 1.50, a). With an increase in reverse strain the more highly alloyed steels quickly return their properties (parameters $\beta_{\sigma 2}$ and $\beta_{\sigma 3}$ for the more highly alloyed steels may be lower than for the lower alloyed steels on Figure 1.50,b,c). Permanent softening, Figure 1.50, d, does not show a simple relationship with either strength level or steel composition, which indicates the need for more detailed microstructural characterisation (dislocation-particle interaction parameters). The increase in permanent softening with a particle volume fraction increase, Figure 1.51, can be related to an increase in particle number density and number density of dislocation-particle interaction sites. However, a difference in slope between the carbon steel and the HSLA steel indicates the influence of particle size and particle chemistry on dislocation-particle interaction. Hence, during the initial stage of reverse loading the Bauschinger effect is higher in the more highly alloyed steels, although the permanent softening, due to the Bauschinger effect, does not show a definite dependence on the amount of alloying. Similar values of softening for different steels (in terms of chemistry) can be explained if there are similar particle-dislocation interactions.

For the same chemistry steels the Bauschinger effect has been observed to be independent of ferrite grain size [65], Figure 1.52, although differences may exist in slope – this cannot be

confirmed without more details of grain structure. Recent investigation of the Bauschinger effect dependence on steel microstructure has shown that, for steels of the same chemistry but differently heat-treated to change the microstructure and phase distribution, the Bauschinger stress parameter is different (see dual phase, DP, and HSLA in Figure 1.53). The authors of that paper [67] reported that this difference is related to the relaxation of residual stresses, which are higher in a material with a greater difference in phase plasticity (such as ferrite and martensite in the DP steel). However it is obvious, that formation of approximately 20 % martensite in the DP steel leads to the generation of a dislocation structure in the surrounding ferrite (to accommodate the transformation strain) with a higher dislocation density compared to that in the HSLA steel. The higher cooling rate used to produce the DP steel may also have resulted in a greater number of finer particles, compared to the HSLA steel, leading to an increased number density of dislocation-particle interaction sites. Thus the DP steel would be expected to show a higher Bauschinger effect than the HSLA steel. The low carbon steel, LC in Figure 1.53, exhibited a lower Bauschinger effect than the DP and HSLA steels, which can be explained if the LC steel had a lower particle number density due to a lower alloying element content. However, in the paper [67] these data are not presented.

The difference in steel behaviour during reverse deformation due to chemistry differences can be approximately summarised in Figure 1.54. Here, a more highly alloyed steel starts yielding at a lower strain on reverse deformation, but, having a larger work-hardening rate in the reverse direction, more quickly returns to its previous property value. On the basis of the literature data it can be seen, that if a plain carbon steel and a HSLA steel were pre-stressed to the same stress value the Bauschinger response would be equal at a certain strain (approximately 0.02 - 0.05 reverse strain in Figure 1.54).

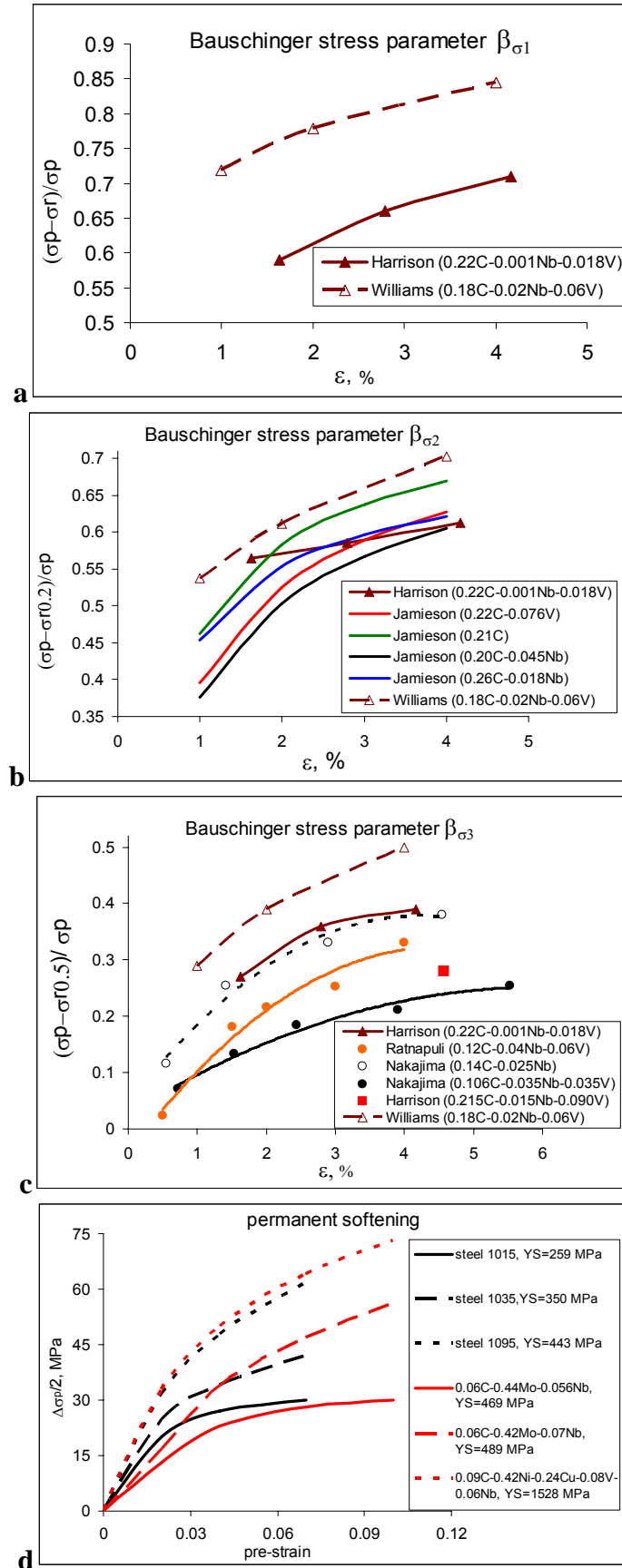


Figure 1.50 The Bauschinger stress parameter (a) $\beta_{\sigma 1}$, (b) $\beta_{\sigma 2}$, (c) $\beta_{\sigma 3}$ (derived from [64, 65, 68-70]) and (d) permanent softening dependences on pre-strain [61]; the shown parameters are defined in section 1.2.1

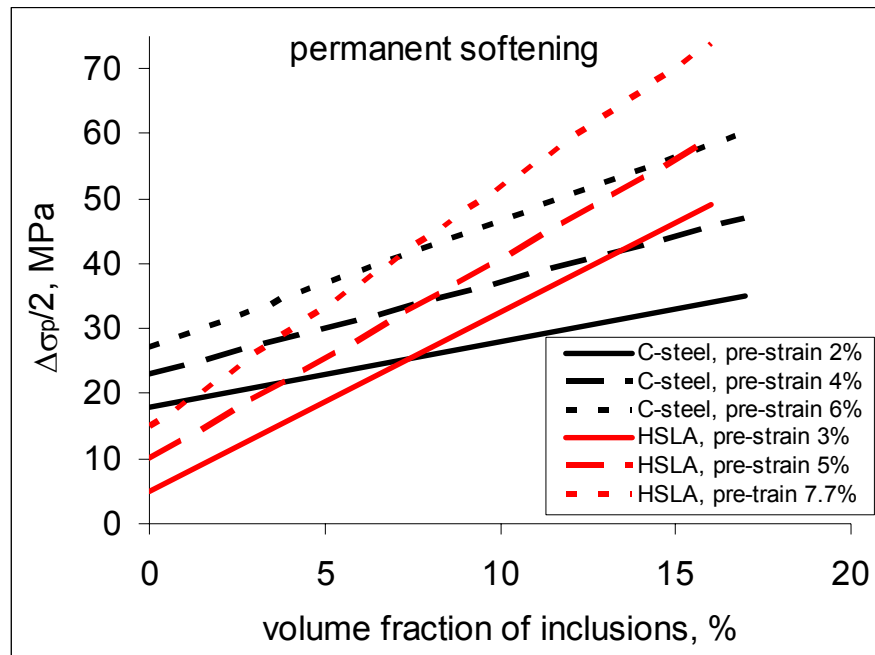


Figure 1.51 Permanent softening dependence on particle volume fraction in carbon and HSLA steels (derived from [61])

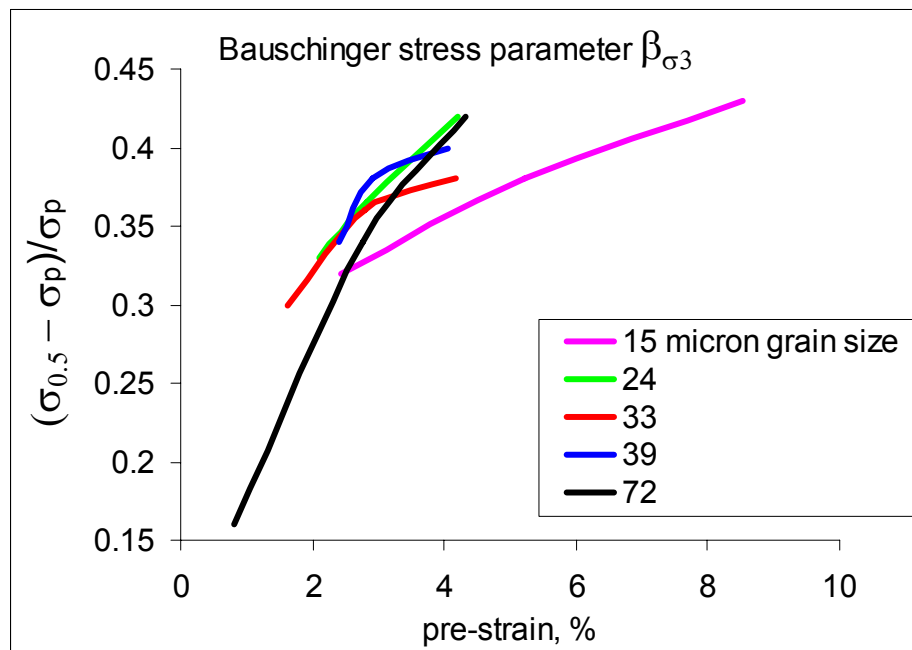


Figure 1.52 The Bauschinger stress parameter dependence on grain size (derived from [65])

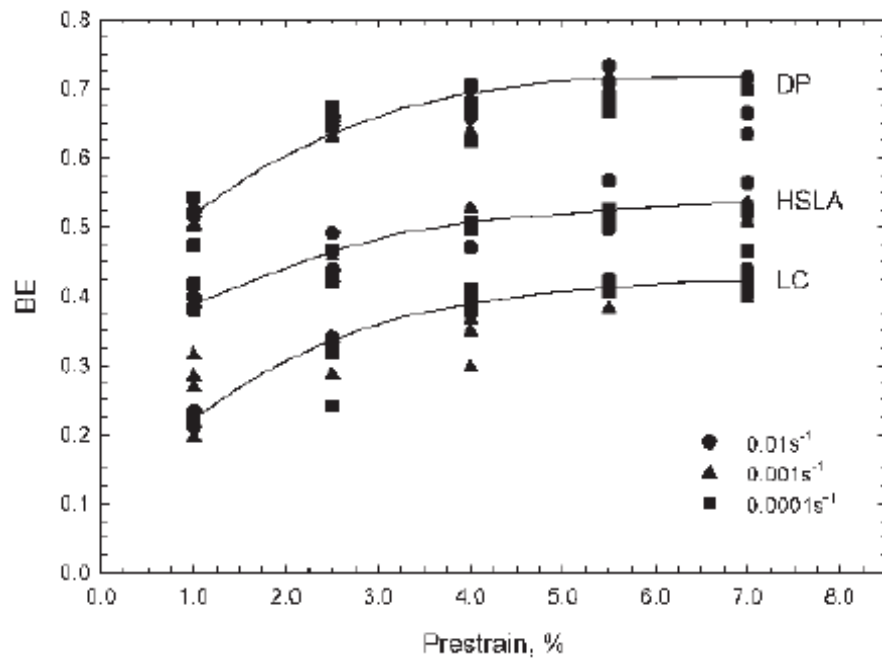


Figure 1.53 The Bauschinger stress parameter dependence on pre-strain for steels with different microstructure: LC, a low carbon steel with a ferrite-pearlite microstructure, contains 0.062 C-0.094 Cu-0.014 Mo; DP, a dual phase steel with a ferrite-martensite microstructure, and HSLA steel, with a ferrite-pearlite microstructure, both contain 0.1 C-0.39 Cu-0.047 Mo-0.021 Nb [67]

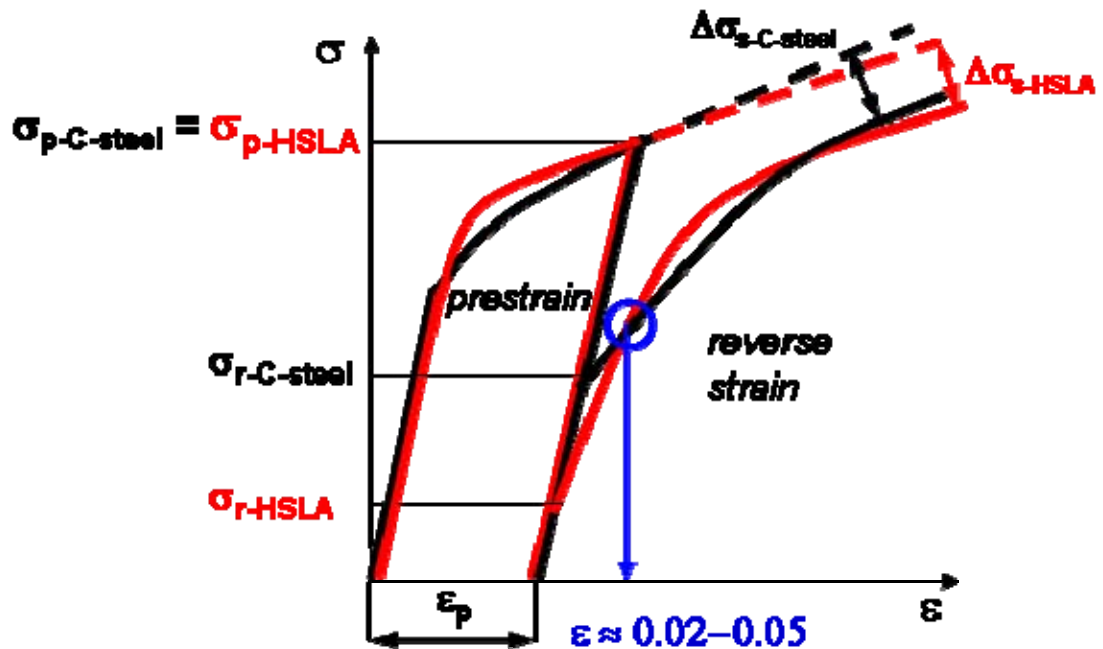


Figure 1.54 Schematic presentation of the Bauschinger effect in a plain C-steel (black line) and a HSLA steel (red line)

1.3 Precipitation of alloying elements in HSLA steels

High strength low alloy (HSLA) steels achieve high combined strength and toughness through small additions of Ti, Nb and/or V at low carbon levels to give fine grain size and precipitate strengthening.

The precipitation strengthening effect depends on the amount of precipitates formed, their size, their location and when they form during processing. The tendency for precipitation is often represented by the solubility product [71]:

$$k_s = [M][X],$$

where [M] and [X] are weight percentages of the alloying metal and interstitial solute element respectively, and its temperature dependence (Figure 1.55):

$$\log k_s = A - B/T,$$

where A and B are constants for a given system. Solubility products are a guide as they do not take into account the effects of other alloying elements in solution or of kinetic effects.

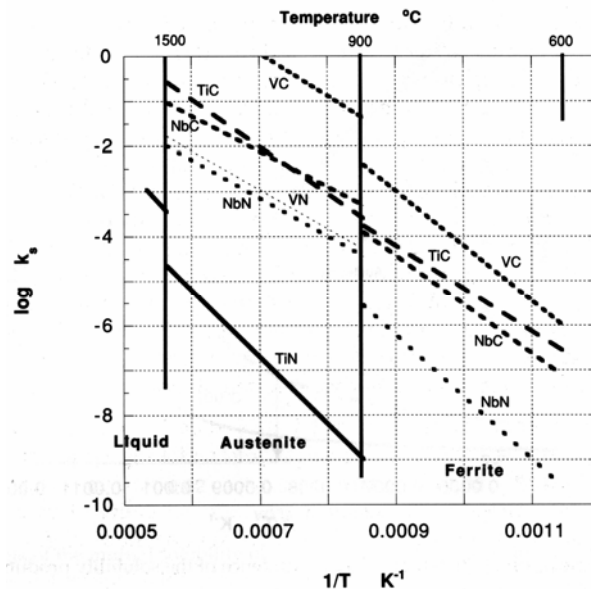


Figure 1.55 Dependence of selected alloying element compound precipitation on temperature [71]

In terms of precipitate strengthening then higher solubility systems, e.g. VC, are favoured as these precipitate at lower temperatures tend to be finer, whereas precipitates with lower

solubility products at higher temperatures, e.g. TiN, can precipitate to pin grain boundaries and restrict recrystallisation. The characteristics and effects of the various microalloying element carbo-nitrides are summarised below.

Precipitation of titanium-rich phases

In titanium-alloyed steels there may exist several compounds of Ti, TiN, TiC, Ti(C,N) and TiV(C,N).

TiN

TiN can form in the liquid – giving coarse particles (0.5 – 8 μm [72-75]) or in austenite, when the size range is below 500 nm (Table 1.1).

Usually TiN and Ti(C,N) particles have a cubic shape and thus may appear in the plane of micrograph in the form of squares, trapezoids and triangles (Figure 1.56). Coarse TiN has been shown to reduce fracture toughness [74], which places an upper limit on the Ti and N levels, but finer TiN can be effective as a grain refiner at temperatures up to 1350 °C [76,77].

TiC

TiC precipitates with a plate-like or spherical shape precipitate at the austenite-ferrite interface [78] to form fine particles (2 – 200 nm) in sheets separated by 10-60 nm (Table 1.1). Decreasing $\gamma \rightarrow \alpha$ transformation temperatures lead to a decrease in size and spacing [78]. TiC precipitation temperature increases with an increase in titanium content [77]. If formed above the recrystallisation stop temperature, TiC affects prior austenite grain size via grain boundary pinning. TiC can form on pre-existing TiN [75] and can give strain-induced precipitation on dislocations [80]. Hence, TiC can provide grain refinement, if formed at temperatures in the γ -phase field, and precipitation strengthening, if formed in the α -phase.

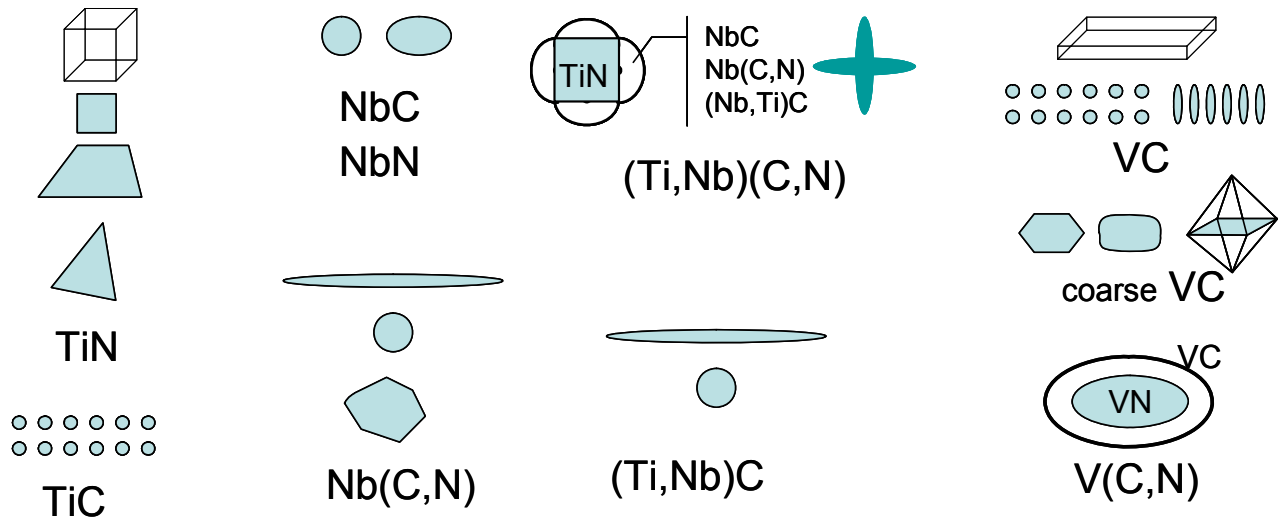


Figure 1.56 Typical morphologies of alloying element carbonitrides

Table 1.1 Summary of reported Ti-rich particle sizes

particle type	steel composition, wt%	diameter, μm
TiN	0.125C-0.021Cr-0.0265Ni-0.016Ti-0.006N [72]	0.017-0.025
	0.37C-1.45Mn-0.56Si-0.015Ti-0.0162N [74]	2 - 5
	0.35C-1.56Mn-0.33Si-0.028Ti-0.0089N [74]	1 - 3
	0.23C-1.72Mn-0.23Si-0.044Ti-0.0075N [74]	2 – 8
	0.077C-0.005N and Ti in the range 0.044-0.132 [75]	0.1 – 0.7
TiC	0.004C-0.17Ti [79]	0.010
	0.077C-0.005N and Ti in the range 0.044-0.132 [75]	0.002 – 0.030
Ti(C,N)	0.077C-0.005N and Ti in the range 0.044-0.132 [75]	> 0.050

Precipitation of niobium-rich phases

In niobium-alloyed steels Nb precipitates mostly in the form of NbC, Nb (C,N), (Nb,Ti)C, (Ti, Nb)(C,N), (Nb,V)(C,N) and NbN; these form over a range of temperatures with those forming at higher temperatures controlling prior austenite grain size and those at lower temperatures (which may be strain-induced on dislocations [81]) contributing to precipitate strengthening. The overall observed characteristics of Nb-rich particles are given in Table 1.2

[81-97]. Nb-rich particles form under diffusion-controlled growth so that higher finish rolling temperatures and faster post-rolling cooling result in finer particles (3 – 15 nm) and so higher strength values.

Table 1.2 Summary of reported characteristics of Nb-rich particles formed in HSLA steels

particle type	steel composition, wt%	diameter, nm	shape	place of precipitation
NbC	0.041C-0.025Si-1.61Mn-0.063Nb [82]	2-20	Round	
	30Ni – 0.1C – 1.61Mn – 0.1Nb [83]	2.5-15		dislocations
	0.04C-0.82Mn-1.59Cu-3.45Ni-0.58Cr-0.51Mo- <0.05Nb [84]	10 - 25		boundary, ferrite matrix
	0.10 C-0.50Mn-0.28Si and Nb in the range 0.012-0.043 [85]	3		
	0.03...0.10C-0.15...0.25Si-0.50...1.50Mn-0.020...0.050Nb-0.009N [86]	2-12		dislocations, boundary
NbN	0.0790 Nb - 0.0120 C - 0.0010 N – 0.0010 S – 0.0020 Mn – 0.0060 Al [87]	40-50	Ellipsoid	boundary
		14-30		dislocations
Nb(C,N)	0.0790 Nb - 0.0120 C - 0.0010 N [87]	3-200	lens [87], round, polyhedral [88]	
	0.08C-1.43 Mn-0.290Si-0.090Nb-0.008N [88]	10-30		
	0.060-0.097 C, 0.0049-0.0082 N, 0.016-0.025 Nb, 0.008-0.022 Ti [89]	< 10		grain boundary, ferrite grain
	0.19C-1.5 Mn-0.45Si-0.1Cr-0.035Nb-0.125V-0.0088N [90]	< 100		dislocations
	0.042-0.097 C, 0.31-0.39Si, 1.21-1.72 Mn, 0.0078-0.0120 N, 0.027-0.052 Nb, 0.002-0.052 V [91,81]	2-15		dislocations

	0.11C-1.3Mn-0.25Si-0.010N and Nb in the range 0.005 - 0.21 [92]	40-400	Cubic	
	0.038C-1.84Mn-0.28Si-0.42Cu-0.09Nb-0.017Ti-0.0092N [93]	5-20	round	ferrite-ferrite boundary, grain
(NbTi)(C,N)	0.038C-1.84Mn-0.28Si-0.42Cu-0.09Nb-0.017Ti-0.0092N [93]	60-100	cube	ferrite-ferrite boundary, grain
	0.060-0.097 C, 0.0049-0.0082 N, 0.016-0.025 Nb, 0.008-0.022 Ti [94]	15-50, 50-1000 core and 40-70 cap	cube TiN core and NbC cap	
	0.09-0.11 C, 1.39-0.53 Mn, 0.023-0.057 Nb [95]	15-150	round	grain
(NbTi)C	0.07 C-1.35Mn-0.14Si-0.047Ti-0.086Nb-0.007N [96]	7-12	round	grain/subgrain boundary
		3-6 length and 0.7-0.9 diam.	needle	dislocations
		3-5	sphere	dislocations
	0.05C-1.5Mn HSLA steel [97]	4-20	sphere	grain
	0.06C-1.5Mn-0.08Nb-0.07Ti [98]	20-120	sphere, plate	grain
		3-5 length	needle	dislocations
(NbTi)N	0.05C-1.5Mn HSLA steel [97]	300-3000	cube	grain

Precipitation of vanadium-rich phases

V-rich precipitates, such as VC, V(CN) and (Ti,V)(C,N), are usually the last of the microalloying carbo-nitrides to form, either at the γ/α interface or in ferrite. As for TiC this can give sheets of precipitates (diameter up to 10 nm and spacing ≈ 35 nm) or complex shapes formed on pre-existing particles (Figure 1.56). This can result in a wide range of particle sizes, Table 1.3, although single VC particles tend to be fine (<10 nm) and provide strengthening of ferrite.

Table 1.3 Summary of reported characteristics of the V-rich particles

particle type	steel composition, wt%	diameter, nm	shape	place of precipitation
VC	0.12C-0.30Si-1.5Mn-0.45V [99]	1.5-3.5		grain
		1.5-10		baundary
	0.4C-0.15V [100]	10-30	sphere	grain
		5-10		ferrite lamella of pearlite
	0.4C-2V [100]	500		
	0.7C-1V [100]	6 - 8		baundary
	0.8C-12Mn-0.3V [101]	10-50	octahedron	
	V in the range 5-6, C in the range 1.7-2.1 [102]		strip, rod	
	V in the range 7-10, C in the range 2.4-3.2 [102]		lumpy, chrysanthemum	uniform distribution
	0.79C-11.81Mn-0.30V-0.0011N [103]	50-150 (up to 440 after aging)	(square, polyhedral)	
	0.03...0.10C-0.15...0.25Si-0.50...1.50Mn-0.020...0.050V-0.009N [86]	5-15	sphere	dislocations, boundary
V(C,N)	HSLA steels [104]	5-10	lens	
	HSLA steels [105]	< 30		
	0.10C-0.50Mn-0.28Si and V in the range 0.10-0.15[85]	5-100		

(V,Ti)(C,N)	0.38C-0.107V-0.010Ti- 0.026Al-0.015N [106]	10-50	square	
(TiNbV)(CN)	0.15C-0.03Si-0.56Mn- 2.44Cr-1.03Mo-0.28V- 0.015Ti-0.05Nb [107]	50-300	irregular sphere, rounded cube, flat-faced cube	boundary, grain
(TiNbV)C	0.06C-1.5Mn-0.1V-0.02Ti- 0.07Nb [98]	10-200	sphere, plate	grain
		3-5 length	needle	dislocations

Precipitation of Cu-rich phases

Copper can precipitate in the form of separate CuS or Cu₂S particles [108] or as an outer layer on top of already existing particles, for example MnS [109]. Particle size has been observed to be in a broad range of diameters, increasing with a Cu content increase in the steel composition (Table 1.4). As Cu precipitation occurs completely at temperatures in the ferrite phase region, Figure 1.57, Cu-rich particles are observed within the ferrite grains, at the ferrite/ferrite boundaries or on dislocations [111,112]. Prior-deformation enhances the nucleation of Cu-rich particle on dislocations, which can lead to significant strengthening. Annealing of Cu-containing steels results in additional strengthening [113], obviously due to existing particle growth and precipitation of new particles, leading to an increase in precipitate number density

Table 1.4 Summary of reported characteristics of the Cu-rich particles

Particle type	steel composition, wt%	diameter, nm	shape	place of precipitation
CuS Cu₂S	0.11...0.14C-0.6Mn-0.25Si-0.22Cu- 0.025...0.037S [108]	10-80	sphere	grain
Cu-rich	0.01C-1.21Mn-0.21Si-0.55Mo-1.6Cu- 0.05Nb-0.105Ti-0.008S [110]	5-55		dislocations, grain
	Fe - 1.5Cu [111]	20 - 800		dislocations

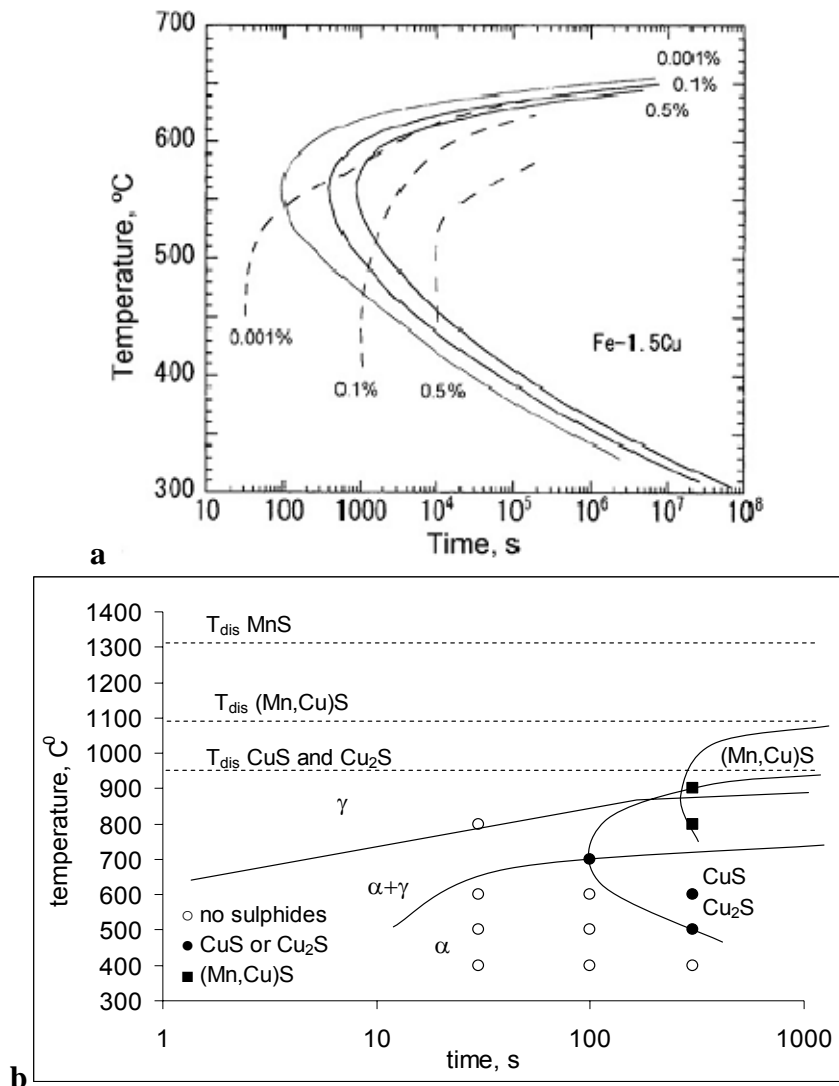


Figure 1.57 (a) Calculated time-temperature-transformation (solid line) and continuously cooled transformation (dashed line) diagrams of a 1.5 % Cu-containing alloy [111]; and (b) experimental TTT diagram of a 0.22 % Cu-containing alloy [108]

1.4 Strengthening mechanisms in carbon steels

Contemporary steels exhibit a wide range of mechanical properties, the yield stress is observed to vary from 200 to 5500 MPa [114,115]. Strengthening can be achieved by one or more of the following mechanisms: grain refinement, solid solution strengthening, phase balance strengthening, precipitation strengthening and work hardening. Of these only grain refinement results in higher toughness; the others reduce it. The precise mix of mechanisms used will depend on the specific application of the steel along with other properties such as

weldability for construction steels, formability for further metal forming and machinability for engineering steels.

1.4.1 Grain refinement

The main relationship between average ferrite grain size, d , and the yield stress in steels, σ_y , is described by the Hall – Petch equation [71]:

$$\sigma_y = \sigma_0 + k_y d^{-1/2}$$

where σ_0 and k_y are constants.

The constant σ_0 , friction stress, represents the stress required to move free dislocations along the slip planes in the iron bcc crystal, and can be regarded as the yield stress of a single crystal. This stress is very sensitive to temperature and the chemical composition of the steel as seen by the different intercepts in Figure 1.58.

k_y is determined from the slope of the line plot between σ_y and $d^{-1/2}$ (Figure 1.58). It is found to be independent of temperature, Figure 1.58, a; chemical composition of the steel grade, Figure 1.58, b; and strain rate.

Different authors have reported variable values for σ_0 and k_y due to the different steel grades examined (Table 1.5). Reported k_y values vary by 9%, which is within experimental scatter, but σ_0 varies by up to 4.5 times, which indicates a strong dependence of σ_0 on steel composition. The effects of elements in solution on the yield stress σ_0 can be represented as:

$$\sigma_0 = \sigma_1 + \sum_{i=1}^n k_i \cdot c_i ,$$

where σ_1 is the friction stress of iron, c_i is a concentration of i^{th} solute and k_i is the strengthening coefficient of i^{th} solute.

σ_l , determined from $\sigma_y - d^{-1/2}$ plots for pure iron (with 0.001 – 0.004 at. % of C and N and other impurities between 0.03 and 0.1 at. %), has been quoted between 14 and 35 MPa [3, 117, 118].

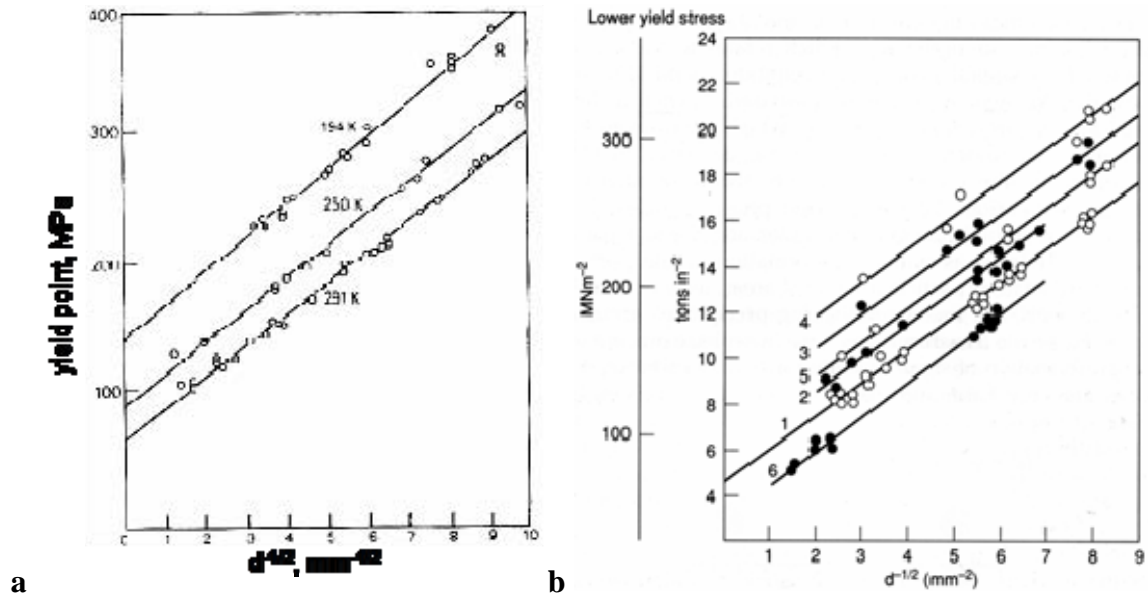


Figure 1.58 Dependence of yield stress on grain size: a – for mild steel at different temperatures [115], b – for different solute contents of C+N obtained via different quenching procedures [116]

Table 1.5 Experimental values for stress σ_0 and k_y terms in Hall-Petch equation

composition, wt%	σ_0 , MPa	k_y , MPa·mm ^{1/2}
<0.001C-0.001Mn-0.006Si-0.006S-0.002P-0.0003N [117]	14	-
0.0008C-0.00075N [3]	15	21.4
0.0012C-0.0002N-0.0029O-0.014(mainly Ni and Cu) [118]	21 - 35	-
0.115C-0.51Mn-0.02Si-0.05S-0.029P-0.08Ni-0.05Cr-0.0085N [116]	47	23.5
0.12C-0.5Mn-0.02Si-0.05S-0.03P-0.0085N [119]	71	22.4
0.1C-1.4Mn-0.2Si-0.04Nb-0.07V-0.008N [71]	54	21.4
0.0017C-0.00005Mn-0.0010Si-0.0006S-0.0009P-0.0004N [120]	24.5	23.5
0.014C-0.002Mn-0.06Si-0.011S-0.003P-0.003N [121]	62.7	21.6
0.12C-0.51Mn-0.02Si-0.05S-0.03P-0.008N [122]	70	23.4

1.4.2 Solid solution strengthening

The main interstitial elements in steel are carbon and nitrogen. Free carbon and nitrogen form interstitial atmospheres around the dislocations, which lead to dislocation immobilisation and yield strength increase. However, the solubility of C and N in α -iron is limited to 0.02 wt% for C at 723 °C and to 0.1 wt% for N at 590 °C decreasing to < 0.00005 wt% (C) and <0.0001 wt% (N) at 20 °C. Formation of cementite Fe_3C and other alloy carbides and nitrides takes free carbon and nitrogen from the solution. Hence, the interstitial solute strengthening effect is limited.

Many metallic elements form substitutional solutions with iron. This also leads to an increase in strength through elastic straining of the iron matrix, which arises from the size mismatch between the alloying element and iron atom (Hume-Rothery effect). With an increase in solute element content strength usually increases (Figure 1.59). In addition to elastic strain, substitutional solute elements also influence the grain size, amount and interlamellar spacing of pearlite, and the free content of carbon and nitrogen. Thus the negative influence of Cr on strength (Figure 1.59) can be explained by its removal of free N from solution as chromium nitride [71].

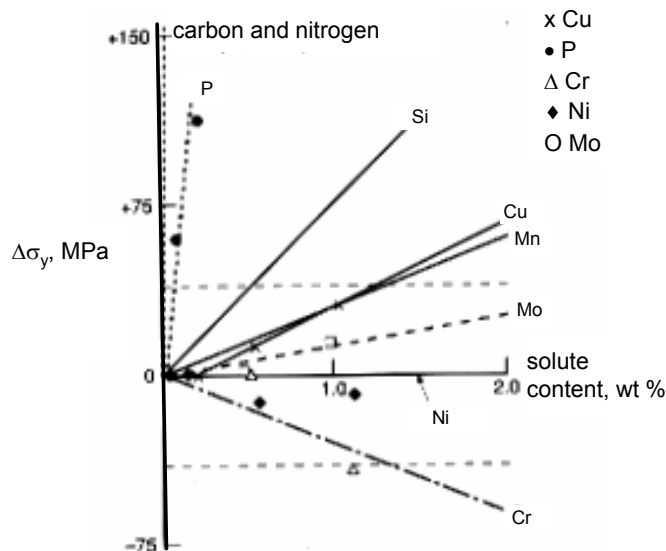


Figure 1.59 Strengthening effects of substitutional solute atoms in iron [71]

Strengthening coefficients for various alloying elements can be found in the literature, Table 1.6, and incorporated into the Hall-Petch equation as:

$$\sigma_y = \sigma_I + \sum_{i=1}^n k_i \cdot c_i + k_y d^{-1/2}$$

Table 1.6 Strengthening coefficients for a number of solutes [71]

Solute	C and N	P	Si	Cu	Mn	Mn	Mo	Ni	Cr
$\Delta\sigma_y, \text{MPa}$	5544	678	83	39	32	31	11	0	- 31

Generally, solid solution strengthening is used with other mechanisms as it is limited by solubility limits and other property requirements, such as toughness and formability.

1.4.3 Phase balance strengthening

The microstructure of steels often consists of several phases. In plain carbon steels the predominant phase is ferrite with pearlite being the commonest second phase. Apart from these phases in alloyed carbon steels carbides, nitrides, carbo-nitrides and intermetallic compounds of alloying elements may be present. These phases also influence strength. Increased hardenability and / or cooling may replace pearlite by bainite or martensite, which provide increased strength.

For C-Mn steels, increase in carbon content leads to an increase in pearlite content, and, at constant Mn content, an increase in tensile strength (Figure 1.60), which is due to a faster work hardening rate (Figure 1.61). The influence of carbon on the yield stress is not so high (Figure 1.62). At constant carbon content, an increase in Mn (γ -stabiliser) content lowers the eutectoid composition of carbon increasing the pearlite proportion, whilst Mn itself contributes to strength via solid solution strengthening and grain refinement.

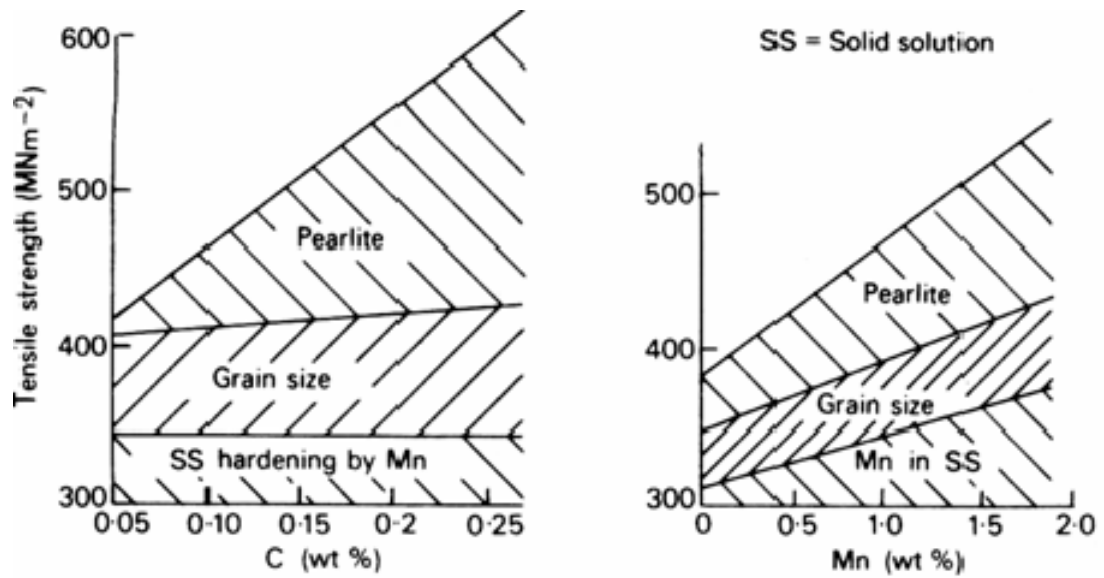


Figure 1.60 Factors contributing to the strength content of C-Mn steel [123]

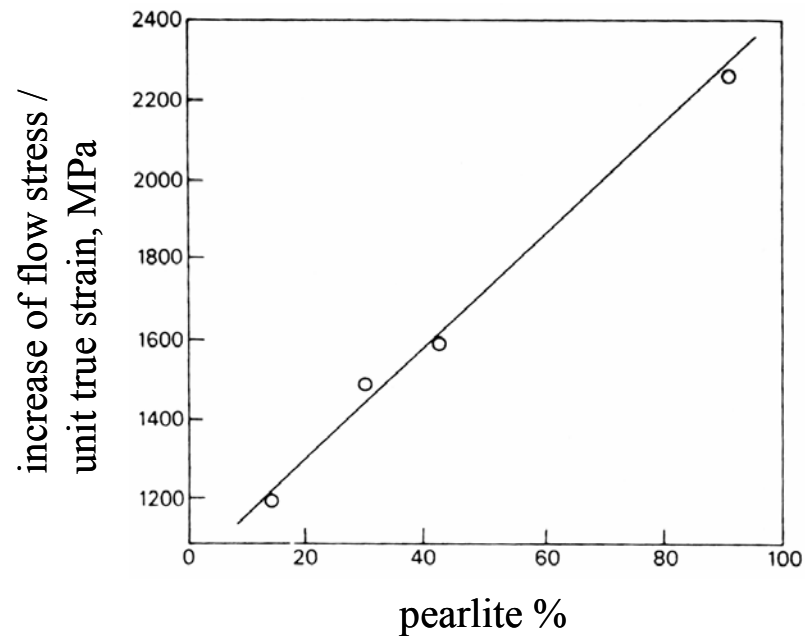


Figure 1.61 Effect of pearlite on work hardening rate [124]

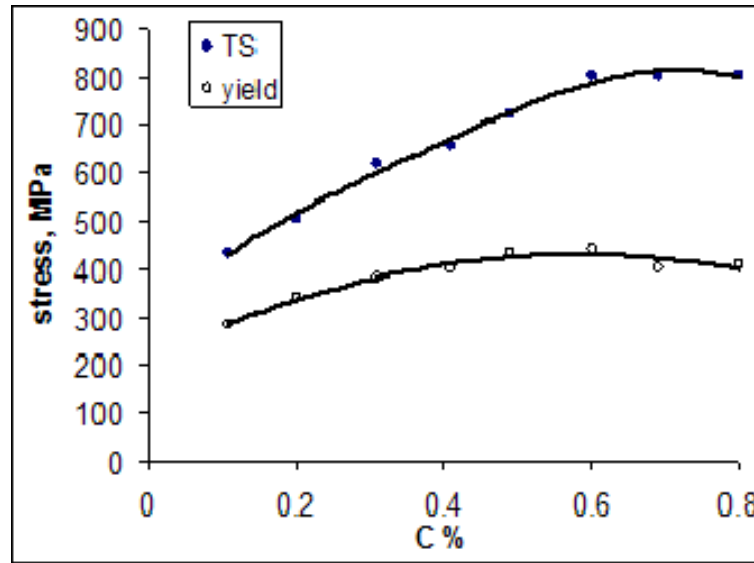


Figure 1.62 Influence of carbon content on strength of plain carbon steel [124]

In the literature there are several empirical equations derived for various mechanical properties to extend the Hall-Petch and solid solution equation. An example for ferrite-pearlite steels containing up to 0.2 wt% C (pearlite content of about 25-30%) is as follows [125]:

$$\sigma_y, \text{ MPa} = 53.9 + 32.3 \cdot c_{\text{Mn}} + 83.2 \cdot c_{\text{Si}} + 354 \cdot c_{\text{N}} + 17.4 \cdot d^{-1/2},$$

$$\sigma_t, \text{ MPa} = 294 + 27.7 \cdot c_{\text{Mn}} + 83.2 \cdot c_{\text{Si}} + 3.85 \cdot c_{\text{pearlite}} + 7.7 \cdot d^{-1/2},$$

$$\text{ITT}, ^\circ\text{C} = 19 + 44 \cdot c_{\text{Si}} + 700 \cdot \sqrt{c_{\text{N}}} + 2.2 \cdot c_{\text{pearlite}} - 11.5 \cdot d^{-1/2},$$

where σ_t - ultimate tensile strength, ITT – impact transition temperature and c_{Mn} , c_{Si} , c_{N} , c_{pearlite} – weight percent of Mn, Si, free soluble N and pearlite percentage respectively.

The strength of pearlite is influenced by its interlamellar spacing in a similar way to the Hall-Petch equation for ferrite structures [71]:

$$\sigma_p = \sigma_{0p} + k_p s^{-1/2},$$

here σ_p is the yield stress of pearlite and s is the ferrite path in the pearlite structure.

For the two-phase steels with more than 25 % pearlite the Rule of Mixtures can be used to give mechanical properties as [126]:

$$\sigma_y, \text{ MPa} = f^{1/3}(35+58.5 \cdot c_{\text{Mn}}+17.4 \cdot d^{-1/2})+(1-f^{1/3})(178+3.85 \cdot s^{-1/2})+63.1 \cdot c_{\text{Si}}+425 \cdot \sqrt{c_{\text{N}}},$$

$$\sigma_t, \text{ MPa} = f^{1/3}(246 + 1142 \cdot \sqrt{c_{\text{N}}} + 18.2 \cdot d^{-1/2})+(1-f^{1/3})(719+3.56 \cdot s^{-1/2})+ 97 \cdot c_{\text{Si}},$$

$$\text{ITT}, ^\circ\text{C} = f(-46 -11.5 \cdot d^{-1/2}) + (1-f) (-335 +5.6 \cdot s^{-1/2} -13.3 \cdot p^{-1/2} +3.48 \cdot 10^6 t)+49 \cdot c_{\text{Si}}+762 \cdot \sqrt{c_{\text{N}}},$$

where f is the volume fraction of ferrite, p is the pearlite colony size and t is the carbide lamella thickness.

Fast cooling from the austenite field restricts carbon diffusion, which results in bainite and/or martensite formation instead of pearlite (Figure 1.63). Strength increase due to phase balance change depends on carbon content, and the tensile strength may reach 1600 MPa in bainite and to 2000 MPa in martensite [115]. At the same time increase in carbon content reduces weldability and formability due to reduced toughness.

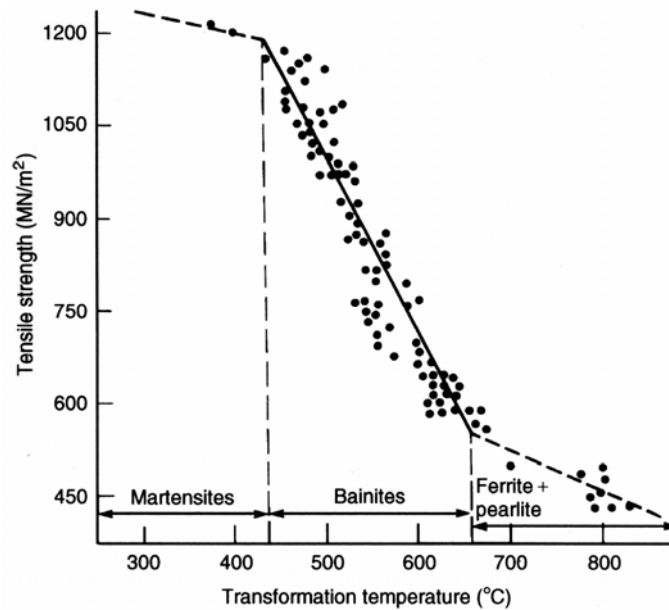


Figure 1.63 Influence of 50% transformation temperature on tensile strength via formation of different steel structures [125]

1.4.4 Precipitation strengthening

Addition of strong carbo-nitride formers, e.g. Ti, Nb and V, leads to an increase in

strength (Figure 1.64). Precipitation strengthening, which arises from the dislocation-particle interactions during slip, can be described by the Orowan equation [71]:

$$\Delta\tau_y = \frac{Gb}{L},$$

where G is shear modulus, b is Burgers vector and L is the spacing between the particle centres. L is related to the particle volume fraction (f) and particle diameter (X) by:

$$L = \left(\frac{2 \cdot \pi}{3 \cdot f} \right)^{\frac{1}{2}} \cdot \frac{X}{2},$$

which gives:

$$\Delta\tau_y = 2Gb \frac{\left(\frac{3f}{2\pi} \right)^{\frac{1}{2}}}{X}.$$

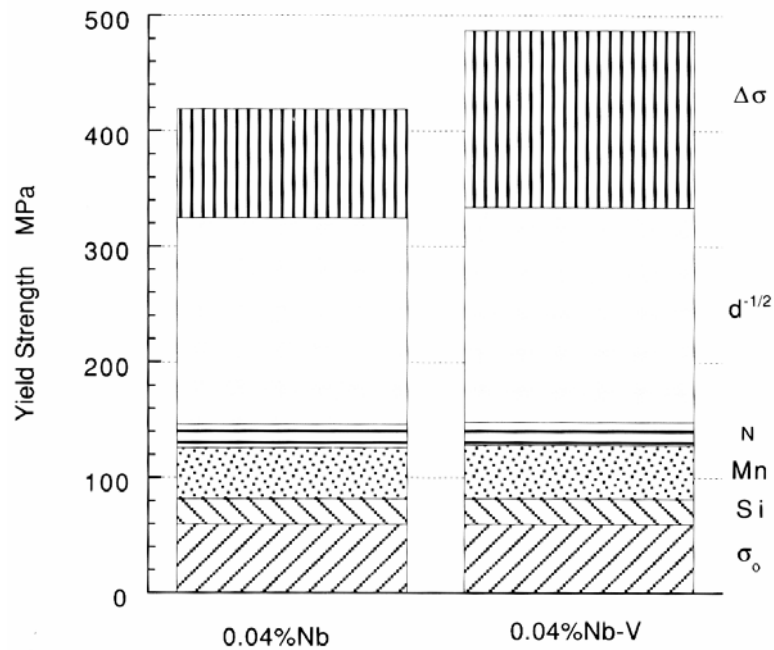


Figure 1.64 Strengthening contributions of different parameters on yield strength of hot-rolled 0.1% C-0.2% Si-1.4% Mn steel containing either 0.04% Nb or 0.04% Nb-0.07% V [71]: $\Delta\sigma$ - is precipitate strengthening

Assuming a random distribution of particles the addition to the yield stress from precipitation can be calculated using the Ashby-Orowan equation:

$$\Delta\sigma_y = \frac{10.8\sqrt{f}}{X} \ln\left(\frac{X}{6.125 \cdot 10^{-4}}\right),$$

where X is in μm .

The comparison between the last equation and experimental data for Nb- and V-alloyed steels showed that, for the particles larger than 5 nm and with 0.003 – 0.0015 volume fraction, the Ashby-Orowan equation gives a better prediction than the Orowan equation (Figure 1.65), due to the use of an effective spacing in the Ashby-Orowan equation not the minimum spacing, as in the Orowan model.

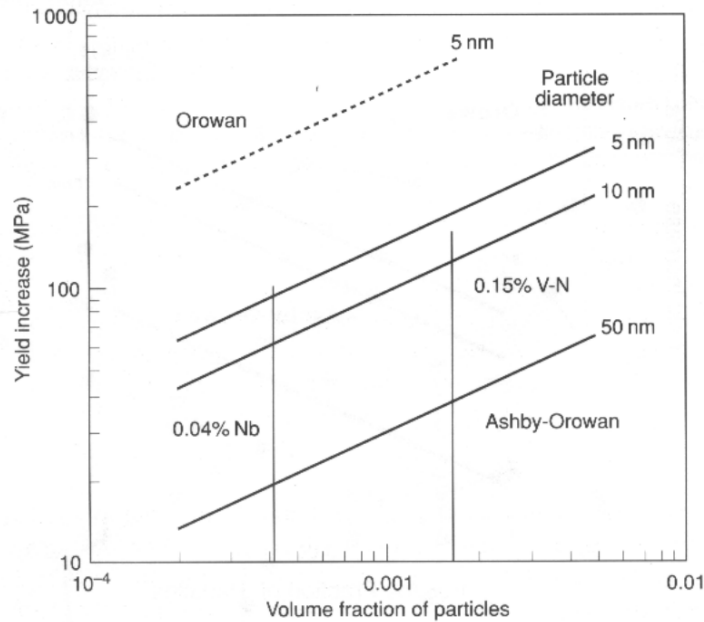


Figure 1.65 Addition to strength predicted by Orowan and Ashby-Orowan equations compared with the observed increments of yield strength in microalloyed steels (vertical lines are experimental data) [71]

More complex modifications of the Orowan equation have been developed by Melander for a random distribution of hard, spherical particles [16].

$$\sigma_i = \frac{3.56Gb}{4\pi l_r} \left(\frac{1 + \nu - \frac{3\nu}{2}}{1 - \nu} \right) \ln\left(\frac{l_r}{b}\right) \left[\frac{\ln\left(\frac{2D_g l_r}{b(D_g + l_r)}\right)}{\ln\left(\frac{l_r}{b}\right)} \right]^{3/2},$$

where ν = Poisson's ratio, $l_r = \left(\frac{\pi D_g^2}{6f} \right)^{\frac{1}{2}}$ is average distance between obstacle centres in the

glide plane, D_g is geometrical mean particle diameter.

This equation has been found to give values within 2 – 11 % of experimental data for small (3-5 nm diameter) VC particles with volume fractions from 0.0033 – 0.0316, but, as the particle size increases, the Ashby-Orowan equation again becomes more suitable.

In general, all the shown equations indicate, that greater strengthening results from greater volume fractions of finer particles, which depend on composition and processing. The strength increase for various microalloyed steels have been reported between 40 and 150 MPa [128-130] (Table 1.7).

Table 1.7 Increment to the yield stress from the microalloying elements precipitation

Author	Steel composition	Precipitates	Processing	Yield increment, MPa
Irvine and Baker [128]	0.04 wt%C-1.6%Mn-0.064%Nb	4-16 nm NbC	rolling	40 – 85
A.M. Sage, D.M. Hayes, C.C. Early, E.A. Almond [129]	0.12 wt%C-1.45%Mn-0.025Nb	VC	normalising	70
			controlled rolling	120
Gladman, Holmes and McIvor [130]	0.10 wt%C-0.50%Mn-0.28%Si Nb range 0.012-0.043 %	3-5 nm, f=0.0003-0.0004 NbC	fast cooling after rolling	100
	V range 0.10-0.15 wt%	5-100 nm, f=0.0010-0.0015 V(C,N)		150

Depending on the precipitate type and processing route some strengthening may come from ferrite grain refinement and the retention of work hardening.

1.4.5 Work hardening

In the absence of recrystallisation, an increase in dislocation density results in an increase in yield stress, however toughness and ductility may decrease. An increase in the shear stress can be represented by [115]:

$$\tau = \tau^* + \tau_i,$$

where τ^* describes the dislocation interactions with the short range obstacles [131] and τ_i - with the long range obstacles [132]:

$$\tau^* = \frac{1}{V} \left[\Delta H_0 + kT \ln \frac{l\dot{\epsilon}}{\rho m A b \gamma} \right], \quad \tau_i = \alpha \mu b \rho^2,$$

where V – activation volume, ΔH_0 – activation enthalpy at $\tau = 0$, k – Boltzmann's constant, T – temperature, l – length of dislocation line activated, $\dot{\epsilon}$ - strain rate, m – mobile dislocation density, A – area of glide plane covered by dislocation, γ - frequency of vibration of dislocation line length, α - constant, μ - shear modulus, ρ - dislocation density.

1.5 Thermo-mechanical controlled processing (TMCP) of HSLA steel plate

Severe application conditions (e.g. low temperature, high internal pressure, corrosive environment) require high strength with simultaneously high toughness for the line-pipe material. Together with the need for good weldability, this has led to decreasing carbon content and increasing microalloying element level in the steel chemistry (Table 1.8). The combined action of microalloying element additions and TMCR processing results in significant grain refinement and precipitation strengthening. Introduction of accelerated cooling and decreasing finish rolling temperatures gives further plate strength increase. General aspects of steel making and plate rolling parameters that influence mechanical properties are presented below.

Table 1.8 Typical compositions and mechanical properties of different grades of line-pipe steel plates

Steel grade	Typical composition, wt%	Process	Mechanical properties			Ref
			Yield, MPa	UTS, MPa	CVN*, J	
X60	0.12C-0.33Si-1.35Mn-0.04Nb-0.06V	TMCR	485	565		[64]
X65	0.08C-0.3Si-1.6Mn-0.08Nb-0.08V-0.017Ti-0.27Ni	TMCR	485-500	570-600	260 (-30 ⁰ C)	[133, 134]
X70	0.09C-0.25Si-1.69Mn-0.05Nb-0.08V-0.003Ti-0.22Ni-0.01Mo	TMCR	500-580	600-790	200 (-10 ⁰ C)	[134]
X80	0.08C-0.4Si-1.9Mn-0.044Nb-0.019Ti-0.2Ni-0.01Mo-0.03Cr	TMCR + acc.cooling	600	730	180 (-20 ⁰ C)	[134]
X100	0.06C-0.33Si-1.95Mn-0.048Nb-0.019Ti-0.24Ni-0.3Mo	TMCR + acc.cooling	740-760	780-820	270 (-10 ⁰ C)	[135]
X120	0.05C-0.30Si-1.80Mn-0.80Cr-0.042Nb-0.017Ti-2.1Ni-0.70Mo	TMCR + acc.cooling	840-860	940-1130	260 (-30 ⁰ C)	[135, 136]

* CVN - Charpy V-notch energy

1.5.1 Plate rolling technology

High quality standards on the final rolled product induce the same requirements to the steel making technology. First steelmaking is carried out in modern blast furnaces (from raw material) or in electric arc furnaces (from scrap). Secondary steelmaking consists of several steps of steel cleaning and composition control (Figure 1.66). Hot rolling includes slab reheating, several deformation stages in a multi-stand rolling unit and an accelerated cooling line, to carry out the thermo-mechanically controlled processing (Figure 1.67). The desired mechanical properties are obtained via time-deformation-temperature combinations. The main technological parameters, responsible for the plate properties, are slab reheating temperature, number of deformation passes and reduction per pass, start and finish roll temperatures, time and temperature of holding (during thermo-mechanical control processing) and cooling rate. Choosing different absolute values of these parameters make it possible to control the microstructure grain size, second phase type and microalloy precipitate size and distribution. Finally the microstructure will influence the mechanical properties via the strengthening mechanisms described above.

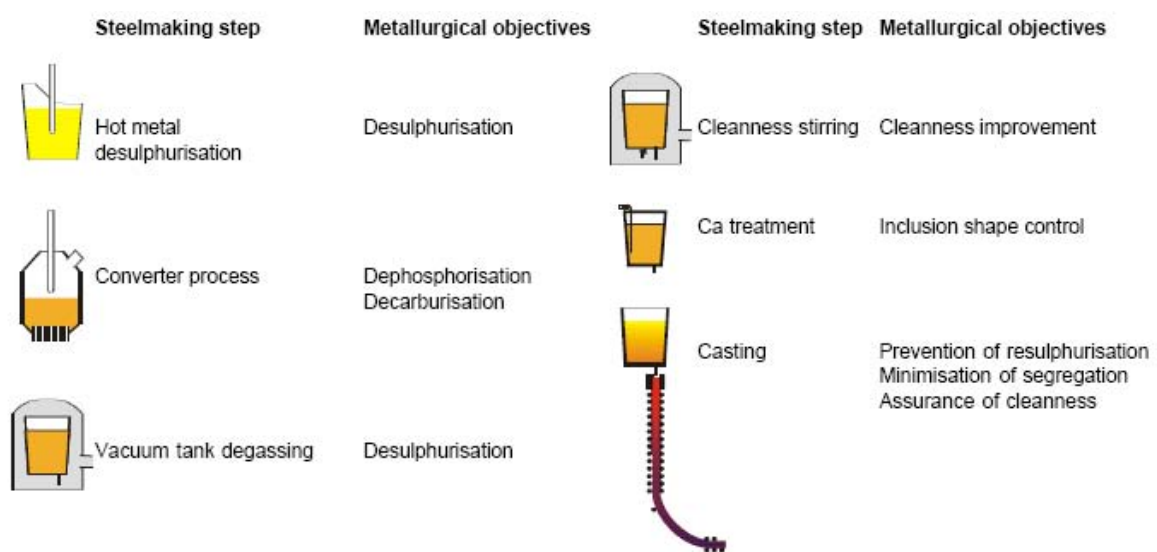


Figure 1.66 Schematic illustration of secondary steel making [134]

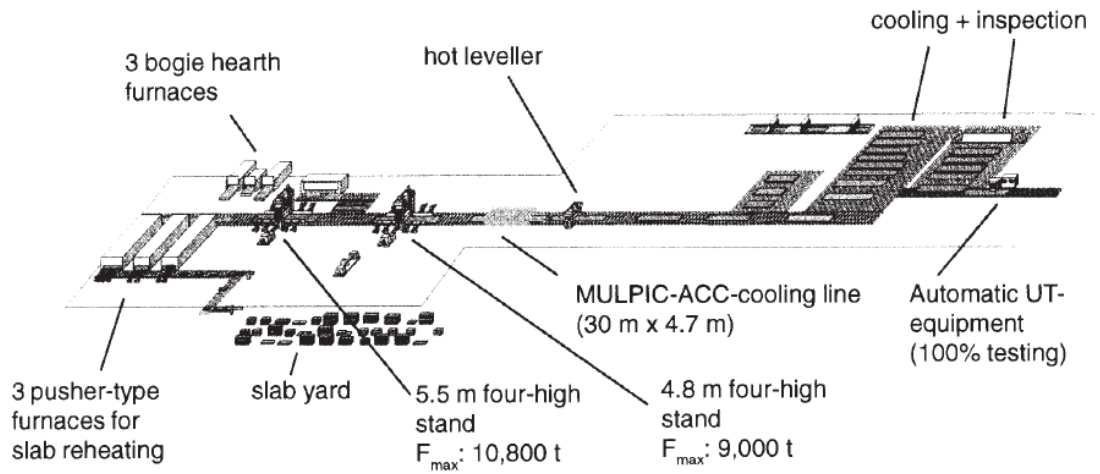


Figure 1.67 Rolling mill layout; MULPIC – multipurpose interrupted cooling, ACC – accelerated cooling, UT – ultrasonic testing [137]

1.5.2 Plate properties development

For the production of HSLA steel plates different processing schedules have been developed, Figure 1.68,a [137,138]. The schedules can be roughly divided into three main types, with increasing levels of yield stress and tensile strength from “N” to “TM” and to “TM + AC” scheme (Figure 1.68,b):

1. hot rolling in austenite temperature region + air cooling + normalising (N),
2. hot rolling in austenite below recrystallisation or in two-phase (austenite + ferrite) temperature region + air cooling (TM),
3. hot rolling in austenite below recrystallisation or in two-phase (austenite + ferrite) temperature region + accelerated cooling (TM+AC).

This plate strength increase can be related to grain refinement, formation of bainite as the second phase (instead of pearlite), dislocation density and particle number density increase (Figure 1.69).

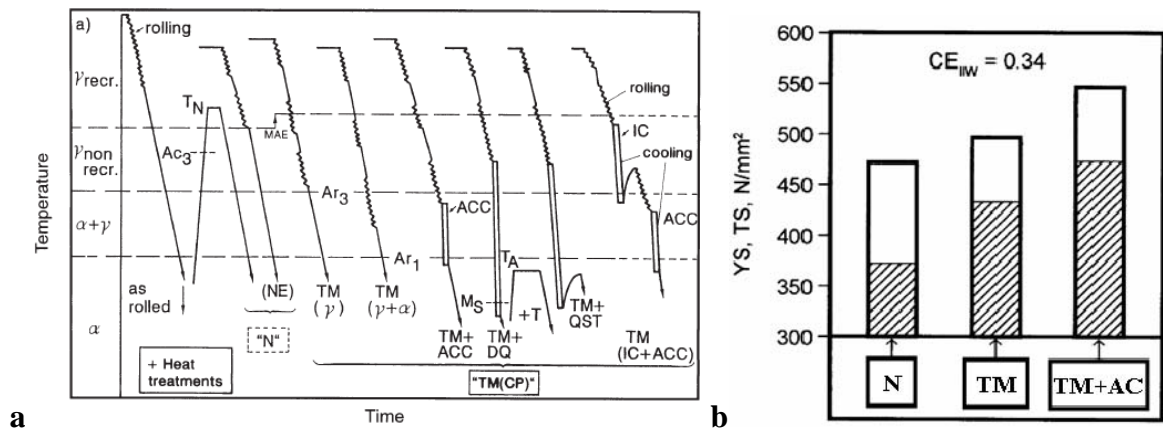


Figure 1.68 (a) Rolling schedules and (b) mechanical properties of steels processed according to different schedules [137]; TM – thermo-mechanical treatment, ACC – accelerated cooling, DQ – direct quenching, QST – quenching and self-tempering, IC – intermediate cooling, MAE – maximum likelihood estimation

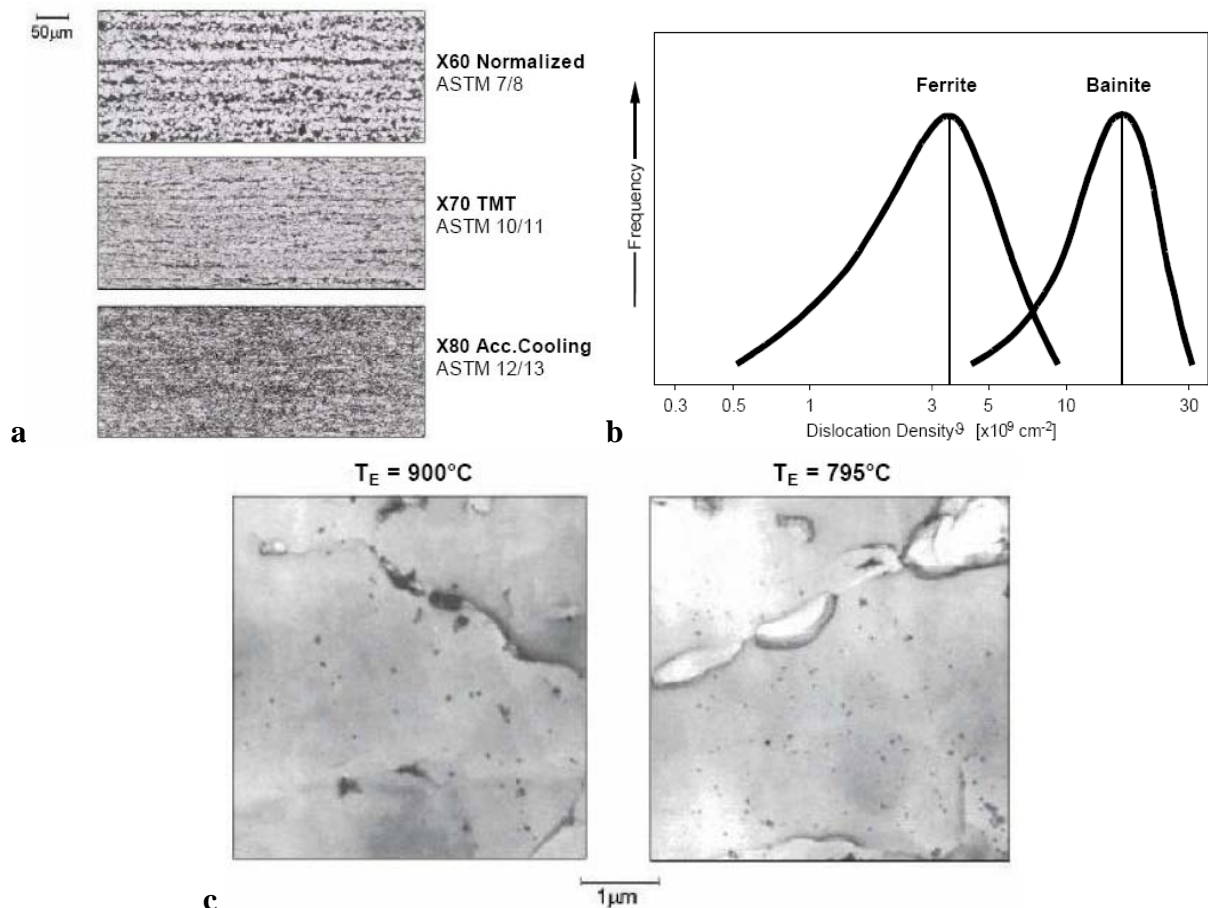


Figure 1.69 (a) Typical microstructures of steels processed to different schedules, (b) dislocation density increase from the predominantly ferritic to bainitic microstructure (c) carbon extraction replicas of Nb-rich particles (showing particle size decrease with finish roll temperature, T_E , decrease) [134]

During *hot rolling* the yield stress increases with a decrease in rolling temperature due to grain size decrease, although tensile strength does not show any significant changes (Figure 1.70 a, b). Increase in strength with increase in soaking temperature, for the Nb-alloyed steel in Figure 1.70, can be attributed to Nb-rich particle dissolution and further precipitation during rolling at a finer scale. Nb-rich particle number density increase leads to significant grain boundary pinning during recrystallisation, which finally results in the grain size decrease. Increase in strength with deformation increase is due to grain size decrease and dislocation density increase (Figure 1.70, c). Lower yield stress for 25% deformation after soaking, than before it, can be related to dislocation annihilation and grain growth during soaking.

During *thermo-mechanically controlled processing* finish rolling temperature and cooling rate significantly influence the microstructure and mechanical properties. With finish rolling temperature decrease, below the austenite recrystallisation temperature ($<900^{\circ}\text{C}$) and into the two-phase ($\alpha+\gamma$) region, the grain size decreases (Figure 1.71 and 1.72, a). Consequently the yield stress and tensile strength increase, and the impact transition temperature decreases (Figure 1.72, a). Further decrease in finish rolling temperature to 700°C results in the appearance of a maximum on the temperature-strength curve and, then, significant strength decrease (Figure 1.72, b). This behaviour has been explained by the reduction in contribution from accelerated cooling [141]. Thus, as finish rolling temperature decreases for constant finish cooling temperature, the temperature interval of accelerated cooling decreases. This leads to the acicular ferrite constituent in polygonal ferrite matrix, Figure 1.73, and strength, Figure 1.72, b, decreasing.

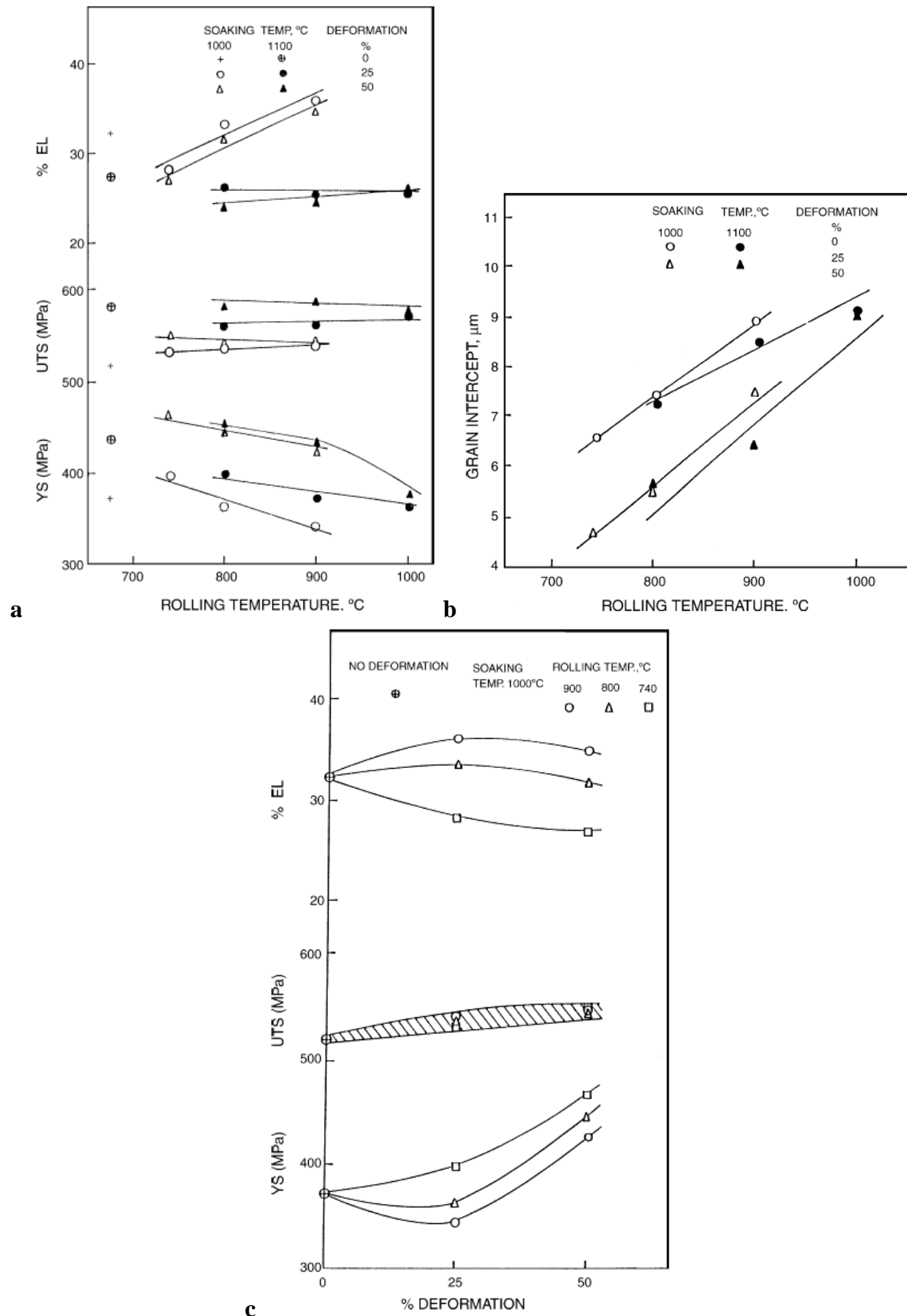


Figure 1.70 Rolling temperature influence on (a) the mechanical properties of a 0.11C-0.47Cr-0.47Cu-0.024Nb steel and (b) grain size; (c) deformation influence on the mechanical properties [139]

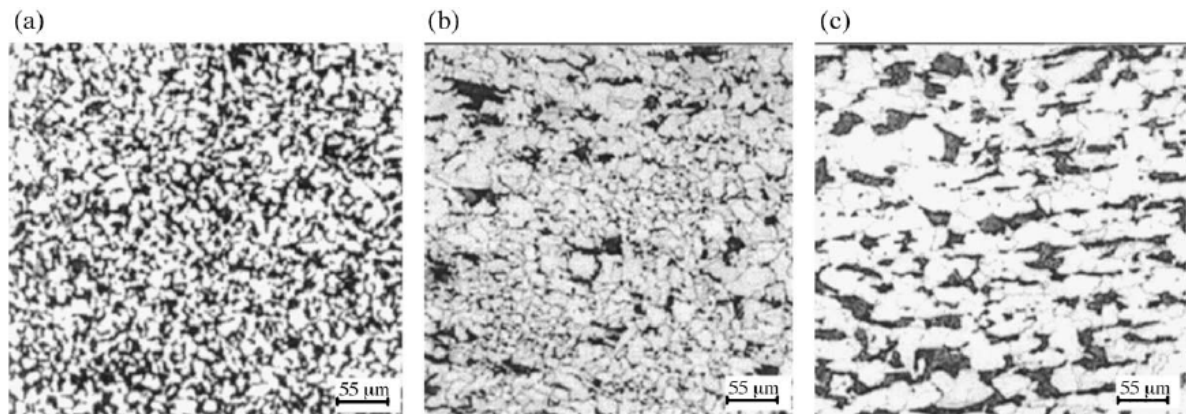


Figure 1.71 Effect of finish rolling temperature on steel microstructure at 30% deformation: (a) – 740 °C, (b) – 780 °C, (c) – 820 °C [140]

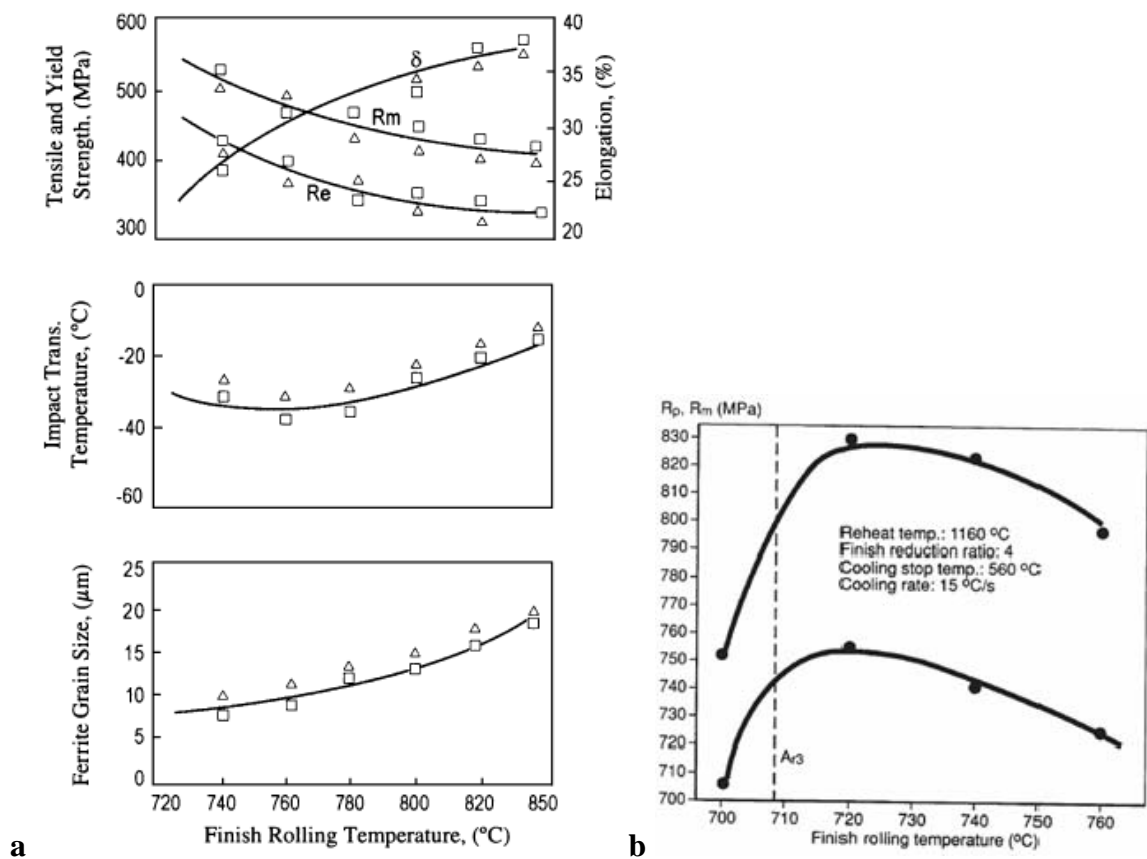


Figure 1.72 Influence of finish rolling temperature on mechanical properties of (a) a X52 steel containing 0.10C-0.036Nb-0.010V [140], and (b) a X100 steel containing 0.070C-0.050Nb-0.27Mo-0.017Ti [141]

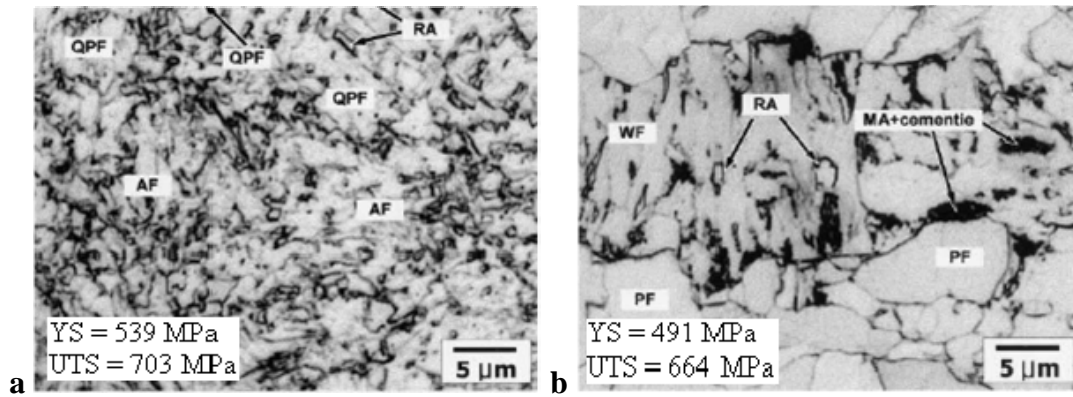


Figure 1.73 Microstructure and mechanical properties of a X70 steel after (a) 840 °C finish rolling temperature and 580 °C finish cooling temperature and (b) 720 °C finish rolling temperature and 600 °C finish cooling temperature: AF – acicular ferrite, PF – polygonal ferrite [142]

With an increase in cooling rate the ferrite grain size decreases, Figure 1.74, which results in a yield stress and tensile strength increase, Figure 1.75. However, the impact upper shelf energy decreases with increasing cooling rate. As it is undesirable when producing high toughness material, absolute values of cooling rate should be restricted to certain optimum value ranges. Depending on prior deformation either bainite or acicular ferrite can be formed (Figure 1.76, a, b). Their volume fraction increases with cooling rate increase, which also adds to steel strength increase. Cooling rate increase leads to an increase in the yield stress to tensile strength ratio (curves A and B on Figure 1.76, c). Coiling after cooling results in YS/UTS ratio decrease due to dislocation annihilation (curves C and D on Figure 1.76, c). Prior deformation results in YS/UTS ratio increase due to dislocation density increase and, probably, due to particle number density increase by dislocation-induced precipitation (curve E on Figure 1.76, c).

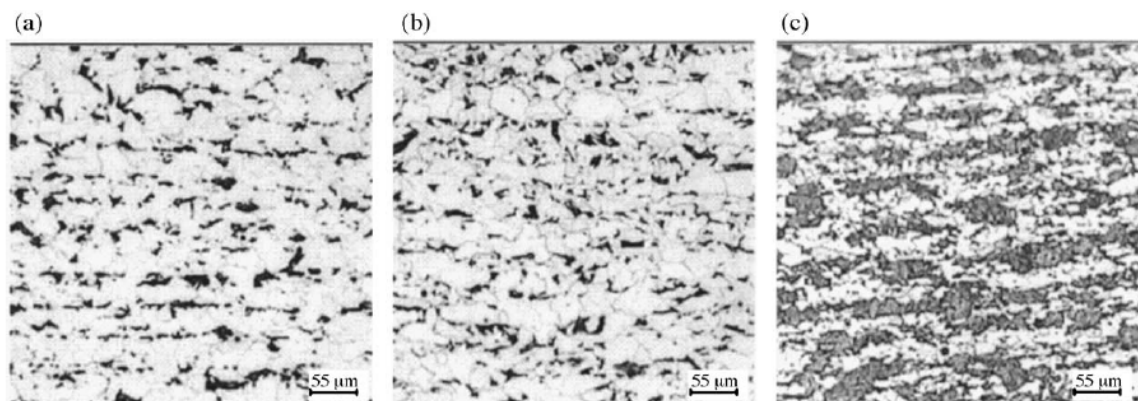


Figure 1.74 Effect of cooling rate on steel microstructure at 30% deformation and 780 °C finish rolling temperature: (a) – 5 °C/s, (b) – 10 °C/s, (c) – 20 °C/s [140]

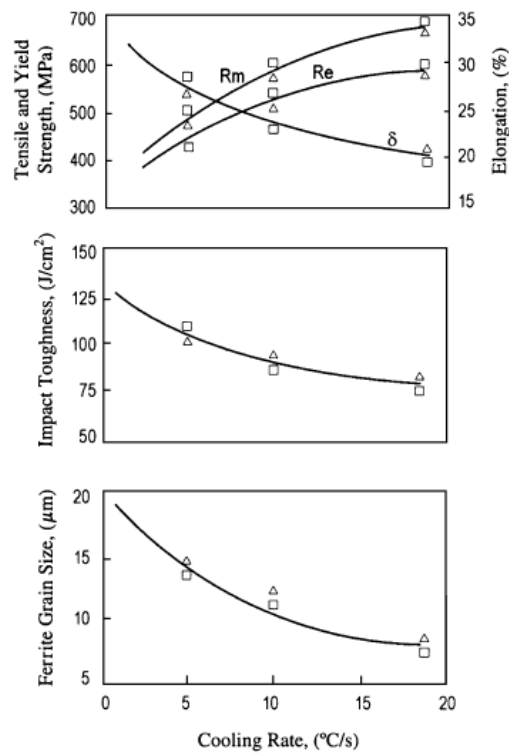


Figure 1.75 Cooling rate influence on mechanical properties of an X52 steel containing 0.10C-0.036Nb-0.010V [140]

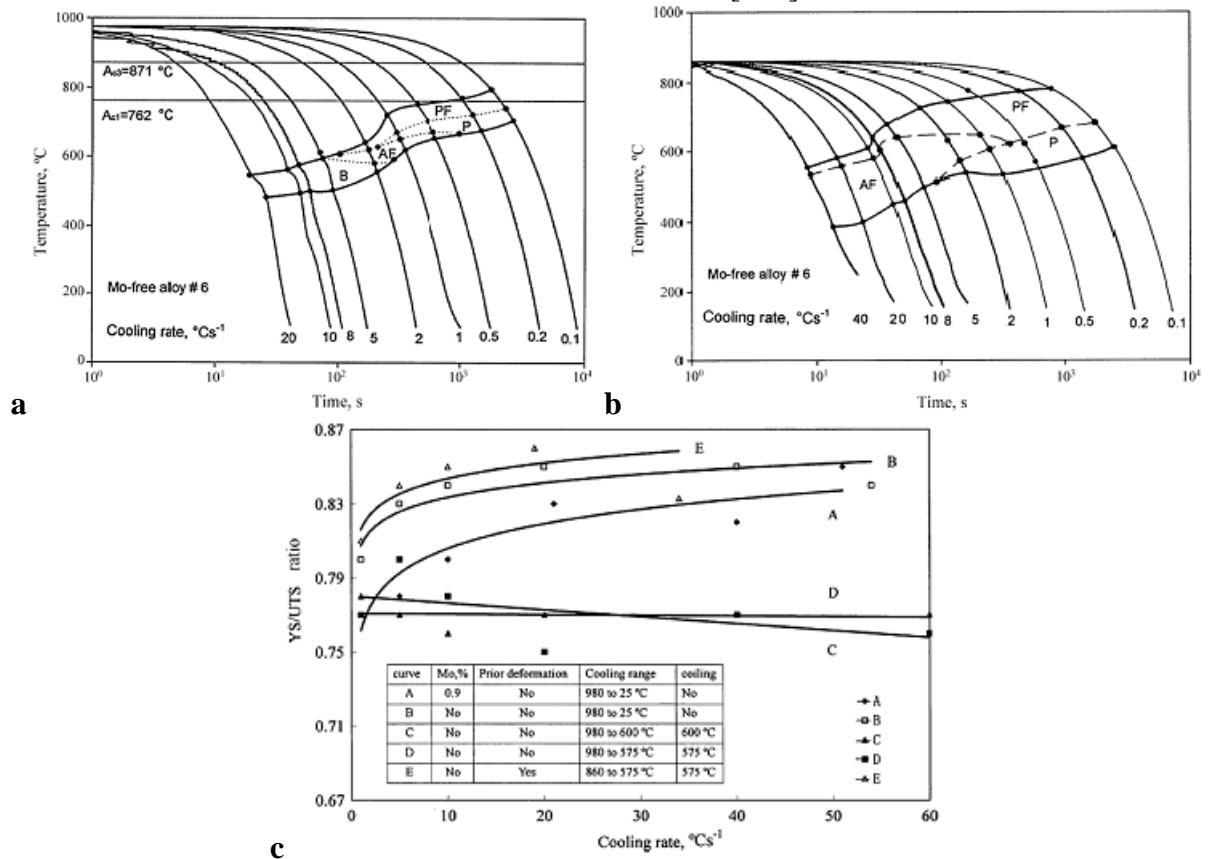


Figure 1.76 Continuous cooling transformation diagram of a 0.066C-0.037Nb-0.062V-0.017Ti steel (a) without prior deformation and (b) with 0.6 strain prior deformation at 860°C : PF – polygonal ferrite, P – pearlite, AF – acicular ferrite, B – bainite; and (c) YS/UTS ratio dependence on cooling rate [143]

Finish cooling temperature in the range below 600 °C from the same finish rolling temperature does not influence the microstructure and the yield stress significantly, but the tensile strength was observed to increase with finish cooling temperature decrease [142] (Figure 1.77).

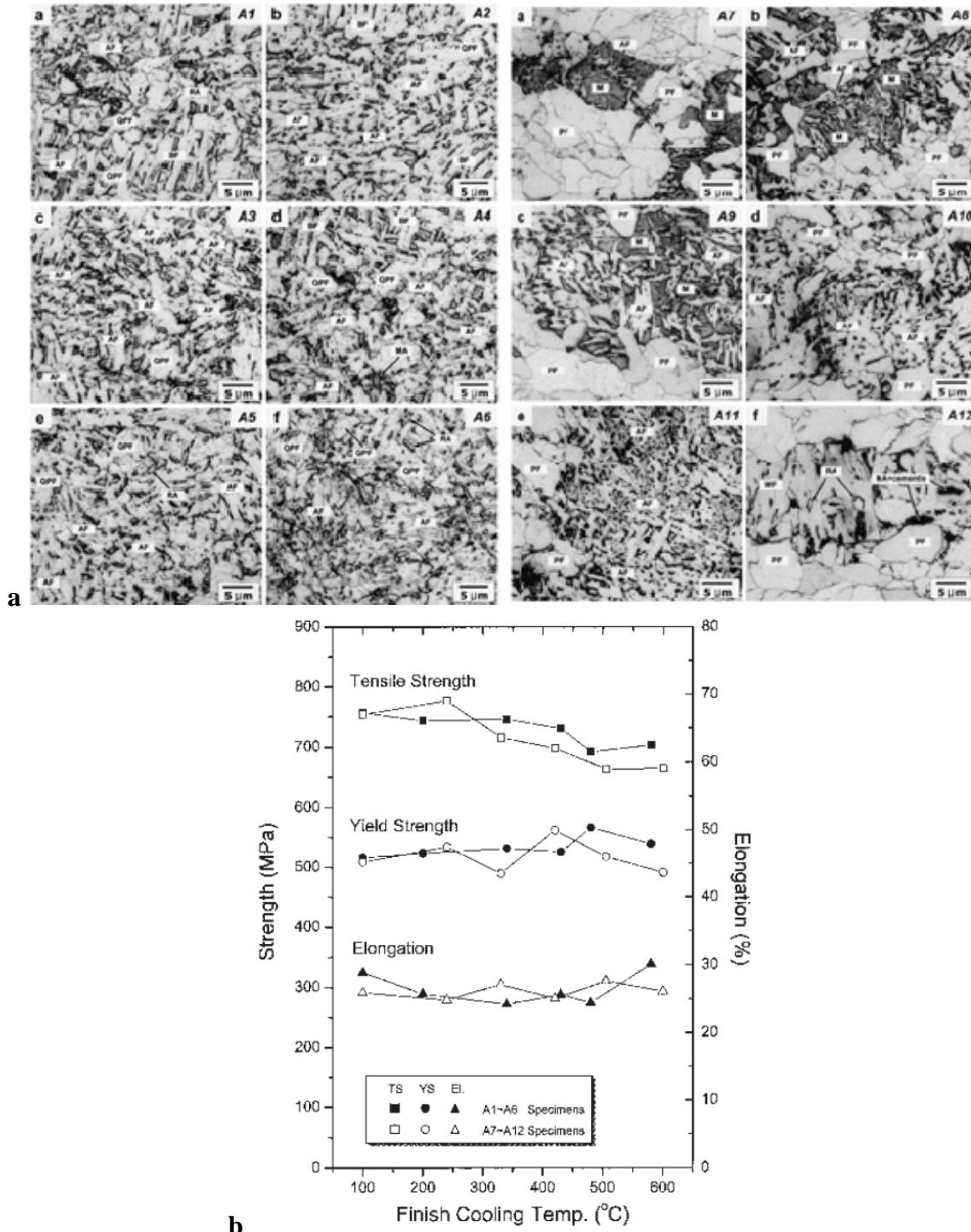


Figure 1.77 (a) Microstructures and (b) the mechanical properties dependence on finish cooling temperature for a X70 steel: A1-A6 - finish rolling temperature 840 °C, A1 – finish cooling temperature 100 °C, A2 - 200 °C, A3 - 340 °C, A4 - 430 °C, A5 - 480 °C, A6 - 580 °C ; A7-A12 - finish rolling temperature 720 °C, A7 – finish cooling temperature 100 °C, A8 - 240 °C, A9 - 330 °C, A10 - 420 °C, A11 - 505 °C, A12 - 600 °C [142]

As can be seen from the above, steels with the same chemistry but rolled according to the different temperature-deformation schedules can exhibit a wide range of microstructures and mechanical properties. In general, to increase strength finish rolling temperature should be decreased, deformation increased and cooling rate increased (to some extent so as not to lose toughness). When producing the HSLA plate steels for line pipe forming, precise correlation between rolling parameters, microstructure and plate properties is needed, due to high requirements simultaneously for pipe strength and toughness. During pipe forming, cold deformation adds to the pipe properties via work-hardening or work-softening (due to the Bauschinger effect). Although quantitative description of work-hardening can be considered as having been established, quantitative dependencies of work-softening based on microstructure parameters have not. If quantitative dependence of the Bauschinger effect on microstructure (dislocation density and precipitate distributions) were found, the rolling parameters might be chosen with respect to the mechanical property change during pipe forming. Thus the Bauschinger effect investigation in this project is closely connected to rolling technology development.

1.6 Large diameter pipe forming

1.6.1 UOE forming process

The UOE pipe forming process consists of several stages schematically shown in the Figure 1.78 [144]. A hot rolled or thermo-mechanically controlled processed plate is typically supplied at a given length, e.g. 12.5 m, and at a width corresponding to the pipe diameter (Figure 1.78, a). After cleaning, four tabs are welded to the plate, one at each corner (Figure 1.78, b). These tabs provide run-on and run-off strips, which enable stabilisation of the arc

during welding of the pipe body. Next is the edge preparation stage, Figure 1.78, c, where the edges are machined to give parallel planes, and then a required welding angle is machined, to ensure full penetration of the weld through the wall thickness of the pipe. After that the edges are bent with a special crimping press to the pipe diameter form, for better control of the pipe final shape after the O-ing stage.

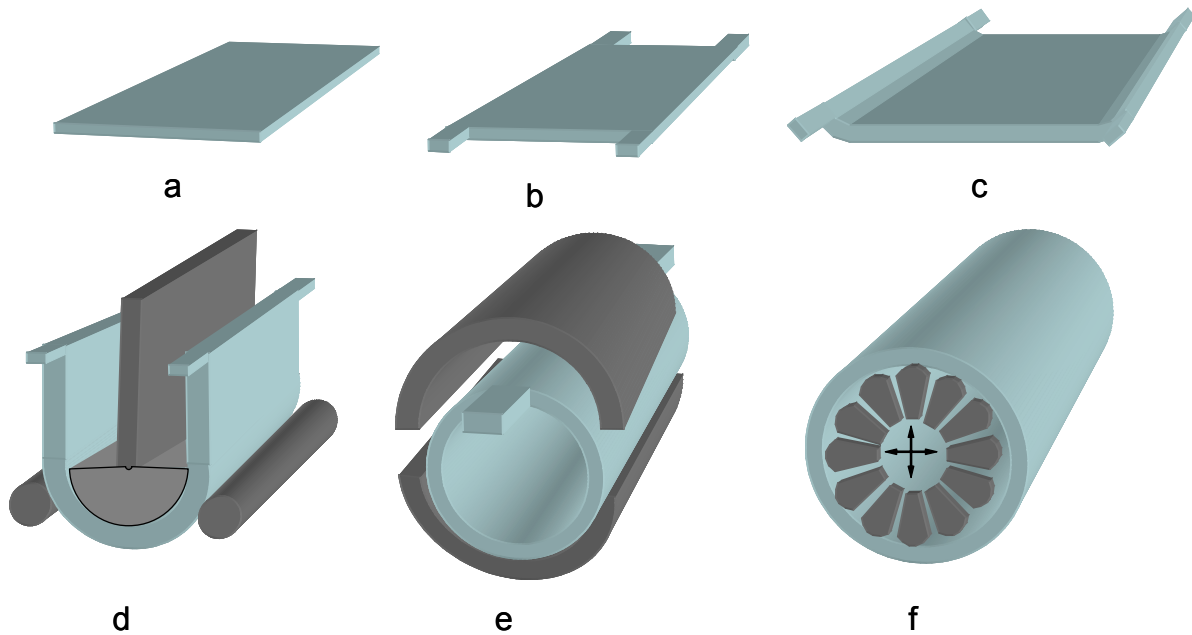


Figure 1.78 Schematic diagram of the UOE pipe forming process: (a) – initial plate, (b) – welding of the tabs, (c) – pre-forming of the plate edges, (d) – U-ing stage, (e) – O-ing stage, (f) – expansion

After edge preparation the plate goes to the U-ing press, which has a U shaped die and rollers at each side of the plate (Figure 1.78, d). At the beginning of this stage the U-bulb die is lowered in the middle of the plate. Then the rollers go inwards and finish plate bending around the U-bulb. The length of the U-die equals the length of the pipe and the radius is chosen with respect to the internal radius of the pipe. During forming of high strength steels, such as X120 grade, severe spring back after the U-ing stage may occur. By increasing the U-bulb radius in the vertical direction it is possible to reduce the extent of spring back (Figure 1.79).

The O-ing stage is carried out by a separate press with two semicircular dies (Figure 1.78,e). After the U skelp is lubricated the two dies are moved towards each other to form a

cylinder. The edges of the plate are brought together and the U-shape plate transforms into an O-shape through a series of plastic hinges around the pipe cross section. The radius of the U-part of the plate cross section is increased and the parallel parts of the plate continue bending in the same direction as at the U-ing stage. After the plate reaches the O-shape the semi-circular dies continue moving inwards to “kill” the pipe and ensure no spring back on unloading. This also gives full contact between the plate edges providing better weld quality. Thus after the O-ing stage the pipe has an approximately 1% smaller diameter than the final, customer required, one.

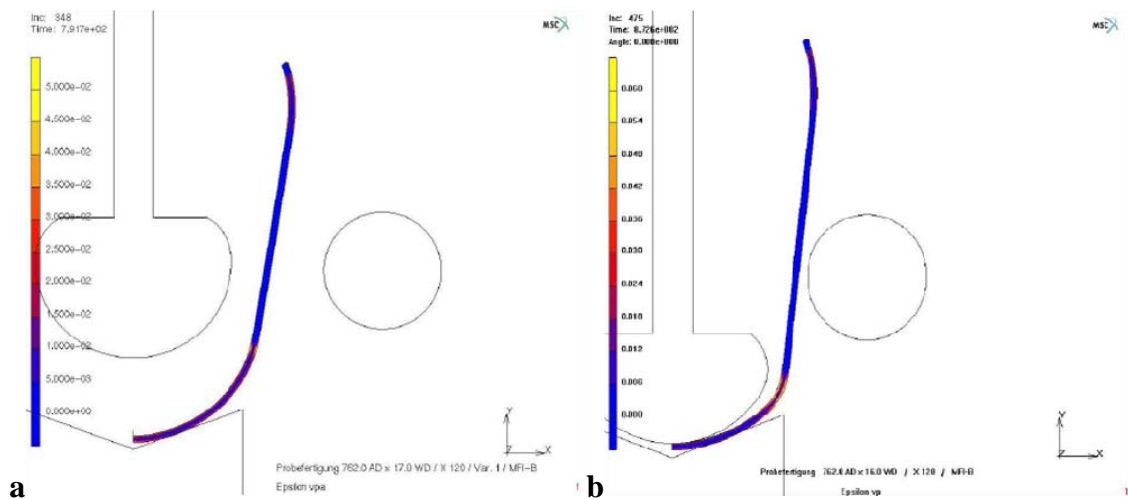


Figure 1.79 U-bulb shape development with FEM simulation:
a – conventional form, b – modified form [145]

The “O” pre-form is washed and dried to remove any residual lubricant and moisture and prevent hydrogen entering the weld. Then the “O” pre-form goes to the continuous tack welding station, where each pipe passes through a series of pressure rolls, to ensure edge alignment, and a single wire gas metal arc weld is made. This weld is subsequently inspected visually and all the necessary repairs are made. At the main welding stage two welds are made by the multi-wire feed submerged arc welders: first is from the inside of the pipe and another from the outside. After non destructive testing the pipe moves to the final forming stage – mechanical expansion (E-ing).

Twelve internally tapered expander shoes are placed inside the pipe (Figure 1.78, f). One of the shoes has a notch into which the internal weld bead fits. A tapered mandrel is driven inside the pipe forcing the expander shoes outwards. Thus the pipe perimeter is stretched. Mechanical expansion compared to hydraulic expansion provides good roundness and straightness of the pipe wall. All the deformation stages of the process are carried out at room temperature.

1.6.2 Strain distribution during pipe forming

In the process of simple bending the strain magnitude can be calculated according to Figure 1.80. If shear deformation across the bar is neglected, which is possible at low strains, the neutral layer can be accepted as being at the mid-thickness of the bar. In this case the elongation of the outer layer will then be as follows:

$$\varepsilon_{\text{out}} = \frac{l_0 - l_n}{l_n} = \frac{\alpha R_0 - \alpha \left(R_0 - \frac{t}{2} \right)}{\alpha \left(R_0 - \frac{t}{2} \right)} = \frac{t}{2 \left(R_0 - \frac{t}{2} \right)}. \quad (1.1)$$

The inner layer is compressed by the same magnitude of strain:

$$\varepsilon_{\text{in}} = -\frac{t}{2 \left(R_0 - \frac{t}{2} \right)}.$$

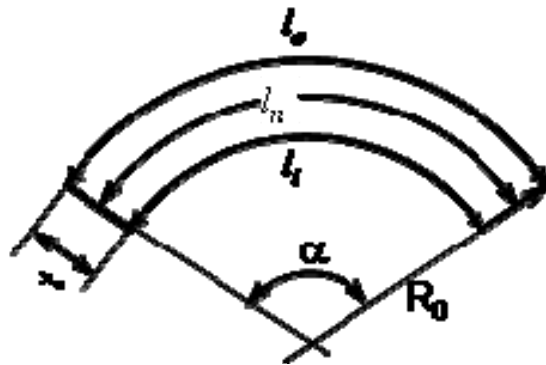


Figure 1.80 Schematic diagram of the bar cross section in the process of simple bending: R_0 – outside diameter of the bar after bending, t – thickness of the bar

In the process of pipe diameter expansion, or reduction, deformation of a pipe can be calculated as the cross section perimeter change (Figure 1.81):

$$\varepsilon_e = \frac{2\pi R - 2\pi r}{2\pi r} = \frac{R - r}{r} \text{ - for expansion and}$$

$$\varepsilon_r = \frac{2\pi r - 2\pi R}{2\pi R} = \frac{r - R}{R} \text{ - for reduction.} \quad (1.2)$$

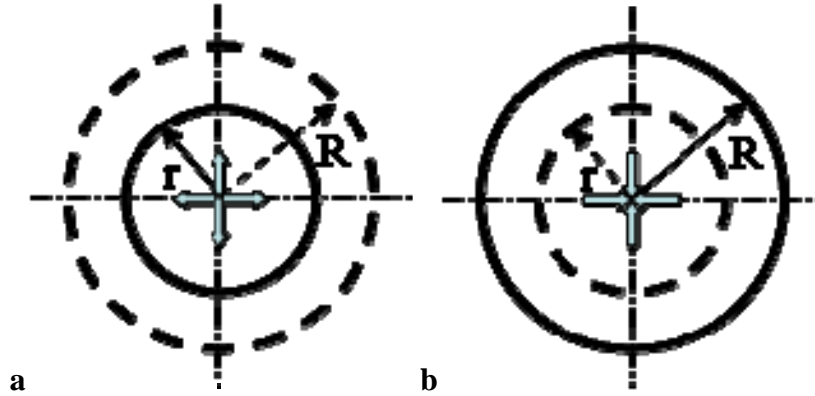


Figure 1.81 Schematic diagram of the pipe cross section in the process of (a) diameter expansion and (b) diameter reduction

Using equations (1.1) and (1.2) it is possible to assess the strain at each stage of the UOE forming process. A comparison between calculated values using the above equation and the limited literature data available is presented below.

U-ing stage

Example – 1, a

For a 914 mm final diameter pipe with 25 mm wall thickness the U-radius is reported to be 286 mm [146]. Substituting $t = 25$ mm and $R_0 = 286$ mm into equation (1.1) the maximum strain in the pipe wall can be estimated as follows:

$$\varepsilon = \frac{25}{2\left(286 - \frac{25}{2}\right)} = 0.046 .$$

Example – 1, b

In this situation, subtraction of 25 mm wall thickness from 286 mm outside radius gives $R_{bulb} = 261$ mm for the U-bulb radius (Figure 1.82). If the U-bulb radius is assumed to be the same for another pipe wall thickness, then for plate of thickness $t = 38$ mm the pipe section outside radius after U-ing will be:

$$R_0 = R_{bulb} + t = 261 + 38 = 299 \text{ mm.}$$

Substituting the latter figure into equation (1.1) gives the maximum strain in the plate outer layer as:

$$\varepsilon = \frac{38}{2 \left(299 - \frac{38}{2} \right)} = 0.068 .$$

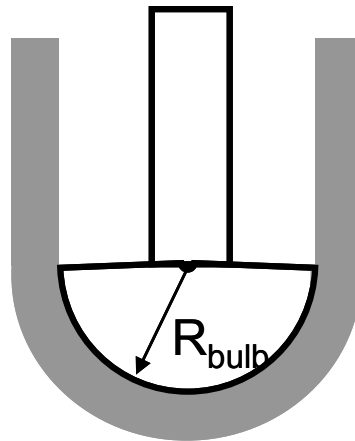


Figure 1.82 Schematic diagram of the U-ing stage cross section

FE modelling of a 914 x 38 mm pipe U-ing stage by Hilton and Usherwood (a reference to the “British Steel technical note” in [146]), gave the maximum strain $\varepsilon = 0.036 \dots 0.054$. Comparison of this value with the equation (1.1) calculation gives 20 – 47 % accuracy. Lower reported values, than calculated with the equation (1.1), can be related to two aspects, not taken into account in equation (1.1). First – friction between the tool and work-piece (plate – U-bulb) leads to a decrease in tensile deformation in the outer layer of the plate. Second – the neutral layer shifts from the centre-line of the plate towards the U-bulb resulting in compression deformation decreasing at the inner-surface of the plate.

Example – 2

For a 610 x 12.7 mm pipe U-bulb diameter is reported to be 483 mm [64]. Thus the plate radius after U-ing is:

$$R_0 = R_{\text{bulb}} + t = 483/2 + 12.7 = 254.2 \text{ mm.}$$

Maximum strain calculated with equation (1.1) is as follows:

$$\varepsilon = \frac{12.7}{2 \left(254.2 - \frac{12.7}{2} \right)} = 0.0256.$$

According to a theoretical estimation [64], the maximum strain for this pipe during U-ing is $\varepsilon=0.028$, which is 8.6 % higher than calculated. The larger reported value in this case may be related to a neutral layer shift from the centre-line inwards. It is worth highlighting that the agreement, between reported values and equation (1.1) calculations, was better for lower values of deformation.

O-ing stage

For a 914 x 25 mm pipe the O-stage outside diameter is reported to be 454 mm. Strain in the edges, where bending occurs inwards (Figure 1.83, a), according to equation (1) is:

$$\varepsilon_{\text{edge}} = \frac{25}{2 \left(454 - \frac{25}{2} \right)} = 0.028.$$

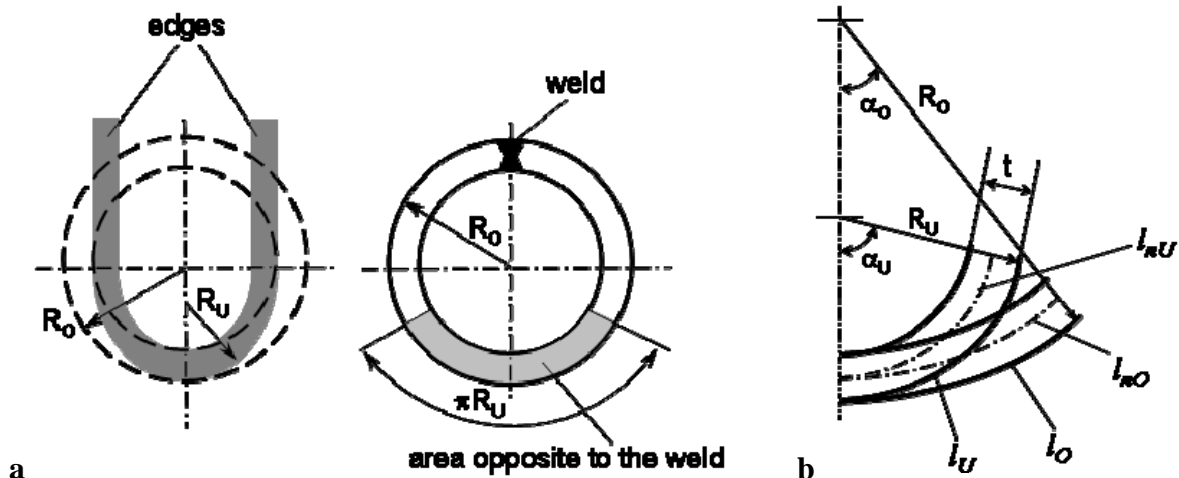


Figure 1.83 Schematic diagram of (a) the O-ing stage cross section and (b) opposite to the weld plate segment deformation

The total strain in the area opposite to the weld can be determined by summing the strain values after O-ing and U-ing. Strain during U-ing can be calculated with equation (1.1). Strain during O-ing can be calculated considering Figure 1.83, b; the maximum strain in the outer layer of a selected plate segment during O-ing is as follows:

$$\varepsilon_{O-out} = \frac{l_O - l_U}{l_U} = \frac{\alpha_O R_O - \alpha_U R_U}{\alpha_U R_U} = \frac{\alpha_U \left(\frac{\alpha_O}{\alpha_U} R_O - R_U \right)}{\alpha_U R_U} = \frac{\frac{\alpha_O}{\alpha_U} R_O - R_U}{R_U}.$$

As the neutral layer length remains constant then:

$$l_{nO} = l_{nU}, \quad \alpha_O \left(R_O - \frac{t}{2} \right) = \alpha_U \left(R_U - \frac{t}{2} \right),$$

$$\frac{\alpha_O}{\alpha_U} = \frac{\left(R_U - \frac{t}{2} \right)}{\left(R_O - \frac{t}{2} \right)} = \frac{2R_U - t}{2R_O - t},$$

and

$$\varepsilon_{O-out} = \frac{\frac{2R_U - t}{2R_O - t} R_O - R_U}{R_U}.$$

And the maximum strain in the inner layer is:

$$\varepsilon_{O-in} = \frac{\frac{2R_U - t}{2R_O - t} (R_O - t) - (R_U - t)}{R_U - t}$$

Substituting the numerical values for the example discussed gives:

$$\varepsilon_{U-out} = \frac{25}{2 \left(286 - \frac{25}{2} \right)} = 0.046, \quad \varepsilon_{U-in} = -0.046$$

$$\varepsilon_{O-out} = \frac{\frac{2 \cdot 286 - 25}{2 \cdot 454 - 25} \cdot 454 - 286}{286} = -0.017,$$

$$\varepsilon_{O-in} = \frac{\frac{2 \cdot 286 - 25}{2 \cdot 454 - 25} \cdot (454 - 25) - (286 - 25)}{286 - 25} = 0.018 .$$

Therefore the total strain in the outer layer after O-ing is as follows:

$$\varepsilon_{U+O-out} = 0.046 - 0.017 = 0.029 ,$$

and at the inner surface

$$\varepsilon_{U+O-in} = -0.046 + 0.018 = -0.028 .$$

For the 914 x 25 mm pipe Harris and Senogles, according to [146], reported that the maximum strain after O-ing, ε_{U+O} , to be -0.046...0.032, where negative values denote compression on the inside surface of the pipe and positive values denote tension on the outside surface. Larger reported values of tension on the outside surface, as in the case of Example-2 for U-ing, can be related to a neutral layer shift inwards. Larger compressive strain on the inside surface can be explained if compression on the inside layer at the edges propagates to the cross section area opposite to the weld. This may occur due to the boundaries of the “area opposite to the weld” being unstable, as they assume their position with respect to the circumferential stress equilibrium.

“Killing” and Expansion

The outside diameter of the 914 mm pipe after “killing” was reported to be 905 mm [146]. Thus for the diameter reduction from the O-stage, $454 \cdot 2 = 908$ mm, to 905 mm equation (1.2) gives:

$$\varepsilon_K = \frac{905 - 908}{908} = -0.003 .$$

Strain in the outside layer after expansion is:

$$\varepsilon_E = \frac{914 - 905}{905} = 0.010 .$$

Inner surface strain does not depend significantly on the pipe wall thickness and for the E-stage for different pipe wall thicknesses equates to:

$$\varepsilon|_{t=25} = 0.0105, \quad \varepsilon|_{t=38} = 0.0108, \quad \varepsilon|_{t=50.8} = 0.0112.$$

Strain gauge and grid measurements by Harris and Senogles show that, for the E-stage, strain at the inner surface to be 0.011 – 0.013 and at the outer surface to be 0.013 – 0.016 depending on pipe wall thickness (Table 1.9). For the outer surface the measured data are 30 - 115 % higher than calculated, and for the inner surface – only 1 – 20 % higher. Lower strain values and better correspondence between reported and calculated values at the inner surface can be related to the presence of an internal tool during expansion. Obviously expansion shoes, being in contact with the metal, retard metal flow on the internal surface of a pipe and the neutral layer shifts inwards. But on the outside surface the metal flow is unconstrained.

On a whole, a theoretical estimation of strains during UOE forming, proposed in the present work, shows lower values of strain than experimental measurements. This is a result of assumptions, taking during theoretical derivation, such as: neutral layer positioning in the centre line of the pipe wall cross section; absence of friction on the inside and outside surfaces of the pipe wall; equal cross section radius for all the points of the described segment (plate edges, opposite to the weld area); equal pipe wall thickness during the whole process of bending; constant mechanical properties of the pipe material.

Table 1.9 Strain levels during the E-stage for the 914 mm diameter pipe with different wall thicknesses

Pipe wall thickness, mm	Measured		Calculated	
	ε_{inner}	ε_{outer}	ε_{inner}	ε_{outer}
25.0	0.013	0.013	0.011	0.010
38.0	0.011	0.022	0.011	0.010
50.8	0.012	0.016	0.011	0.010

Comparison between strain values for all the stages of the UOE forming process shows that maximum deformation occurs during the U-ing stage in the area opposite to the weld (Table 1.10). The absolute values of deformation after O-ing are approximately the same in the edges and in the area opposite to the weld (Figure 1.83, a). However, differences in strain path should be taken into consideration when evaluating mechanical properties. Thus, the edge material is subjected to unidirectional deformation followed by a full cycle of reverse loading, and the material opposite to the weld undergoes two full cycles of reverse deformation. In terms of pipe property development, after such deformation schedules it is possible to expect lower strength in the area opposite to the weld, compared to the plate edges (areas around the pipe weld).

Table 1.10 Strain values during forming of a 914 x 25 mm pipe (calculation)

Forming stage	Outer surface		Inner surface	
	Opposite to the weld	Plate edges	Opposite to the weld	Plate edges
U-ing	0.046	0	- 0.046	0
O-ing	- 0.017	0.028	0.018	- 0.028
“Killing”	- 0.003	- 0.003	- 0.003	- 0.003
Expansion	0.010	0.010	0.011	0.011

1.6.3 Pipe property evaluation

The pipe body mechanical properties are developed in two ways. The first is microstructure formation during plate rolling and its influence on the properties via strengthening mechanisms, described in sections 1.4 and 1.5. The second is the cold deformation schedule during forming, which may result in strength increase due to unidirectional loading (work-hardening) or decrease due to the reverse loading (the

Bauschinger effect). The main feature of the UOE forming process, affecting the property distribution in the pipe cross-section, is inequality of strain magnitude and deformation direction sequence for different areas of the plate cross-section (Table 1.10, Figure 1.84).

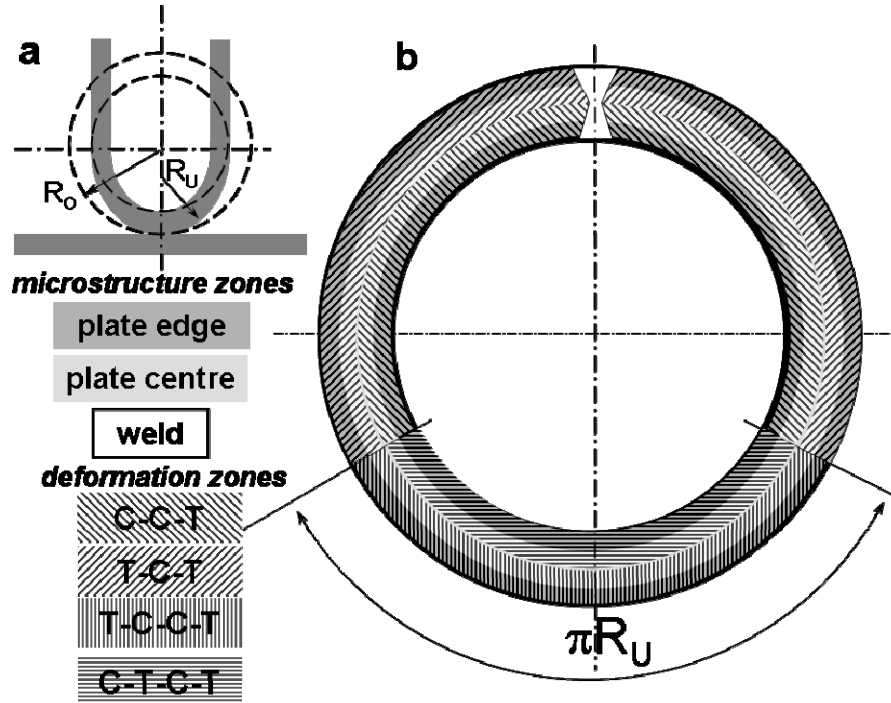


Figure 1.84 (a) Schematic diagram of the pipe cross-section after U-ing and O-ing: R_U and R_O – outer radius of a pipe after U-ing and O-ing; (b) property zones in the pipe cross-section after the UOE forming: C – compression, T – tension

Qualitatively the properties are formed in the following way. As a result of bending during U-ing, the inside surface of the segment opposite to the weld is subjected to compression and outside surface to tension. Absolute values of strain on this deformation stage in the range 0.025 - 0.068 result in work-hardening in these areas. During O-ing the plate edges are bent inwards and opposite to the weld segment outwards, as the U-bulb radius R_U is smaller than the radius of the pipe after O-ing R_O (Figure 1.84). So after O-ing with strains of about 0.02, the strength in the segment opposite to the weld should decrease, due to the full cycle of forward-reverse deformation, and increase in the edges, due to unidirectional deformation and further work hardening. “Killing”, with subsequent expansion with more than 0.01 strain, adds another cycle of forward-reverse deformation: during “Killing” the pipe

experiences whole cross-section compression and during expansion whole cross-section tension. Finally, the segment opposite to the weld undergoes two full cycles of forward-reverse deformation and the plate edges one cycle of unidirectional and one of forward-reverse deformation. This may result in work-softening from plate to pipe, especially in the segment opposite to the weld [64, 65]. The amount of possible strength loss depends on the pipe geometry (with pipe wall thickness increase and outside diameter decrease the strain increases), microstructure and initial mechanical properties of the plate material.

Quantitative measurements of the pipe body mechanical properties are performed using test coupons cut mainly from the 180° position (opposite to the weld) in the transverse and longitudinal directions, but the 90° or 270° positions may be also used according to customer requirements. In the transverse direction the test samples are machined either directly from a pipe segment or after flattening (Figure 1.85). There is an additional deformation half cycle during flattening, which can result in softening due to the Bauschinger effect, meaning that, the strength in transverse orientation measured using flattened specimens may be lower than that measured with other methods. On the other hand, in the longitudinal direction strength may increase due to work-hardening. Thus, pipe material strength change during flattening should be considered when assessing the real magnitude of the pipe properties. As an alternative, an hydraulic expansion test can be done using a full cross-section pipe ring. As a pipe ring includes the weld area, the last method gives the yield stress for the pipe body, and also the yield stress (YS) and ultimate tensile strength (UTS) for the weld metal. It allows more accurate measurement of the pipe body yield stress in the transverse direction than any other method, but it requires specialised test equipment.

Recent investigations into the influence of test methods on mechanical property data obtained in the transverse direction have shown the following (Table 1.11):

- in all but one case, flattening leads to a significant yield stress decrease, compared to the

round bar and hydraulic expansion tests, which are performed without prior deformation of a test piece,

- the YS decrease due to flattening may reach 10 - 30 %, which is consistent with earlier reported data of 20 % YS decrease for a 610 x 12.7 mm pipe [64],
- the UTS change due to flattening is significantly smaller than the YS change (Figure 1.85, a), as YS reflects the dislocation-obstacle interaction conditions (level of work-hardening/work-softening) prior to/on start of deformation and UTS shows more of the inherent ability of the material to accumulate work-hardening and prevent crack propagation,
- the YS and UTS drop, because of flattening, increases with microalloying element content and absolute values of strength increase, i.e the drop is higher for the X100 steel than for the X80, and for the X80 is higher than for X70 steel.

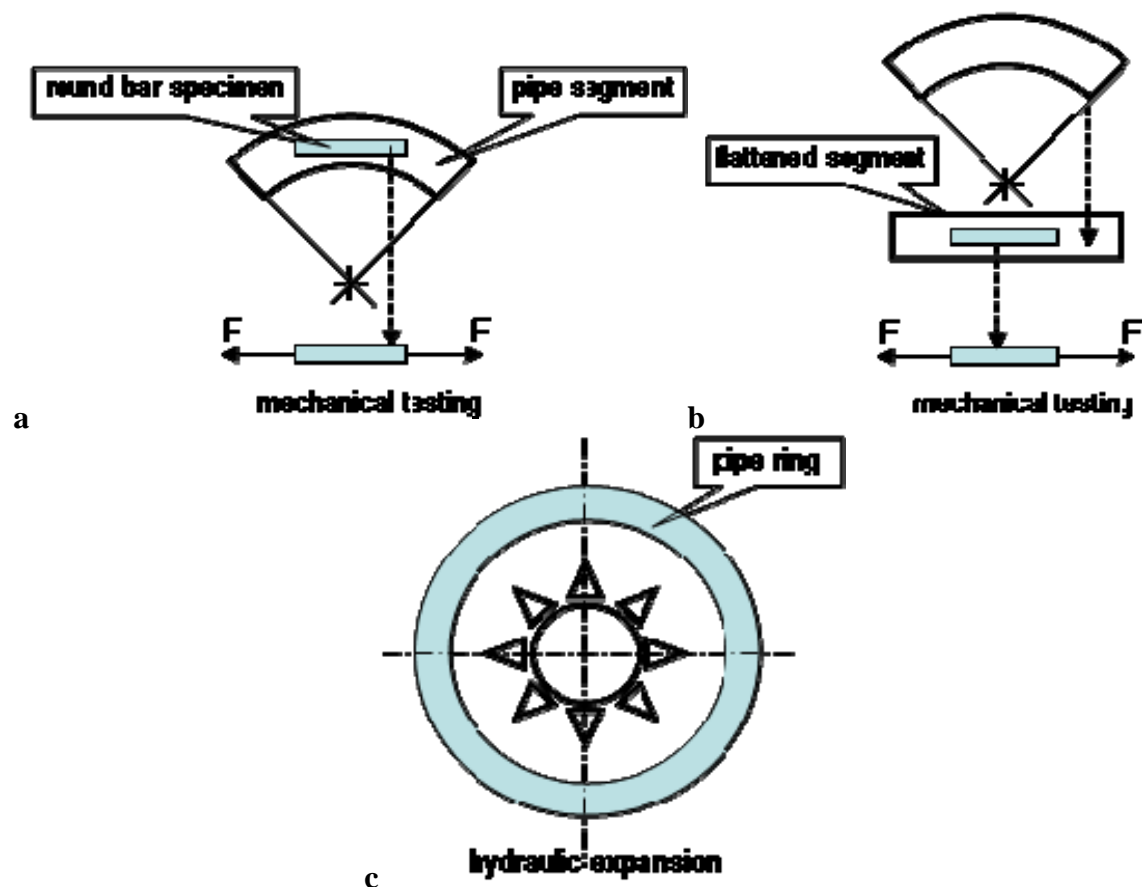


Figure 1.85 Schematic diagram of the (a) round bar tension test, (b) flattened specimen tension test and (c) hydraulic ring expansion

As can be seen from Table 1.11, apart from the alloying element content and initial strength level, microstructure phase balance influences property variation with a test method. Thus the ferrite-pearlite X60 steel grade, although being of a lower absolute strength, showed higher the YS and UTS drop due to flattening than X70 steel, which has an acicular ferrite microstructure and higher microalloy and strength levels. This may be related to different dislocation-particle interaction conditions for different steel grades, however this aspect was not reported in the reference [147].

Table 1.11 Mechanical properties of pipe material in the transverse direction measured using different methods (derived from [147]), MPa

Steel grade		X60	X70	X80	X100
Pipe diameter x wall thickness, mm		914 x 25.4	1016 x 21.0	1066.8 x 25.0	914.4 x 19.0
Alloying elements		Nb-V	Cu-Ni-Mo-Nb-V	Cu-Ni-Mo-Nb	Cu-Ni-Mo-Nb
Microstructure		F* + P	AF	AF	LB + M
Flattened	0.5%YS _F	479	551	583	668
	UTS _F	578	629	678	829
Round bar	0.5%YS _R	495	550	603	807
	UTS _R	574	623	684	839
Hydraulic, 0.5%YS _H		565	610	648	849
YS _F - YS _R		- 16	+ 1	- 20	- 139
YS _F - YS _H		- 86	- 59	- 65	- 181
UTS _F - UTS _R		+ 4	+ 6	- 6	- 10

*F – ferrite, P – pearlite, AF – acicular ferrite, LB – lower bainite, M – martensite;
 YS_F and UTS_F – yield stress and tensile strength after flattening, YS_R and UTS_R – yield stress and tensile strength measured using the round bar test method, YS_H – yield stress measured with the hydraulic ring expansion test

Comparing the influence of flattening on mechanical property change in different directions it can be seen, Figure 1.85, that in the longitudinal direction the absolute values of the YS and UTS do not depend on the method of testing, however in the transverse orientation the YS obtained with flattened specimens is lower than that obtained with the round bar specimens. The difference in the YS data in transverse direction increases with material strength increase, as the Bauschinger effect tends to increase with microalloying element content and work-hardening increase (see section 1.2.4).

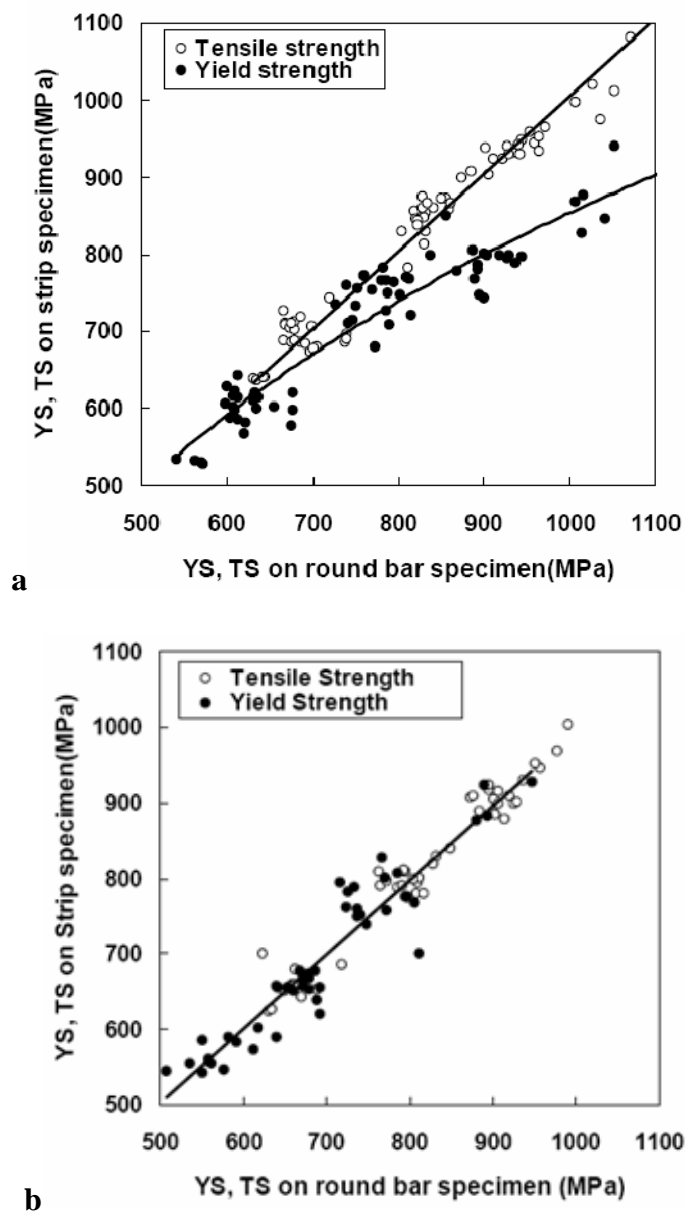


Figure 1.85 Flattened specimen vs round bar specimen mechanical property data in (a) transverse and (b) longitudinal direction [147]

1.6.4 Plate to pipe property change

Quantitative data of plate to pipe property changes are very scarce, due to difficulties involved in experimentally reproducing the pipe forming stages and property evaluation described above. However, it is known that strength may increase, decrease or remain the same, and this change depends on steel chemistry and the initial properties, as discussed above.

Recent studies of plate to pipe property changes have shown an increase in both YS and UTS from plate to pipe due to work-hardening, but this depended on steel chemistry, namely microalloying element content, Table 1.12 [146]. In the pipe longitudinal direction, where the reverse deformation as a source of work-softening might be considered less prominent due to the Bauschinger effect dependence on test direction (see Figure 1.49 in section 1.2.3), the YS increase from plate to pipe is lower for more highly alloyed steels and the UTS increment steadily decreases with increase in microalloying. In the transverse orientation a decrease in the YS from plate to pipe was observed and the YS drop increased with microalloying element content increase. On the basis of these data and some earlier work [69] it is possible to conclude, that, during pipe forming, two competitive processes take place in the pipe material at the same time – work hardening due to the unidirectional straining and work softening due to the reverse cold deformation (the Bauschinger effect).

According to the Bauschinger effect theories (see section 1.2) the yield strength decrease in alloyed steels depends on their dislocation structure and microalloy particle distributions. The dislocation structure, formed during thermo-mechanically controlled rolling, is influenced by the processing parameters, such as absolute strain levels, deformation start and finish temperatures, and cooling rate. During plate to pipe cold forming the strain levels and deformation direction add to the dislocation structure formation. The microalloy particle

distributions in their turn depend on the alloying element types and plate rolling parameters. At present, the qualitative influence of the Bauschinger effect on plate to pipe property change is understood, i.e. *with increase in microalloying and work-hardening the Bauschinger effect increases*. However, further development of plate and pipe processing technology and product quality control requires a quantitative understanding of how the mechanical properties depend on processing parameters and steel chemistry.

Table 1.12 Plate to pipe property change (derived from [146]), MPa

Steel grade			X52	X60	X65
longitudinal orientation	plate	YS _{pl}	357	458	498
		UTS _{pl}	493	543	568
	pipe	YS _{pipe}	378	473	514
		UTS _{pipe}	511	551	564
	flattened pipe	YS _{fp}	397	447	523
		UTS _{fp}	501	539	567
	YS _{pipe} - YS _{pl}		+ 21	+ 15	+ 16
	UTS _{pipe} - UTS _{pl}		+ 18	+ 8	- 4
	YS _{fp} - YS _{pl}		+ 40	- 11	+ 25
	UTS _{fp} - UTS _{pl}		+ 8	- 4	-1
transverse orientation	plate	YS _{pl}	352	481	528
		UTS _{pl}	490	557	571
	flattened pipe	YS _{fp}	390	478	519
		UTS _{fp}	500	555	573
	YS _{fp} - YS _{pl}		+ 38	- 3	- 9
	UTS _{fp} - UTS _{pl}		+ 10	- 2	+ 2

1.7 Aims and objectives of the project

The mechanical properties of the pipes are dependent on the rolled plate microstructure / properties and the cold deformation schedule during pipe forming. In their turn, the plate microstructure and properties are significantly dependent on plate processing (section 1.5.1) and plate to pipe property change depends on strain magnitude and direction during forming (section 1.6). Microstructure-property correlation equations (section 1.4) predict these relationships well within the steel chemistries for which they were developed. Work-hardening due to unidirectional cold deformation can be considered quantitatively understood (section 1.1.7), however work-softening due the reverse deformation is known only qualitatively (section 1.2). Thus to fully understand and predict pipe mechanical properties quantitative understanding of the *microstructure* (dislocation sub-structure, precipitate distribution) *influence on work-softening is needed*.

In the present work this problem is being solved for materials with the same processing parameters but different chemistry, namely microalloying element content. This allows the influences of plate processing parameters on pipe properties via plate microstructure to be separated. Chemistry, namely microalloying element content, influence on the Bauschinger effect is assessed via dislocation-particle interaction, for which the microalloy particle distributions and dislocation densities are studied separately and correlated to the property change. The aims and objectives of this project are summarised in the Table 1.13.

Table 1.13 Aims and objectives of the project

Field of study	AIM	OBJECTIVES
microstructure of the plate material	theoretical prediction	Thermo-Calc computer modelling of phase balance
	experimental characterisation	phase constituents, ferrite grain size, pearlite content, solute element inclusions
		microalloying element content distribution
		Microalloy precipitates size, morphology, chemistry and distribution in the ferrite matrix
		dislocation structure type and dislocation density
UOE pipe forming process	cold deformation schedule	strain magnitude, direction, and distribution in the pipe cross section
mechanical properties of the plate material	unidirectional deformation	yield stress and tensile strength dependence on steel chemistry, dislocation structure and microalloy particle distributions
	forward-reverse deformation	yield stress in the reverse direction <i>quantitative</i> dependence on steel chemistry, dislocation structure and microalloy particle distributions

2. MATERIALS AND EXPERIMENTAL TECHNIQUES

2.1 Materials

Three different steel plates originally provided by Corus plc, Plates and Commercial Steels (SPCS), were used (Table 2.1). The C-Mn steel plate was 8.1 mm in thickness, C-Nb 10.2 mm and C-Nb-V 10.5 mm. Mechanical properties meet the requirements of the American Petroleum Institute for B grade (C-Mn), X60 (C-Nb), and X65 (C-Nb-V) (Table 2.2).

The C-Nb and C-Nb-V steel microstructure and mechanical property investigations were carried out for both steels in the as-rolled and annealed conditions. Annealing at 400 °C and 550 °C for 30 min was applied to modify the dislocation structure and microalloy particle distributions, without affecting the grain size and the second phase (pearlite) content.

Table 2.1 Plate compositions in weight %

Steel	C	Si	Mn	P	S	Cr	Al	Ni	Cu	Nb	V	N	Ti	Mo
C-Mn	0.12	0.23	1.09	0.019	0.100	0.023	0.33	-	0.015	0.001	0.002	0.020	0.001	0.002
C-Nb	0.10	0.37	1.36	0.012	0.006	0.017	-	0.016	0.009	0.034	0.001	0.002	0.001	0.002
C-Nb-V	0.07	0.34	1.47	0.012	0.003	0.013	-	0.021	0.015	0.046	0.061	0.004	0.002	0.002

Table 2.2 Plate tensile properties in transverse orientation (courtesy of Corus SPCS)

Steel	YS, MPa	UTS, MPa	Elongation to failure, %
C-Mn	359	494	25
C-Nb	487	568	21
C-Nb-V	557	590	19

2.2 Experimental techniques

2.2.1 Thermodynamic modelling

Computer modelling of the microstructure was carried out using versions L and Q of Thermo-Calc. The bulk alloy compositions were used as the software input. Equilibrium phase balances within the temperature range 600-1600 K were calculated along with phase compositions for all the three studied steels.

2.2.2 Optical microscopy and image analysis

For optical microscopy, sections of approximately 10 mm x 10 mm x 10 mm in size were cut from the as-rolled and annealed plates, mounted in conductive bakelite parallel and perpendicular to the rolling direction, ground and polished to a 1 μm finish then etched in 2% nital. The specimens were imaged using Leica DMRX and Zeiss Axioskop2 microscopes and analysed using KS 300 and KS 400 software. Grain size was measured as an average equivalent circle diameter for 800-2000 grains for each point. Pearlite percent was measured using 5 images for each point at a magnification of 100x (0.161 mm^2) or at a magnification of 200x (0.039 mm^2) depending on the steel grade. Measurements were made across the plate thickness in 0.4 mm steps.

2.2.3 Scanning electron microscopy (SEM)

SEM imaging of Mn-, Si- and Al-rich particles was carried out on a Jeol-6300 SEM across plate thickness for all three steels.

SEM imaging of Nb- and Nb-Ti-rich precipitates was carried out using a Jeol JSM-7000F field emission gun scanning electron microscope. Nb-Ti-rich particles were imaged from 4 regions, ferrite and pearlite, sub-surface and mid-thickness, and characterised in terms of morphology, size, volume fraction and number density. For the determination of the particle size distributions and area fraction in the C-Nb steel 630 particles from 15585 μm^2 and in the C-Nb-V steel 1064 particles from 10780 μm^2 total area were imaged.

2.2.4 Transmission electron microscopy (TEM)

Microalloy particle investigation in as-rolled and annealed C-Nb and C-Nb-V steels was carried out on Philips-CM20 (LaB₆) and Philips Tecnai F20 (field emission gun) TEMs. NbTiV- and Cu-rich particles in the C-Nb-V steel were imaged from 2 regions, plate mid-thickness and sub-surface (Table 2.3). Determination of the foil thickness was carried out using a convergent beam diffraction technique [148]. The foil thickness was measured to be in the range 76-120 nm.

Table 2.3 TEM studied area and particle number imaged for the C-Nb-V steel

Place of precipitation		As-rolled	Annealed 400 °C	Annealed 550 °C
Sub-surface	Particle number	469	not measured	152
	Total area, μm^2	3.91		0.81
Mid-thickness	Particle number	918	362	688
	Total area, μm^2	3.12	0.53	3.35

Dislocation sub-structures were studied using Philips-CM20 and Philips Tecnai F20 TEMs. For the dislocation density determination 20 representative regions were imaged in each of the as-rolled and annealed C-Nb and C-Nb-V steels from the plate mid-thickness position. For each representative region 3 - 4 images were taken for different beam directions from the same zone

axis. The mid-thickness position was selected to correlate the dislocation density with the mechanical property data obtained from the compression-tension samples.

2.2.5 Energy dispersive X-ray spectroscopy (EDS)

For the precipitate composition determination EDS point analysis was carried out in the Jeol-6300 SEM (Noran EDS, Vantage software), Jeol-7000F SEM (Inca Oxford EDS), Philips-CM20 TEM (Link Oxford EDS) and Philips Tecnai F20 TEM (Link ISIS Oxford EDS). For the chemical composition investigation of the Nb-Ti-rich precipitates (larger than 50 nm) 48 particles in the C-Nb and 58 particles in the C-Nb-V steel were used for SEM-EDS. For the chemical composition investigation of the NbTiV- and Cu-rich precipitates (smaller than 50 nm) 51 particles in the as-rolled, 25 particles in the annealed at 400 °C and 55 particles in the sample annealed at 550 °C C-Nb-V steel were used for TEM-EDS.

2.2.6 Hardness testing

For ferrite *micro-hardness* distributions across the plate thickness 5 indents for each point were measured using a Shimadzu Vickers micro-hardness tester at intervals of 0.2 mm. 500 g load was used for the three studied steels. For macrohardness distribution across plate thickness 5 indents for each point were measured using an Indentec Vickers Hardness Testing machine. 10 kg load was used for the three studied steels in the as-rolled and annealed conditions.

2.2.7 Mechanical testing

Mechanical properties of microalloyed steels were studied with compression-tension

specimens and compression testing of cylindrical samples. Compression-tension specimens were cut from the plate mid-thickness (Figure 2.1, a). Compression samples also included sub-surface areas of the plate material (Figure 2.1, b).

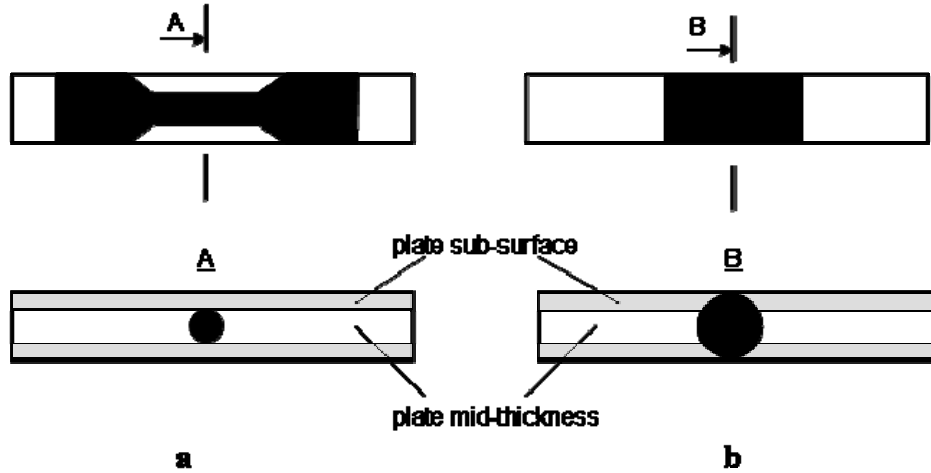


Figure 2.1 schematic diagram of test samples to measure the (a) plate mid-thickness and (b) average plate mechanical properties

Compression-tension testing was carried out on an ESH 250 kN servo-hydraulic twin column low speed ramp universal testing machine. For the forward-reverse stress-strain curve determination 4 cylindrical specimens of 4.5 mm diameter and 13 mm gauge length were cut in the transverse orientation to the rolling direction from the C-Nb and C-Nb-V as-rolled and annealed steel plates. The Bauschinger tests were carried out at room temperature, in the 0.3 - 4.9 % plastic strain range, at 1.3×10^{-4} strain rate.

Compression testing was carried out on a Zwick screw-driven tensile testing machine. To determine total (through plate thickness) yield stress 3 samples of 10 mm diameter and 10 mm length from the C-Nb and C-Nb-V steels in the as-rolled and 550 °C annealed conditions were cut in the transverse orientation to the rolling direction. Four separate sets of samples, of 5 – 6 specimens each from the C-Nb and C-Nb-V steel in the as-rolled and 550 °C annealed conditions, were compressed to different levels of strain to investigate the stored energy dependence on strain.

2.2.8 Differential scanning calorimetry (DSC)

Stored energy dependence on strain, in the as-rolled and 550 °C annealed C-Nb and C-Nb-V steels, was investigated using differential scanning calorimetry (DSC) in a Netzsch DSC 404C calorimeter. The DSC samples of 70 – 80 mg mass were cut from the central axis area of cylindrical samples previously compressed up to 7.1 % strain. The heating curves exhibit two exothermal peaks in the 200 – 380 °C and 400 – 550 °C temperature ranges (Figure 2.2). The first peak was used for the stored energy analysis, as TEM measurements showed insignificant dislocation density decrease with annealing temperature increase from 400 °C to 550 °C. The second peak is mainly related to second phase (pearlite) and microalloy particle precipitation. A degree of oxidation of the sample outside surface may also be a reason, as the samples were not mounted in protective coating, though the experiments were carried out in a flowing argon (100 ml min⁻¹) atmosphere.

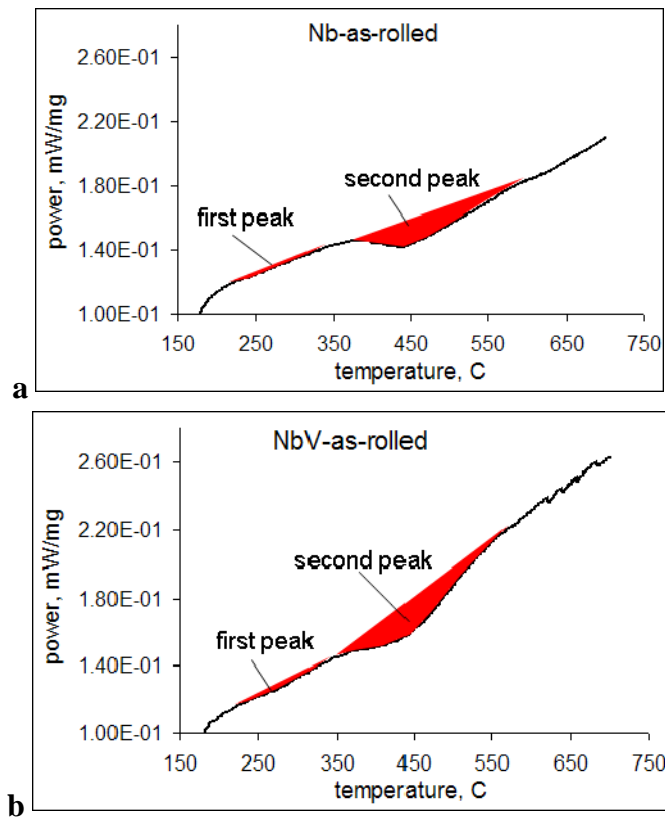


Figure 2.2 DSC heating curves of the (a) C-Nb and (b) C-Nb-V steel samples cut from the plate mid-thickness position; shaded areas represent energy release

3. MICROSTRUCTURE AND MECHANICAL PROPERTIES OF PLATE STEELS

3.1 Thermodynamic modelling of the microstructure with Thermo-Calc

As the main aim of the present project is a quantitative determination of the dependence of strength development on microstructure during cold deformation, the accuracy of microstructure measurement influences the reliability of the result. Thus, in addition to the experimental investigation, microstructures of the steels used in the project were assessed theoretically using Thermo-Calc software [149]. In order to predict the equilibrium microstructures the steel full chemical compositions, Table 2.1, were used as input for Thermo-Calc. Phase balances, cementite and carbo-nitride phase content, and microalloying element content in the carbo-nitride phase were obtained as a function of temperature. As the second phase (pearlite) is actually a mixture consisting of ferrite and cementite, Thermo-Calc software can not calculate the amount of pearlite directly. However, having the cementite percent in pearlite and cementite percent in a steel it is possible to calculate the pearlite percent.

Second phase (pearlite) content

The cementite mass and volume in one mole of steel was taken at 900 K (627 °C), as the ferrite-pearlite phase-balance can be considered stable below this temperature (Table 3.1). For all the three steels cementite percent in pearlite was considered being equal and calculated using the basic Fe-C diagram and lever rule:

$$\text{Fe}_3\text{C \% in pearlite} = \frac{C_{\text{pearlite}} - \max C_{\alpha}}{C_{\text{Fe}_3\text{C}} - \max C_{\alpha}} 100\% = \frac{0.8 - 0.02}{6.7 - 0.02} 100\% = 11.7\% .$$

Pearlite % was calculated as follows:

$$\text{pearlite \%} = \frac{m_{\text{Fe}_3\text{C}} \cdot 100\% \cdot 100\%}{\rho_{\text{Fe}_3\text{C}} \cdot V \cdot \text{Fe}_3\text{C \% in pearlite}}$$

where $m_{\text{Fe}_3\text{C}}$ - mass of cementite in one mole of steel calculated with Thermo-Calc, $\rho_{\text{Fe}_3\text{C}}$ - density of cementite, V – total volume of one mole of steel.

For one mole of the C-Mn steel at 900 K the following values were obtained:

$$m_{\text{Fe}_3\text{C}} = 0.948 \text{ g}, \quad \rho_{\text{Fe}_3\text{C}} = 7.66 \text{ g/cm}^3, \quad V = 7.057 \text{ cm}^3 \text{ and}$$

$$\text{pearlite \%} = \frac{0.948 \cdot 100 \cdot 100}{7.66 \cdot 7.057 \cdot 11.7} = 15.0\%.$$

For one mole of the C-Nb steel:

$$m_{\text{Fe}_3\text{C}} = 0.767 \text{ g}, \quad \rho_{\text{Fe}_3\text{C}} = 7.66 \text{ g/cm}^3, \quad V = 7.086 \text{ cm}^3 \text{ and}$$

$$\text{pearlite \%} = \frac{0.767 \cdot 100 \cdot 100}{7.66 \cdot 7.086 \cdot 11.7} = 12.1\%.$$

For one mole of the C-Nb-V steel:

$$m_{\text{Fe}_3\text{C}} = 0.414 \text{ g}, \quad \rho_{\text{Fe}_3\text{C}} = 7.66 \text{ g/cm}^3, \quad V = 7.083 \text{ cm}^3 \text{ and}$$

$$\text{pearlite \%} = \frac{0.414 \cdot 100 \cdot 100}{7.66 \cdot 7.083 \cdot 11.7} = 6.5\%.$$

As seen, with a decrease in carbon content in steel composition the pearlite content decreases (Table 3.1).

Table 3.1 Equilibrium transformation temperatures and matrix phase balance for steels studied

Steel	$\gamma \rightarrow (\alpha + \gamma)$ temperature, A_3		$(\alpha + \gamma) \rightarrow \alpha$ temperature, A_1		Pearlite content, (%)
	K	°C	K	°C	
C-Mn	1147	874	987	714	15.0
C-Nb	1113	840	960	687	12.1
C-Nb-V	1123	850	947	674	6.5

Carbo-nitride phase content

To calculate the precipitate volume fraction, the mole fraction of the carbo-nitride phase was plotted as a function of temperature for all three steels (Figures 3.1,a - 3.3,a). The carbo-nitride phase volume fraction increases with a decrease in temperature, due to the solubility of the alloying elements decreasing. The chemical composition of this phase changes with temperature and steel grade, as different microalloying elements precipitate at different temperatures. To assess the chemical composition of the carbo-nitride phase Ti, Nb and V contents were plotted versus temperature (Figures 3.1, b, c; 3.2, b; 3.3, b).

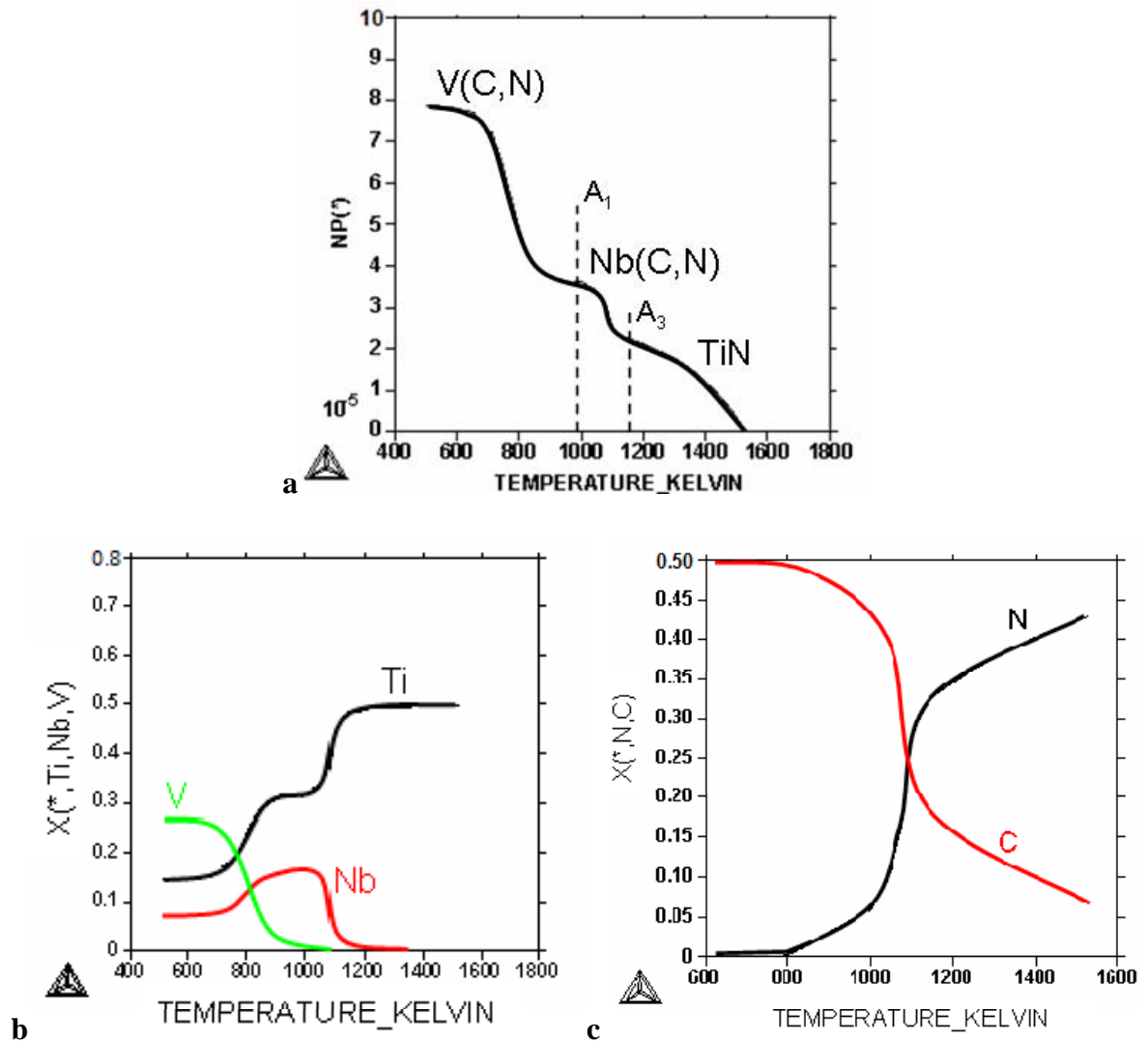


Figure 3.1 (a) Dependence of the carbo-nitride phase mole fraction in the C-Mn steel on temperature; (b) Ti, Nb, V and (c) N and C content in the carbo-nitride phase

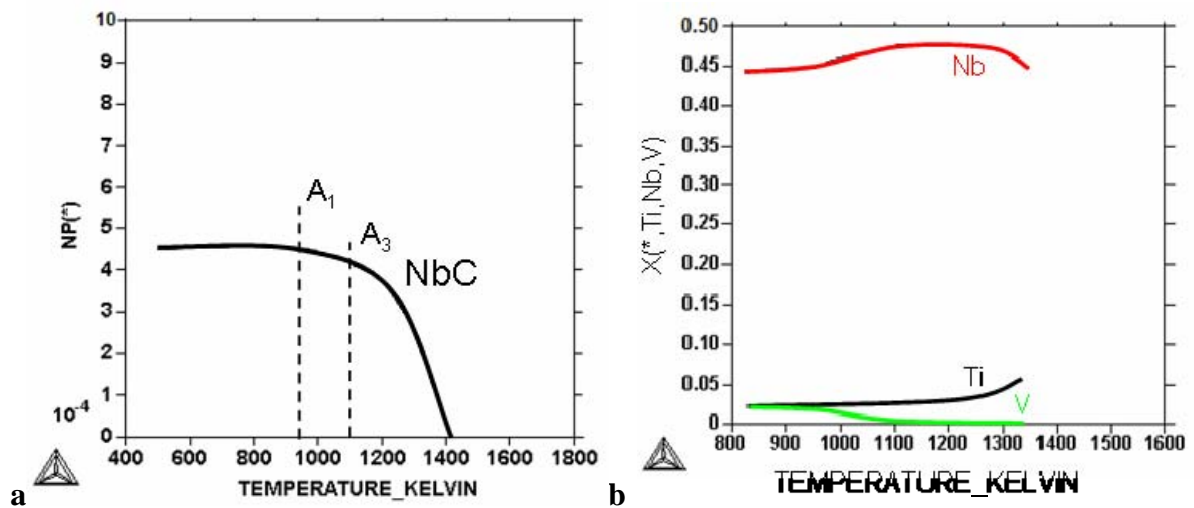


Figure 3.2 (a) Dependence of the carbo-nitride phase mole fraction in the C-Nb steel on temperature and (b) Ti, Nb and V content in the carbo-nitride phase

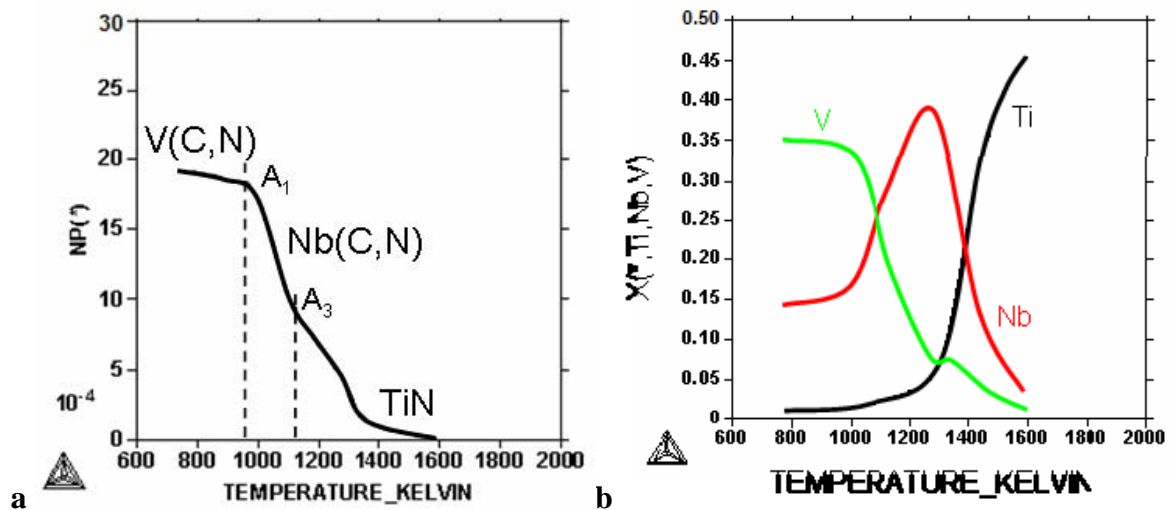


Figure 3.3 (a) Dependence of the carbo-nitride phase mole fraction in the C-Nb-V steel on temperature and (b) Ti, Nb and V content in the carbo-nitride phase

In the C-Mn steel, from the start of solidification down to 1200 K (927 °C), the carbo-nitride phase consists mainly of TiN (Figure 3.1). From 1200 to 1000 K (727 °C) Nb(C,N) precipitates and below 1000 K V(C,N) adds to the volume fraction. With a decrease in temperature the carbon content in the carbo-nitride phase increases and the nitrogen content decreases, as nitrides precipitate at higher temperatures due to their greater thermodynamic stability compared to carbides [115]. In the C-Nb steel the carbo-nitride phase consists mainly of NbC, Figure 3.2, since the Ti, V and N contents in this steel are low (Table 2.1). In the

C-Nb-V steel the carbo-nitride phase from the start of solidification down to 1300 K (1026 °C) consists of TiN, NbN and NbC (Figure 3.3). Below this temperature VC starts precipitating and adds to the volume fraction. Higher precipitation start temperatures of NbC in the C-Nb steel and VC in the C-Nb-V steel, compared to the C-Mn steel, can be explained by the higher microalloying element content.

In the C-Mn steel the total volume fraction of (Ti,Nb,V)(C,N) phase was calculated as being $f = 6.5 \cdot 10^{-5}$ at a temperature 500 K (227 °C). In the C-Nb steel the volume fraction of NbC was calculated to be $f = 0.000365$ (Table 3.2).

In the C-Nb-V steel the volume fraction of the Nb-Ti-rich precipitates was calculated separately from that of the V-rich ones. It was assumed that Nb-Ti-rich particles fully precipitate above 1275 K (1002 °C) because the equilibrium carbo-nitride phase mole fraction curve slope changes at this temperature (Figure 3.3, a). The volume fraction of Nb-Ti-rich precipitates was calculated to be $f_{(Ti,Nb)(C,N)} = 0.000345$ and the volume fraction of V-rich particles to be $f_{V(C,N)} = 0.0011$. However, the mole fraction slope change at 1275 K indicates that the V-rich particle precipitation starts and not that the Nb-Ti-rich particle precipitation finishes. So, the calculation may underestimate the Nb-Ti-rich particle volume fraction and overestimate the V-rich particle volume fraction. As seen from Table 3.2, a larger content of microalloying elements in the steel leads to a larger volume fraction of the carbo-nitride phase in the solid state.

Table 3.2 Predicted equilibrium precipitation finish temperatures (T_{ppt}) and volume fraction (f) of carbo-nitrides at 500 K for the C-Mn and C-Nb steels, and at 800 K for the C-Nb-V steel

Steel	Ti-rich		Nb-rich		V-rich	
	T_{ppt} (°C)	f	T_{ppt} (°C)	f	T_{ppt} (°C)	f
C-Mn	852	0.000019	714	0.000012	327	0.000034
C-Nb	-	-	680	0.000365	-	-
C-Nb-V	1127	0.000040	851	0.000305	527	0.0011

3.2 Ferrite grain size distributions

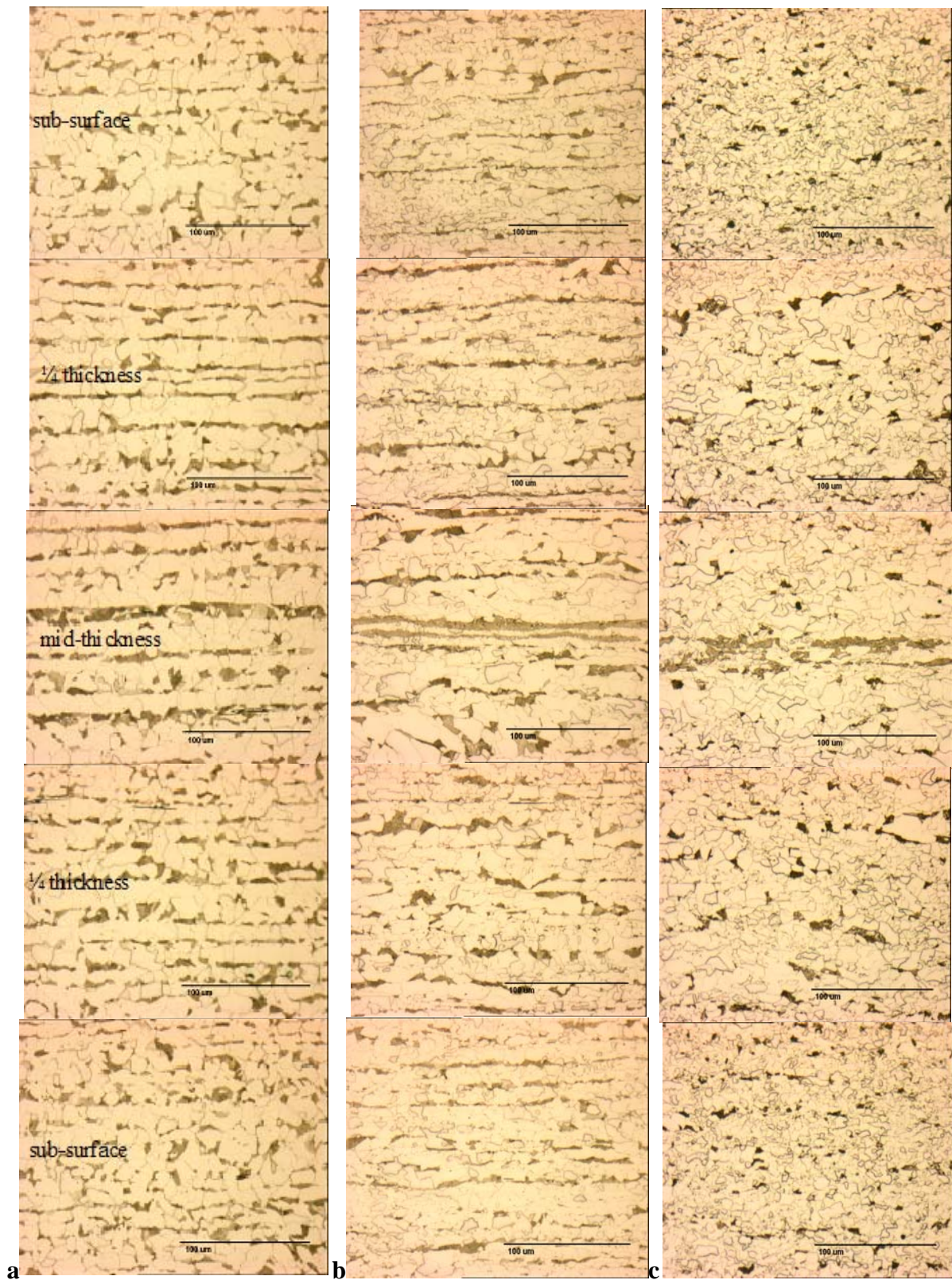


Figure 3.4 Optical micrographs of the (a) C-Mn, (b) C-Nb and (c) C-Nb-V steels across thickness in the plane parallel to the rolling direction

The microstructure of the three as-rolled steel plates consists of two phases: ferrite and pearlite (Figure 3.4). The amount of pearlite increases towards the mid-thickness of the plates due to segregation of carbon (and other elements) during solidification. A decrease in pearlite content from the C-Mn to the C-Nb and to the C-Nb-V steel corresponds to the carbon content decrease in the steel composition. In the plane parallel to the rolling direction the ferrite and pearlite grains are banded along the rolling direction. It is more distinctly visible in the centreline of the C-Mn and C-Nb steel plates, where complete second phase bands can be observed (Figure 3.4, a, b).

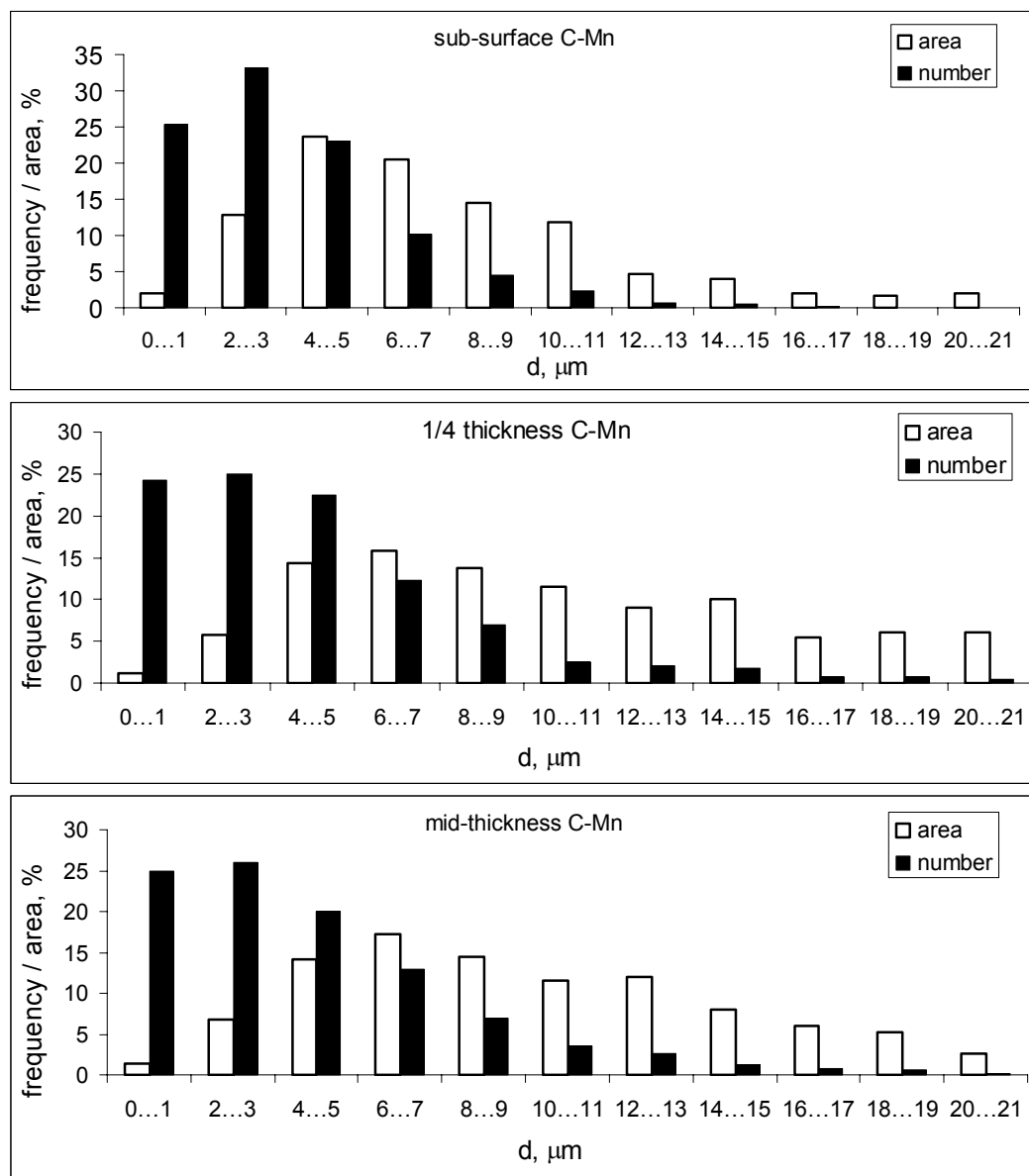


Figure 3.5 Grain diameter frequency and grain area distributions across plate thickness in the C-Mn steel

As the ferrite grain aspect ratio was in the range of 0.8 - 0.85, the grain size was assessed as an equivalent grain diameter (Figures 3.5 - 3.7). The grain area, automatically measured with the computer software using digital images of the microstructure, was accepted being equal to the area of the circular grain. Thus the grain diameter, d , was calculated as follows:

$$d = \sqrt{\frac{4A}{\pi}},$$

where A is the measured grain area.

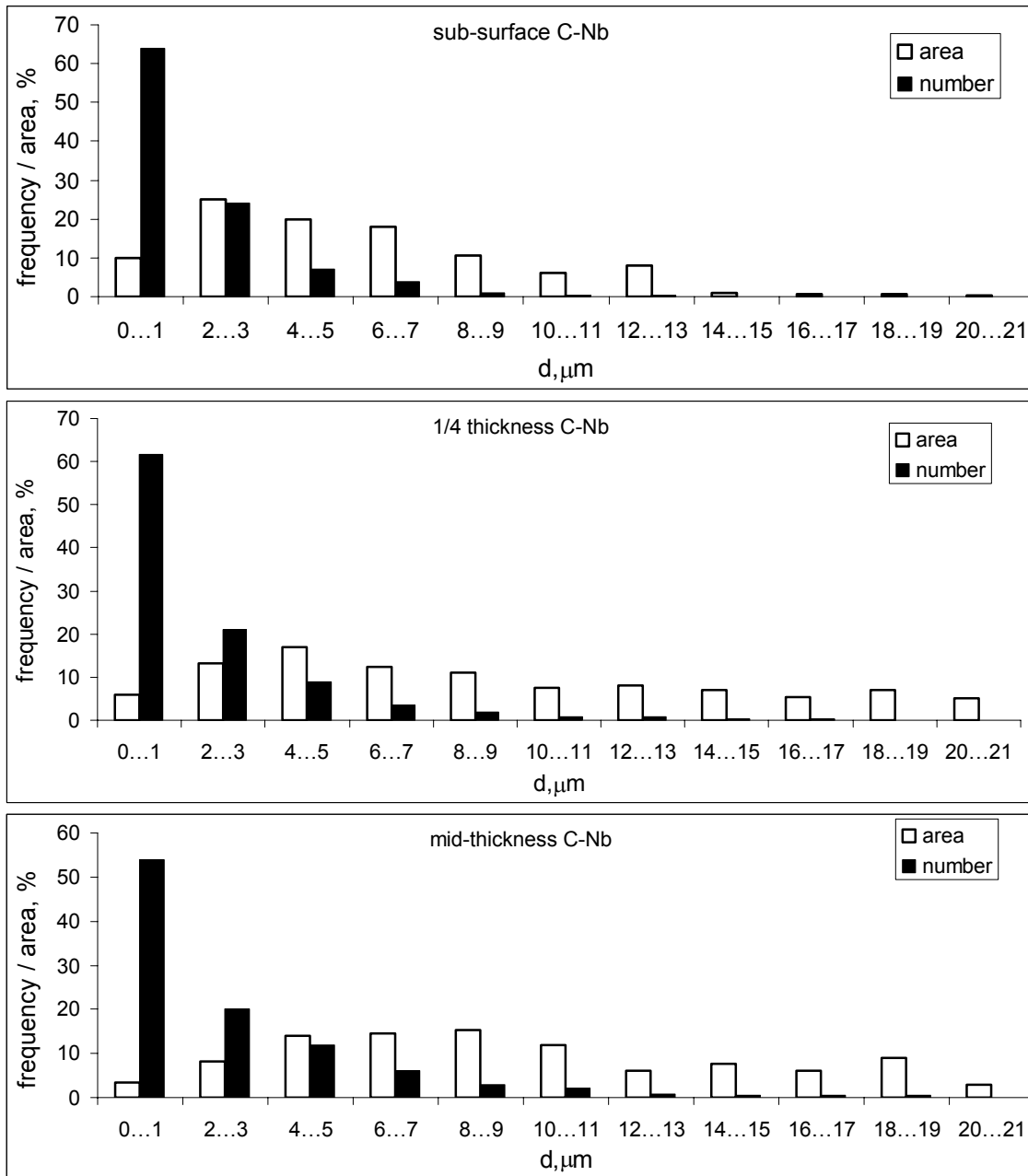


Figure 3.6 Grain diameter frequency and grain area distributions across plate thickness in the C-Nb steel

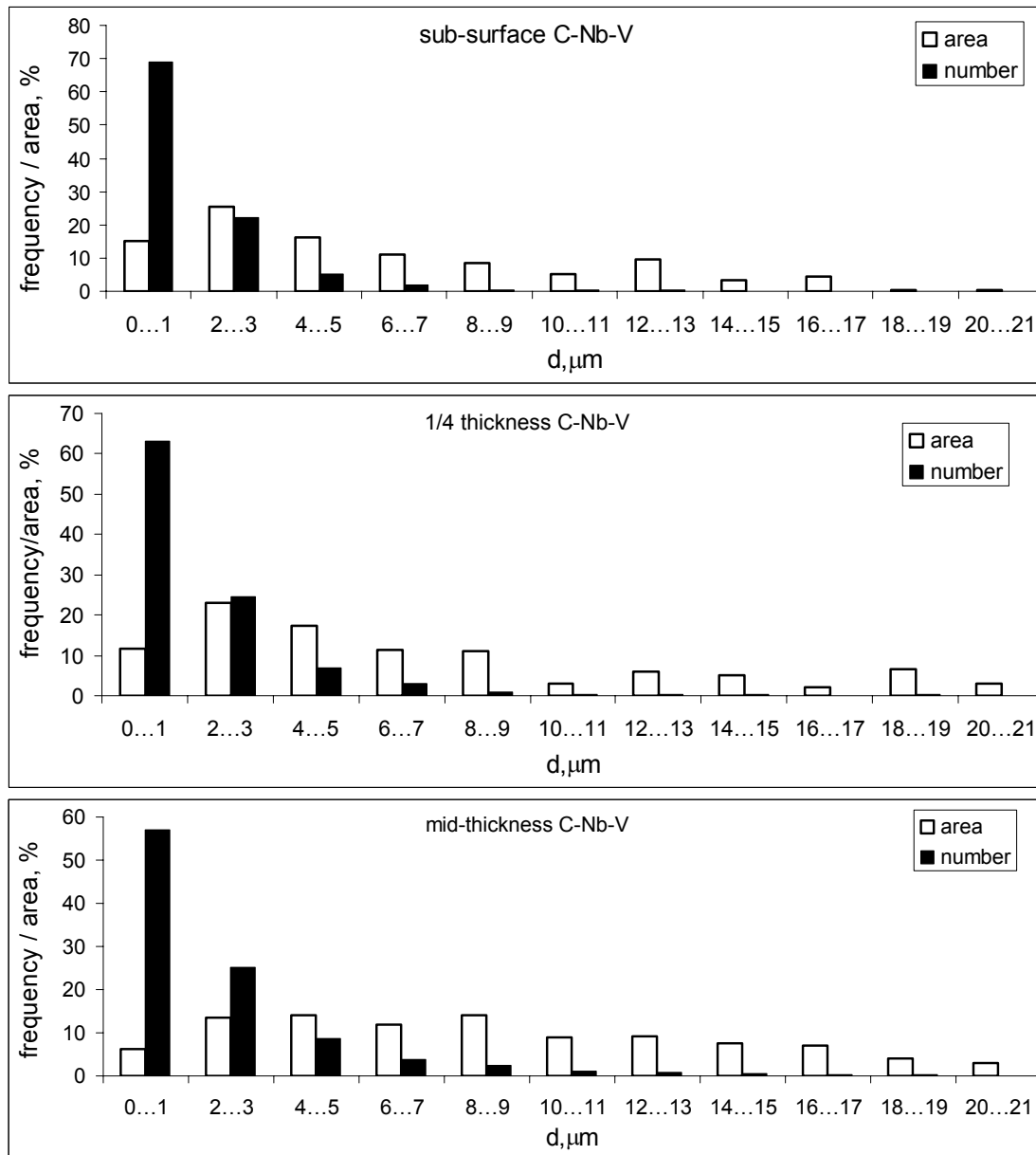


Figure 3.7 Grain diameter frequency and grain area distributions across plate thickness in the C-Nb-V steel

The average through thickness grain diameter was calculated using grain number frequency distributions as 4.8 μm in the C-Mn steel, 2.6 μm in the C-Nb steel and 2.3 μm in the C-Nb-V steel (Figures 3.5-3.8). The grain size decreases from the C-Mn to the alloyed steels, due to the Zener drag effect and precipitation increase with an increase in microalloying element content. As alloying element content increases, as from the C-Mn to the C-Nb and C-Nb-V steels, a corresponding increase in the number density of the carbonitride precipitates occurs. The particles, pinning the grain boundaries during hot rolling,

prevent recrystallisation and grain growth. Thus the grain size is refined. Some contribution to the grain size refinement may come from a difference in finish rolling temperature. According to the data provided by Corus, the finish rolling temperature decreased from 770 °C for the C-Mn to 745 °C for the C-Nb and to 735 °C for the C-Nb-V steel. With a decrease in finish rolling temperature and increase in the recrystallisation stop temperature (due to microalloying) there is a large amount of deformation stored in the austenite grains leading to increased ferrite nucleation sites and hence smaller ferrite grain size.

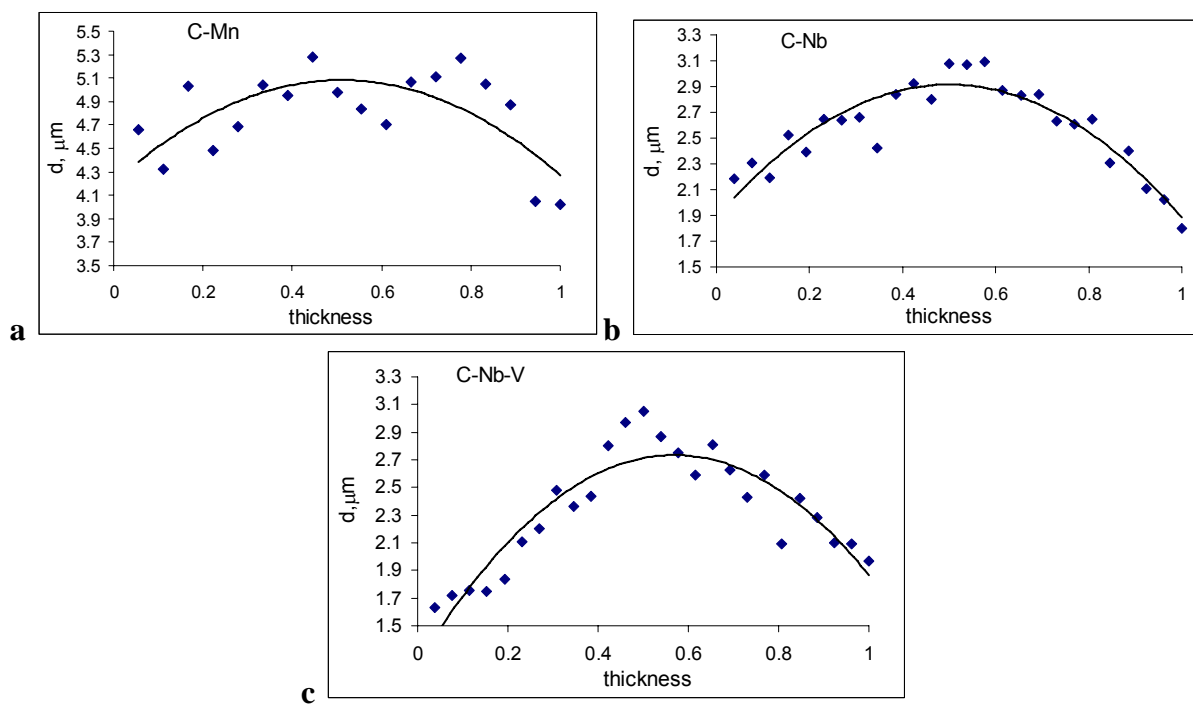


Figure 3.8 Grain diameter distributions across plate thickness (as a fraction of total thickness) for the (a) C-Mn, (b) C-Nb and (c) C-Nb-V steels

The ferrite grain size distribution across plate thickness, Figure 3.8, shows a maximum at the mid-thickness of the plates. This can be explained by several factors influencing the grain size distribution: initial distribution in the slab after solidification; temperature and strain gradient across thickness during rolling; and segregation of microalloying elements leading to the inhomogeneous precipitation of carbonitrides.

Previous investigations of grain size distribution in as-cast slabs of niobium and niobium-vanadium alloyed steels showed an increase in the ferrite grain size from the slab sub-surface

to the mid-thickness [150]. This was explained by the difference in cooling rates: the slab sub-surface areas experience faster cooling during solidification than the mid-thickness areas.

During rolling the plate sub-surface regions experience a lower temperature deformation, compared to the mid-thickness, due to plate surface contact with the rolls and roll cooling liquids. This may retard recrystallisation and lead to the grain size decreasing in the sub-surface areas of the plates.

Strain distribution during plate rolling may have a minimum or a maximum at the plate mid-thickness; depending on the deformation zone geometry (roll diameter to plate thickness ratio), deformation in each stand (per pass for reversing mills), conditions of friction on the contact roll-plate. For the studied steels the technological information is scarce and direct assessment of strain distribution using the rolling parameters is impossible. However, the dislocation density measurements, described in section 3.8, show an increase in dislocation density towards the plate mid-thickness. This supports the strain increasing towards the plate mid-thickness and, thus, a tendency for the grain size decreasing towards the plate mid-thickness.

In the alloyed steels the precipitation of Nb- and Nb-Ti-rich carbonitrides greatly contributes to the grain size refinement: with an increase in particle number density the grain size decreases. The Nb-Ti-rich particle precipitation study, described in section 3.6, shows an increase in the particle number density from the mid-thickness ferrite to the sub-surface ferrite. This corresponds to the ferrite grain size decreasing towards the plate sub-surface.

As can be seen, the grain size distribution in as-cast slabs, temperature gradient during rolling and particle distribution in the C-Nb and C-Nb-V steels result in the grain size decreasing towards the plate sub-surface.

3.3 Second phase content

The amount of the second phase (assumed to be pearlite percent) in the C-Mn steel was measured as being in the range 13 – 17 %, in the C-Nb steel 6 - 13 % and in the C-Nb-V steel 2 - 7% (Figure 3.9). The pearlite content decreases from the C-Mn to the C-Nb and to the C-Nb-V steel corresponding to the steel chemistries, i.e. a decrease in carbon content leads to the pearlite percent decrease. The pearlite distributions across the plate thickness show a maximum at the mid-thickness of the plates, which can be explained by carbon macrosegregation.

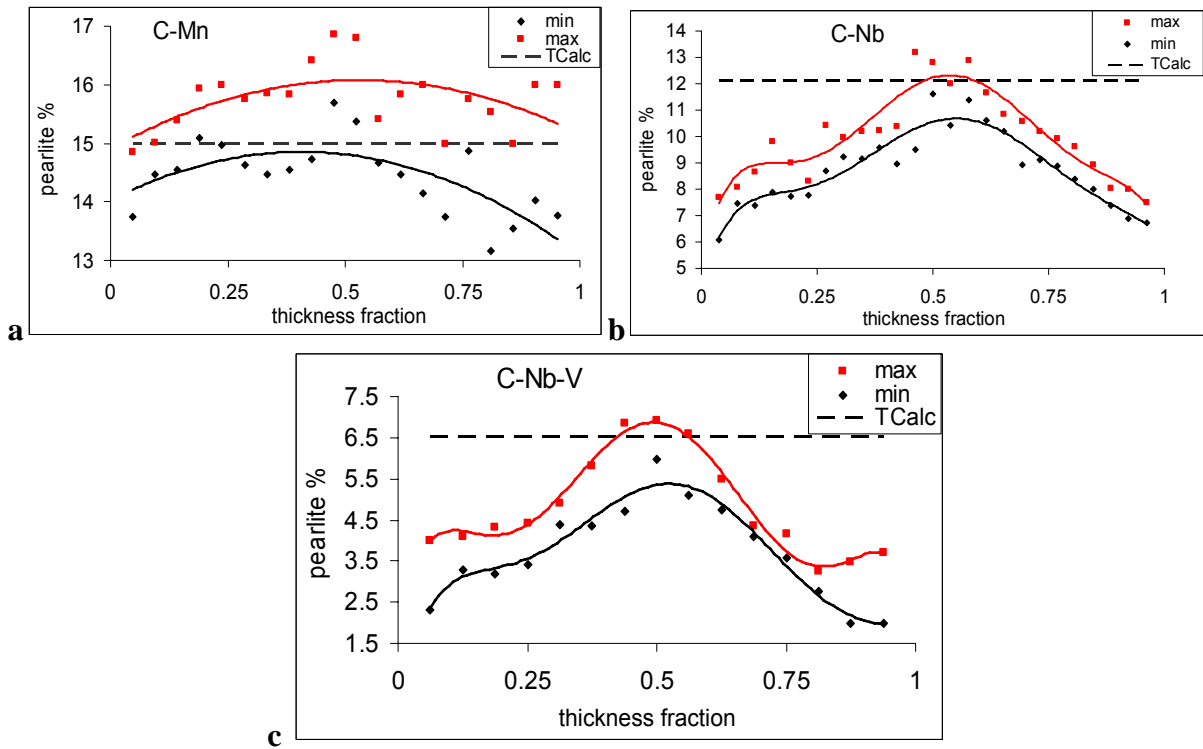


Figure 3.9 Pearlite content distributions (maximum and minimum values) across plate thickness for the as-rolled (a) C-Mn, (b) C-Nb and (c) C-Nb-V steels

The average measured data for pearlite percent corresponds reasonably well to the Thermo-Calc calculated value in the C-Mn steel (Table 3.3). In the alloyed steels the Thermo-Calc calculations show higher than measured average values of pearlite percent. A decreased measured value could be explained, if due to the faster cooling conditions not all the

cementite contributed to pearlite formation, as in steels with spheroidised Fe_3C morphology [46], or some carbon was left dissolved in the ferrite matrix, as in strain-aged steels [4]. After annealing at 550°C for 30 min the pearlite content in the C-Nb steel increased to 10.9 % average value, from 9.7 % in the as-rolled steel, and in the C-Nb-V steel increased to 5.6 %, from 4.7 % in the as-rolled steel, which is closer to the predicted value for the equilibrium cooling conditions (Figure 3.10).

Table 3.3 Measured and calculated data for pearlite content, %

Steel grade	Measured							Thermo- Calc
	centre			sub-surface			Total average	
	min	max	av	min	max	av		
C-Mn	15.7	16.9	16.3	13.5	15.4	14.5	15.4	15.0
C-Nb	11.6	13.2	12.4	6.4	7.6	7.0	9.7	12.1
C-Nb-V	6.0	6.8	6.4	2.2	3.8	3.0	4.7	6.5

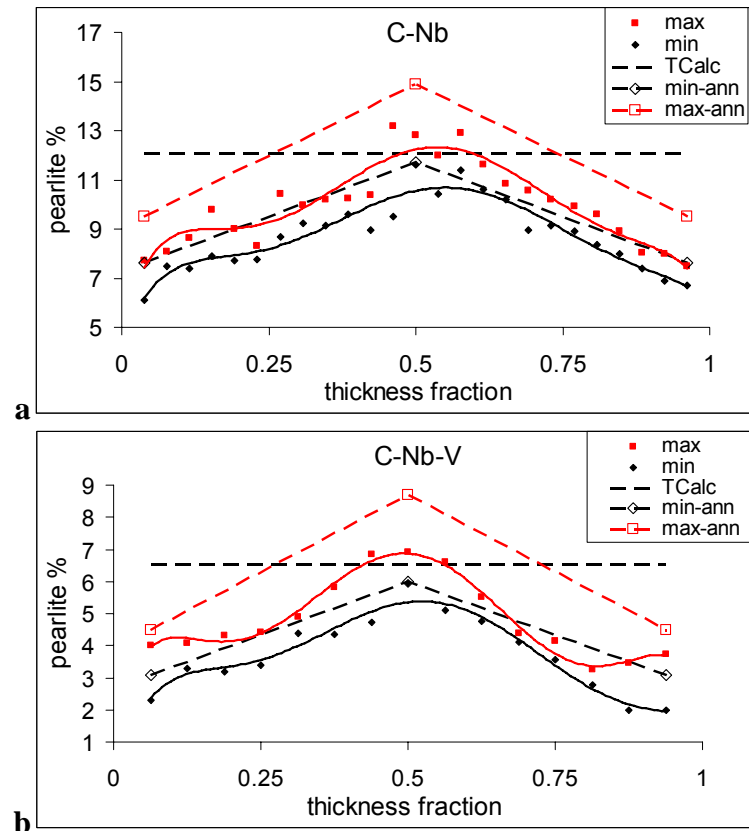


Figure 3.10 Pearlite content distributions across plate thickness for the annealed (a) C-Nb and (b) C-Nb-V steels (plotted with the as-rolled for comparison)

3.4 Mn-, Al- and Si-rich phases (optical and SEM analysis)

Optical and SEM analysis of the microstructures revealed the presence of Mn-, Al- and Si-rich inclusions (Figure 3.11, a-c).

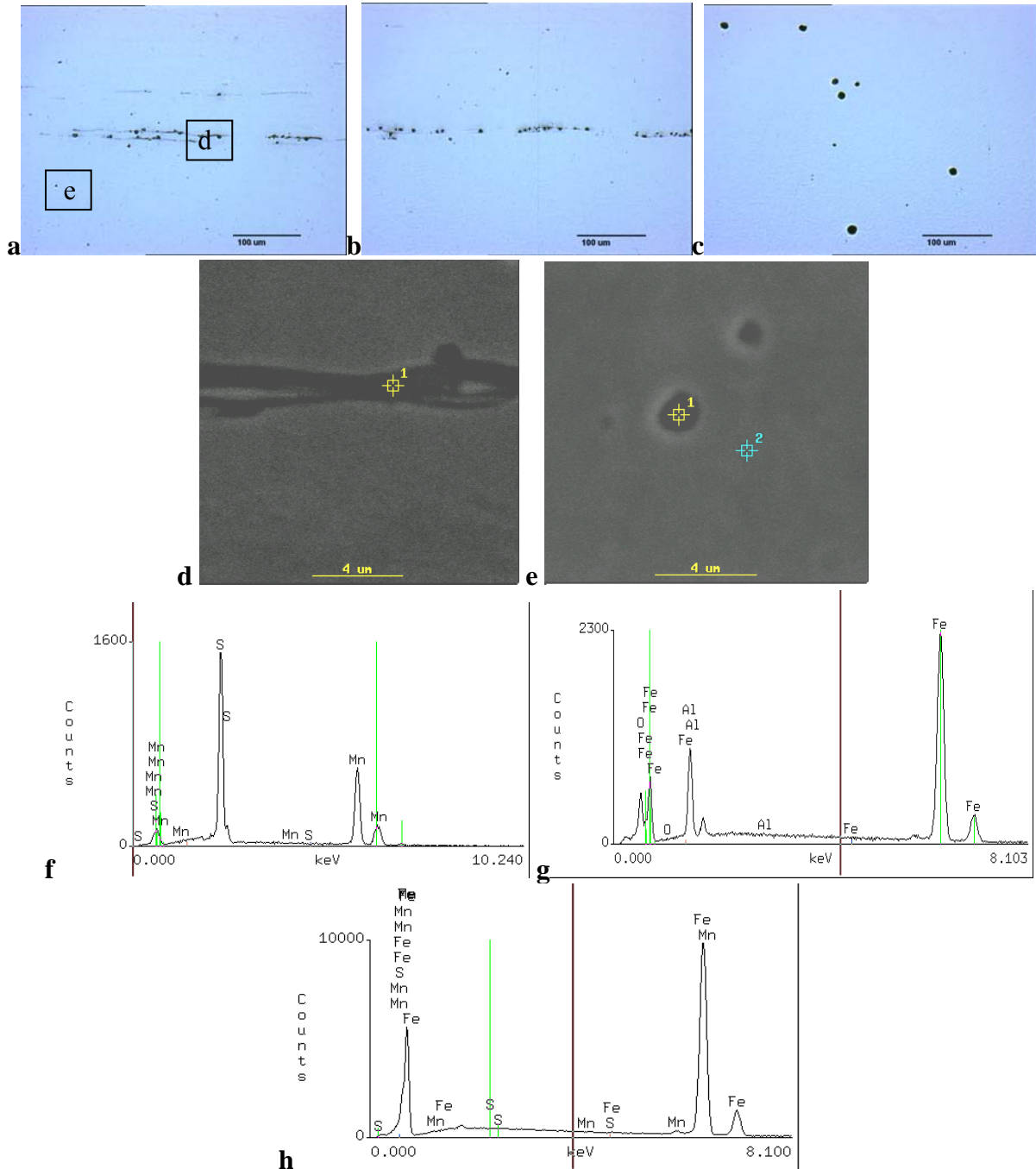


Figure 3.11 Typical optical micrographs of non-etched plate centreline area in the (a) C-Mn (showing locations of images (d) and (e)), (b) C-Nb and (c) C-Nb-V steels; SEM images of (d) MnS and (e) Al₂O₃ particles; EDX spectrum (f) from point 1 on (d) – MnS particle, (g) from point 1 on (e) – Al₂O₃ particle, and (h) from point 2 on (e) – the ferrite matrix

MnS particles were present in greater amounts in the C-Mn steel compared to the C-Nb steel, due to the higher sulphur content in the C-Mn steel. In the C-Nb-V steel MnS particles were not observed, which can be related to the very low sulphur content in this steel. MnS particles in the mid-thickness area of the C-Mn and C-Nb plate steels were observed in the form of thin bands elongated in the rolling direction (Figure 3.11, d, f). MnS particles in the C-Mn steel greater than 200 μm in length were observed, though in the C-Nb steel they were no longer than 100 μm .

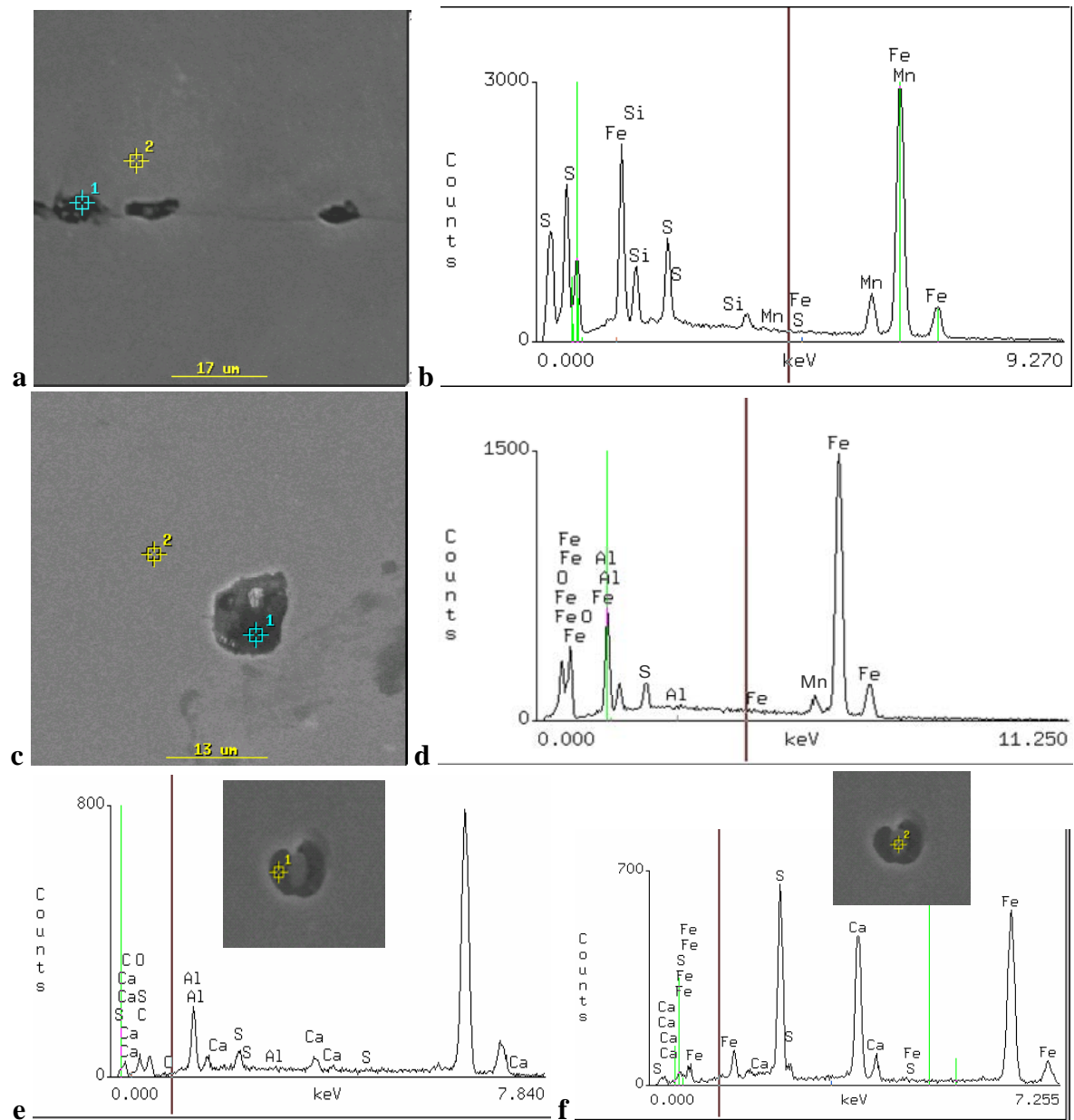


Figure 3.12 Typical (a) SEM image and (b) EDX spectra of a complex $\text{SiO}_2 + \text{MnS}$ particle; typical (c) SEM image and (d) EDX spectra of a complex $\text{Al}_2\text{O}_3 + \text{MnS}$ particle; (e) a Al-rich particle with (f) a CaS particle attached to it

Spherical Al_2O_3 particles were found randomly distributed through the volume in all the three steels (Figure 3.11, e, g). The Al_2O_3 diameter was measured to be in the range 1 - 6 μm .

Some complex (Mn,Si,Al)-rich particles were also observed. Thus at the C-Nb steel mid-thickness position 9 μm SiO_2+MnS particles were found aligned with their longer axis parallel to the rolling direction, Figure 3.12, a, b, and in the C-Nb-V steel $\text{Al}_2\text{O}_3+\text{MnS}$ particles of up to 14 μm diameter were present, Figure 3.12, c, d. In the C-Nb-V steel, instead of MnS particles, CaS particles of about 2 μm diameter were observed (Figure 3.12, e, f).

3.5 Alloying element content distribution

To assess the solid solution strengthening level in the steels the Mn and Si contents were studied across the plate thickness for the C-Nb and C-Nb-V steels. Average values obtained by SEM-EDS, Figure 3.13, show a good agreement between measured Mn and Si contents and the steel compositions provided by Corus (Table 2.1). Quantitative area EDS shows a slight increase in the silicon content from the plate sub-surface to the mid-thickness position, by 0.02 wt % in the C-Nb and 0.08 wt % in the C-Nb-V steel, which can be disregarded as being within the experimental scatter of 0.15 - 0.25 wt %. No significant difference in the manganese content across plate thickness was identified in either steel.

Investigation of the microalloying element distributions across plate thickness in the C-Nb-V steel showed the average EDS measured value to be higher than provided data, 0.008 wt% for the Nb content and 0.017 wt% for the V content, Figure 3.14, which is a good agreement as the experimental scatter is 0.04 wt%. No change in vanadium content across plate thickness was observed. The Nb content was found to be 0.008 wt% higher in pearlite than in ferrite, which is within the experimental scatter, and about 0.05 wt% higher at the mid-thickness than at the sub-surface. This is due to segregation of Nb during solidification between dendrite centres

and interdendritic areas, which was previously reported for steels with similar chemistries [151]. Qualitatively the Nb content increase towards the plate mid-thickness corresponds to the measured values of Nb-rich particle volume fraction, described below in section 3.6.

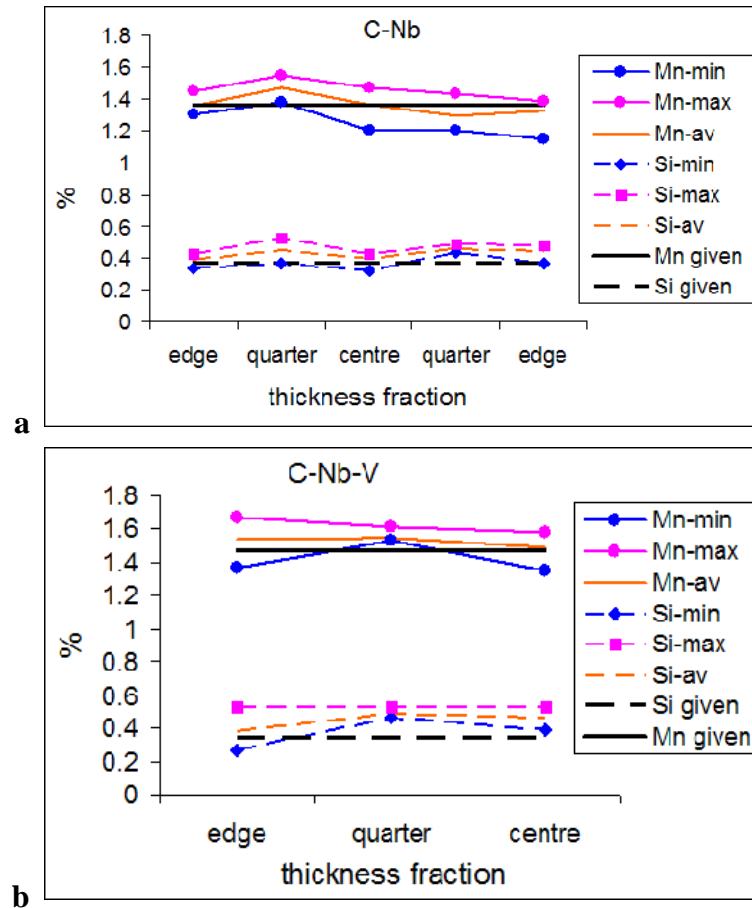


Figure 3.13 Mn and Si content distributions across plate thickness in the (a) C-Nb and (b) C-Nb-V steels

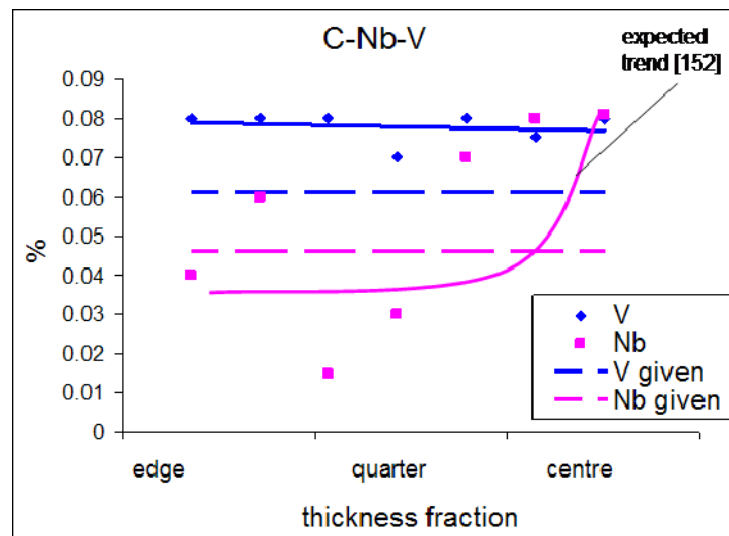


Figure 3.14 Nb and V content distributions across plate thickness in the C-Nb-V steel

3.6 Ti-Nb-rich phases (SEM analysis)

Precipitation at high temperatures (above A_3) results in particles of microalloying elements that pin the austenite grain boundaries retarding recrystallisation, leading to a decrease in ferrite grain size. Precipitation at lower temperature (between A_3 and A_1 or below A_1) results in particles that block the dislocation motion during deformation. Thus in alloyed steels carbonitride particles play a significant role in mechanical property behaviour, either by grain refinement or precipitation strengthening mechanisms. Quantitative influence of particles on strength depends on their chemistry, size, number density and distribution in the matrix. In the microalloyed steels studied the carbonitride particles were imaged and analysed using SEM and TEM combined with EDS. Results from these analyses are presented below. This data will be used for prediction of the mechanical properties of steels, presented in section 3.10.

Particle morphology, distribution and chemistry

High resolution SEM of polished and slightly etched samples, cut from the C-Nb and C-Nb-V steel plates, revealed precipitates of 20-220 nm in size (Figures 3.15, 3.16). Mainly the particles were of a rounded or ellipsoid shape (in the micrograph plane), although near-cuboidal particles of up to 330 nm in size were also observed occasionally. The distribution of the particles is not uniform: pearlite regions exhibit larger particle sizes and number densities compared to ferrite regions. In both steels larger particles and a higher number density were observed in the plate mid-thickness pearlite regions compared to the sub-surface pearlite regions. However, ferrite regions showed the opposite distribution across plate thickness, with particle number density in the mid-thickness ferrite being lower than in the sub-surface ferrite. Larger precipitates were observed along the ferrite/ferrite grain boundaries and smaller ones in the centre of the ferrite grains.

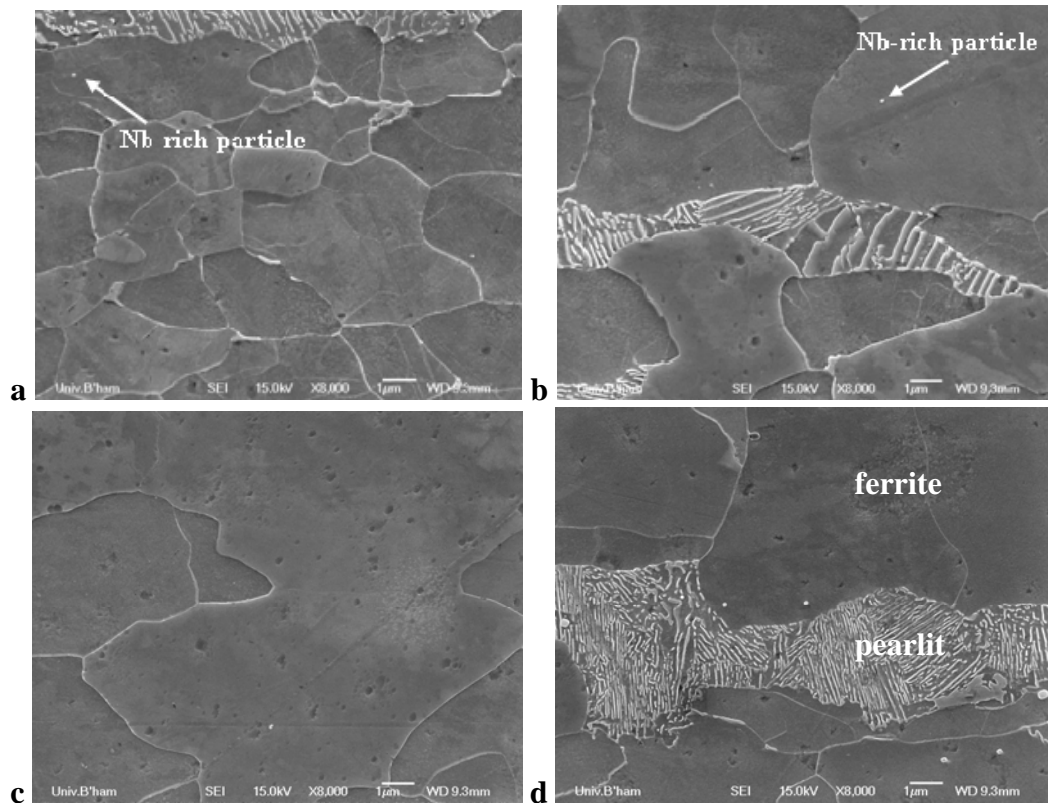


Figure 3.15 Typical SEM images from the C-Nb steel: a – sub-surface ferrite region, b - sub-surface pearlite region, c – centre ferrite region, d - centre pearlite region

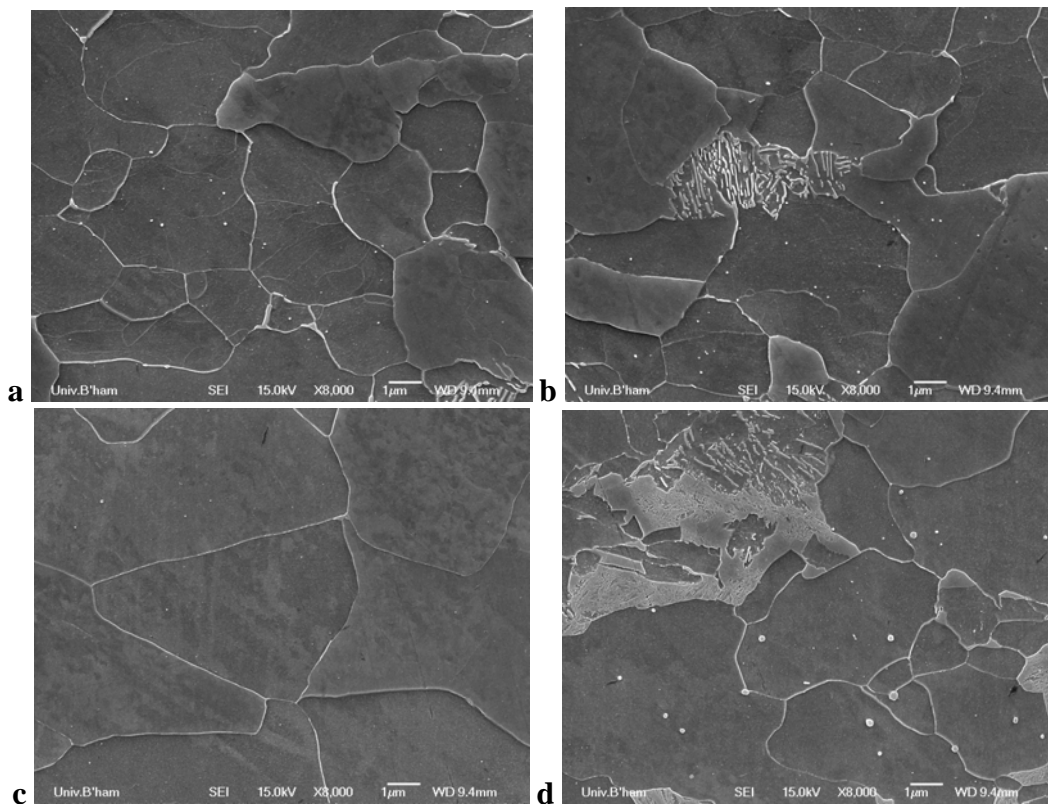


Figure 3.16 Typical SEM images from the C-Nb-V steel: a – sub-surface ferrite region, b - sub-surface pearlite region, c – centre ferrite region, d - centre pearlite region
(The pearlite regions are taken to include the adjacent ferrite grains and are not just the pearlite colonies)

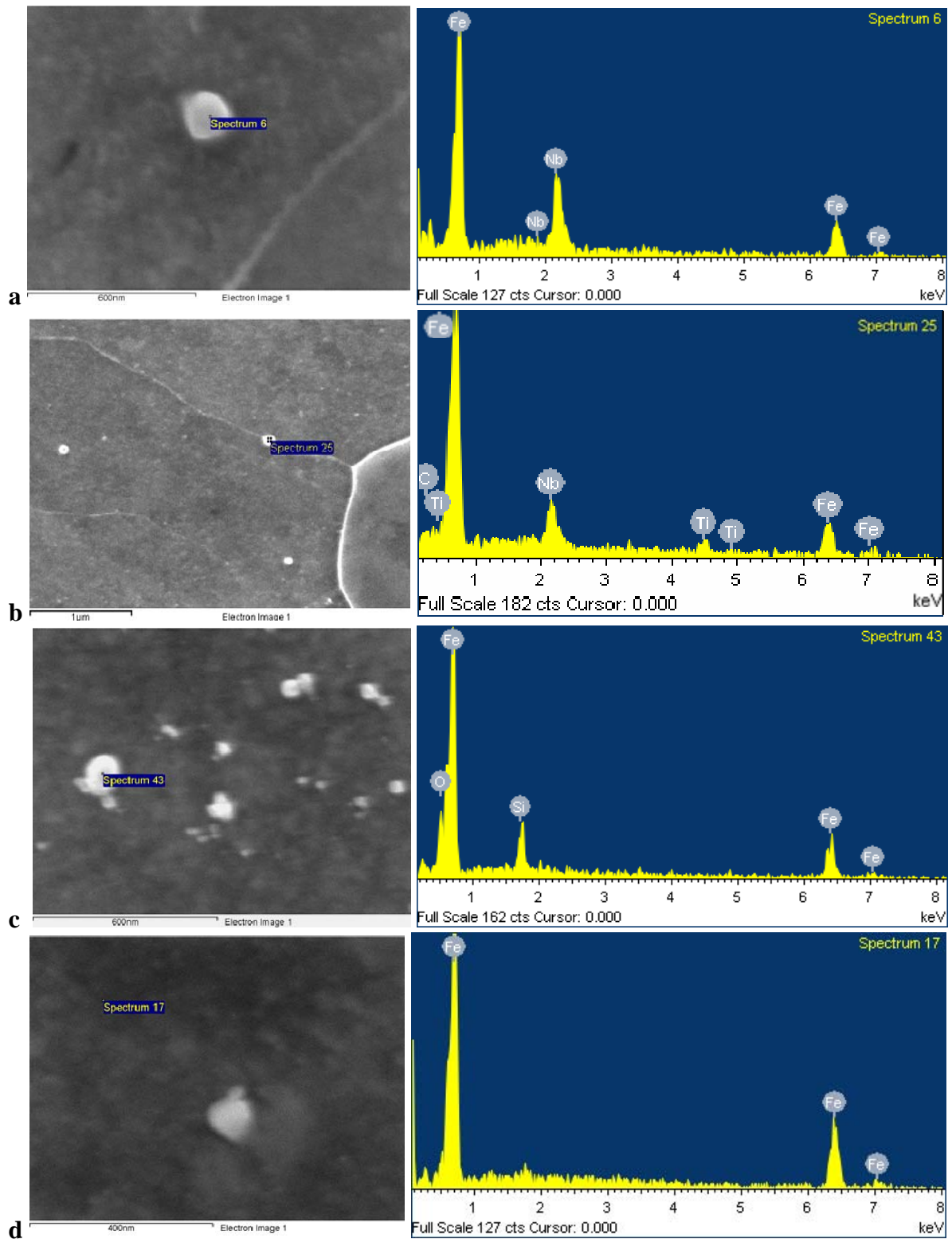


Figure 3.17 Typical SEM images and EDS spectra of the particles present in the C-Nb and C-Nb-V steels: a - Nb-rich, b – Nb-Ti-rich, c – SiO₂; d – typical spectrum of the ferrite matrix

To determine particle chemistry, and assess any size-composition relationships, 48 particles in the C-Nb steel and 58 particles in the C-Nb-V steel were analysed by SEM-EDS (Figure 3.17, Tables 3.4, 3.5). Several different types of particles were identified: Nb-rich (carbonitrides), Nb-Ti-rich (carbonitrides), Si- and Al-rich oxides. V-containing particles were not observed in the C-Nb steel as the vanadium content in this steel is very low (0.001 wt %). The low number of V-rich particles observed in the C-Nb-V steel can be explained by their expected small size, below 30 nm, which is difficult to detect with SEM imaging. The analysed particles were separated into three size groups: less than 50 nm, 50 – 100 nm, more than 100 nm. The majority of the Nb-Ti-rich particles, namely 97% in the C-Nb and 90% in the C-Nb-V steel, fall into the > 50 nm diameter range. There were few particles less than 50 nm in diameter (3/48 in the C-Nb steel and 10/58 in the C-Nb-V steel) and the majority of these are Si-rich. Therefore, when calculating the volume fraction and number density of the Nb-Ti-rich particles only > 50 nm particles were considered. Smaller than 50 nm particles were quantified with TEM (see section 3.7)

Table 3.4 Size and chemistry of the particles analysed by SEM-EDS in the C-Nb steel

particle size, nm	elements present (except Fe)	number	total number	microalloy presence, %
< 50	Nb	1	3	30
	Si	2		
50 – 100	Nb	9	14	78
	Nb, Al, O	1		
	Si,	2		
	Si, O	1		
> 100	Ti	1	31	94
	Nb	28		
	Nb, Si	1		
	Si, O	1		
	Si, Al, O	1		

Table 3.5 Size and chemistry of the particles analysed by SEM-EDS in the C-Nb-V steel

particles size, nm	elements present (except Fe)	number	total number	microalloy presence, %
< 50	V	1	10	50
	Nb	4		
	Si	5		
50 – 100	Nb	23	33	91
	Nb, Ti	4		
	Nb, Si	2		
	Si	3		
	Ti	1		
> 100	Nb	10	15	100
	Nb, Ti	5		

Particle size, volume fraction and number density

Measurements of the Nb-Ti-rich particle characteristics were made separately for the ferrite and pearlite (including adjacent ferrite) regions at the sub-surface and mid-thickness positions, as it is known that microsegregation occurs in Nb-microalloyed plate steels [95], and clear differences in number densities were observed during SEM analysis (Figures 3.15, 3.16). In the C-Nb steel ferrite and pearlite bands were easily distinguished (Figure 3.18,a). In the sub-surface area of the C-Nb-V steel whilst the pearlite percent is less than 2.5 %, it is possible to identify regions without pearlite and regions containing a higher pearlite fraction as shown in Figure 3.18,b. As a ferrite band is approximately two times broader than a pearlite band, the average plate sub-surface and mid-thickness values of the precipitate characteristics were calculated as follows:

$$\text{Average} = (1 \times \text{In-pearlite} + 2 \times \text{In-ferrite}) / 3.$$

For the large number of particles measured in this work, 630 particles in the C-Nb steel and 1064 particles in the C-Nb-V steel, area fraction can be considered equal to the volume fraction and compared to the Thermo-Calc theoretical prediction for the carbonitride phase.

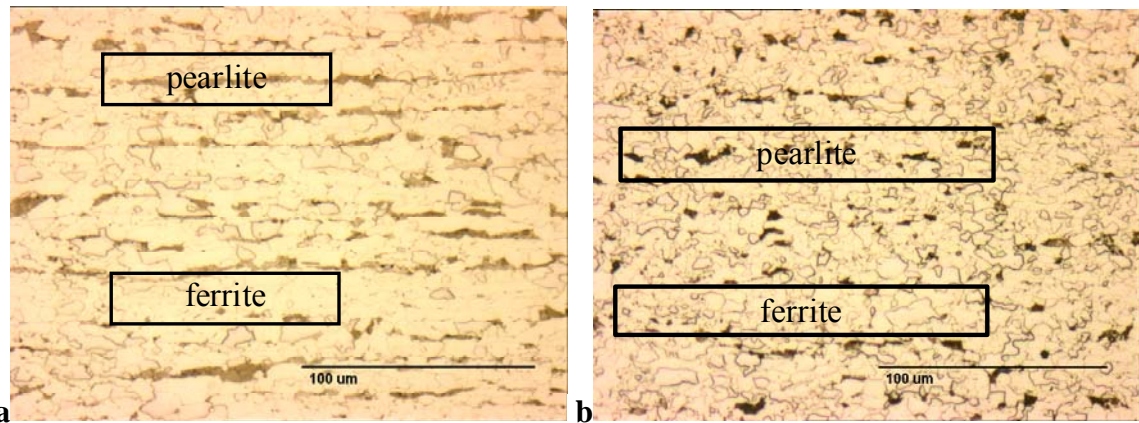


Figure 3.18 Sub-surface area micrographs for the (a) C-Nb and (b) C-Nb-V steels showing the ferrite and pearlite regions

Qualitative analysis of the particle diameter distributions, Figure 3.19 and 3.20, shows that for both steels there is an increase in diameter in the pearlite regions compared to the ferrite regions, which is due to the C and Nb microsegregation. The mid-thickness pearlite regions exhibit a larger particle diameter and a broader minimum to maximum diameter range, compared to the sub-surface pearlite areas. This is due to macrosegregation of C and Nb during solidification, and the slower cooling rates at the mid-thickness resulting in particle growth (along with earlier nucleation giving greater time for growth).

Quantitative analysis, Table 3.6, shows that for both steels the particle volume fraction and number density is higher in the pearlite regions compared to the ferrite regions. In the C-Nb steel the particle volume fraction and number density is higher at the plate mid-thickness than at the sub-surface. However, in the C-Nb-V steel this trend was not observed: the particle volume fraction increases insignificantly and the number density decreases towards the mid-thickness. With an increase in microalloying element content, from the C-Nb to the C-Nb-V steel, the particle volume fraction and number density increases. However, the average particle diameter is lower in the C-Nb-V than in the C-Nb steel. This can be explained by a higher level of strain-induced precipitation in the C-Nb-V steel, due to a higher dislocation density in the C-Nb-V compared to the C-Nb steel (see section 3.8).

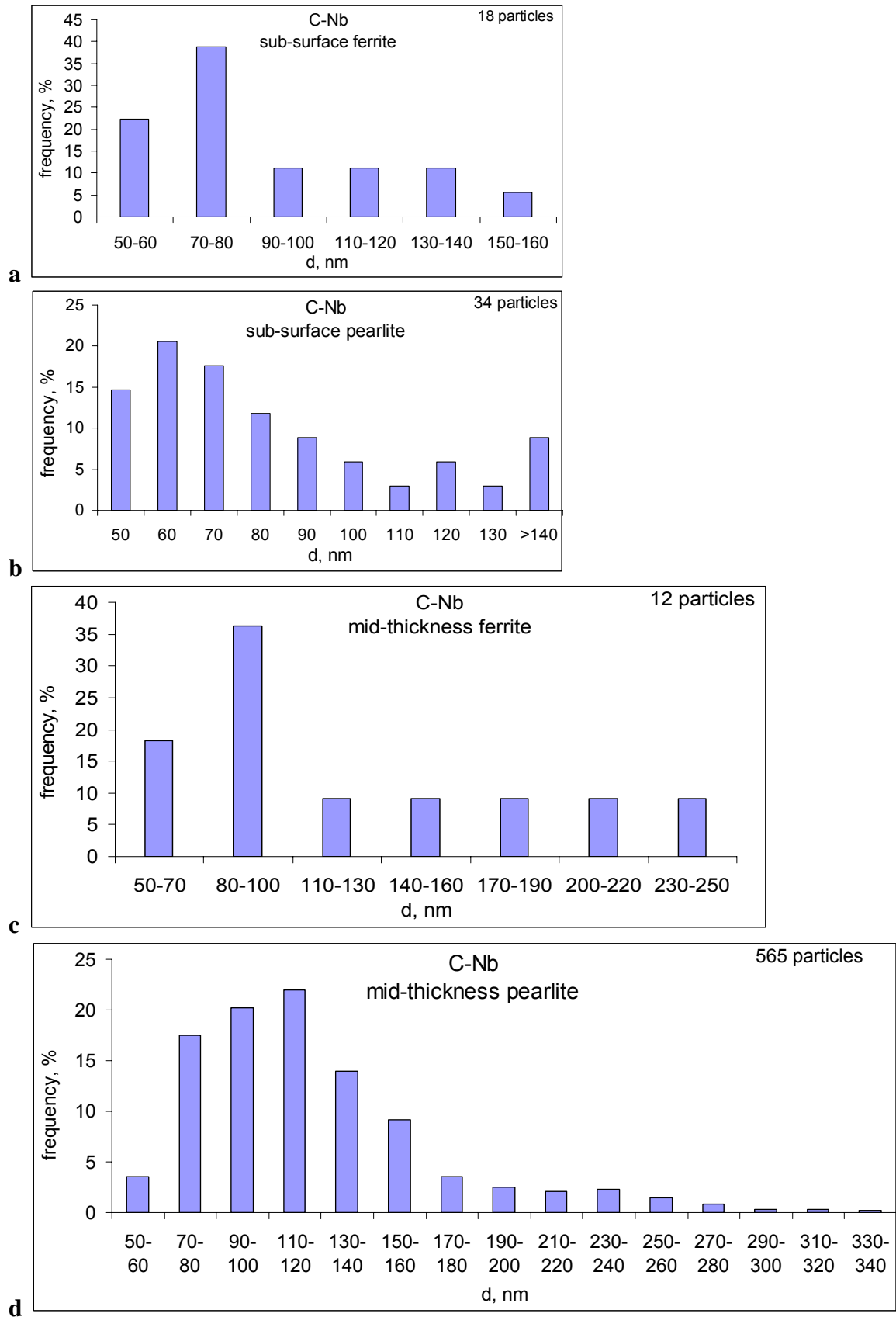


Figure 3.19 Histograms of the Nb-Ti-rich particle diameters in the (a) sub-surface ferrite, (b) sub-surface pearlite, (c) mid-thickness ferrite and (d) mid-thickness pearlite regions of the C-Nb steel

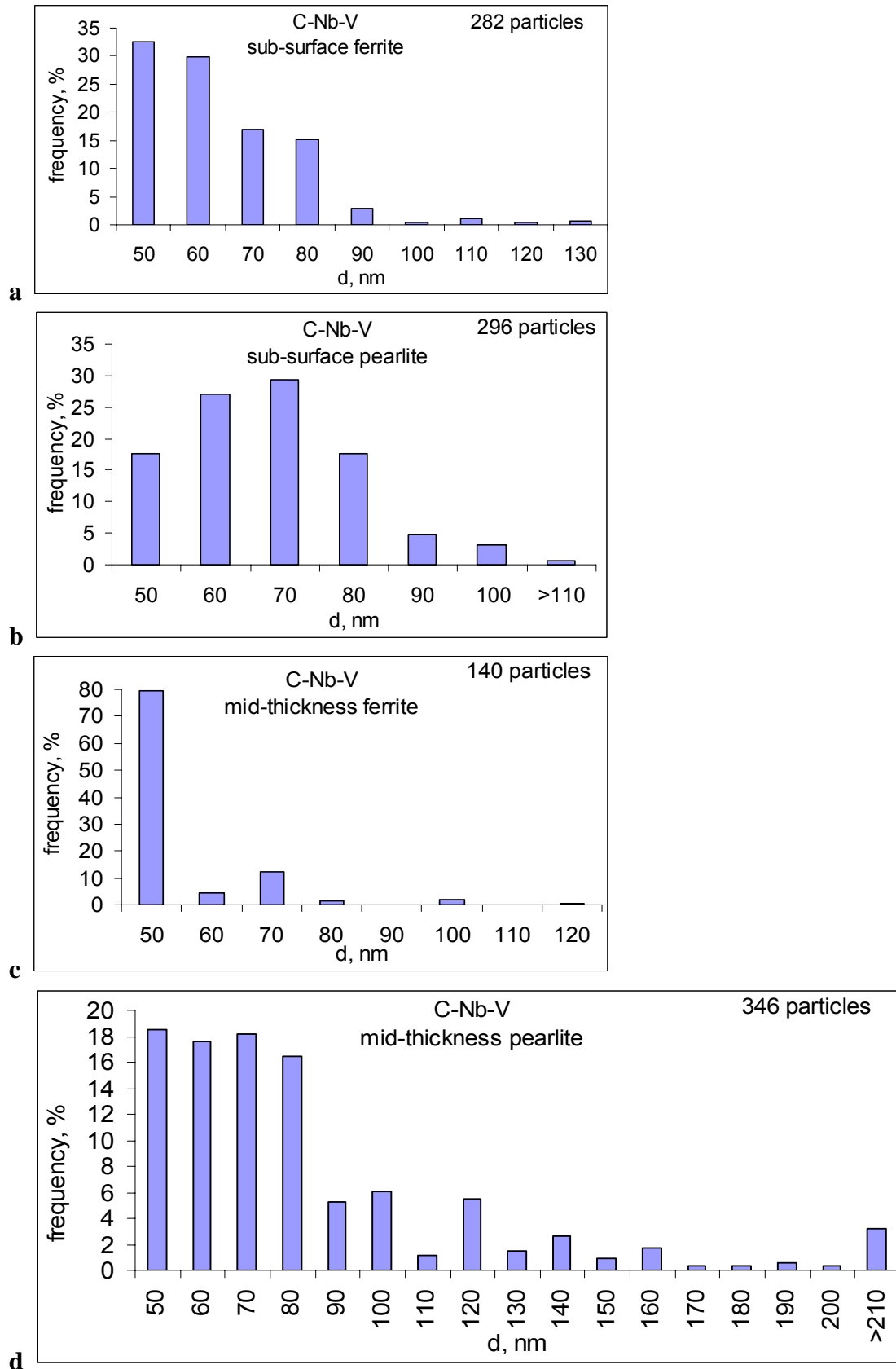


Figure 3.20 Histograms of the Nb-Ti-rich particle diameters in the (a) sub-surface ferrite, (b) sub-surface pearlite, (c) mid-thickness ferrite and (d) mid-thickness pearlite regions of the C-Nb-V steel

Table 3.6 Larger than 50 nm Nb-Ti-rich particle characteristics measured with SEM

area of precipitation		average diameter, nm				volume fraction				number density, μm^{-3}			
		C-Nb		C-Nb-V		C-Nb		C-Nb-V		C-Nb		C-Nb-V	
						$*f_{\text{TC}} = 0.000365$		$*f_{\text{TC-NbTi}} = 0.000345$ $*f_{\text{TC}} = 0.001445$					
sub-surface	ferrite	88	89	67	68	$4.4 \cdot 10^{-5}$	$6 \cdot 10^{-5}$	0.000372	$4.07 \cdot 10^{-4}$	0.12	0.16	2.36	2.42
	pearlite	90		71		$9.7 \cdot 10^{-5}$		0.000476		0.25		2.54	
mid-thickness	ferrite	132	131	58	68	$6.7 \cdot 10^{-5}$	$5 \cdot 10^{-4}$	0.000165	$4.22 \cdot 10^{-4}$	0.06	0.44	1.61	1.95
	pearlite	128		88		0.001325		0.000937		1.21		2.63	

* f_{TC} – total particle volume fraction calculated with Thermo-Calc

* $f_{\text{TC-NbTi}}$ – NbTi-rich particle volume fraction calculated with Thermo-Calc

The average through-thickness particle volume fraction in the C-Nb steel was measured to be $f = 0.000280$, which is in reasonably good agreement with the Thermo-Calc calculation, namely $f_{\text{TC}} = 0.000365$. A lower measured than calculated value, by 23 %, can be explained by the particles with diameters < 50 nm not being included in the analysis of the experimental data. The average volume fraction in the C-Nb-V steel was measured to be $f = 0.000414$, which is 17 % higher than the Thermo-Calc calculated value for the Nb-Ti-rich particles, i.e. $f_{\text{TC-NbTi}} = 0.000345$, and 3.5 times lower than the total volume fraction of the carbonitride phase, i.e. $f_{\text{TC-}\Sigma} = 0.001445$. A higher measured value for the Nb-Ti-rich particles can be explained by an underestimation of the Nb-Ti-rich particle volume fraction during the thermodynamic calculations. In the calculation the Nb-rich particle precipitation stop temperature was set as the V-rich particle precipitation start temperature. However, V precipitation start does not mean Nb precipitation finish, as Nb continues to precipitate, together with V, and adds to the Nb-rich particle volume fraction. If Nb precipitated on other particles, such as Si and Al oxides, it would also add to the Nb-rich particle diameter leading to an increased measured particle volume fraction.

A lower measured value than calculated for the total carbonitride phase volume fraction can be explained by V-rich particles not being included as they are expected to be below the SEM resolution limit. These particles were assessed by TEM.

3.7 Nb-, V- and Cu-rich phases (TEM analysis)

TEM investigation of the microalloying element precipitates was carried out for the as-rolled and annealed C-Nb and C-Nb-V steels. The annealing schedule (400 °C and 550 °C for 30 min.) was chosen to modify the dislocation density and particle distributions to examine their influence on the mechanical property change during cold deformation. Nb-Ti-rich particle distributions in both steels were not affected by the annealing schedules, which is consistent with the behaviour predicted by Thermo-Calc with (Nb,Ti)(C,N) being stable below 680 °C (Table 3.2). However, in the C-Nb-V steel, alloyed with V and Cu, substantial particle growth was observed after annealing, hence the TEM particle study concentrated on this steel grade.

C-Nb steel

Thin foil TEM of the C-Nb steel revealed widely dispersed Nb-rich particles of 6 – 50 nm size (Figure 3.21). They had a rounded or ellipsoid shape (in 2D) and were distributed throughout the ferrite grains far from the grain boundaries. The volume fraction of the particles smaller than 50 nm was measured to be $f = 0.000117$. When added to the SEM measured volume fraction, i.e. 0.000280, the total measured volume fraction of the Nb-Ti-rich particles is 0.000397, which shows a good agreement with the Thermo-Calc predicted value 0.000365.

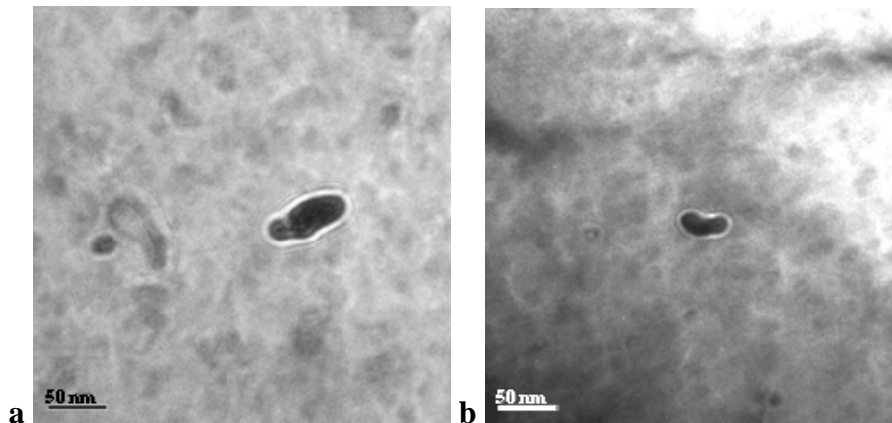


Figure 3.21 Selected TEM images from the C-Nb steel plate mid-thickness showing Nb-rich particles: (a) as-rolled and (b) annealed at 550 °C for 30 min. (images are defocused to improve contrast)

C-Nb-V steel

Particle morphology, distribution and chemistry

Particle imaging, measurements and chemical analysis for the C-Nb-V steel in the as-rolled and annealed conditions were made separately for the plate sub-surface and mid-thickness areas. It was observed that there was an increase in the particle number density in the ferrite close to the pearlite colonies. Precipitates were observed in the size range of 4 – 100 nm. For analysis the particles were characterised into two groups, < 50 nm and > 50 nm. In the < 50 nm size range the particles have a close to round shape and are uniformly distributed through the sample volume. With an increase in annealing temperature these particles show significant growth at the mid-thickness position (Figure 3.22). At the sub-surface the particle diameter change with annealing is not significant, although there is an increase in particle number density (Figure 3.23). In the > 50 nm size range the particles were of a rounded or ellipsoid shape and separated by a relatively large distance from each other. Annealing at up to 550 °C did not affect the particle diameter in this size range.

TEM-EDS of the particles revealed them to be of the following chemistries: CuS, NbCuS, NbTiCuS, NbTiVCu-, Nb-, NbV-, NbTiV-rich, Figure 3.24, which were divided into two groups: Cu-rich and NbTiV-rich.

In the as-rolled steel particles smaller than 50 nm were mainly Cu-rich at the mid-thickness position and NbTiV-rich at the sub-surface position (Table 3.7). In the > 50 nm size range Cu-rich particles were not observed.

With annealing the Cu-rich particle percentage at the mid-thickness position was found to decrease in the < 50 nm size range and increase in the > 50 nm size range. At the sub-surface position annealing leads to an increase in the Cu-rich particle percentage in both size ranges, due to precipitation of new CuS particles in the < 50 nm size range and Cu precipitation on top of the existing NbTiV-rich particles in the > 50 nm size range, along with some CuS

particle growth. This corresponds to earlier reports of Cu precipitation during annealing temperatures of 450-500 °C depending on time [108, 109].

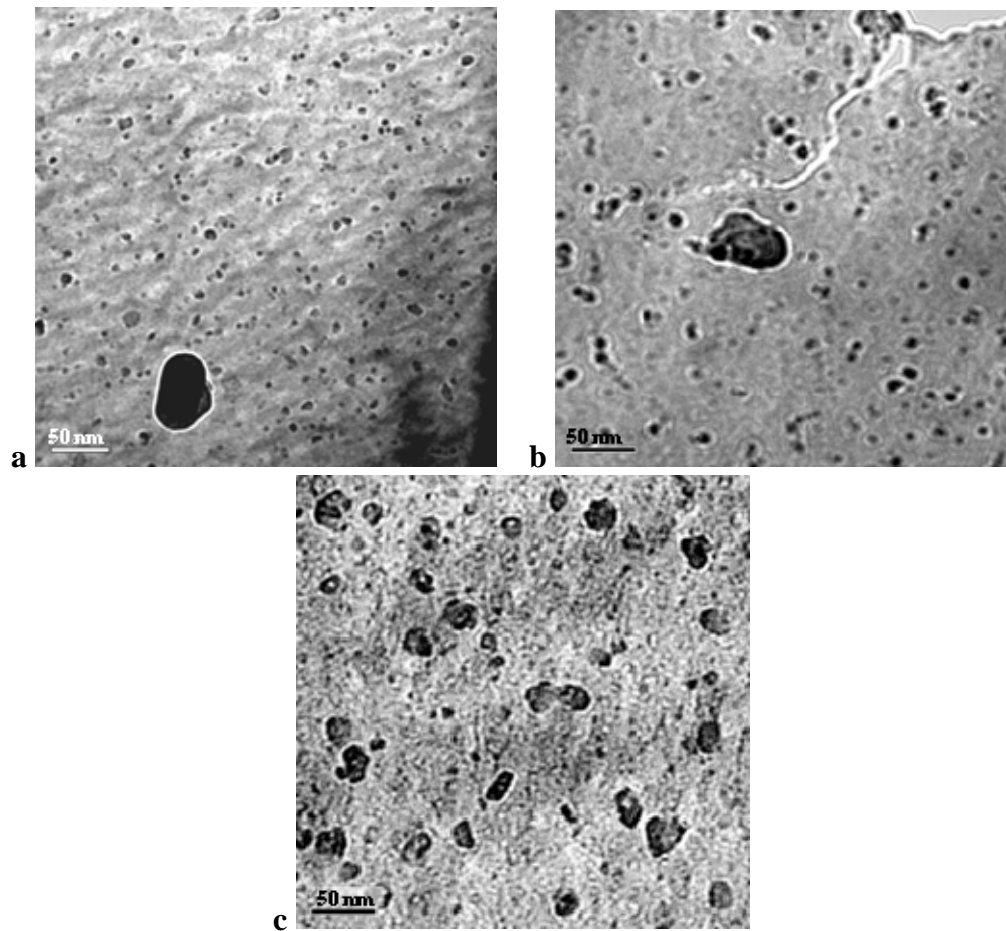


Figure 3.22 Typical TEM images from the C-Nb-V steel plate mid-thickness: (a) as-rolled, (b) annealed at 400 °C for 30 min and (c) annealed at 550 °C for 30 min

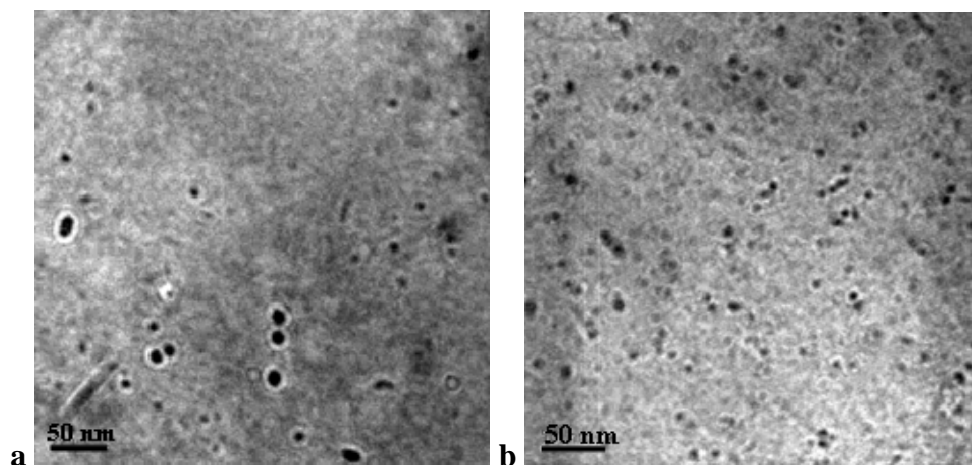


Figure 3.23 Typical TEM images from the C-Nb-V steel plate sub-surface area: (a) as-rolled, (b) annealed at 550 °C for 30 min

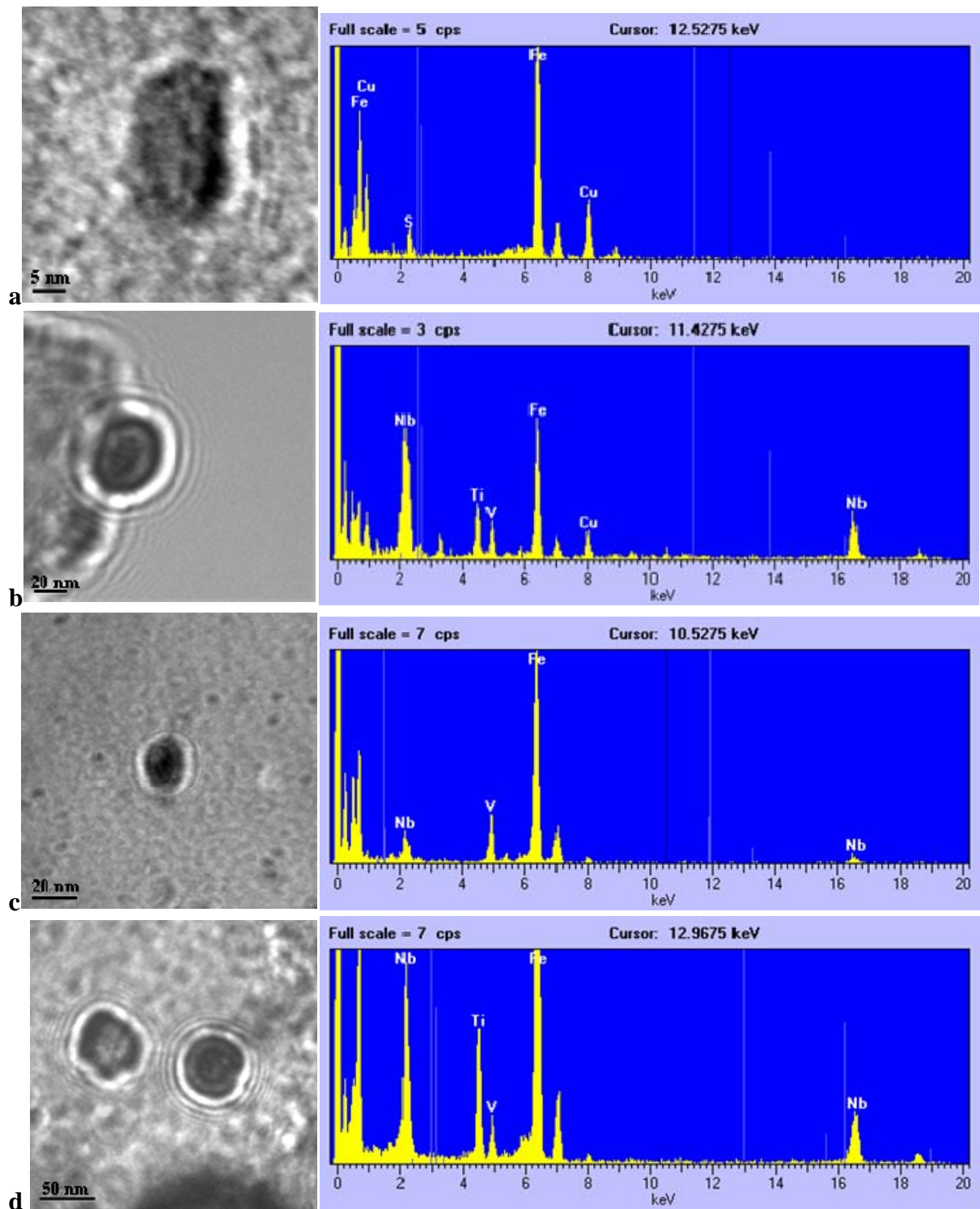


Figure 3.24 Typical TEM images and EDS spectra of (a) CuS, (b) NbTiVCu-rich, (c) NbV-rich and (d) NbTiV-rich particles in the C-Nb-V steel

Table 3.7 Size and chemistry of the particles analysed by TEM-EDS in the C-Nb-V steel

size range	elements (apart from Fe)	amount	number percentage	elements (apart from Fe)	amount	number percentage
	Mid-thickness			Sub-surface		
	As-rolled					
< 50 nm	CuS	31	97 %	NbTiVCu	2	14 %
	CuSCa	2	Cu-rich	Nb	2	Cu-rich
	V	1	3 %	NbV, Si	1	86 %
			NbTiV-rich	NbTi, Si	5	NbTiV-rich
				NbTiV, Si	4	
50 nm <	Nb	2	100% NbTiV-rich	Nb	1	100% NbTiV-rich
Annealed 400 °C for 30 min						
< 50 nm	CuS	1	81 %			
	CuSNb	6	Cu-rich			
	CuSNbV	10	19 %			
	V	2	NbTiV-rich			
	NbV	2				
50 nm <	TiNbV	3	100% NbTiV-rich			
Annealed 550 °C for 30 min						
< 50 nm	CuS	7	75 %	CuS	1	71 %
	CuSSi	3	Cu-rich	CuSNb	4	Cu-rich
	CuSNb	2		CuNbV	1	
	CuSCaTi	1	25 %	NbTiVCu	4	29 %
	CuSNbV	2	NbTiV-rich	Nb	1	NbTiV-rich
	V	1		NbV	1	
	Nb	2		NbTiV	2	
	NbV	2				
50 nm <	CuNbTi	1	12 %	CuSNbV	1	31 %
	Nb	2	Cu-rich	NbTiVCu	3	Cu-rich
	NbTi	1	88 %	Nb	1	69 %
	NbTiV	4	NbTiV-rich	NbTi	1	NbTiV-rich
				NbTiV	7	

Particle size, volume fraction and number density

Particles larger than 50 nm were quantified using SEM, so during the TEM studies these particles were excluded from the diameter distributions (Figures 3.25). The Cu-containing and Cu-free particles were quantified together (Table 3.8). Annealing at 550 °C for 30 min. did not result in a significant diameter distribution change at the sub-surface position, Figure 3.25, a, as particles in this area are mainly NbTiV-rich and the annealing temperature is not high enough to cause growth. At the mid-thickness position there is a significantly shift to higher diameters with an increase in annealing temperature, Figure 3.25, b, which is due to Cu-rich particle growth at 550 °C.

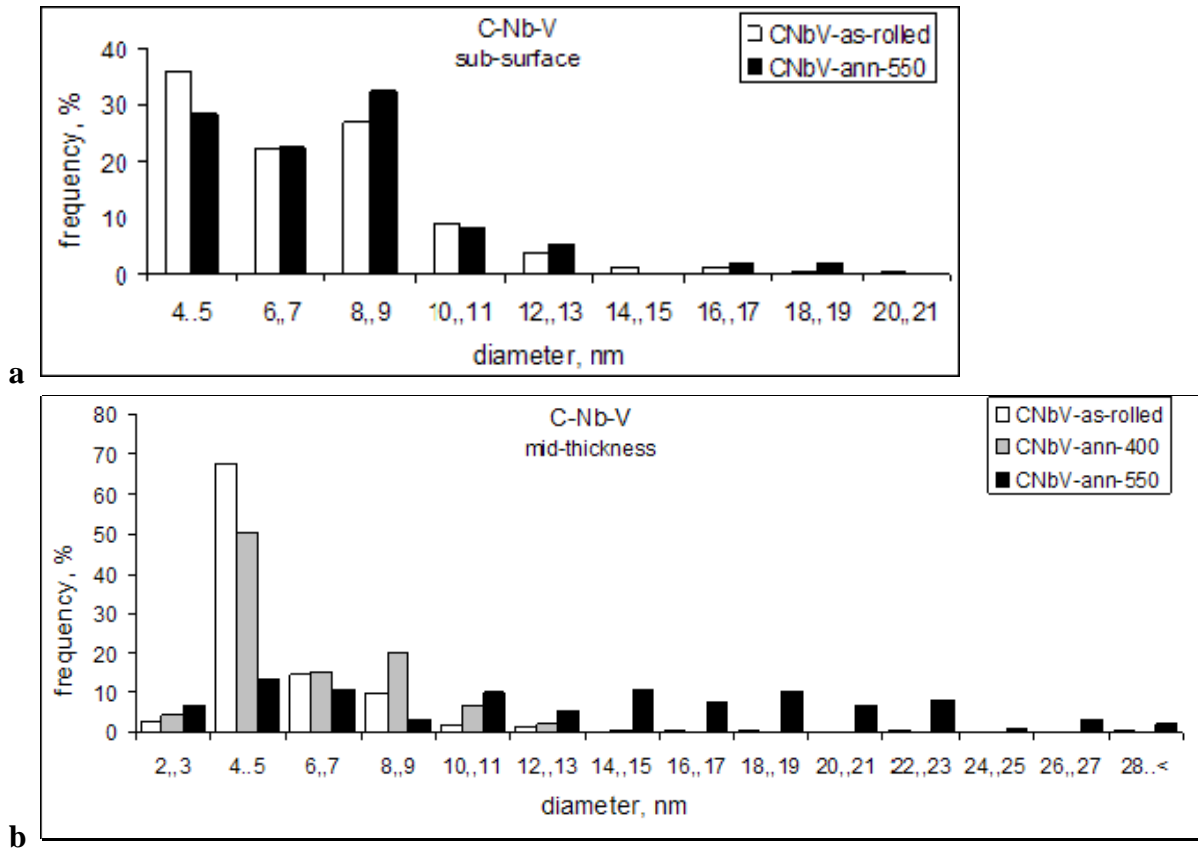


Figure 3.25 (Cu+NbTiV)-rich particle diameter distributions at the (a) sub-surface and (b) mid-thickness positions of the as-rolled and annealed C-Nb-V steel plate

Table 3.8 Smaller than 50 nm (Cu+NbTiV)-rich particle characteristics measured with TEM in the C-Nb-V steel

Parameter	As-rolled		Annealed 400 °C		Annealed 550 °C	
	sub-surface	mid-thickness	sub-surface	mid-thickness	sub-surface	mid-thickness
predominant chemistry	NbTiV	Cu	not measured	Cu	NbTiV + Cu	Cu
average diameter, nm	8.5	6.2		7.1	7.1	16.3
volume fraction	0.00166	0.00118		0.00210	0.00125	0.00384
number density, μm^{-3}	1579	3856		8619	5075	1419

In the as-rolled steel the particle average diameter and volume fraction decreased and number density increased toward the plate mid-thickness (Table 3.8). The average particle volume fraction in the as-rolled C-Nb-V steel was measured to be 0.00142, which together with the SEM measured volume fraction, i.e. 0.000414, gives 0.001834 of total particle volume fraction. This is 27 % higher than the Thermo-Calc predicted value of 0.001445, as the total measured particle volume fraction includes CuS, (Cu+NbTiV)-rich and NbTiV-rich particles, whilst the ThermoCalc calculation reflects only the (Nb,Ti,V)(C,N) volume fraction with no CuS as a constituent phase, all the Cu dissolved in the ferrite matrix and only traces of Cu in the carbonitride phase.

After annealing the measured particle volume fraction and the average diameter increase at the mid-thickness position, although the particle number density at mid-thickness has its maximum at 400 °C and then decreases at 550 °C. This is due to precipitation of new Cu-rich particles during the first stages of annealing followed by the particle growth of larger ones via dissolution of smaller ones. Particle number density increase and the average diameter decrease at the sub-surface position can be related to the new Cu-rich particles that precipitate.

3.8 Dislocation structures and dislocation density (TEM analysis)

The dislocation structure study was carried out for the as-rolled and annealed C-Nb and C-Nb-V steels at the mid-thickness position. For the dislocation density measurements the same samples were used as for the microalloy particle distribution study. Annealing schedules, i.e. 400 °C and 550 °C for 30 min., and place of measurement, i.e. mid-thickness position, were selected to allow correlation of the results to the mechanical properties obtained with compression-tension testing. In addition, the dislocation density was measured at the C-Nb-V steel sub-surface to correlate to the mechanical property distribution across plate thickness.

TEM thin foil imaging revealed an irregular dislocation structure with uniform dislocation density in both steels, Figure 3.26, with a tendency to the cell structure in the C-Nb-V steel, Figure 3.26, b. Different ferrite grains exhibited a difference in absolute values of dislocation density, Figure 3.27, and apart from the irregular dislocation structure, which is mainly observed, areas of regular straight lined structure and dislocation clusters (nets) were also present, Figure 3.28. This is consistent with earlier reported data for the two phase ferrite-pearlite microstructures [17, 22, 23]. As strain increases the dislocation structure develops from the straight lined to the irregular and, then, to cluster formation [16, 19], presence of all these dislocation structure types in the studied steels supports inhomogeneity of local strain experienced by these steels during plate production. Inhomogeneity of local strains is related to the difference in phase plasticity [18].

In the as-rolled C-Nb steel the dislocations show numerous interactions in the form of knots and bundles (Figure 3.29). As in this steel the small (< 50 nm) microalloy precipitates are absent and the spacing between the NbC particles is relatively large, the dislocation structures show only dislocation-dislocation interactions and no dislocation-particle interactions were observed.

In the as-rolled C-Nb-V steel numerous dislocation loops between microalloy particles were observed, Figure 3.30, which reflect dislocation-particle interaction during slip.

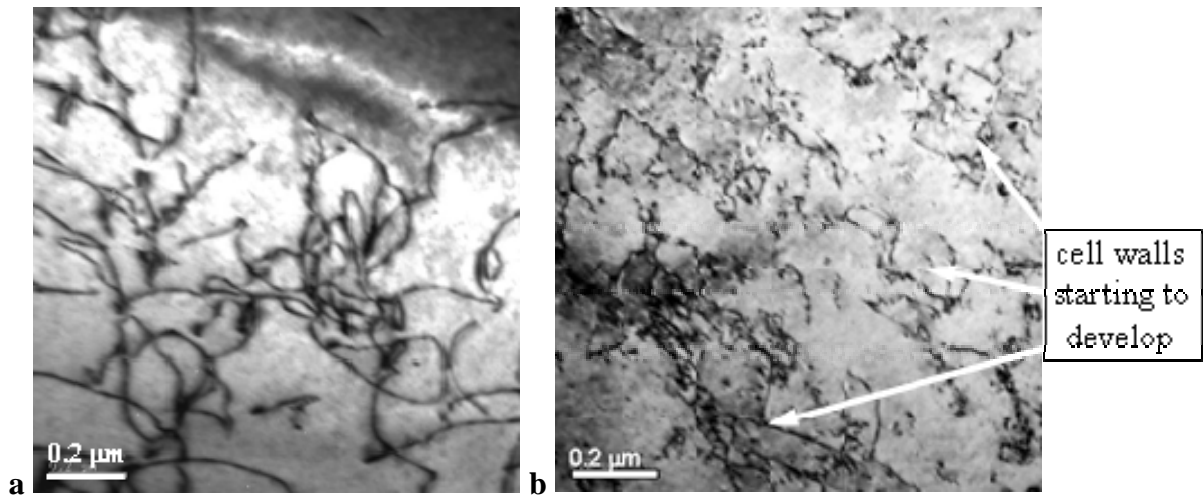


Figure 3.26 Typical two-beam TEM images of dislocation structure in the (a) C-Nb as-rolled, and (b) C-Nb-V as-rolled steel, electron beam direction $g = [200]$

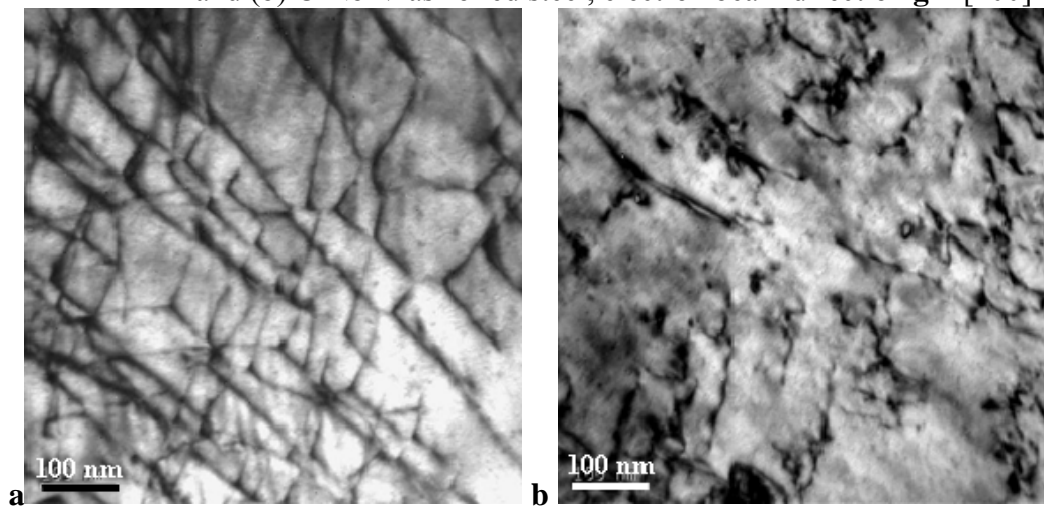


Figure 3.27 Two-beam TEM micrographs of the dislocation structure in the as-rolled C-Nb-V steel with (a) high and (b) low dislocation density, $g = [200]$

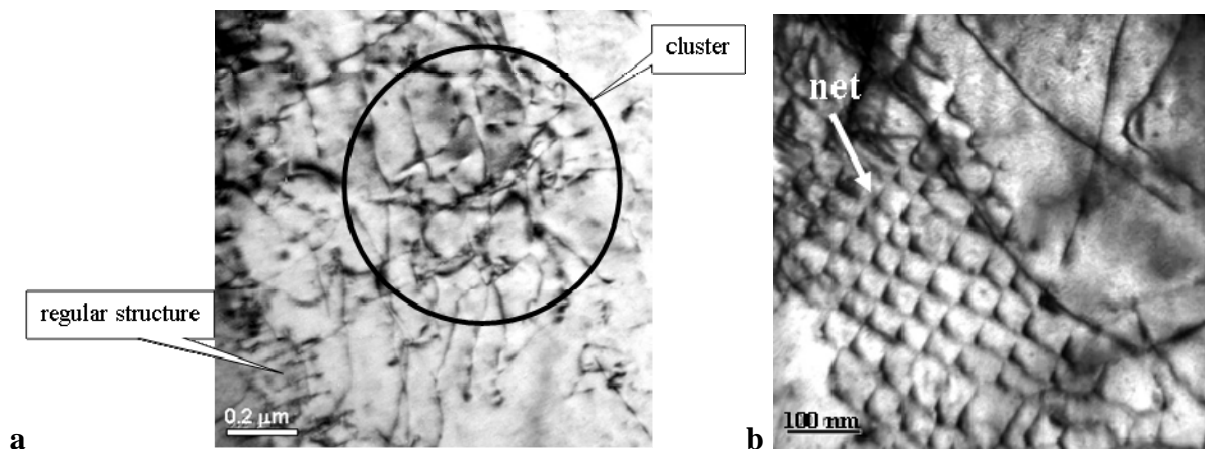


Figure 3.28 The regular straight line structure and a dislocation cluster in the (a) C-Nb as-rolled, $g = [200]$, and (b) a net in the C-Nb-V as-rolled steel, $g = [1\bar{1}0]$

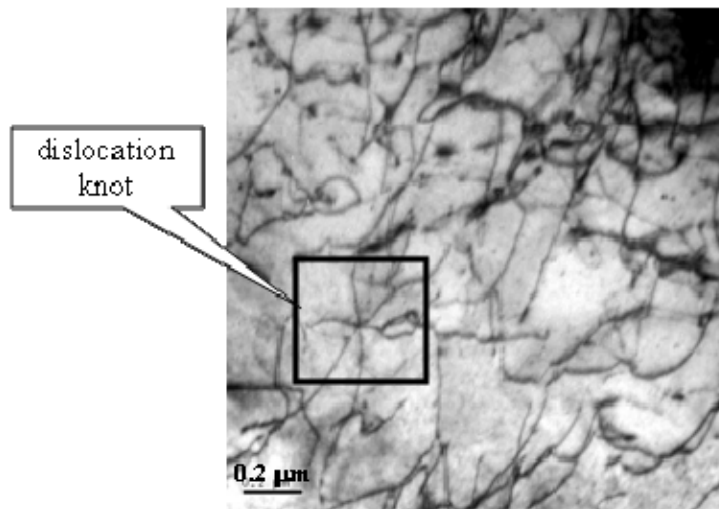


Figure 3.29 Two-beam TEM image of the C-Nb as-rolled steel with a dislocation knot, $g = [020]$

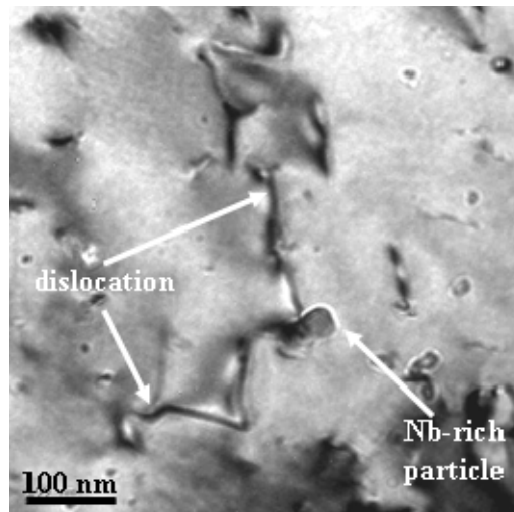


Figure 3.30 Multi-beam TEM image of the C-Nb-V as-rolled steel with the dislocation looping around a microalloy particle

The average dislocation density was measured to be $2.3 \times 10^{14} \text{ m}^{-2}$ in the C-Nb and $4.0 \times 10^{14} \text{ m}^{-2}$ in the C-Nb-V as-rolled steels, which agrees with literature data for hot-rolled ferritic steels (Table 3.9). Measurements have shown higher values of dislocation density in the C-Nb-V steel, compared to the C-Nb steel. This can be related to the following factors:

1. The finish rolling temperature for the C-Nb-V steel, 735°C , is lower than for the C-Nb steel, 745°C . Due to a larger number density of microalloy particles, the recrystallization stop temperature in the C-Nb-V steel is likely to be higher. These would lead to a greater rolling

reduction below the recrystallization stop temperature and hence a higher dislocation density.

2. Dislocations, blocked by particles, may become new dislocation sources, in accordance to the Frank-Read dislocation generation mechanism [7]. Thus in the C-Nb-V steel it is possible to expect a larger number of dislocation sources and, consequently, a larger dislocation generation rate.

Table 3.9 Dislocation density in ferrite-pearlite steels, $\times 10^{14} \text{ m}^{-2}$

steel	condition	min	max	average
C-Nb mid-thickness	as-rolled	1.9	3.1	2.3
	annealed 550 ⁰ C	0.8	2.0	1.1
C-Nb-V mid-thickness	as-rolled	2.9	5.2	4.0
	annealed 400 ⁰ C	1.0	2.3	1.6
	annealed 550 ⁰ C	1.0	2.8	1.5
0.05C-0.14Cu [19]	hot rolled in austenite field (positron annihilation)	0.3, 0.5, 1.0 depending on technology		
0.15C [21]	hot rolled (TEM imaging)	0.9		
	annealed at 450 ⁰ C (TEM imaging)	0.1...0.5		
0.15C-0.1P [21]	hot rolled (TEM imaging)	2.3		
	annealed at 450 ⁰ C (TEM imaging)	0.2...0.7		
0.16C-0.01Cu [28]	hot rolled (neutron diffraction)	0.6		
API X80 [134]	TMCR	0.1...1.0 in ferrite of ferrite-bainite structure		

Annealing at 550 ⁰C for 30 min. resulted in the dislocation structure changing. In the C-Nb steel the number of knots and bundles significantly decreased (Figure 3.31, a). And in the C-Nb-V steel the number of dislocation loops decreased (Figure 3.31, b). In both steels the straight lined dislocation structure became more frequently observed (Figure 3.31, c, d). With annealing, the dislocation density decreased due to annihilation. As a result of annealing at 550 ⁰C for 30 min. the dislocation density in the C-Nb steel decreased by a factor of 2.1 and in the C-Nb-V steel by a factor of 2.7.

The dislocation structure investigation at the sub-surface position of the C-Nb-V as-rolled steel plate showed the dislocation density to be in the range $(0.90 \dots 1.65) \times 10^{14} \text{ m}^{-2}$ with an average value of $1.22 \times 10^{14} \text{ m}^{-2}$. The dislocation density increase towards the plate mid-thickness by 3.3 times can be explained if the plate mid-thickness experienced higher strain levels during rolling.

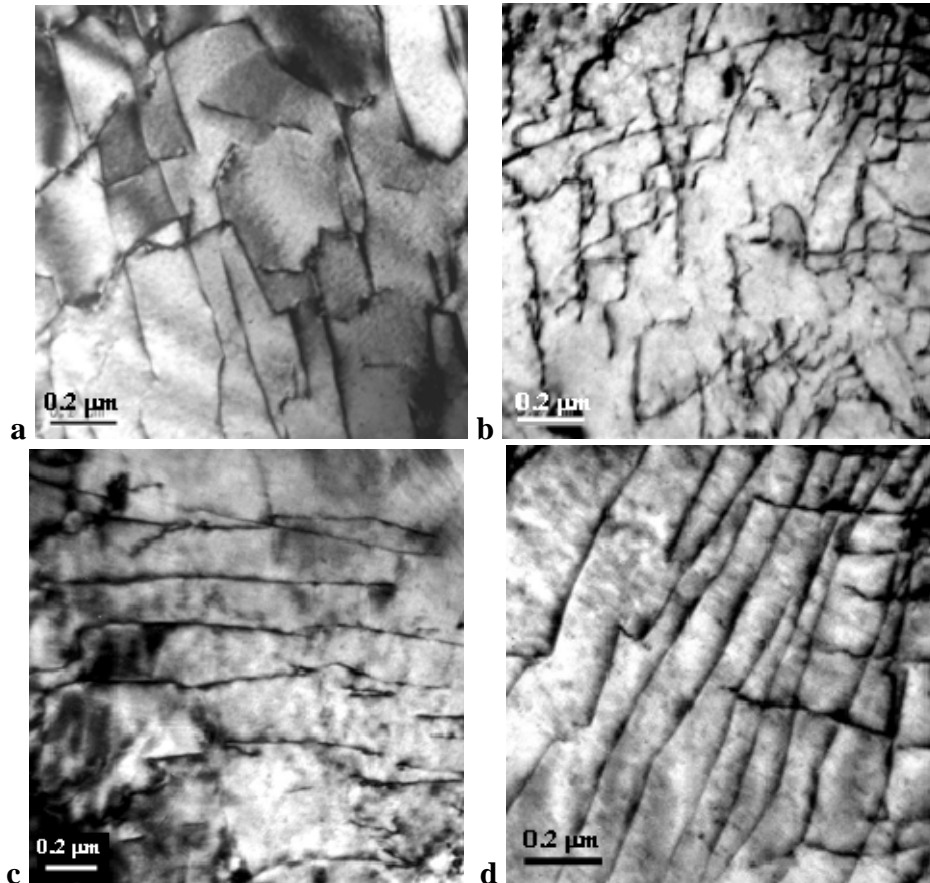


Figure 3.31 Typical two-beam TEM images of the dislocation structure in the (a) C-Nb steel annealed at 550 °C for 30 min. and (b) C-Nb-V steel annealed at 550 °C for 30 min., $\mathbf{g} = [2\bar{1}1]$; selected TEM images of the (c) straight line dislocation structure in the C-Nb annealed and (d) C-Nb-V annealed steel, $\mathbf{g} = [110]$

3.9 Dislocation-particle interaction (TEM analysis)

Dislocation-particle interaction is the source of precipitation strengthening, which plays a significant role in the microalloyed steel property development. Existing theoretical descriptions of mechanical property change during unidirectional deformation work reasonably well for the experimental conditions for which they were developed [71], but may

give an inaccurate result for other conditions (different chemistry, particle distributions, dislocation density). Mechanical property dependence on particles and dislocations during reverse cold deformation is known only qualitatively, through the Orowan theory for the Bauschinger effect, but no quantitative description exists so far. Thus, quantitative data for dislocation-particle interaction are needed: first – for the development of mechanical property changes during reverse deformation, and second – for possible incorporation into existing relationships for unidirectional deformation.

Interaction mechanism

A moving dislocation can bypass particles in two ways: either by cutting the particles or looping between them, depending on which process requires less energy. TEM imaging in the present work revealed no circular dislocations around the by-passed particles, which supports the non-occurrence of the looping mechanism in the studied steels. The cutting mechanism was observed over the whole particle diameter range (Figure 3.32). However, at the earlier stages of contact the dislocation is bowing between particles (around a particle) until the energy of loop curvature starts to exceed the energy needed for cutting, and then cutting proceeds with a constant or decreasing dislocation line curvature (Figure 3.33).

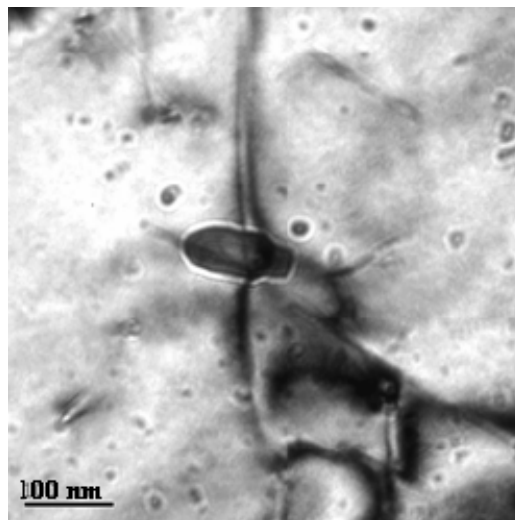


Figure 3.32 Dislocation interaction with a NbTiV-rich particle in the C-Nb-V as-rolled steel

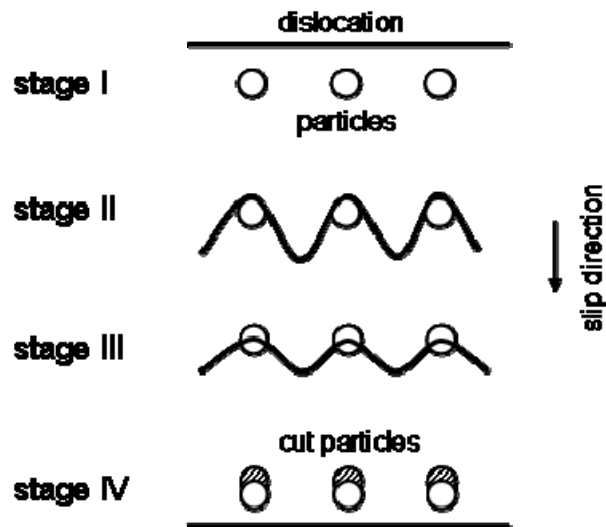


Figure 3.33 Dislocation-particle interaction mechanism observed in the present work

Obviously, with an increase in particle number density and dislocation density the number of potential dislocation-particle interaction sites will increase. However, there are several aspects that will influence the quantitative outcome of this interaction with respect to the mechanical properties:

- “Small” particles do not produce a strong barrier for the moving dislocation and thus do not contribute significantly to the strengthening effect. The effective particle diameter (a minimum diameter which blocks dislocations “effectively”) is discussed in this section below;
- Particle strength varies with particle chemistry, as interatomic bonds vary with element type. So, the effective particle diameter will be dependent on particle chemistry;
- The number of dislocation-particle interactions will depend on the “dislocation length – interparticle spacing” ratio. Short dislocations may pass between widely set particles without any interaction.

Quantitative analysis of interaction

In the C-Nb and C-Nb-V steels the NbTiV-rich particles were all larger than 50 nm and were observed to effectively block the dislocations, i.e. dislocation bowing around the particles prior to cutting was observed (Figure 3.32). Particles smaller than 50 nm were predominantly Cu-rich in

the C-Nb-V steel. So in the present work, a minimum value of the effective particle diameter was studied only for the Cu-rich particles. Analysis of 45 dislocation-particle interaction sites showed the minimum effective particle diameter to be 12 nm (Figure 3.34). This means that Cu-rich particles smaller than 12 nm do not effectively pin the moving dislocations and can be disregarded during analysis of the particle distribution influence on mechanical properties.

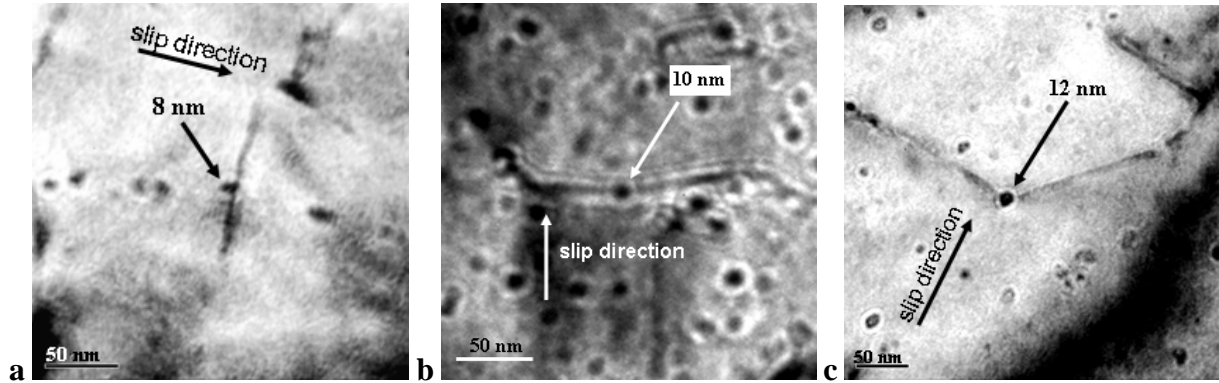


Figure 3.34 Dislocation-particle interaction sites for the smallest particles observed in the C-Nb-V annealed steel: (a) 8 nm and (b) 10 nm particles do not block the dislocation, (c) 12 nm particle blocks the dislocation

If a dislocation interacts with an ellipsoidal particle the interaction result will depend on which side of the particle is approached by the dislocation. If the short axis of the ellipsoidal particle is smaller than the effective particle diameter this particle may not block a dislocation, if a dislocation line interacts with the short axis (Figure 3.35, a). On the other hand, a dislocation approaching the particle may be blocked, if the interaction length is along the ellipsoid long axis and this is larger than the minimum effective particle diameter (Figure 3.35, b).

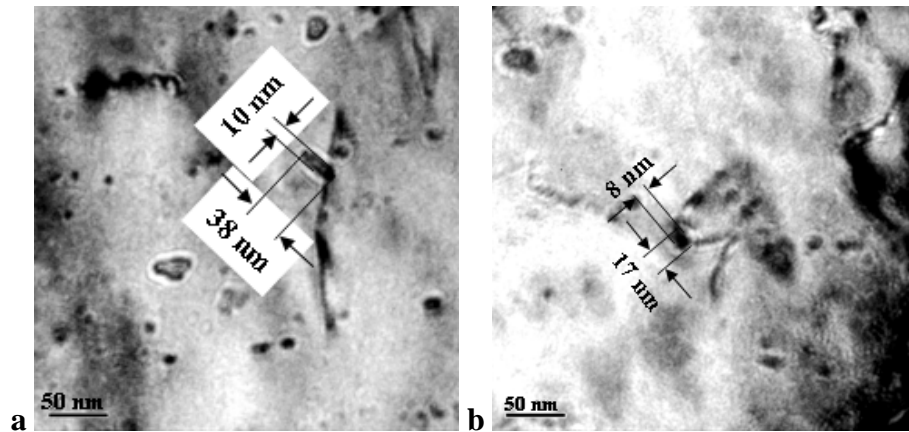


Figure 3.35 Dislocation interaction with ellipsoid particles: a particle is approached by a dislocation along the (a) long and (b) short ellipsoid axis

The interparticle spacing in the plane of the micrograph can be theoretically assessed assuming a particle homogeneous distribution, which implies equal particle diameter and interparticle spacing (Figure 3.36). The shaded area, on Figure 3.36, can be calculated as follows:

$$4\left(\frac{s}{2}\right)^2 + \frac{4sd}{2} + d^2 = A ,$$

where d – particle diameter, s – interparticle spacing

Total area of the micrograph A_{Σ} will be:

$$A_{\Sigma} = N \cdot A ,$$

where N is the number of particles;

or after substitution of A

$$A_{\Sigma} = N4\left(\frac{s}{2}\right)^2 + \frac{N4sd}{2} + Nd^2 ,$$

One of the solutions gives the interparticle spacing, s , as follows:

$$s = \sqrt{\frac{A_{\Sigma}}{N}} - d .$$

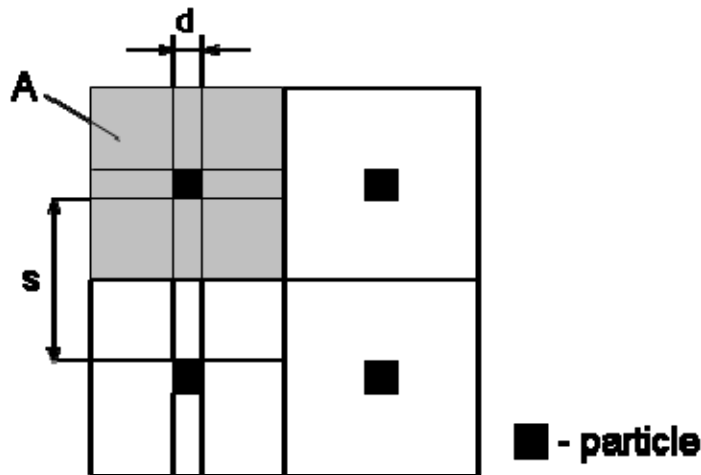


Figure 3.36 Schematic diagram of the particle homogeneous distribution

Using the SEM experimental data, Table 3.6, for the larger than 50 nm particles, the interparticle spacing was calculated to be 15.2 μm in the C-Nb steel and 4.0 μm in the C-Nb-V steel. As the average dislocation length, 0.90 μm in the C-Nb and 0.47 μm in the C-Nb-V

steel (measured in the plane of TEM micrographs), is several times smaller than the interparticle spacing, moving dislocations may pass between the > 50 nm particles without interaction. However, measurements of the dislocation length did not take into account an angle between dislocation lines and the plane of the micrograph. This results in a decreased average value of the dislocation length. Regarding a possibility of dislocation-particle interaction above and below the micrograph plane, occasionally observed dislocation interaction sites with the > 50 nm particles might be considered as weak sources of precipitation strengthening. However, inaccuracy in the dislocation length determination in the present project should be eliminated in the future work.

In the < 50 nm size range the particle number density and average interparticle spacing depend on steel grade, namely microalloying element content, and annealing schedule (Table 3.10). Thus, with an increase in microalloying element content the particle number density increases and the interparticle spacing decreases. Annealing of the C-Nb-V steel results in the 12-50 nm particle number density increasing and the interparticle spacing decreasing, which is due to precipitation of the Cu-rich particles. The difference between the measured and calculated values for the interparticle spacing is likely to be due to calculation assuming the particles are distributed homogeneously even though the particle precipitation is inhomogeneous. With annealing the particle homogeneity increases, as can be seen from the better agreement between the interparticle spacing values and the shift in distribution to lower values (Figure 3.37). The particle number density increase, due to alloying or as a result of annealing, leads to a consequent increase in the potential number of dislocation-particle interaction sites, presented in the Table 3.10 for one dislocation. During deformation a larger number of particles interacting with dislocations will provide a stronger dislocation immobilization and strength increase.

On the basis of the obtained results it is possible to conclude that 12-50 nm diameter Cu-rich particles are the major sources of precipitation strengthening in the C-Nb-V steel plate

mid-thickness. However, particle chemistry, due to its influence on the particle strength, should be considered when determining the effective particle size range.

Table 3.10 Dislocation-particle interaction parameters for the 12-50 nm particles at the plate mid-thickness

Parameter		C-Nb	C-Nb-V		
		As-rolled	As-rolled	Annealed at 400 °C	Annealed at 550 °C
particle	volume fraction	0.00011	0.00076	0.00126	0.00374
	average diameter, nm	19.7	19.3	15.8	19.0
	number density, μm^{-3}	72	186	262	894
interparticle spacing in the micrograph plane	measured, μm		0.132	0.098	0.071
	calculated, μm	0.397	0.253	0.203	0.104
average dislocation length in the micrograph plane, μm		0.895	0.468	0.422	0.594
maximum number of interactions per dislocation (according to homogeneous particle distribution and a used method of the dislocation length determination)		3 (calculated)	4	5	9

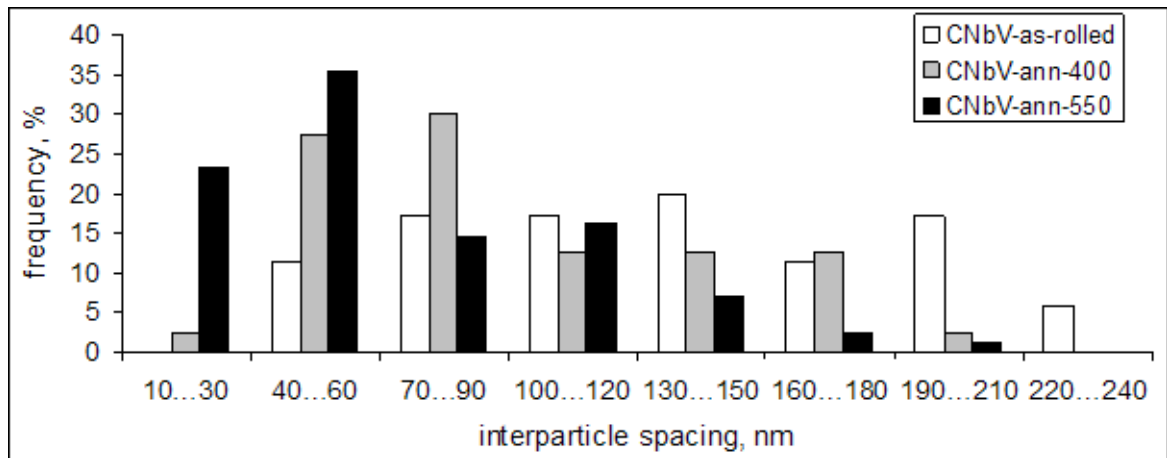


Figure 3.37 Measured interparticle spacing frequency distributions for the C-Nb-V steel

3.10 Hardness and yield stress dependence on microstructure

Experimental analysis of hardness

The average ferrite microhardness was measured to be 144 ± 6 H_V in the C-Mn, 188 ± 12 H_V in the C-Nb and 195 ± 10 H_V in the C-Nb-V as-rolled steels (Figure 3.38).

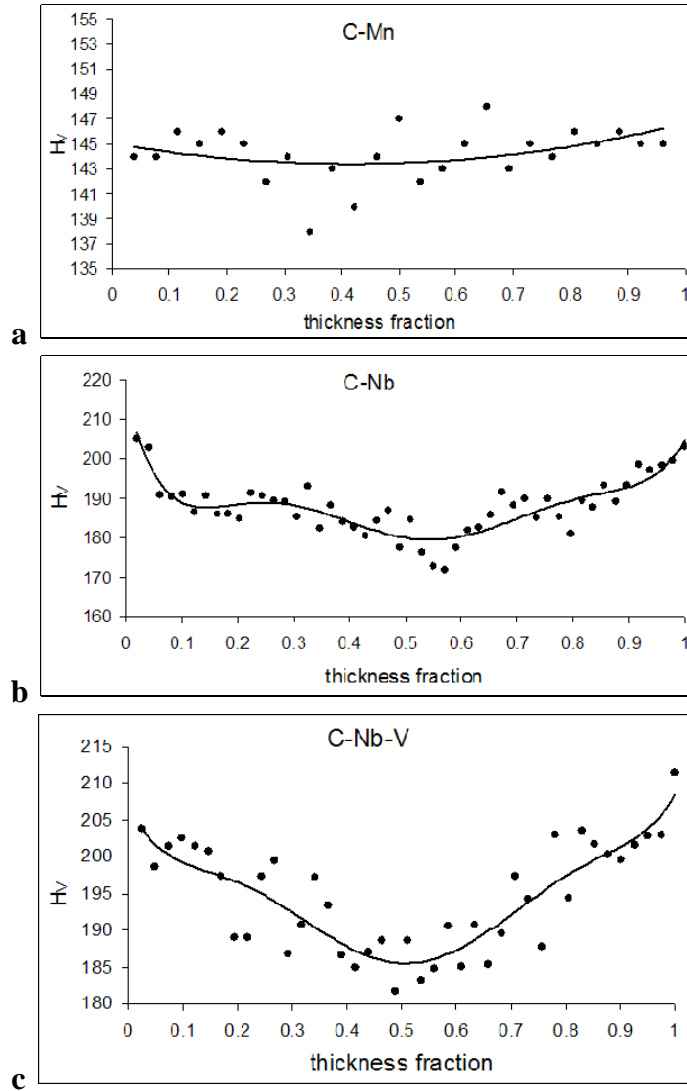


Figure 3.38 The average ferrite microhardness distribution across plate thickness for the (a) C-Mn, (b) C-Nb and (c) C-Nb-V steels

In the alloyed steels the ferrite microhardness increases towards the plate sub-surface, by 4.9 % in the C-Nb and 5.3 % in the C-Nb-V steel, which is consistent with the ferrite grain size decrease, by 14 % in the C-Nb and 26 % in the C-Nb-V steel, and 12-50 nm particle number

density increase in the C-Nb-V steel by 12 % (Table 3.11). However, in the C-Mn steel this trend is not observed, the microhardness value is equal across the plate thickness (within the experimental scatter), which can be explained by the small difference in grain size between the sub-surface and mid-thickness, 6% in the C-Mn steel.

Table 3.11 Microstructure–hardness correlation for the as-rolled condition of the studied steels

Steel grade		Microstructure parameters						H _V	
		grain size, μm	second phase, pearlite %	particle number density, μm ⁻³			dislocation density, x10 ¹⁴ m ⁻³	micro	macro
				50 + nm	< 50 nm	12-50 nm			
C-Mn	sub-surface	4.7	14.5	-	-	-	not measured	145	172
	mid-thickness	5.0	16.3	-	-	-		143	167
C-Nb	sub-surface	2.4	7.0	0.16	not measured			191	190
	mid-thickness	2.8	12.4	0.44	86	72	2.3	182	193
C-Nb-V	sub-surface	2.0	3.0	2.42	1579	208	1.2	198	196
	mid-thickness	2.7	6.4	1.95	3856	186	4.0	188	209

The average macrohardness was measured to be $170 \pm 6 \text{ H}_V$ in the C-Mn, $192 \pm 10 \text{ H}_V$ in the C-Nb and $200 \pm 10 \text{ H}_V$ in the C-Nb-V as-rolled steels (Figure 3.39). In the alloyed steels the macrohardness increased towards the plate mid-thickness, by 1.6 % in the C-Nb and 6.6 % in the C-Nb-V steels, which is consistent with the second phase (pearlite) content increase, by 1.8 times in the C-Nb and 2.1 times in the C-Nb-V steel, and the dislocation density increase by 3.3 times in the C-Nb-V steel. Obviously, strengthening due to the dislocation density increasing is

compensated by softening due to the 12 – 50 nm particle number density decreasing and the ferrite grain size increasing. In the C-Mn steel the macrohardness decreases towards the plate mid-thickness, which can be related to the grain size increase, as the pearlite content difference of 12 % is not significant.

The macrohardness, compared to the ferrite microhardness, is 26 HV higher for the C-Mn, 4 HV higher for the C-Nb and 5 HV higher for the C-Nb-V steel. A larger microhardness-macrohardness difference in the C-Mn steel can be explained by the second phase strengthening. In the C-Mn steel the second phase (pearlite) content is 1.6 times higher than in the C-Nb and 3.3 times higher than in the C-Nb-V steel.

With an increase in microalloying element content, from the C-Mn to the C-Nb and C-Nb-V steel, the average ferrite microhardness and macrohardness increase due to the grain refinement, solid solution and precipitation strengthening, and work-hardening.

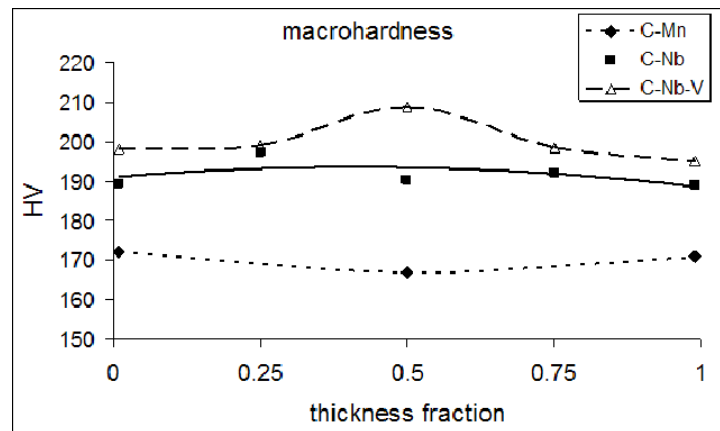


Figure 3.39 The average macrohardness distribution across plate thickness

Theoretical and experimental analysis of the yield stress

To separate the influence of the different strengthening mechanisms in the steels the components of the yield stress from the different microstructural features were calculated using the relevant theoretical equations.

The grain refinement effect was assessed with the Hall-Petch equation. In the literature [71] it is possible to find different numerical values of the equation coefficients, which apart

from the grain refinement may take into account solid solution strengthening. As solid solution strengthening was assessed using separate equations, the Hall-Petch equation coefficients were chosen for pure iron [3]:

$$\sigma_{gs} = 15 + 21.4 \cdot d^{-1/2}.$$

Substitution of the measured grain size will give:

327 MPa at the sub-surface and 318 MPa at the mid-thickness of the C-Mn steel plate,

452 MPa at the sub-surface and 419 MPa at the mid-thickness of the C-Nb steel plate,

489 MPa at the sub-surface and 427 MPa at the mid-thickness of the C-Nb-V steel plate.

The difference between grain size strengthening and the measured yield stress, Table 3.12, comes in the C-Mn steel from solid solution strengthening and work-hardening; and in the microalloyed steels from work-hardening, solid solution and precipitation strengthening.

The Thermo-Calc calculations have shown that 1 % of Mn and 50 % of Si content in the C-Mn, 30 % of Mn and 50 % of Si content in the C-Nb and 80 % of Mn and 50 % of Si content in the C-Nb-V steel are dissolved in the ferrite matrix. As the strengthening coefficient for Mn is 31 MPa/% and for Si is 83 MPa/% [71], the solid solution strengthening was calculated as follows:

in the C-Mn steel $1.09 \times 0.01 \times 31 + 0.23 \times 0.5 \times 83 = 10$ MPa,

in the C-Nb steel $1.36 \times 0.3 \times 31 + 0.37 \times 0.5 \times 83 = 28$ MPa,

in the C-Nb-V steel $1.47 \times 0.8 \times 31 + 0.34 \times 0.5 \times 83 = 51$ MPa.

Work-hardening in the C-Mn steel can be assessed using the macrohardness change during annealing (Figure 3.40). If the hardness drop is multiplied by the yield/hardness ratio the approximate yield stress drop during annealing can be obtained and related to dislocation annihilation:

$$\text{at the sub-surface } \Delta\sigma_{wh}^{C-Mn} = \Delta H_V \cdot \frac{YS}{\text{macro}H_{V \text{ average}}} = (172 - 156) \cdot \frac{359}{170} = 34 \text{ MPa},$$

at the mid-thickness $\Delta\sigma_{wh}^{C-Mn} = \Delta H_V \cdot \frac{YS}{macroH_{V_{average}}} = (167 - 156) \cdot \frac{359}{170} = 23 \text{ MPa}$.

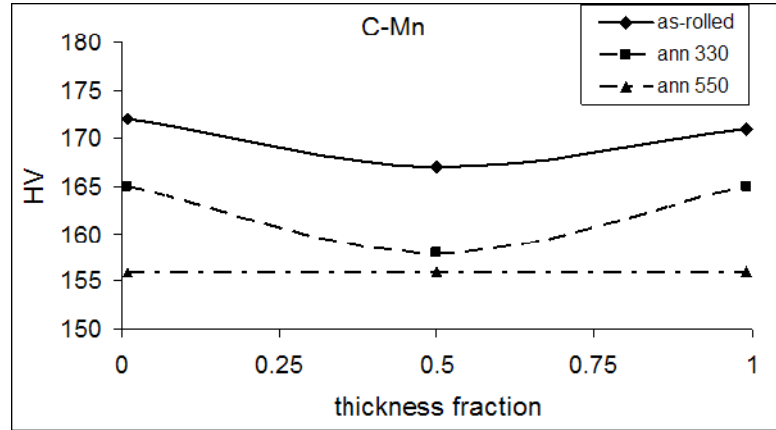


Figure 3.40 Macrohardness of the C-Mn steel in as-rolled and annealed at 330 °C and 550 °C for 30 min conditions

Work-hardening in the microalloyed steels can be assessed using the long range work-hardening theory:

$$\Delta\sigma_{wh} = \frac{\alpha}{2\pi} Gb\sqrt{\rho},$$

where $\alpha = 0.5$ – constant, $G = 85000 \text{ MPa}$ is shear modulus, $b = 0.286 \text{ nm}$ is Burgers vector and ρ is the dislocation density in m^{-2} .

Dislocation density at the sub-surface position of the C-Nb steel plate was not measured. However, the similarity of deformation schedules for the C-Nb and C-Nb-V steel plates [146] allows the same ratio between the mid-thickness and sub-surface dislocation densities to be assumed for both steels. The calculation gave $0.7 \times 10^{14} \text{ m}^{-2}$ for the dislocation density at the C-Nb steel plate sub-surface. Substitution of the dislocation densities, measured with TEM, gives the work-hardening increment

at the C-Nb steel plate sub-surface

$$\Delta\sigma_{wh}^{C-Nb} = \frac{0.5}{2 \cdot 3.14} \cdot 85000 \cdot 2.86 \cdot 10^{-10} \cdot \sqrt{0.7 \cdot 10^{14}} = 16 \text{ MPa},$$

at the C-Nb steel plate mid-thickness

$$\Delta\sigma_{wh}^{C-Nb} = \frac{0.5}{2 \cdot 3.14} \cdot 85000 \cdot 2.86 \cdot 10^{-10} \cdot \sqrt{2.3 \cdot 10^{14}} = 29 \text{ MPa},$$

at the C-Nb-V steel plate sub-surface

$$\Delta\sigma_{wh}^{C-Nb-V} = \frac{0.5}{2 \cdot 3.14} \cdot 85000 \cdot 2.86 \cdot 10^{-10} \cdot \sqrt{1.2 \cdot 10^{14}} = 21 \text{ MPa}.$$

at the C-Nb-V steel plate mid-thickness

$$\Delta\sigma_{wh}^{C-Nb-V} = \frac{0.5}{2 \cdot 3.14} \cdot 85000 \cdot 2.86 \cdot 10^{-10} \cdot \sqrt{4.0 \cdot 10^{14}} = 39 \text{ MPa}.$$

Precipitation strengthening in the microalloyed steels can be assessed with the Gladman equation [71]

$$\Delta\sigma_{ps} = \frac{10.8\sqrt{f}}{X} \ln\left(\frac{X}{6.125 \cdot 10^{-4}}\right),$$

where f is the particle volume fraction and X is the particle diameter in μm .

Substitution of the larger than 50 nm particle average diameter and volume fraction, measured using SEM, gives:

at the C-Nb steel plate sub-surface

$$\Delta\sigma_{psl}^{C-Nb} = \frac{10.8\sqrt{0.00006}}{0.089} \ln\left(\frac{0.089}{6.125 \cdot 10^{-4}}\right) = 5 \text{ MPa},$$

at the C-Nb steel plate mid-thickness

$$\Delta\sigma_{psl}^{C-Nb} = \frac{10.8\sqrt{0.0005}}{0.131} \ln\left(\frac{0.131}{6.125 \cdot 10^{-4}}\right) = 10 \text{ MPa},$$

at the C-Nb-V steel plate sub-surface

$$\Delta\sigma_{psl}^{C-Nb-V} = \frac{10.8\sqrt{0.000407}}{0.068} \ln\left(\frac{0.068}{6.125 \cdot 10^{-4}}\right) = 15 \text{ MPa}.$$

at the C-Nb-V steel plate mid-thickness

$$\Delta\sigma_{psl}^{C-Nb-V} = \frac{10.8\sqrt{0.000422}}{0.068} \ln\left(\frac{0.068}{6.125 \cdot 10^{-4}}\right) = 15 \text{ MPa}.$$

Measurements of the < 50 nm particle volume fraction at the C-Nb steel plate mid-thickness showed a good agreement with the Thermo-Calc calculated average value of the

carbo-nitride phase volume fraction. Based on this a uniform distribution of < 50 nm particles across the C-Nb steel plate thickness was assumed. Thus, substitution of the 12 - 50 nm particle average diameter and volume fraction, measured using TEM, gives:

at the C-Nb steel plate sub-surface and mid-thickness

$$\Delta\sigma_{ps2}^{C-Nb} = \frac{10.8\sqrt{0.00011}}{0.0197} \ln\left(\frac{0.0197}{6.125 \cdot 10^{-4}}\right) = 20 \text{ MPa},$$

at the C-Nb-V steel plate sub-surface

$$\Delta\sigma_{ps2}^{C-Nb-V} = \frac{10.8\sqrt{0.00138}}{0.018} \ln\left(\frac{0.018}{6.125 \cdot 10^{-4}}\right) = 75 \text{ MPa},$$

at the C-Nb-V steel plate mid-thickness

$$\Delta\sigma_{ps2}^{C-Nb-V} = \frac{10.8\sqrt{0.00076}}{0.0193} \ln\left(\frac{0.0193}{6.125 \cdot 10^{-4}}\right) = 53 \text{ MPa}.$$

As seen from the Table 3.12, theoretical values of the yield stress, calculated on the basis of the measured microstructure characteristics, give a reasonably good correspondence with the measured values of the yield stress, which indicates that the main contributing factors to strength are being considered. However, a discrepancy between the calculated and measured values of the yield stress increases with an increase in microalloying element content. Obviously, not all the dislocations and particles equally contribute to strengthening via dislocation-particle interaction. However this requires further investigation.

Table 3.12 Components of the predicted and the measured yield stress for the studied steels in as-rolled condition, MPa

Steel grade		Calculated											Measured		Accuracy, %	
		grain size		solid solution	work- hardening		precipitates				total		this work			Corus
							50 + nm		12-50 nm							
C-Mn	sub- surface	327	323	10	34	29	-	-	-	-	371	361	-		359	0.5
	mid- thickness	318			23		-		-		351					
C-Nb	sub- surface	452	436	28	16	23	5	8	20	20	521	514		483	487	5.5
	mid- thickness	419			29		10		20		506		480			
C-Nb-V	sub- surface	489	461	51	21	30	15	15	75	64	651	618		489	557	10.9
	mid- thickness	427			39		15		53		585		487			

4. MECHANICAL PROPERTY CHANGE WITH COLD DEFORMATION

4.1 Mechanical properties during unidirectional deformation

The strength of the microalloyed steels was studied in the as-rolled and annealed conditions to correlate any property change to microstructural changes. In addition differential scanning calorimetry (DSC) was carried out to assess any change in stored energy due to cold deformation. The DSC data in the 200 – 400 °C temperature range allows a qualitative and quantitative assessment of the mobile dislocation content, which influences strength levels and work-hardening rate. As the microstructure varies across plate thickness, mechanical properties were measured separately for the mid-thickness position (using samples of 4.5 mm diameter machined from the plate mid-thickness position) and as an average through plate thickness (using samples of 10 mm diameter, which include the plate sub-surface material).

Yield stress analysis

The average compressive yield stress measured in the as-rolled steels using plate mid-thickness samples corresponds to the yield stress measured using through-thickness samples, which take into account plate sub-surface (Table 4.1). After annealing the total yield stress and the mid-thickness yield stress in the C-Nb steel decrease, due to dislocation annihilation. However, in the C-Nb-V steel, the total yield stress does not show any change and the mid-thickness yield stress increases. Obviously, an addition to the yield stress from Cu-rich particle coarsening at the C-Nb-V plate mid-thickness position is prevailing over the yield stress drop due to dislocation annihilation.

Table 4.1 The average yield stress and macrohardness

Steel grade	Macrohardness		Yield stress, MPa	
	Mid-thickness	Total	Mid-thickness	Total
C-Nb as-rolled	193	192	480	483
C-Nb ann 550 °C	178	178	476	469
C-Nb-V as-rolled	209	200	487	489
C-Nb-V ann 400 °C	186	186	508	not measured
C-Nb-V ann 550 °C	187	187	499	487

To support the yield stress development with annealing, the macrohardness change with annealing was studied. As seen from Figure 4.1, the macrohardness in the C-Mn steel steadily decreases both at the sub-surface and mid-thickness positions with annealing temperature increase, due to the dislocation annihilation. In the alloyed steels dislocation movement is retarded by the microalloying element particles, so in these steels hardness decrease is not observed for heating to less than 350 °C. In the C-Nb-V steel the macrohardness at the mid-thickness position shows a minimum at 450 °C and then is increasing with an increase in annealing temperature up to 550 °C. At the sub-surface position the hardness value remains constant in the 450–550 °C annealing temperature range (Figure 4.1, c). This is due to the Cu-rich particle growth and precipitation of new CuS particles. At the mid-thickness position, where the Cu-rich particles are in majority, the hardness growth due to precipitation overcomes a decrease in hardness due to dislocation annihilation. At the sub-surface position, where the Cu-rich particles are in minority, the hardness growth due to precipitation is covered by the hardness drop due to dislocation annihilation, and the resulting measured value remains constant. With an increase in annealing time, from 30 min. to 8 hours, hardness increases both at the sub-surface and mid-thickness, as more particles precipitate. The average macrohardness drop with annealing temperature decreases with an increase in alloying (Figure 4.1, d). This corresponds to the observed behaviour in yield stress.

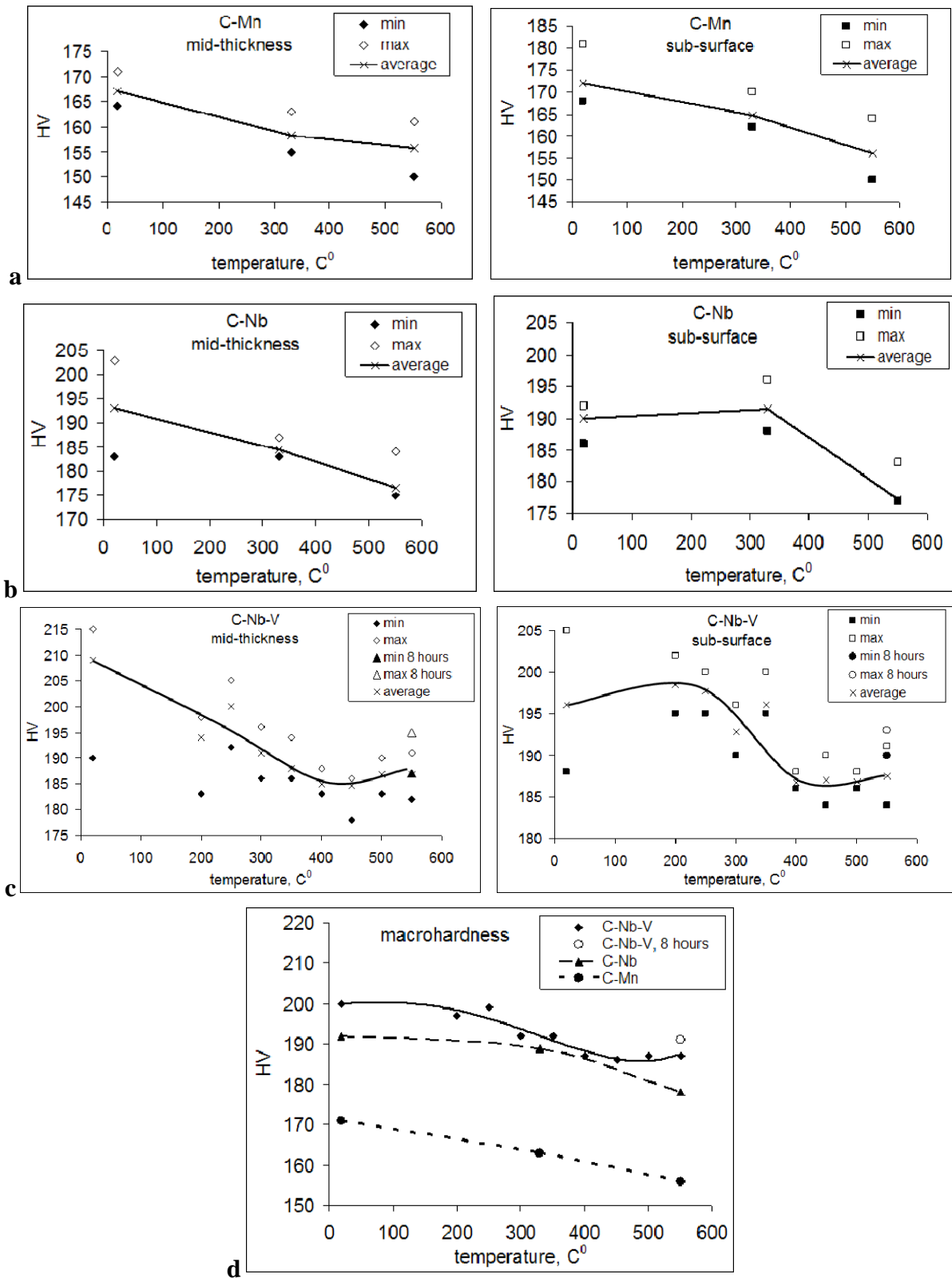


Figure 4.1 Macrohardness change with annealing temperature at the plate mid-thickness and sub-surface positions for the (a) C-Mn, (b) C-Nb and (c) C-Nb-V steels; (d) average macrohardness change with annealing

Work-hardening behaviour

In the initially as-rolled steels the stress-strain curve shape was not observed to depend on steel chemistry: the yield point is followed by work-hardening (Figure 4.2,a,b). Within the applied strain range it is possible to distinguish two stages of work-hardening: the first stage is up to 3 % strain, with a lower work-hardening rate, and the second stage is above 3 %, with an increased work-hardening rate. According to the long range work-hardening theory, during the first stage of work-hardening slip occurs on favourable crystal planes and during the second stage on all the possible slip planes, when favourable slip planes become blocked by pile-ups [6]. A decrease in the mobile dislocation density and the formation of pile-ups during deformation of the as-rolled steels is supported by the DSC measured values of stored energy decreasing as strain increases. The energy released during DSC heating within the 200 – 400 °C temperature range is due to dislocation annihilation. Mobile dislocations annihilate more easily than the dislocations blocked in pile-ups. So, a decrease in the released energy with strain is due to a decrease in the mobile dislocation density with strain.

In contrast, the stress-strain curves of the initially annealed steels show a Lüders strain region, a part of the stress-strain curve parallel to the strain axis where yielding occurs without stress increase (Figure 4.2, c, d). This can be explained by the following: as a result of annealing the number of pile-ups and the total dislocation density decreases. During subsequent cold deformation the dislocations, left free after annealing, glide without stress increase until they meet new obstacles. As a result of dislocation interaction with other dislocations and particles the dislocation motion might be retarded. However, new mobile dislocations are generated by the dislocation sources, and easy glide continues. This can be supported by the DSC curves increasing with strain increase. As the mobile dislocation density increases with strain, the released energy during DSC heating increases as a result of the mobile dislocation annihilation. Higher Lüders strain in the C-Nb-V steel compared to the

C-Nb steel for the same annealing conditions can be related to a greater number of possible dislocation sources in the C-Nb-V steel. As the particle number density and the dislocation density are higher in the C-Nb-V steel, moving dislocations can be more easily stopped by the obstacles and become dislocation generation sources.

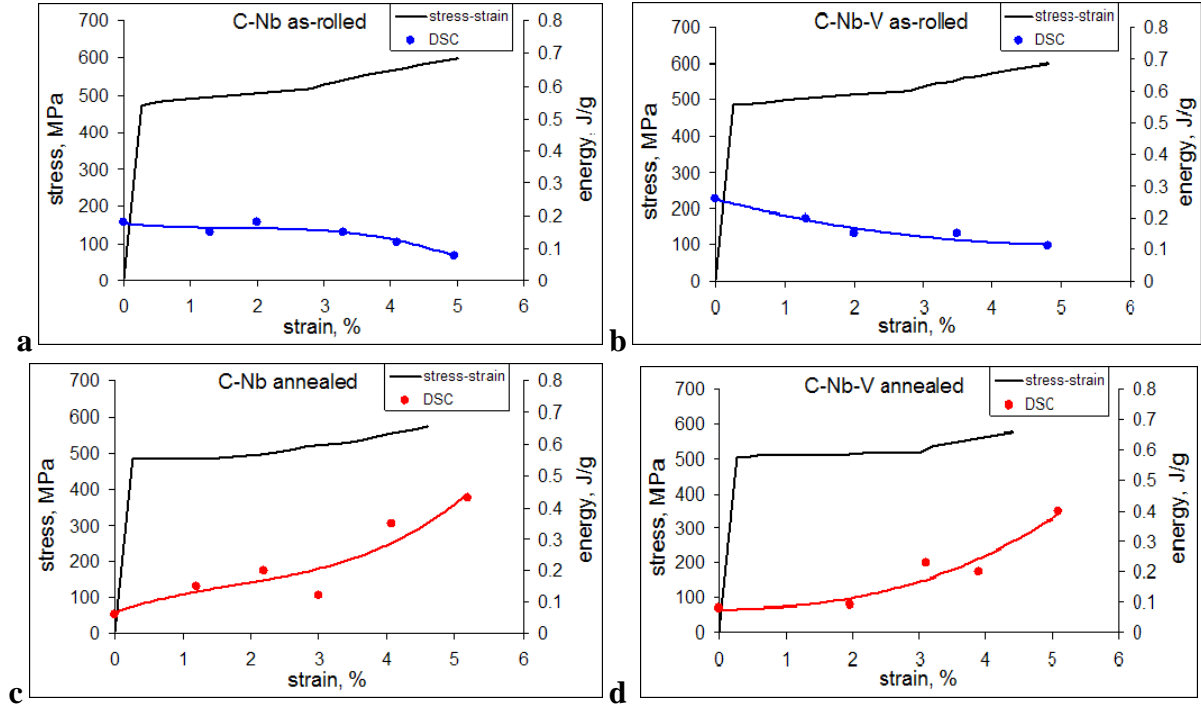


Figure 4.2 Plate mid-thickness position stress-strain curves with the corresponding stored energy data, measured using DSC from peaks in the 200 – 400 °C range, for the (a) C-Nb and (b) C-Nb-V steels in the as-rolled initial condition; and (c) C-Nb and (d) C-Nb-V steels in the annealed at 550 °C for 30 min. condition

The stress-strain experimental curves can be approximated by a power equation:

$$\sigma = K\varepsilon^n, \quad (4.1)$$

where σ is stress, ε is strain, K is a work-hardening coefficient and n is work-hardening exponent.

Approximation with equation (4.1) gave for the C-Nb as-rolled steel (Figure 4.3):

$$\sigma = 490\varepsilon^{0.06} \text{ - below 3 \% strain}$$

and

$$\sigma = 410\varepsilon^{0.24} \text{ - above 3 \% strain;}$$

for the C-Nb-V as-rolled steel

$$\sigma = 490\varepsilon^{0.06} \text{ - below 3 \% strain}$$

and

$$\sigma = 410\varepsilon^{0.25} \text{ - above 3 \% strain.}$$

For the studied steels in the as-rolled condition the work-hardening exponents above 3% strain, 0.24 in the C-Nb and 0.25 C-Nb-V steel, corresponds to previously obtained data for the same steel grades [146].

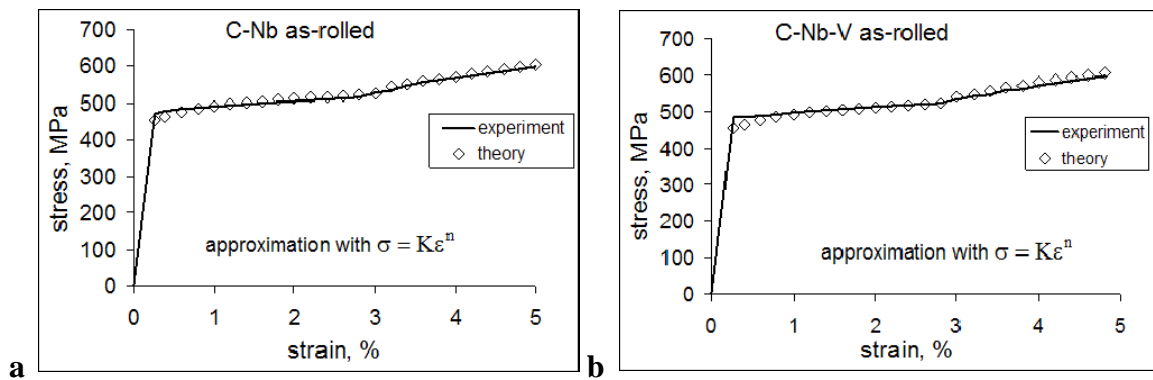


Figure 4.3 Theoretical calculation of the stress-strain curves of the (a) C-Nb and (b) C-Nb-V steel with the equation $\sigma = K\varepsilon^n$

The discrepancy between the measured value and the data calculated from equation (4.1) may reach 4 % below 1 % strain. A better fit for strains below 1 % may be given by the following model:

$$\sigma = \sigma_0 + a\varepsilon^b, \quad (4.2)$$

where σ_0 is the initial yield stress.

Approximation with the equation (4.2) gave for the C-Nb as-rolled steel (Figure 4.4):

$$\sigma = 472 + 18\varepsilon^{0.80} \text{ - below 3 \% strain}$$

and

$$\sigma = 472 + 18\varepsilon^{1.18} \text{ - above 3 \% strain;}$$

for the C-Nb-V as-rolled steel

$$\sigma = 484 + 15\varepsilon^{0.90} \text{ - below 3 \% strain}$$

and

$$\sigma = 484 + 15\varepsilon^{1.28} \text{ - above 3\% strain.}$$

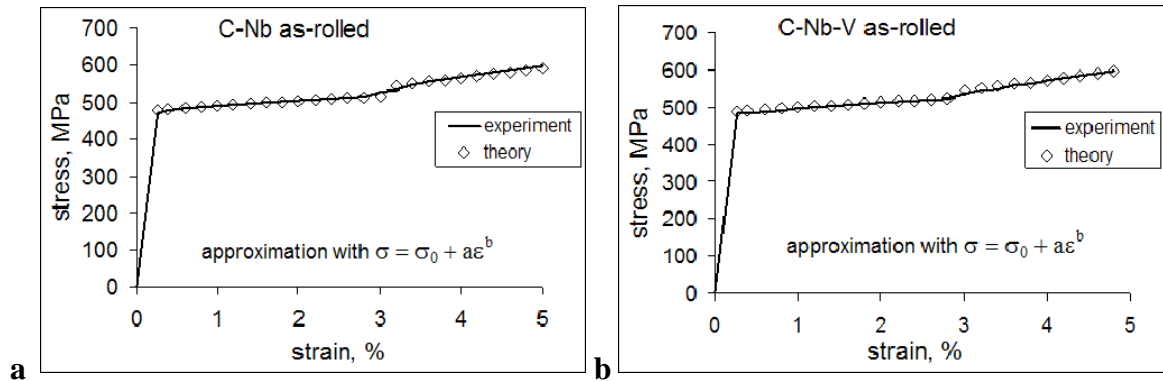


Figure 4.4 Theoretical calculation of the stress-strain curves of the (a) C-Nb and (b) C-Nb-V steels with the equation $\sigma = \sigma_0 + a\varepsilon^b$

Work-hardening exponent dependence on steel chemistry was not observed in the as-rolled steels (Table 4.2). However, alloying influences the work-hardening rate change with annealing. In the C-Nb steel the work-hardening exponent decreases with annealing due to dislocation annihilation. In the C-Nb-V steel the work-hardening exponent also decreases after annealing at 400 °C due to dislocation annihilation. However, with annealing temperature increase to 550 °C the work-hardening exponent increases due to particle growth, namely an increase in 12-50 nm particle number density. An increase in the work-hardening exponent from the C-Nb to the C-Nb-V steel, annealed at 550 °C, can be related to the particle number density increase with an increase in the microalloying element content.

Analysis of the work-hardening behaviour dependence on the microstructural parameters has shown that with an increase in dislocation density and particle number density the work-hardening exponent increases, Figure 4.5, a, and the work-hardening coefficient decreases, Figure 4.5, b. Relative influence of the dislocation density on the parameters of work-hardening was observed to be 3 – 4 times higher than that of the particle number density.

Table 4.2 The measured yield stress and work-hardening exponent for the plate mid-thickness material

Steel grade	Yield stress, MPa	Work-hardening exponent		
		stage 0	stage I	stage II
C-Nb as-rolled	480	-	n = 0.06 < 3 %	n = 0.24 3% <
C-Nb ann 550 °C	476	n = 0 Lüders strain < 1.5 %	n = 0.15 1.5 % <	
C-Nb-V as-rolled	487	-	n = 0.06 < 3 %	n = 0.25 3 % <
C-Nb-V ann 400 °C	508	n = 0 Lüders strain < 0.8 %	n = 0.04 0.8 - 2.5 %	n = 0.15 2.5 % <
C-Nb-V ann 550 °C	499	n = 0 Lüders strain < 3 %	n = 0.28 3 % <	

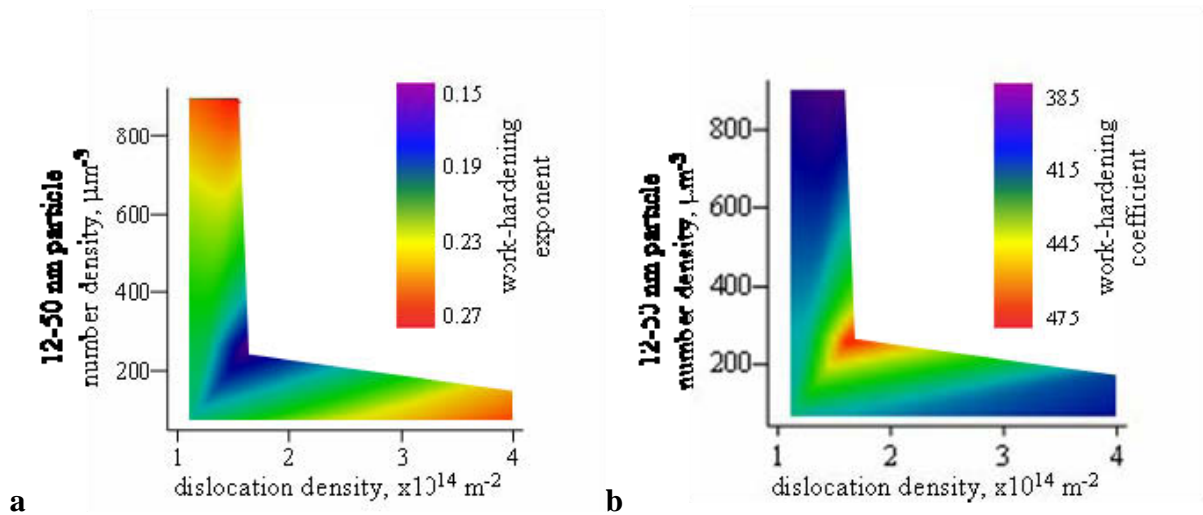


Figure 4.5 (a) The work-hardening exponent and (b) work-hardening coefficient dependence on dislocation density and particle number density for above 3 % forward strain

4.2 Mechanical properties during reverse deformation

The strength change during reverse cold deformation was studied for the microalloyed steels in the as-rolled and annealed initial conditions. The stress-strain curves were obtained during compression-tension experiments using samples machined from the plate mid-

thickness area. The yield stress change during reverse deformation was assessed using the Bauschinger stress parameter. An understanding of the dependence of the Bauschinger stress parameter on the microstructure was developed via correlation of the particle number density, dislocation density and the yield stress.

Stress-strain curve

The reverse stress-strain curves, if plotted in the direction of positive strain, show lower stress values than the corresponding forward stress-strain curve due to work-softening (Figures 4.6, 4.7). A reverse stress-strain curve can be roughly divided by strain into three regions: straight lined area of elastic deformation to the yield point, a region of high work-hardening rate and a region of low work-hardening rate. If unloading after forward pre-strain occurs from the region of low work-hardening rate or Lüders strain, i.e. below 2.8 % plastic pre-strain in the studied steels, a region of easy flow at a constant or decreasing stress is present on the reverse stress-strain curve. This type of behaviour during reverse shear strain after forward shear pre-strain of $\gamma = 0.26$ has been observed by Rauch et al. in fcc [34] and bcc [31] materials. In fcc materials [34] the stagnation of the work-hardening rate during reverse deformation was explained by the dissolution of the dislocation sub-structure during reverse loading, which, according to Hasegawa et al. [29], may be accompanied by a dislocation density decrease. However, in a later work by Vincze et al. [31] the same behaviour was also observed for homogeneous dislocation structures, and the main reason mentioned was the single dislocation-obstacle interaction process. The microstructure investigation, carried out in the present work, supports the latter explanation related to dislocation-obstacle interaction. Thus in the studied steels:

1. no dislocation cell structure was observed, but a plateau of constant or slightly decreasing stress, on the reverse stress-strain curve, is present;

2. the plateau length and depth depend on pre-strain, although the dislocation structure type is not expected to change with pre-strain in the studied strain range;
3. the plateau length and depth changes with annealing, which leads to a decrease in dislocation density and an increase in precipitate number density in the effective particle diameter range (12 – 50 nm), but does not influence significantly the dislocation structure type.

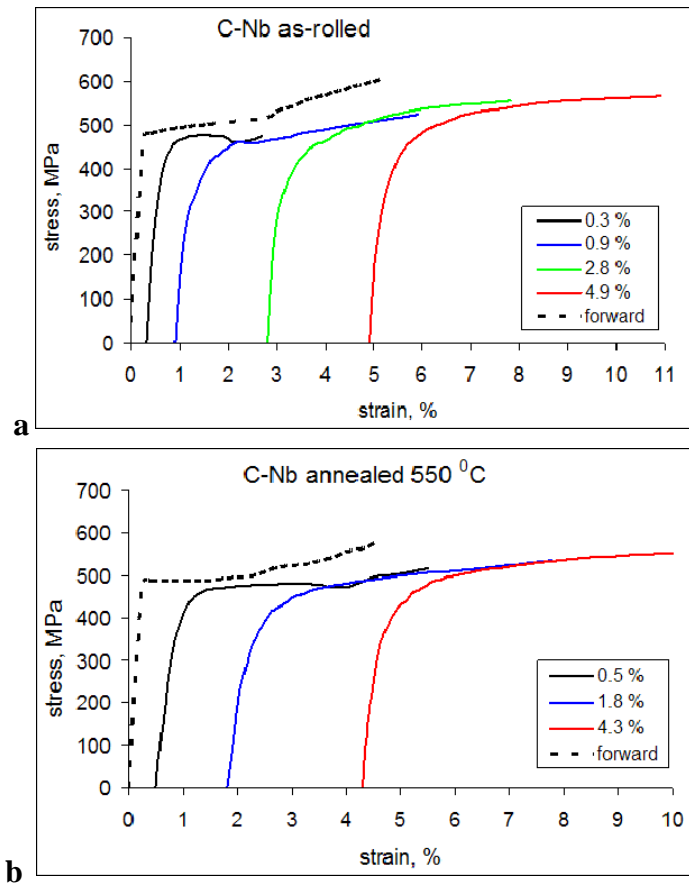


Figure 4.6 The reverse stress-strain curves of the C-Nb steel in (a) as-rolled and (b) annealed initial conditions for different levels of forward pre-strain

The observations made are not enough for a quantitative analysis of the plateau development with dislocation structure. However, from Figures 4.6 and 4.7 it can be seen that the plateau length decreases with an increase in pre-strain. With a decrease in dislocation density, due to annealing, the plateau length increases (compare the traces for C-Nb-V as-rolled and annealed at 400 °C, and for C-Nb as-rolled and annealed at 550 °C). With an

increase in the particle number density, as a result of annealing temperature increase and precipitation of new particles, the plateau length decreases (compare the traces for C-Nb-V annealed at 400 °C and at 550 °C). This means that, with an increase in the number of potential dislocation-particle interaction sites, the plateau length on the reverse stress-strain curve decreases and finally disappears.

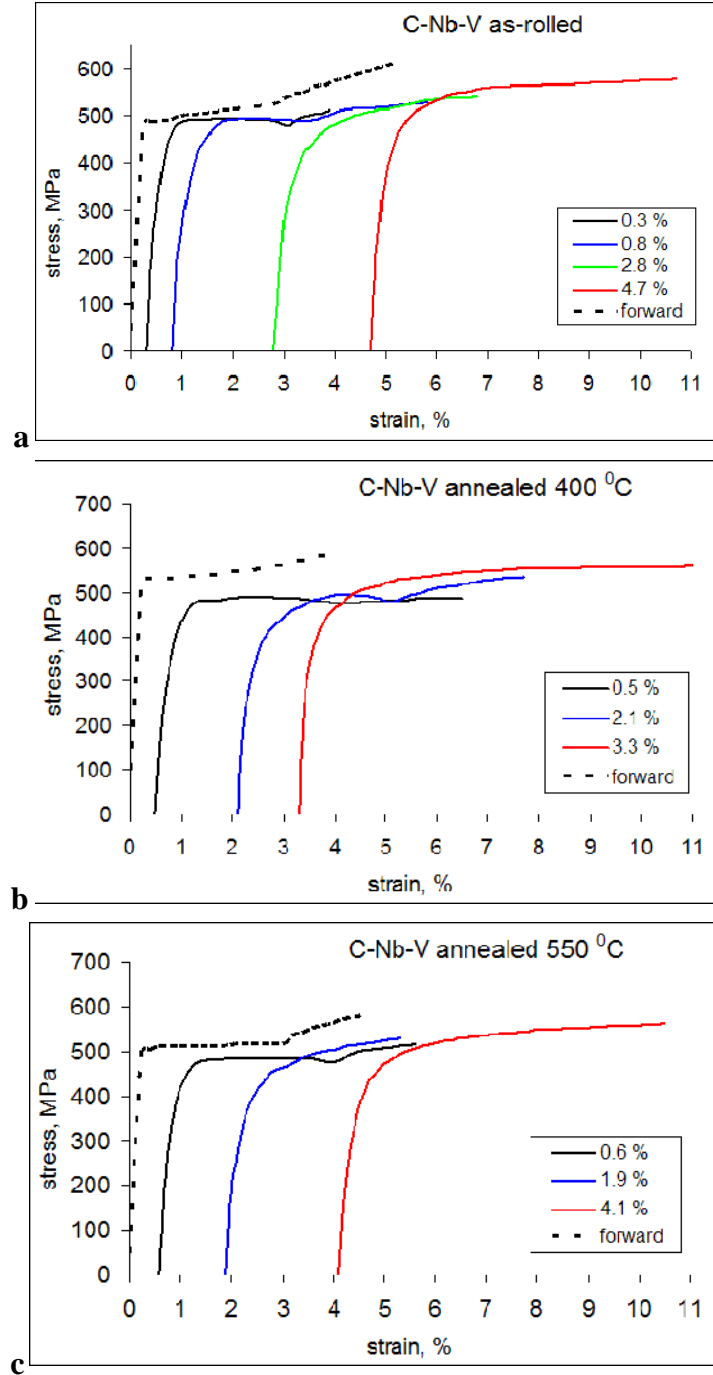


Figure 4.7 The reverse stress-strain curves of the C-Nb-V steel in (a) as-rolled and (b),(c) annealed initial conditions for different levels of forward pre-strain

The yield stress

The reverse stress-strain curve quantitative analysis has shown that the yield stress:

- decreases ($\beta_{\sigma 1}$ increases) with an increase in forward pre-strain, which qualitatively corresponds to the earlier observed dependence of the Bauschinger stress parameter on pre-strain (Figure 4.8);
- decreases with an increase in microalloying element content;
- increases ($\beta_{\sigma 1}$ decreases) with annealing.

The magnitude of the reverse yield stress value can be explained by the dislocation-particle interaction during forward pre-strain. An increase in the number of dislocation-particle interaction sites leads to an increase in the back stress and the yield stress during reverse strain decreases by the value of the back stress. The number of dislocation-particle interactions increases as a result of either the dislocation density or particle number density increasing. In the present study the dislocation density increases:

- with an increase in forward pre-strain,
- with an increase in initial work-hardening (compare the C-Nb and C-Nb-V steels in as-rolled condition),
- from the annealed to as-rolled condition (compare the C-Nb steel annealed at 550 °C and as-rolled and the C-Nb-V steel annealed at 400 °C and as-rolled conditions);

and the particle number density increases:

- with an increase in microalloying element content (compare the C-Nb and C-Nb-V steels in as-rolled condition),
- with particle precipitation (compare the C-Nb-V steel annealed at 400 °C and 550 °C).

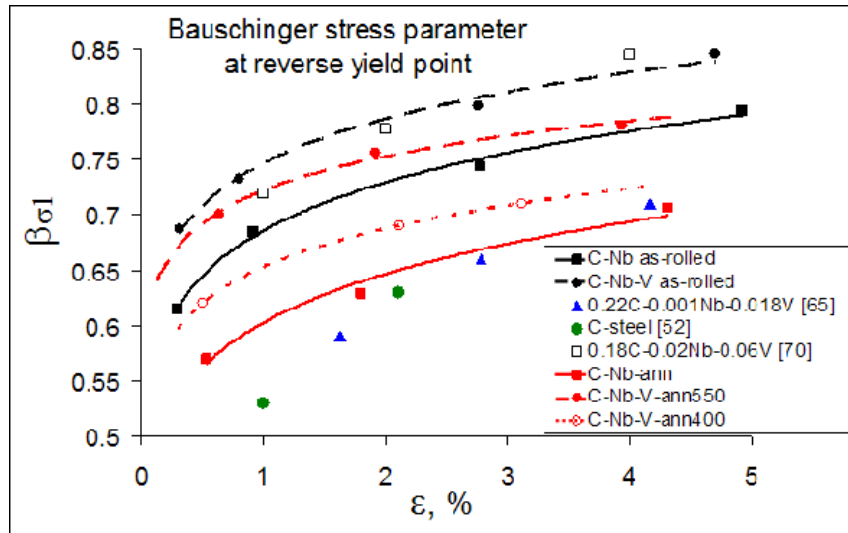


Figure 4.8 The Bauschinger stress parameter measured for the reverse yield point (approximately 0.1 % reverse strain)

Correlating the results of the microstructural investigation and the mechanical property study for the same material conditions, it is possible to obtain a quantitative dependence of the Bauschinger stress parameter on dislocation density and particle number density within the ranges studied in this work (Figure 4.9). Quantitative contribution of the dislocation density to the reverse yield stress drop is observed to be approximately 4.6 times higher than the particle number density contribution, i.e. a 2.7 times increase in the dislocation density brings about the same Bauschinger stress parameter increase as 12.5 times increase in the particle number density.

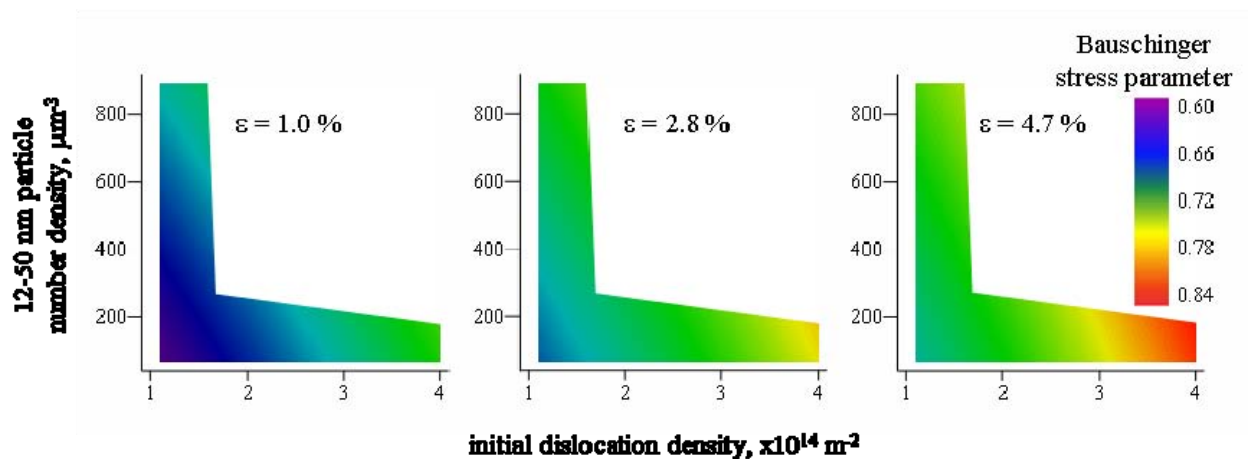


Figure 4.9 The Bauschinger stress parameter dependence on dislocation density and particle number density for 1.0 %, 2.8 % and 4.7 % forward pre-strain

The Bauschinger stress parameter measured at 0.5 % reverse strain reflects the yield stress change with work-hardening in the reverse direction (Figure 4.10). The higher alloyed steels show a faster return to their forward direction yield stress than the lower alloyed steels ($\beta_{0.5}$ decreases with an increase in alloying element content, Figure 4.10 and 4.11, a). This is in good agreement with literature data and can be explained by dislocation immobilization by particles during reverse slip leading to the work-hardening rate increasing. However, steels which are higher work-hardened in the forward direction show a slower return to their forward direction yield stress than the lower work-hardened steels ($\beta_{0.5}$ increases with pre-strain and decreases with annealing, Figures 4.10 and 4.11, b). A decrease in the reverse work-hardening rate with dislocation density increase during forward straining might be explained by dislocation pile-ups on the favourable slip planes leading to cross-slip, which is a reason for the work-hardening rate stagnation widely reported during unidirectional deformation [6].

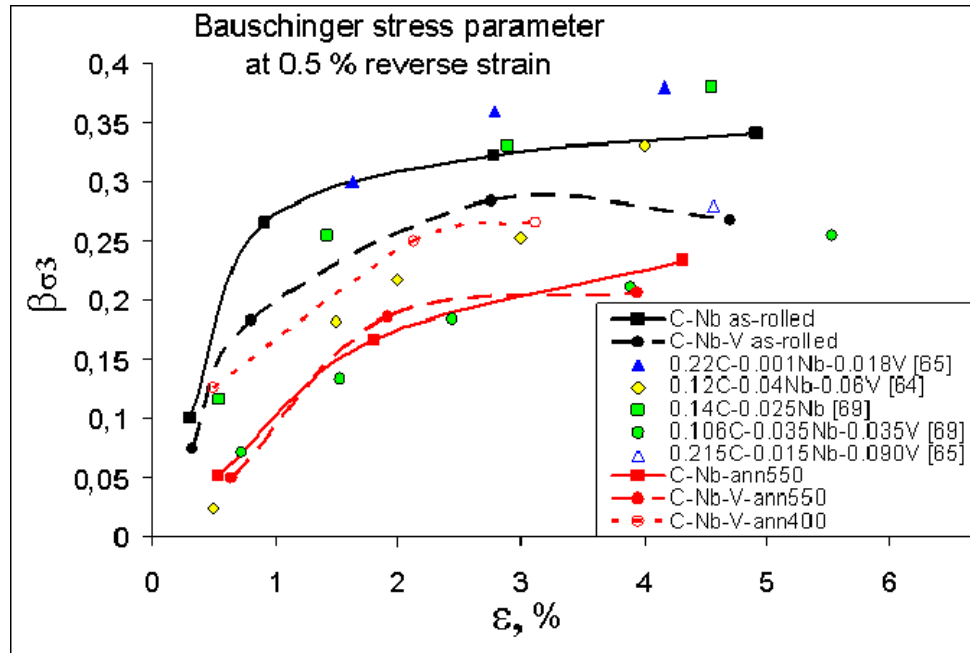


Figure 4.10 The Bauschinger stress parameter measured for 0.5 % reverse strain

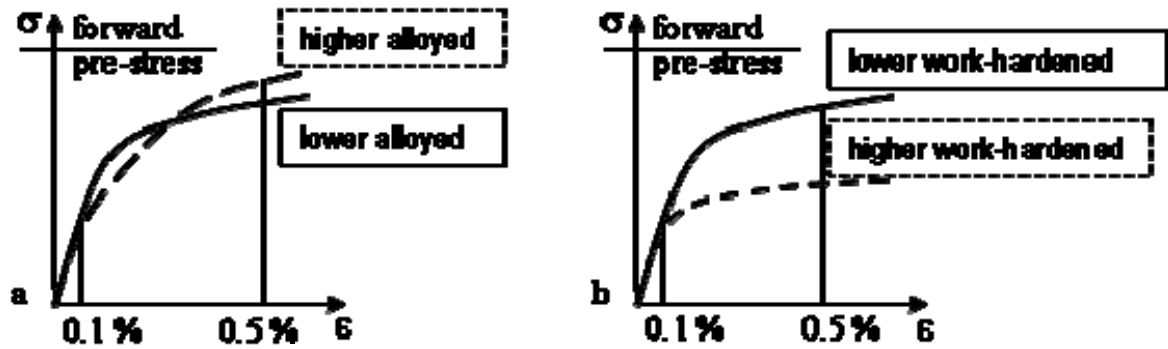


Figure 4.11 Schematic presentation of the reverse stress-strain curves on the basis of the obtained data for the Bauschinger stress parameters (Figures 4.8 and 4.10)

Work-hardening behaviour

Approximation of the reverse stress-strain curves, Figures 4.6 and 4.7, by the power equation $\sigma = K\epsilon^n$ has shown that the work-hardening exponent is independent, and the work-hardening coefficient is dependent, on pre-strain. For the “below 0.7 %” reverse strain range the work-hardening coefficient increases with an increase in forward pre-strain, after a minimum at 1 - 3 % pre-strain (Table 4.3, Figure 4.12, a). This minimum can be explained by the generation of new dislocations, free from obstacles, during the first stages of forward pre-straining, i.e. below 3 %, which facilitates slip during reverse deformation. With an increase in forward pre-strain the dislocation density and the number of dislocation-obstacle interaction sites increases significantly, which leads to the work-hardening coefficient in the reverse direction increasing. For the “above 0.7 %” reverse strain range the work-hardening coefficient steadily increases with an increase in forward pre-strain, due to the total increase in dislocation density (Figure 4.12, b).

Table 4.3 Approximate equations for the reverse stress-strain curves

Steel grade	Forward pre-strain, %	Reverse stress-strain curve approximation equation	
		below 0.7 %	0.7 – 5.0 %
C-Nb as-rolled	0.3	$560 \cdot \epsilon^{0.42}$	475 MPa
	0.9	$480 \cdot \epsilon^{0.42}$	$430 \cdot \epsilon^{0.11}$
	2.8	$500 \cdot \epsilon^{0.42}$	$460 \cdot \epsilon^{0.11}$
	4.9	$520 \cdot \epsilon^{0.42}$	$480 \cdot \epsilon^{0.11}$
C-Nb ann 550 °C	0.5	$530 \cdot \epsilon^{0.42}$	478 MPa
	1.8	$450 \cdot \epsilon^{0.42}$	$(425 \cdot \epsilon^{0.11} \text{ above } 4\%)$ $440 \cdot \epsilon^{0.11}$
	4.3	$510 \cdot \epsilon^{0.42}$	$465 \cdot \epsilon^{0.11}$
C-Nb-V as-rolled	0.3	$565 \cdot \epsilon^{0.36}$	487 MPa
	0.8	$525 \cdot \epsilon^{0.36}$	$(445 \cdot \epsilon^{0.09} \text{ above } 3\%)$ 497 MPa
	2.8	$505 \cdot \epsilon^{0.36}$	$(455 \cdot \epsilon^{0.09} \text{ above } 3\%)$ $473 \cdot \epsilon^{0.09}$
	4.7	$565 \cdot \epsilon^{0.36}$	$510 \cdot \epsilon^{0.09}$
C-Nb-V ann 400 °C	0.5	$530 \cdot \epsilon^{0.32}$	485 MPa
	2.1	$475 \cdot \epsilon^{0.32}$	$(425 \cdot \epsilon^{0.08} \text{ above } 4\%)$ $460 \cdot \epsilon^{0.08}$
	3.3	$530 \cdot \epsilon^{0.32}$	$493 \cdot \epsilon^{0.08}$
C-Nb-V ann 550 °C	0.6	$560 \cdot \epsilon^{0.39}$	490 MPa
	1.9	$500 \cdot \epsilon^{0.39}$	$(445 \cdot \epsilon^{0.09} \text{ above } 4\%)$ $465 \cdot \epsilon^{0.09}$
	4.1	$520 \cdot \epsilon^{0.39}$	$487 \cdot \epsilon^{0.09}$

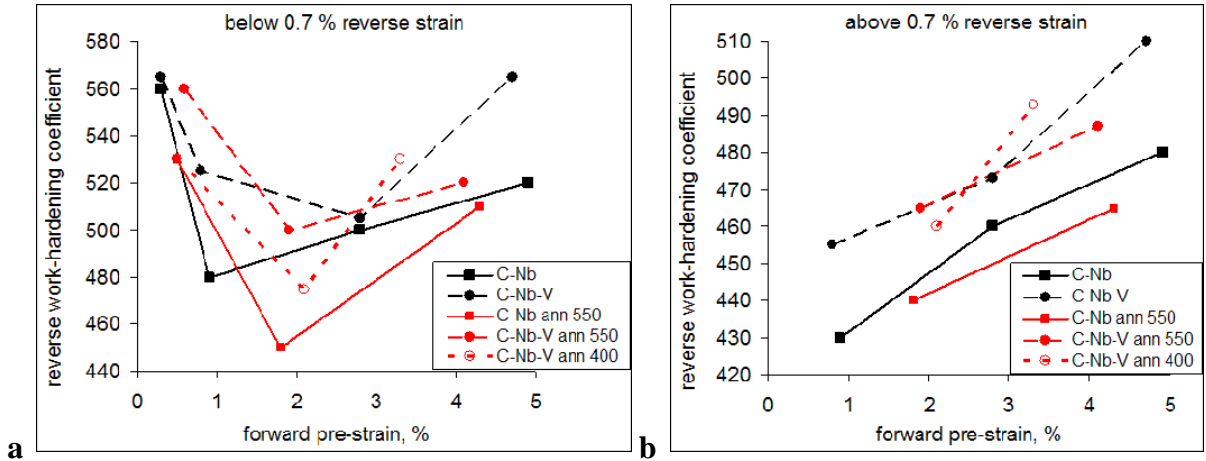


Figure 4.12 The reverse work-hardening coefficient for the (a) below 0.7 % and (b) above 0.7 % reverse strain

The work-hardening exponent decreases with an increase in microalloying element content, i.e. from the C-Nb to the C-Nb-V steel. This corresponds to the decrease in work-hardening exponent with an increase in steel strength observed earlier [50]. The work-hardening coefficient, for the same levels of pre-strain, is larger in the C-Nb-V steel compared to the C-Nb steel. This is due to a larger number of obstacles to the dislocation slip, i.e. dislocations and particles, in the C-Nb-V steel.

In the C-Nb steel, annealing at 550 °C did not affect the work-hardening exponent, although the work-hardening coefficient decreased due to dislocation annihilation. In the C-Nb-V steel both the work-hardening exponent and coefficient for the “below 0.7 %” reverse strain range decrease after annealing at 400 °C, due to dislocation annihilation. However, annealing at 550 °C led to both the work-hardening exponent and coefficient increasing, due to Cu-rich particle precipitation. For the “above 0.7 %” reverse strain range the work-hardening behaviour of the C-Nb-V steel did not change significantly with annealing. Obviously, the work-hardening rate stagnation due to dislocation annihilation was compensated by particle precipitation.

Analysis of the work-hardening behaviour dependence on the microstructural parameters has shown that, with an increase in dislocation density and particle number density, the work-

hardening exponent decreases, Figure 4.13, and the work-hardening coefficient increases, Figure 4.14. Relative influence of the dislocation density on the parameters of work-hardening was observed to be 3 – 4 times higher than the particle number density influence. In summary the effect of alloying and initial work-hardening on the work-hardening behaviour during reverse deformation will result in a lower work-hardened but more highly alloyed steel more quickly returning to its forward direction properties (see also C-Nb and C-Nb-V steels annealed at 550 °C on Figure 4.10).

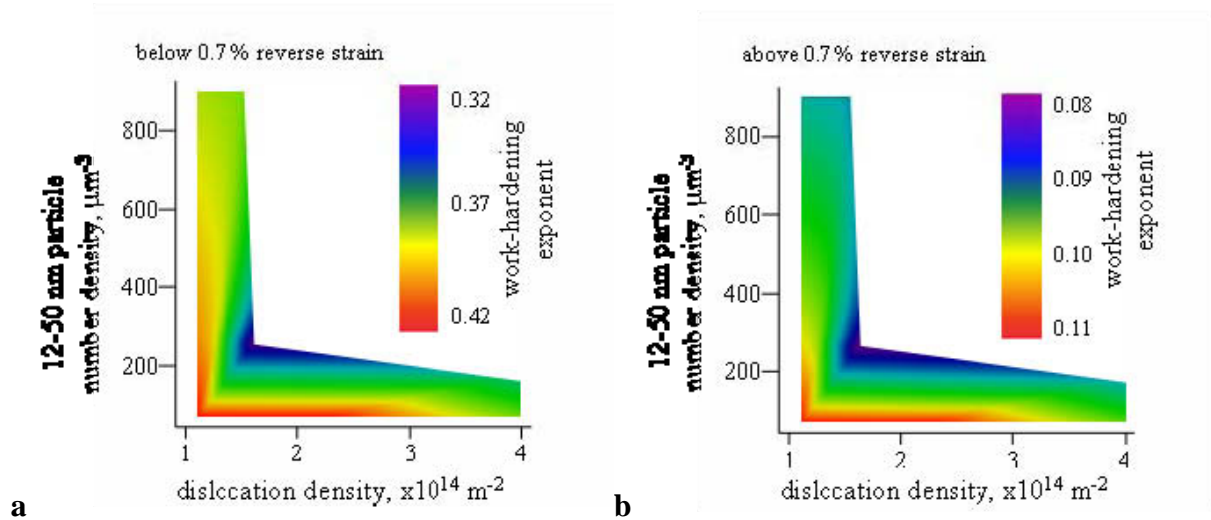


Figure 4.13 The work-hardening exponent dependence on the dislocation density and particle number density for the (a) below 0.7 % and (b) above 0.7 % reverse strain

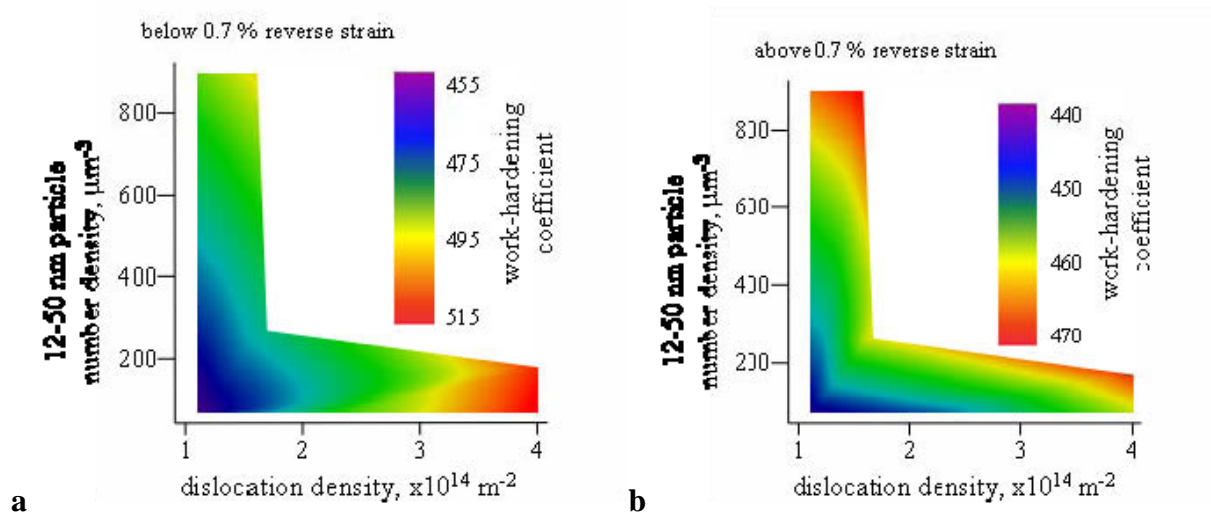


Figure 4.14 The work-hardening coefficient dependence on the dislocation density and particle number density for the (a) below 0.7 % and (b) above 0.7 % reverse strain after 2.0 % forward pre-strain

4.3 Theoretical assessment of property development during UOE pipe-forming

Using the obtained dependences of the work-hardening parameters on microstructure it should be possible to predict strength change during each stage of the UOE pipe forming process and, in particular, plate to pipe property change. An example discussed below shows the yield stress calculation for the area opposite to the weld during pipe forming of a 914 mm outside diameter 25 mm wall thickness pipe from the C-Nb-V steel (Figure 4.15). Property measurements for more than two half-cycle deformations, i.e. forward-reverse-forward and forward-reverse-forward-reverse, were not carried out in the present project. However, earlier research into low cycle fatigue of carbon steels [63, 153] shows that the stress hysteresis loop can be symmetric to the strain axis from the third half-cycle (Figure 4.16). This allows calculation of the strength change during U-ing using equations for forward work-hardening and during all other forming stages using equations for reverse work-hardening. The calculation is separately carried out for the inside and outside surfaces of the pipe wall, taking as initial conditions plate sub-surface microstructure parameters. As, during plate bending, the neutral layer is assumed to be at the plate mid-thickness, deformation at the mid-thickness, and relating property changes to it, is neglected during U-ing and O-ing stages. However, during “Killing” and Expansion the neutral layer deformation is taken into account, as these forming stages are performed as whole cross-section compression and whole cross-section tension respectively.

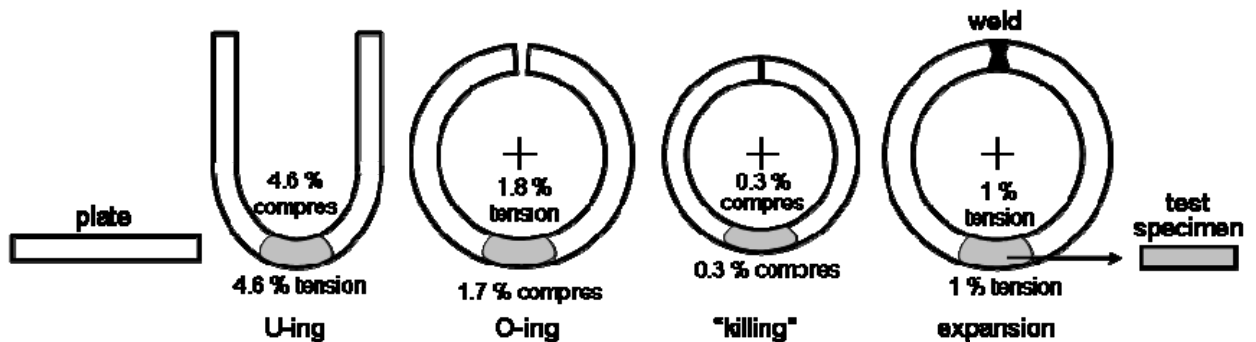


Figure 4.15 Strain development during the UOE forming of a 914 x 25 mm pipe (for strain calculation see section 1.6)

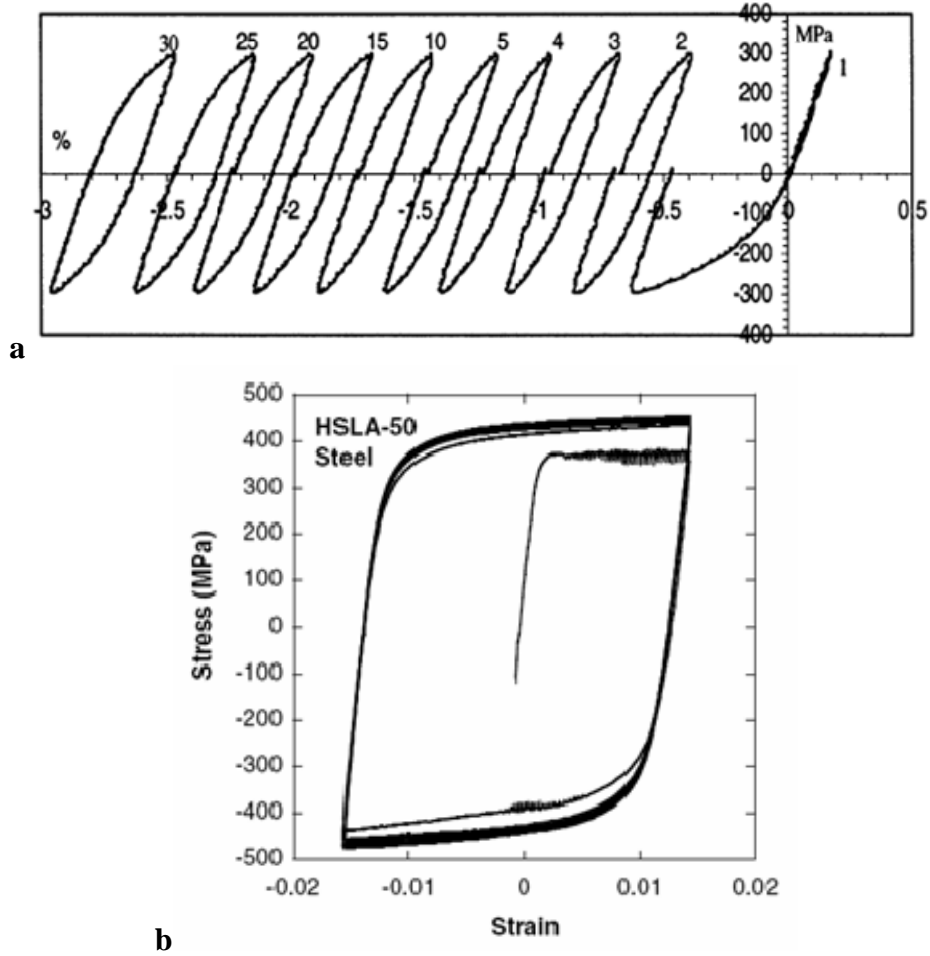


Figure 4.16 Low cycle fatigue stress-strain curves of (a) 0.47C-0.02Mo-0.19Cu-0.09Cr [153] and (b) HSLA-50 steels [63]

U-ing stage

Initial conditions for the inside and outside surfaces: forward strain 4.6 %, dislocation density $1.22 \times 10^{14} \text{ m}^{-2}$, particle number density $208 \text{ } \mu\text{m}^{-3}$. On the basis of the forward work-hardening exponent and work-hardening coefficient dependences on dislocation density and particle number density, Figure 4.5, the stress-strain curve approximation equation can be found as follows:

$$\sigma = 430 \cdot \epsilon^{0.21}.$$

Substitution of strain will give the yield stress for the inside and outside surfaces:

$$\sigma_{\text{in(out)}} = 430 \cdot 4.6^{0.21} = 592 \text{ MPa}.$$

Dislocation density, ρ , increase during U-ing can be calculated using literature data [28]

of the dislocation density dependence on strain (Figure 4.17):

$$\rho_U = (1.22 + 4.6 \cdot 0.15) \times 10^{14} = 1.91 \times 10^{14} \text{ m}^{-2}$$

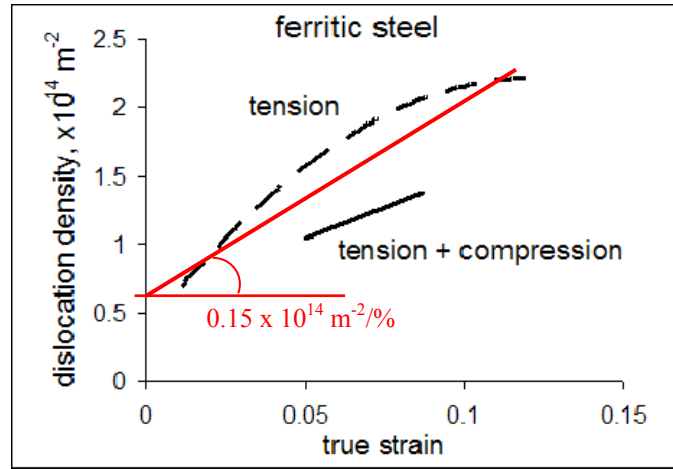


Figure 4.17 Dislocation density dependence on strain, for a ferritic steel 0.16C-1.43Mn-0.41Si [28], approximated by a straight line

O-ing stage

Initial conditions: forward pre-strain 4.6 %, reverse strain 1.8% (inside surface) and 1.7 % (outside surface), dislocation density $1.91 \times 10^{14} \text{ m}^{-2}$, particle number density $208 \mu\text{m}^{-3}$. Using the obtained dependences of the reverse work-hardening exponent and work-hardening coefficient on dislocation density and particle number density, Figures 4.12 - 4.14, b, for 4.6 % pre-strain and more than 0.7 % reverse strain the stress-strain curve approximation equation will be as follows:

$$\sigma = 484 \cdot \epsilon^{0.09}.$$

Substitution of strain will give the yield stress:

for the inside surface $\sigma_{\text{in}} = 484 \cdot 1.8^{0.09} = 510 \text{ MPa}$,

and for the outside surface $\sigma_{\text{out}} = 484 \cdot 1.7^{0.09} = 508 \text{ MPa}$.

From Figure 4.17 it is seen, that for 4.6 % forward pre-strain the dislocation density decrease during reverse straining is about 1.4 times. So, the dislocation density at the end of the O-ing stage will be:

$$\rho_0 = 1.91 \times 10^{14} / 1.4 = 1.36 \times 10^{14} \text{ m}^{-2}.$$

“Killing” stage

Initial conditions for the inside surface: forward pre-strain 1.8 %, reverse strain 0.3%, dislocation density $1.36 \times 10^{14} \text{ m}^{-2}$, particle number density $208 \mu\text{m}^{-3}$. From Figures 4.12-4.14,a, for 1.8 % pre-strain and less than 0.7 % reverse strain the stress-strain curve approximation equation will be as follows:

$$\sigma = 474 \cdot \varepsilon^{0.38}.$$

Substitution of strain will give the yield stress for the inside surface:

$$\sigma_{\text{in}} = 474 \cdot 0.3^{0.38} = 300 \text{ MPa}.$$

Initial conditions for the outside surface: forward pre-strain 1.7 %, forward strain 0.3%, dislocation density $1.36 \times 10^{14} \text{ m}^{-2}$, particle number density $208 \mu\text{m}^{-3}$. As for the outside surface there is no deformation direction change, from the O-ing to the “Killing” stage, the yield stress should be calculated as forward work-hardening, using the equation for the O-ing stage:

$$\sigma = 484 \cdot \varepsilon^{0.09}.$$

Substitution of the total strain after “Killing”, i.e. $1.7 + 0.3 = 2.0$ %, will give the yield stress for the outside surface:

$$\sigma_{\text{out}} = 484 \cdot 2.0^{0.09} = 515 \text{ MPa}.$$

Initial conditions for the plate mid-thickness: forward strain 0.3 %, dislocation density $4.0 \times 10^{14} \text{ m}^{-2}$, particle number density $180 \mu\text{m}^{-3}$. Addition to the yield stress due to work-hardening can be calculated according to the approximation equation for the C-Nb-V steel plate mid-thickness:

$$\Delta\sigma = 15 \cdot \varepsilon^{0.9}.$$

Substitution of strain will give the yield stress at the pipe wall mid-thickness:

$$\sigma_c = 490 + 15 \cdot 0.3^{0.9} = 495 \text{ MPa}$$

Due to small absolute values of deformation the dislocation density change during “Killing” can be neglected for the subsequent calculation.

Expansion

Initial conditions for the inside surface: forward pre-strain 0.3 %, reverse strain 1.0 %, dislocation density $1.36 \times 10^{14} \text{ m}^{-2}$, particle number density $208 \text{ } \mu\text{m}^{-3}$. As a result of very low forward pre-strain, 0.3 %, it is possible to expect a region of Lüders strain at the inside surface up to 3 % reverse deformation. So, for 1.0 % reverse strain the yield stress can be calculated as maximum stress reached by the end of the first work-hardening region, i.e. by 0.7 % reverse strain. From Figures 4.12 - 4.14, a the stress-strain curve approximation equation will be as follows:

$$\sigma = 545 \cdot \epsilon^{0.38}.$$

Substitution of 0.7 % reverse strain, will give the yield stress for the inside surface at 1.0 % strain:

$$\sigma_{in} = 545 \cdot 0.7^{0.38} = 476 \text{ MPa}.$$

Initial conditions for the outside surface: forward pre-strain 2.0 %, reverse strain 1.0 %, dislocation density $1.36 \times 10^{14} \text{ m}^{-2}$, particle number density $208 \text{ } \mu\text{m}^{-3}$. From Figures 4.12-4.14,b, for 2.0 % pre-strain and more than 0.7 % reverse strain the stress-strain curve approximation equation will be as follows:

$$\sigma = 450 \cdot \epsilon^{0.095}.$$

Substitution of strain will give the yield stress for the outside surface:

$$\sigma_{out} = 450 \cdot 1.0^{0.095} = 450 \text{ MPa}.$$

Initial conditions for the plate mid-thickness: forward pre-strain 0.3 %, reverse strain 1 %, dislocation density $4.0 \times 10^{14} \text{ m}^{-2}$, particle number density $180 \text{ } \mu\text{m}^{-3}$. Experimental

observation has shown for these conditions the yield stress to be (Figure 4.7, a):

$$\sigma_c = 490 \text{ MPa.}$$

Flattening for tensile testing

For measurement of pipe mechanical properties in the transverse orientation a segment is cut from the pipe wall and flattened prior to testing. As during flattening additional cold deformation is applied to the pipe wall, mechanical property change during flattening can affect the pipe property value measured with this method of testing [64, 65, 69, 146, 147]. An example of property change for one additional deformation half-cycle during flattening is presented below.

Using a scheme of simple bending, Figure 4.18, strain during flattening can be calculated:
on the inside surface

$$\varepsilon_i = \frac{l_n - l_i}{l_i} = \frac{\alpha \left(R_0 - \frac{t}{2} \right) - \alpha (R_0 - t)}{\alpha (R_0 - t)} = \frac{t}{2(R_0 - t)},$$

on the outside surface

$$\varepsilon_o = \frac{l_n - l_o}{l_o} = \frac{\alpha \left(R_0 - \frac{t}{2} \right) - \alpha R_0}{\alpha R_0} = -\frac{t}{2R_0}.$$

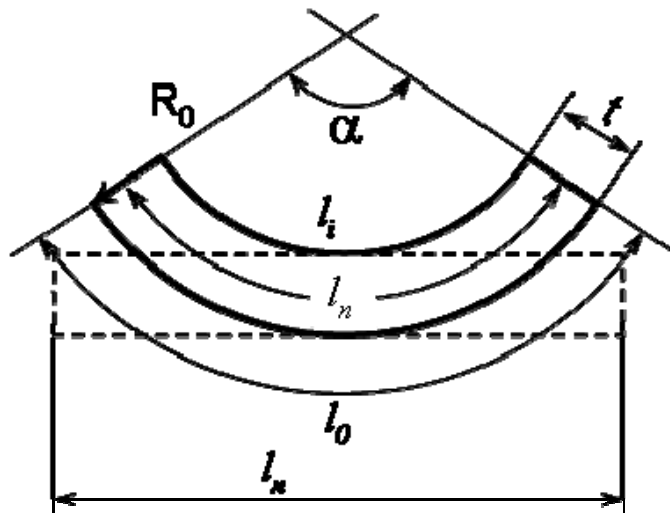


Figure 4.18 Pipe segment cross section flattened for testing;
 R_0 – pipe outside radius, t – pipe wall thickness

Substitution of the 914 x 25 mm pipe geometry will give:

$$\text{for the inside surface } \varepsilon_i = \frac{25}{914-50} = 0.029 ,$$

$$\text{and for the outside surface } \varepsilon_o = -\frac{25}{914} = -0.027 .$$

Initial conditions for the inside surface: forward pre-strain 0.3 % (during “Killing”), reverse strain $(1.0 + 2.9) = 3.9$ % (after expansion and flattening), dislocation density $1.36 \times 10^{14} \text{ m}^{-2}$, particle number density $208 \text{ } \mu\text{m}^{-3}$. From Figures 4.12 - 4.14,b, for 0.3 % pre-strain and more than 3.0 % reverse strain the stress-strain curve approximation equation will be as follows:

$$\sigma = 426 \cdot \varepsilon^{0.095} .$$

Substitution of strain will give the yield stress for the inside surface:

$$\sigma_{in} = 426 \cdot 3.9^{0.095} = 485 \text{ MPa} .$$

Initial conditions for the outside surface: forward pre-strain 1.0 %, reverse strain 2.7 %, dislocation density $1.36 \times 10^{14} \text{ m}^{-2}$, particle number density $208 \text{ } \mu\text{m}^{-3}$. From Figures 4.14-4.14,b, for 1.0 % pre-strain and more than 0.7 % reverse strain we will get the stress-strain curve approximation equation as follows:

$$\sigma = 434 \cdot \varepsilon^{0.095} .$$

Substitution of strain will give the yield stress for the outside surface:

$$\sigma_{out} = 434 \cdot 2.7^{0.095} = 477 \text{ MPa} .$$

As seen from Table 4.4, the calculated average yield stress in the present example decreases from plate to pipe due to the Bauschinger effect. The yield stress development during UOE forming follows the strain development: with a decrease in absolute value of reverse strain the yield stress drop increases (Figure 4.19). The calculation showed that with an increase in microalloying element content, from the C-Nb to the C-Nb-V steel, the yield

stress drop from plate to pipe increases, which corresponds to measured data. This is due to an increase in the Bauschinger effect with an increase in dislocation density and particle number density. The calculated yield stress after flattening lies in the literature data range. However, the calculated yield stress is lower, compared to the measured value for the same steel [146], and increases during flattening, though previously reported data show a decrease in strength from pipe to flattened specimen [64,65,69]. This might be explained if flattening occurs not through one deformation half-cycle leading to work-hardening, as was assumed during calculation, but through a series of forward-reverse deformation cycles leading to work-softening. In addition, the stress-strain curve during the third deformation half-cycle (inside surface during “Killing” and outside surface during Expansion) was assumed to be dependent only on the second half-circle (O-ing) and independent on the first half-cycle (U-ing) (Figure 4.20). If the third half-circle stress-strain curve goes closer to the forward stress-strain curve the yield stress after Expansion will be higher than calculated in the present example, but this requires further investigation.

Table 4.4 The yield stress change from plate to pipe during forming of a 914 x 25mm pipe from the C-Nb-V steel

area	plate	U-ing	O-ing	“Killing”	Expansion	flattening
inside	540	592	510	300	476	485
mid-thickness	490	490	490	495	490	490
outside	540	592	508	515	450	477
average	515	541	500	451	477	486

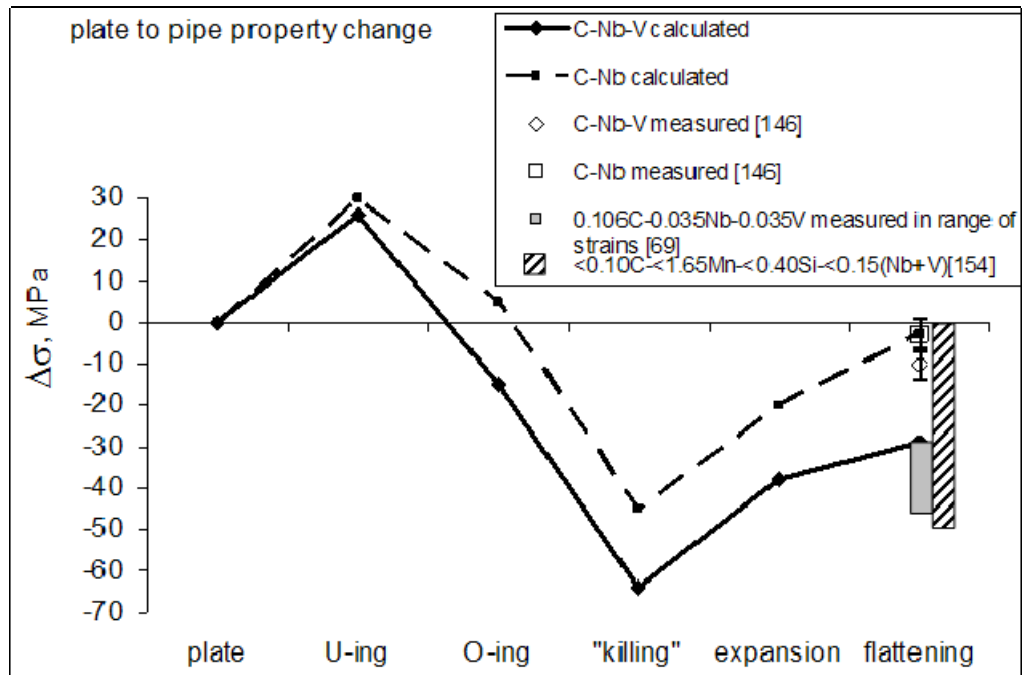


Figure 4.19 Calculated yield stress change during the UOE forming (with respect to the plate yield stress in transverse orientation)

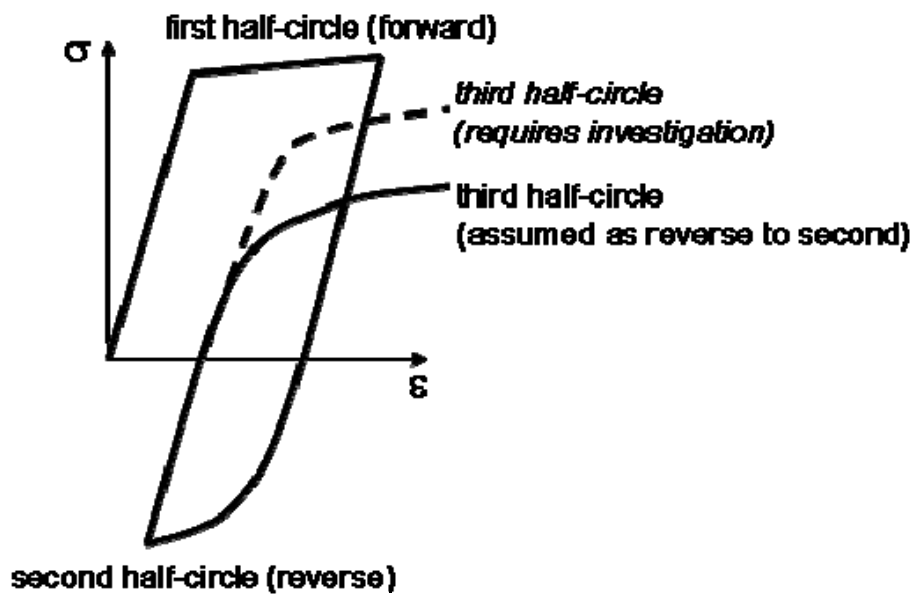


Figure 4.20 Schematic presentation of the stress-strain curve assumed for the calculation

5. CONCLUSIONS

Microstructure and mechanical property investigation of three line pipe steels differing in chemistry but processed according to similar rolling schedules, leads to the following conclusions.

In the area of the plate material microstructure

1. Ferrite grain size increases towards the plate mid-thickness (due to plate processing schedule) and decreases with an increase in microalloying element content, due to Zener drag effect.
2. Second phase (pearlite) content increases towards the plate mid-thickness due to macrosegregation and decreases with carbon content decrease in steel composition. Experimentally measured values correspond to the Thermo-Calc theoretical predictions.
3. Morphology of Mn-, Si- and Al-rich inclusions depends on steel chemistry: the inclusion length along the rolling direction decreases with an increase in Nb and V content.
4. Any significant difference in Si and Mn content across plate thickness was not observed in the C-Nb and C-Nb-V steels. Absolute values of Si and Mn content measured with SEM-EDS correspond to the steel chemistry provided by Corus with a discrepancy 5 – 8 %.
5. In the C-Nb-V steel V content difference across plate thickness was not observed. Nb content was observed increasing towards the plate mid-thickness, which qualitatively corresponds to the measured Nb-rich particle volume fraction.
6. In the C-Nb and C-Nb-V steels Nb-Ti-rich particles larger than 50 nm in diameter were characterized in terms of volume fraction and number density for the plate sub-surface and mid-thickness positions separately for ferrite and pearlite (with adjacent ferrite) regions. Average through thickness measured particle volume fraction increases with an increase

in microalloying element content. Absolute values of the average volume fraction correspond to the Thermo-Calc theoretical predictions.

7. Pearlite areas (including adjacent ferrite) are richer in microalloy particles due to microsegregation, which corresponds to previous research.
8. In the C-Nb steel the diameter, volume fraction and number density of the Nb-Ti-rich particles increase towards the plate mid-thickness. However, in the C-Nb-V steel the difference in particle parameters between the plate sub-surface and mid-thickness is not significant.
9. The volume fraction of Nb-Ti-rich particles smaller than 50 nm in diameter measured at the as-rolled C-Nb steel plate mid-thickness position corresponds to the Thermo-Calc theoretical prediction.
10. The diameter, volume fraction and number density of (Nb,Ti,V+Cu)-rich particles smaller than 50 nm in the C-Nb-V steel have been measured in the sub-surface and mid-thickness areas for the as-rolled and annealed, at 400 °C and 550 °C for 30 min., conditions. In the as-rolled C-Nb-V steel the particle volume fraction decreases towards the plate mid-thickness, which corresponds to the Nb-Ti-rich particle distribution in ferrite measured with SEM.
11. At the C-Nb-V steel plate sub-surface position the particle number density increases with annealing due to precipitation of Cu-rich particles; at the mid-thickness position the particle number density at first increases due to precipitation and then (with an increase in annealing temperature) decreases due to Cu-rich particle growth.
12. Dislocation structures observed in the as-rolled and annealed C-Nb and C-Nb-V steels correspond to earlier reported dislocation structures in the bcc materials. The measured dislocation density in the as-rolled and annealed C-Nb and C-Nb-V steels corresponds to the literature data.

13. The dislocation-particle interaction analysis showed that
- (Nb,Ti,V)-rich particles larger than 50 nm effectively block the dislocations during slip; however these particles cannot cause strong precipitation strengthening, as their interparticle spacing is larger than average dislocation length, determined in 2D,
 - Cu-rich particles smaller than 12 nm may not block dislocations effectively and can be disregarded as sources of precipitation strengthening.

In the area of the plate material mechanical properties

14. For the studied steel grades (average grain size 2.5 – 3.0 μm , 12-50 nm particle number density 70 – 900 μm^{-3} , dislocation density $(1...4) \times 10^{14} \text{ m}^{-2}$) the parameters of work-hardening (coefficient and exponent) during unidirectional deformation were quantified by a dependence on particle number density and dislocation density.
15. The Bauschinger effect (yield stress decrease) and parameters of work-hardening (coefficient and exponent) during reverse deformation were quantified by a dependence on particle number density, dislocation density and forward pre-strain (within 0.3 – 4.9 % pre-strain range).

In the area of the UOE pipe forming process

16. On the basis of the yield stress dependence on microstructure, experimentally obtained in the present work, the yield stress change on each stage of the UOE pipe forming process was calculated. The higher alloyed steel showed a larger yield stress drop from plate to pipe, due to the higher Bauschinger effect.
17. Calculation predicts the plate to pipe yield stress change to be 4 MPa for the C-Nb steel and 29 MPa for the C-Nb-V steel. This is in a good agreement with earlier measured data of 4 ± 4 MPa for the C-Nb and 10 ± 4 MPa for the C-Nb-V steel [146]. An increase in

discrepancy between the measured and calculated data with an increase in microalloying element content can be related to an assumption that work-hardening during the third deformation half-cycle (forward-reverse-*forward*) can be calculated using dependences for the second deformation half-cycle (forward-*reverse*). However, higher alloyed steel, i.e. C-Nb-V, should be expected to return more quickly to its forward direction properties during the third deformation half-cycle. Thus, the assumption in the present work results in a decreased value of the calculated yield stress in the C-Nb-V steel.

6. FUTURE PLAN OF RESEARCH

Microstructure-property research for the line pipe steels can be continued in the following areas:

In the area of the plate material microstructure

1. Influence of plate processing parameters (amount of strain below recrystallization stop temperature, finish rolling temperature and cooling rate) on ferrite grain size and second phase content distribution across plate thickness – can be studied using optical microscopy of samples industrially produced to varying processing schedules.
2. Influence of steel chemistry (microalloying element type and content) and plate processing parameters (soaking time and temperature, finish rolling temperature and cooling rate) on the:
 - microalloying element, i.e. Ti, Nb, V and Cu, segregation across plate thickness – can be studied using SEM-EDS,
 - diameter, volume fraction and number density of microalloying element particle distributions across plate thickness – can be studied using SEM and TEM imaging.
3. Influence of plate processing parameters (amount of strain below recrystallization stop temperature, finish rolling temperature and cooling rate) on dislocation structure development and dislocation density – can be studied using TEM imaging.
4. Influence of particle chemistry on particle diameter range, which effectively blocks dislocations during dislocation-particle interaction – can be studied using TEM imaging and TEM-EDS.

In the area of the plate material mechanical properties

5. The Bauschinger effect and work-hardening behaviour quantitative dependence on ferrite-pearlite microstructure for the following parameter ranges:
 - ferrite grain size up to 3.0 μm , 12-50 nm particle number density above 250 μm^{-3} and dislocation density above $1.5 \times 10^{14} \text{ m}^{-2}$;
 - ferrite grain size above 3.0 μm .
6. The Bauschinger effect and work-hardening behaviour qualitative and quantitative dependence on the second phase type (pearlite, acicular ferrite, bainite).

Mechanical testing should be carried out for up to 0.07 forward pre-strain, at strain rate of 0.001- 0.01 s^{-1} and at room temperature.

In the area of the UOE pipe forming process

7. Experimental investigation of plate to pipe property change for varying microalloying element content: Ti up to 0.05 wt%, (Nb + V) in the range of 0.10...0.15 %, Cu up to 2.0 %, Mo up to 0.70 % and Cr up to 0.80 %.
8. Experimental investigation of stress-strain curve for more than two deformation half-cycles, i.e. forward-reverse-forward and forward-reverse-forward-reverse, in the whole range of microstructure types and dislocation-particle interaction parameters. Mechanical testing should be carried out for up to 0.07 forward pre-strain, up to 0.03 reverse strain, and up to 0.01 forward strain (third deformation half-cycle) at the same strain rate in the range of 0.001- 0.01 s^{-1} and at room temperature.
9. Experimental and theoretical analysis of deformation during flattening of pipe coupons for mechanical testing. Experimental investigation of pipe to flattened specimen property change for varying steel chemistries.

REFERENCES

1. M.C. Smith, Principals of physical metallurgy, Harper and Brothers Publishers, New York, 1956.
2. A.H. Cottrell, Dislocations and plastic flow in crystals, Clarendon Press, Oxford, 1956.
3. D.J. Dingley and D. McLean, Components of the flow stress of iron, *Acta Metallurgica*, Vol. 15, 1967, p. 885 – 901.
4. E. Kerscher, K-H. Lang, O. Vohringer, D. Lohe, Increasing the fatigue limit of a bearing steel by dynamic strain ageing, *International Journal of Fatigue*, Vol. 30, № 10 - 11, 2008, p. 1838 - 1842.
5. W-S Lee, C-Y Liu, The effect of temperature and strain rate on the dynamic flow behaviour of different steels, *Material Science and Engineering A*, Vol. 426, 2006, p. 101 – 113.
6. R.W. Cahn, *Physical Metallurgy*, North-Holland Publishing, Amsterdam, 1970.
7. F.C. Frank and W.T. Read, Multiplication process for slow moving dislocations, *Physical Review Letters*, Vol. 79, 1950, p. 722 – 723.
8. W.T. Read, *Dislocations in crystals*, McGraw-Hill Publishing, 1953.
9. J. Friedel and P. Feltham, The mechanism of work-hardening and slip-band formation, *Proceedings of the Royal Society of London, Series A, Mathematical and Physical Sciences*, Vol. 242, № 1229, Oct. 1957, p. 147 – 159.
10. F. Louchet, Thermally activated dislocation sources in silicon, *Journal of Physics C: Solid State Physics*, Vol. 13, 1980, p. L847 – L849.
11. B. Hutchinson and N. Ridley, On dislocation accumulation and work-hardening in Hadfield steel, *Scripta Materialia*, Vol. 55, 2006, p. 299 – 302.
12. A.K. Roy, S. Bandyopadhyay, S.B. Suresh, D. Maitra, P. Kumar, D. Wells, L. Ma, Relationship of residual stress to dislocation density in cold-worked martensitic alloy, *Material Science and Engineering A*, Vol. 416, 2006, p. 134 – 138.
13. T. Ungar, H. Mughrabi, D. Ronnpagel, M. Wilkens, X-ray line-broadening study of the dislocation cell structure in deformed [001]-orientated copper single crystals, *Acta Metallurgica*, Vol. 32, № 3, 1984, p. 333 – 342.
14. E.M. Viatkina, W.A.M. Brekelmans, M.G.D. Geers, Modelling the evolution of dislocation structures upon stress reversal, *International Journal of Solids and Structures*, Vol. 44, 2007, p. 6030 – 6054.
15. D. Kuhlmann-Wilsdorf and N. Hansen, Geometrically necessary, incidental and subgrain boundaries, *Scripta Metallurgica et Materialia*, Vol. 25, 1991, p. 1557 - 1562.

16. J. Pal'a, O. Stupakov, J. Bydzovsky, I. Tomas and V. Novak, Magnetic behaviour of low carbon steel in parallel and perpendicular directions to tensile deformation, *Journal of Magnetism and Magnetic Materials*, Vol. 310, 2007, p. 57 – 62.
17. C.F. Robertson, K. Obrtlík and B. Marini, Dislocation structures in 16MND5 pressure vessel steel strained in uniaxial tension at different temperatures from – 196 °C up to 25 °C, *Journal of Nuclear Materials*, Vol 366, 2007, p. 58 - 69.
18. M.F. Ashby, The deformation of plastically non-homogeneous materials, *Philosophical Magazine*, Vol. 21, 1970, p. 399 - 424.
19. H. Yu, Y. Kang, H. Dong, Comparison and analysis of dislocation density, morphology and evolution in microstructure of low-carbon steel produced using different technologies, *Journal of University of Science and Technology Beijing*, Vol. 13, № 5, Oct. 2006, p. 406 – 410.
20. S.N. Prasad and D.S. Sarma, Influence of thermomechanical treatment on microstructure and mechanical properties of Nb bearing weather resistant steel, *Material Science and Engineering A*, Vol. 408, 2005, p. 53 – 63.
21. F. Yin, T. Hanamura, O. Umezawa, K. Nagai, Phosphorus-induced dislocation structure variation in the warm-rolled ultrafine-grained low-carbon steel, *Material Science and Engineering A*, Vol. 354, 2003, p. 31 – 39.
22. Yi Hai-long, Du Lin-xiu, Wang Guo-dong, Liu Xiang-hua, Strengthening mechanism of a new 700 MPa hot rolled high strength steel, *Journal of Iron and Steel Research International*, Vol. 15, № 2, 2008, p. 76 – 80.
23. R.D.K. Misra, H. Nathani, J.E. Hartmann, F. Siciliano, Microstructural evolution in a new 770 MPa hot rolled Nb-Ti microalloyed steel, *Material Science and Engineering A*, Vol. 394, 2005, p. 339 – 352.
24. R.D.K. Misra, K.K. Tenneti, G.C. Weatherly, G. Tither, Microstructure and texture of hot-rolled Cb-Ti and V-Cb microalloyed steels with differences in formability and toughness, *Metallurgical and Materials Transactions A*, Vol. 34, Oct. 2003, p. 2341 – 2351.
25. T.S. Wang, R.J. Hou, B. Lv, M. Zhang, F.C. Zhang, Microstructure evolution and deformation mechanism change in 0.98C-8.3Mn-0.04N steel during compressive deformation, *Material Science and Engineering A*, Vol. 456, 2007, p. 68 – 71.
26. I. Karaman, H. Sehitoglu, K. Gall, Y.I. Chumlyakov and H.J. Maier, Deformation of single crystal Hadfield steel by twinning and slip, *Acta Materialia*, Vol. 48, 2000, p. 1345 – 1359.
27. T.S. Byen, N. Hashimoto, K. Farrell, Temperature dependence of strain hardening and plastic instability behaviours in austenitic stainless steels, *Acta Materialia*, Vol. 52, 2004, p. 3889 – 3899.
28. T. Ono, Y. Tomota, P. Lukas, D. Lugovy, D. Neov, N. Tsuchida, K. Nagai, In situ neutron diffraction during tensile straining of fine grained ferrite-pearlite steel, *Material Science and Technology*, Vol. 20, Jan. 2004, p. 121 – 125.

29. T. Hasegawa, T. Yakou, S. Karashima, Deformation behavior and dislocation structures upon stress reversal in polycrystalline aluminium, *Material Science and Engineering*, Vol. 20, 1975, p. 267 – 276.
30. Y. Strauven and E. Aernoudt, Directional strain softening in ferritic steel, *Acta Metallurgica*, Vol. 35, 1987, p. 1029 – 1036.
31. G. Vincze, E.F. Rauch, J.J. Gracio, F. Barlat, A.B. Lopes, A comparison of the mechanical behavior of an AA1050 and a low carbon steel deformed upon strain reversal, *Acta Materialia*, Vol. 53, 2005, p. 1005 – 1013.
32. N. Christodoulou, O.T. Woo, S.R. MacEwen, Effect of stress reversal on the work hardening behavior of polycrystalline copper, *Acta Metallurgica*, Vol. 34, № 8, 1986, p. 1553 – 1562.
33. E.F. Rauch, J-H. Schmitt, Dislocation substructures in mild steel deformed in simple shear, *Material Science and Engineering*, A113, 1989, p. 441 - 448.
34. E.F. Rauch, J.J. Gracio, F. Barlat, A.B. Lopes, J. Ferreira Duarte, Hardening behavior and structural evolution upon strain reversal of aluminum alloys, *Scripta Materialia*, Vol. 46, 2002, p. 881 – 886.
35. P. Haasen and A. Kelly, A yield phenomenon in face-centred cubic single crystals, *Acta Metallurgica*, Vol. 5, Apr. 1957, p. 192 - 199.
36. I. Kovacs, The mechanism of the work-hardening in FCC metals, *Acta Metallurgica*, Vol. 15, Nov. 1967, p. 1731 - 1736.
37. P.N.B. Anongba, J. Bonneville and J.L. Martin, Hardening stages of [112] copper single crystals at intermediate and high temperatures – I. mechanical behaviour, *Acta Metallurgica et Materialia*, Vol. 41, № 10, 1993, p. 2897 - 2906.
38. A.S. Argon and P. Haasen, A new mechanism of work-hardening in the late stages of large strain plastic flow in FCC and diamond cubic crystals, *Acta Metallurgica et Materialia*, Vol. 41, № 11, 1993, p. 3289 - 1306.
39. M. Muller, M. Zehetbauer, A. Borbely and T. Ungar, Stage IV work-hardening in cell forming materials, part I: features of the dislocation structure determined by X-ray line broadening, *Scripta Materialia*, Vol. 35, № 12, 1996, p. 1461-1466.
40. P.N.B. Anongba, J. Bonneville and J.L. Martin, Hardening stages of [112] copper single crystals at intermediate and high temperatures – II. slip systems and microstructures, *Acta Metallurgica et Materialia*, Vol. 41, № 10, 1993, p. 2907 - 2922.
41. T. Ungar and M. Zehetbauer, Stage IV work-hardening in cell forming materials, part II: a new mechanism, *Scripta Materialia*, Vol. 35, № 12, 1996, p. 1467-1473.
42. Y.B. Xu, Y.L. Bai, Q. Xue and L.T. Shen, Formation, microstructure and development of the localized shear deformation in low-carbon steels, *Acta Materialia*, Vol. 44, № 5, 1996, p. 1917-1926.

43. B.J. Brindley, The effect of dynamic strain-ageing on the ductile fracture process in mild steel, *Acta Metallurgica*, Vol. 18, 1970, p. 325-329.
44. K. Ishikawa and S. Tanimura, Strain-rate sensitivity of flow stress at low temperatures in 304N stainless steel, *International Journal of Plasticity*, Vol. 8, 1992, p. 947 - 958.
45. E.I. Samuel, B.K. Choudhary, K.B.S. Rao, Influence of temperature and strain rate on tensile work-hardening behaviour of type 316LN austenitic stainless steel, *Scripta Materialia*, Vol. 46, 2002, p. 507-512.
46. M. Akiyama, T. Kuboki, K. Oikawa, K. Matsui and K. Terada, Influence of carbon content and carbide morphology of carbon steels on stress-strain curve in vicinity of yield point, *Material Science and Technology*, Vol. 18, Nov. 2002, p. 1272 - 1278.
47. L. Geng, Y. Shen, R.H. Wagoner, Anisotropic hardening equations derived from reverse-bend testing, *International Journal of Plasticity*, Vol. 18, 2002, p. 743 – 767.
48. W.B. Jones and J.C. Swearingen, Mechanical stability of ultrahigh strength steels, *Material Science and Engineering*, Vol. 41, 1979, p. 225 – 235.
49. D.L. Baragar, The high temperature and high strain-rate behaviour of a plane carbon and a HSLA steel, *Journal of Mechanical Working Technology*, Vol. 14, 1987, p. 295 – 307.
50. D.V. Wilson, Effect of second-phase particles on formability at room temperature, Effect of second-phase particles on the mechanical properties of steel, *Proceedings of a conference*, The Iron and Steel Institute, London, 1971, p.28 - 36.
51. H-L Dang and C-Y Wang, The effect of Nb and V on the electronic structure of edge dislocation core in Fe, *Computational Material Science*, Vol. 39, 2007, p. 557- 562.
52. A. Abel and H. Muir, The Bauschinger effect and discontinuous yielding, *Philosophical Magazine*, Vol. 26, 1972, p. 489 – 504.
53. P.S. Bate and D.V. Wilson Analysis of the Bauschinger effect. *Acta Metallurgica*, Vol. 34, № 6, 1986, p. 1097 - 1105.
54. A. Abel, Historical perspectives and some of the main features of the Bauschinger effect, *Materials Forum*, Vol. 10, № 1, 1987, p. 11 – 26.
55. J.D. Embury, Structural aspects of the Bauschinger effect, *Materials Forum*, Vol. 10, № 1, 1987, p. 27 – 32.
56. L.M. Brown, Orowan's explanation of the Bauschinger effect, *Scripta Metallurgica*, Vol. 11, 1977, p. 127 – 131.
57. E.F. Rauch, The stresses and work hardening rates of mild steel with different dislocation patterns, *Material Science and Engineering A*, Vol. 234 - 236, 1997, p. 653 – 656.
58. T. Hasegawa, T. Yakou, U.F. Kocks, Forward and reverse rearrangement of dislocations in tangled walls, *Material Science and Engineering*, Vol. 81, 1986, p. 189 – 199.

59. D.V. Wilson and P.S. Bate, Bauschinger effects in strain aged steels, *Materials Forum*, Vol. 10, № 1, 1987, p. 33 – 42.
60. K. Terada, K. Matsui, M. Akiyama, T. Kuboki, Numerical re-examination of the micro-scale mechanism of the Bauschinger effect in carbon steels, *Computational Material Science*, Vol. 31, 2004, p. 67 – 83.
61. D. Uko, R. Sowerby, J.D. Embury, Bauschinger effect in structural steels and role in fabrication of line pipe: Part 1 analysis of Bauschinger effect in structural steels, *Metals Technology*, № 7, 1980, p. 359 – 367.
62. G.D. Moan and J.D. Embury, A study of the Bauschinger effect in Al-Cu alloys, *Acta Metallurgica*, Vol. 27, 1979, p. 903 – 914.
63. R.K. Boger, R.H. Wagoner, F. Barlat, M.G. Lee, K. Chung, Continuous large strain tension/compression testing of sheet material, *International Journal of Plasticity*, Vol. 21, 2005, p. 2319 – 2343.
64. R.C. Ratnapuli and E.C. Rodrigues, Bauschinger effect in API X60 linepipe steels, *Metals Technology*, Vol. 9, Nov. 1982, p. 440 – 445.
65. T.C. Harrison, R.T. Weiner and G.D. Fearnough, Influence of the Bauschinger effect in high-yield steel pipes, *Journal of Iron and Steel Institute*, May 1972, p. 334 – 336.
66. J.P. Ormandy, M. Strangwood and C.L. Davis, Effect of microalloying additions on steel plate to pipe property variations during UOE linepipe processing, *Material Science and Technology*, Vol. 19, May 2003, p. 595 – 601.
67. K. Han, C.J. Van Tyne, B.S. Levy, Effect of strain and strain rate on the Bauschinger effect response of three different steels, *Metallurgical and Material Transactions A*, Vol. 36, Sept. 2005, p. 2379 – 2384.
68. R.M. Jamieson and J.E. Hood, Bauschinger effect in high-strength low-alloyed steels, *Journal of Iron and Steel Institute*, Jan. 1971, p. 46 – 48.
69. K. Nakajima, W. Mizutani, T. Kikuma and H. Matumoto, The Bauschinger effect in pipe forming, *Transactions ISIJ*, Vol. 15, 1975, p. 1 – 10.
70. D.N. Williams, Interaction between the Bauschinger effect and strain aging, *Metallurgical Transactions A*, Vol. 11, Sept. 1980, p. 1629 – 1631.
71. T. Gladman, *The physical metallurgy of microalloyed steels*, The Institute of Materials, Cambridge University Press, Cambridge, 1997.
72. W.B. Li and K.E. Easterling, The influence of particle shape on Zener drag, *Acta Metallurgica et Materialia*, Vol. 38, № 6, 1990, p. 1045 – 1052.
73. S.P. Ringer, R.P. Kuziak and K.E. Easterling, Liquid film simulation of Zener grain boundary pinning by second phase particles, *Material Science and Technology*, Vol. 7, Mar. 1991, p. 193 – 200.

74. S.P. Ringer, W.B. Li and K.E. Easterling, On the interaction and pinning grain boundaries by cubic shape precipitate particles, *Acta Metallurgica*, Vol. 37, № 3, 1989, p. 831 – 841.
75. K. Narita Physical chemistry of the groups IVa (Ti, Zr), Va (V, Nb, Ta) and the rare earth elements in steel, *Transactions of ISIJ*, Vol. 15, №. 3, 1975, p. 145 – 152.
76. N.A. Linaza, J.L. Romero, J.M. Rodriguez-Ibabe, J.L. Urcola, Influence of the microstructure on the fracture toughness and fracture mechanism of forging steels microalloyed with titanium with ferrite-pearlite structures, *Scripta Metallurgica et Materialia*, Vol. 29, № 4, 1993, p. 451 – 456.
77. R. Soto, W. Saikaly, X. Bano, C. Issartel, G. Rigaut and A. Charai, Statistical and theoretical analysis of precipitates in dual-phase steels microalloyed with titanium and their effect on mechanical properties, *Acta Materialia*, Vol. 47, № 12, 1999, p. 3475 – 3481.
78. S. Freeman, Interphase precipitation in a titanium steel, Effect of second-phase particles on the mechanical properties of steel, *Proceedings of a conference*, The Iron and Steel Institute, London, 1971, p. 152 – 156.
79. J. Copreaux, S. Lanteri and J.-H. Schmitt, Effect of precipitation on the development of dislocation substructure in low carbon steels during cold deformation, *Materials Science and Engineering A*, Vol. 164, 1993, p. 201 - 205.
80. W.J. Lin and J.J. Jonas, A stress relaxation method for following carbonitride precipitation in austenite at hot working temperatures, *Metallurgical Transactions A*, Vol. 19, June 1988, p. 1403 – 1413.
81. E.Valdes and C.M. Sellars, Influence of roughing rolling passes on kinetics of strain induced precipitation of Nb(C,N), *Material Science and Technology*, Vol. 7, July 1991, p. 622 – 630.
82. J. Irvine and T.N. Baker, The influence of rolling variables on the strengthening mechanisms operating in niobium steels, *Material Science and Engineering*, Vol. 64, 1984, p. 123 - 134.
83. W.M. Rainforth, M.P. Black, F. Hofer, Precipitation in a model austenitic steel, *Acta Materialia*, Vol. 50, 2002, p. 735 – 747.
84. R. Varughese and P.R. Howell, The application of metallographic techniques to the study of the tempering of HSLA-100 steel, *Materials Characterization*, Vol. 30, 1993, p. 261 – 267.
85. T.Gladman, B. Holmes and I.D. McIvor, Effect of second-phase particles on strength, toughness and ductility, Effect of second-phase particles on the mechanical properties of steel, *Proceedings of a conference*, The Iron and Steel Institute, London, 1971, p. 68 – 78.
86. S. Shanmugan, R.D.K. Misra, T. Mannering, D. Panda, S.G. Jansto, Impact toughness and microstructure relationship in niobium- and vanadium-microalloyed steels

processed with varied cooling rates to similar yield strength, *Material Science and Engineering A*, Vol. 437, 2006, p. 436 – 445.

87. E. Courtois, T. Epicier, C.Scott, EELS study of niobium carbo-nitride nano-precipitates in ferrite, *Micron*, Vol. 37, № 5, July 2006, p. 492 – 502.
88. E.J. Palmiere, C.I. Garcia, A.J. DeArdo, The influence of niobium supersaturation in austenite on the static recrystallisation behaviour of low carbon microalloyed steels, *Metallurgical and Materials Transactions A*, Vol. 27, № 4, 1996, p. 951 – 960.
89. A.J. Craven, K. He, L.A. Garvie, T.N. Baker, Complex heterogeneous precipitation in Ti-Nb microalloyed Al-killed HSLA steels-II. non-titanium based particles, *Acta Materialia*, Vol. 48, 2000, p. 3869 – 3878.
90. Pandit, A. Murugaiyan, A. Saha Podder, A. Haldar, D. Bhattacharjee, S. Chandra, R.K. Ray, Strain induced precipitation of complex carbonitrides in Nb-V and Ti-V microalloyed steels, *Scripta Materialia*, Vol. 53, 2005, p. 1309 – 1314.
91. B.Dutta, E.Valdes and C.M. Sellars, Mechanism and kinetics of stain induced precipitation of Nb(C,N) in austenite, *Acta Metallurgica et Materialia*, Vol.40, № 4, 1992, p. 653 – 662.
92. S.S. Hansen, J.B. Vander Sande and M. Cohen, Niobium carbo-nitride precipitation and austenite recrystallisation in hot-rolled microalloyed steels, *Metallurgical Transactions A*, Vol. 11, Mar. 1980, p. 387 – 402.
93. A.M. Elwazri, R. Varano, F. Siciliano, D. Bai, S. Yue, Characterisation of precipitation of niobium carbide using carbon extraction replicas and thin foils by FESEM, *Material Science and Technology* , Vol. 22, № 5, 2006, p. 537 – 541.
94. A.J. Craven, K. He, L.A. Garvie, T.N. Baker, Complex heterogeneous precipitation in Ti-Nb microalloyed Al-killed HSLA steels – I. (Ti,Nb)(C,N) particles, *Acta Materialia*, Vol. 48, 2000, p. 3857 – 3868.
95. C.L. Davis and M. Strangwood, Preliminary study of the inhomogeneous precipitate distributions in Nb-microalloyed plate steels, *Journal of Material Science*, Vol. 37, 2002, p. 1083 – 1090.
96. M. Charleux, W.J. Poole, M. Militzer, A. Deschamps, Precipitation behaviour and its effect on strengthening of an HSLA-Nb/Ti steel, *Metallurgical and Material Transactions A*, Vol. 32, №7, 2001, p. 1635 – 1647.
97. R.D.K. Misra, G.C. Weatherly, J.E. Hartmann, A.J. Boucek, Ultrahigh strength hot rolled microalloyed steels: microstructure aspects of development, *Material Science and Technology*, Vol. 17, Sept. 2001, p. 1119 – 1129.
98. R.D.K. Misra, K.K. Tenneti, G.C. Weatherly, G. Tither, Microstructure and texture of hot-rolled Nb-Ti and V-Nb microalloyed steels with differences in formability and toughness, *Metallurgical and Materials Transactions A*, Vol. 34, Oct. 2003, p. 2341 – 2351.

99. H.S. Ushbi and T.N. Baker, The influence of manganese and silicon on the precipitation of vanadium carbide in steel, *Material Science and Engineering A*, Vol. 111, 1989, p. 189 – 199.
100. G.Fourlaris, A.J. Baker, G.D. Papadimitriou, A microscopic investigation of the precipitation phenomena observed during the pearlite reaction in vanadium alloyed carbon steels, *Acta Metallurgica et Materialia*, Vol. 43, № 10, 1995, p. 3733 – 3742.
101. T. Furuhashi, T. Shinyoshi, G. Miyamoto, J. Yamaguchi, N. Sugita, N. Kimura, Multiphase crystallography in the nucleation of intergranular ferrite on MnS+V(C,N) complex precipitate in austenite, *ISIJ International*, Vol. 43, № 12, 2003, p.2028 - 2037.
102. S. Wei, J. Zhu and L. Xu, Research on wear resistance of high speed steel with high vanadium content, *Material Science and Engineering A*, Vol. 404, 2005, p. 138 – 145.
103. Y. Yazawa, T. Furuhashi, T. Maki, Effect of matrix recrystallisation on morphology, crystallography and coarsening behaviour of vanadium carbide in austenite, *Acta Materialia*, Vol. 52, 2004, p. 3727 – 3736.
104. J.A. Wilson, A.J. Craven, Improving the analysis of small precipitates in HSLA steels using a plasma cleaner and ELNES, *Ultramicroscopy*, Vol 94, 2003, p. 197 – 207.
105. P. Maugis, M. Goune, Kinetics of vanadium carbo-nitride precipitation in steel: a computer model, *Acta Materialia*, Vol. 53, № 12, 2005, p 3359 – 3367.
106. C.P. Scott, D. Charleix, P. Barges, Quantitative analysis of complex carbo-nitride precipitates in steels, *Scripta Materialia*, Vol. 47, 2002, p. 845 – 849.
107. R.D. Fu, T.S. Wang, W.H. Zhou, W.H. Zhang, F.C. Zhang, Characterization of precipitates in a 2.25Cr-1Mo-0.25V steel for large-scale cast-forged products, *Materials Characterization*, Vol. 58, 2007, p. 968 – 973.
108. B. Garbarz, J. Marcisz, J. Wojtas, TEM analysis of fine sulphides dissolution and precipitation in steel, *Material Chemistry and Physics*, Vol. 81, 2003, p. 486 – 489.
109. I. Madariaga and I. Gutierrez, Nucleation of acicular ferrite enhanced by the precipitation of CuS on MnS particles, *Scripta Materialia*, Vol. 37, № 8, 1997, p. 1185 - 1192.
110. A. Ghosh, Samar Das, S. Chatterjee, B. Mishra, P. Ramachandra Rao, Influence of thermo-mechanical processing and different post cooling techniques on structure and properties of an ultra low carbon Cu bearing HSLA forging, *Material Science and Engineering A*, Vol. 348, 2003, p. 299 – 308.
111. J.B. Yang, T. Yamashita, N. Sano, M. Enomoto, Simulation of competitive Cu precipitation in steel during non-isothermal aging, *Material Science and Engineering A*, Vol. 487, 2008, p. 128 – 136.
112. J.B. Yang, M. Enomoto, C. Zhang, Modeling Cu precipitation in tempered martensitic steel, *Material Science and Engineering A*, Vol. 422, 2006, p. 232 – 240.

113. R.Rana, S.B. Singh, O.N. Mohanty, Effect of composition and pre-deformation on age hardening response in a copper-containing interstitial free steel, *Materials Characterization*, Vol. 59, 2008, p. 969 – 974.
114. J.F. Shackelford and W. Alexander, *Material science and engineering handbook*, CRC Press, Boca Raton, USA, 2001.
115. R. Honeycombe and H.K.D.H. Bhadeshia, *Steels. Microstructure and properties*, Edward Arnold, London, 1995.
116. A. Cracknell and N.J. Petch, Frictional forces on dislocation arrays at the lower yield point in iron, *Acta Metallurgica*, Vol. 3, March 1955, p. 186 – 189.
117. D.F. Stein, J.R. Low and A.V. Seybolt, The mechanical properties of iron single crystals containing less than $5 \cdot 10^{-3}$ ppm carbon, *Acta Metallurgica*, Vol. 11, Nov. 1963, p. 1253 – 1262.
118. N. Brown and R.A. Ekvall, Temperature dependence of the yield point in iron. *Acta Metallurgica*, Vol. 10, Nov. 1962, p. 1101 – 1107.
119. R.Armstrong, I.Codd, R.M. Douthwaite and N.J. Petch, The plastic deformation of polycrystalline aggregates, *Philosophical Magazine*, Vol. 7, 1962, p. 45 – 58.
120. B.W. Christ and G.V. Smith, Comparison of the Hall-Petch parameters of zone-refined iron determined by the grain size and extrapolation methods, *Acta Metallurgica*, Vol.15, May 1967, p. 809 – 816.
121. H. Conrad and G. Schoeck, Cottrell locking and the flow stress in iron, *Acta Metallurgica*, Vol. 8, Nov. 1960, p. 791 – 796.
122. N.J.Petch, The upper yield stress of polycrystalline iron, *Acta Metallurgica*, Vol. 12, Jan. 1964, p. 59 – 65.
123. K.J. Irvine, The development of high-strength steels. *Journal of Iron and Steel Institute*, Vol. 200, Oct. 1962, p. 820 - 836.
124. K.W. Burns and F.B. Pickering, Deformation and fracture of ferrite-pearlite structures. *Journal of Iron and Steel Institute*. 202, Nov. 1964, p. 899 - 906.
125. D. T. Llewellyn and R.C. Hudd, *Steels: metallurgy and application*. Butterworth-Heinemann, Oxford, 1998.
126. T. Gladman, I.D. McIvor, F.B. Pickering, Some aspects of structure-property relationships in high-carbon ferrite-pearlite steel, *Journal of Iron and Steel Institute*, Vol. 210, Dec. 1972, p. 916 - 930.
127. J.A.Todd and P.Li, Microstructure–mechanical property relationships in isothermally transformed vanadium steels, *Metallurgical Transactions*, Vol. 17A, July 1986, p. 1191 – 1202.

128. J. Irvine and T.N. Baker, The influence of rolling variables on the strengthening mechanisms operating in niobium steels, *Material Science and Engineering*, Vol. 64, 1984, p. 123 - 134.
129. A.M.Sage, D.M. Hayes, C.C. Early, E.A. Almond, Effects of some variations in composition on mechanical properties of controlled-rolled and normalized vanadium steel 12 mm plate, *Metals Technology*, Vol. 19, July 1976, p. 293 - 302.
130. T.Gladman, B.Holmes and I.D. McIvor, Effect of second-phase particles on strength, toughness and ductility, Effect of second-phase particles on the mechanical properties of steel, *Proceedings of a conference*, The Iron and Steel Institute, London, 1971, p. 68 – 78.
131. H. Conrad, On the mechanism of yielding and flow in iron, *Journal of Iron and Steel Institute*, Vol. 198, Aug. 1961, p. 364 – 375.
132. J.T. Michalak, The influence of temperature on development of long-range internal stress during the plastic deformation of high purity iron, *Acta Metallurgica*, Vol. 13, Mar. 1965, p. 213 – 222.
133. M. Graf and H.G. Hillenbrand, Production of large diameter line pipe – state of the art and future development trends, EUROPIPE, GmbH, www.europipe.de, 1995.
134. H.G. Hillenbrand, M. Graf and C. Kalwa, Development and production of high strength pipeline steels, EUROPIPE, GmbH, www.europipe.de, 2001.
135. H.G. Hillenbrand, C. Kalwa and A. Liessem, Technological solutions for ultra-high strength gas pipelines, EUROPIPE, GmbH, www.europipe.de, 2005.
136. H.G. Hillenbrand, A. Liessem, K. Biermann, C.J. Heckmann and V. Schwinn, Development of high strength material and pipe production technology for grade X120 line pipe, EUROPIPE, GmbH, www.europipe.de, 2004.
137. A. Streisselberger, J. Bauer, P. Fluss, H.G. Hillenbrand and P. Cordon, High strength steel plates for line pipes in grades up to X100, EUROPIPE, GmbH, www.europipe.de, 2008.
138. J. Bauer, P. Fluss, E. Amoris and V. Schwinn, Microstructure and properties of thermo-mechanical controlled processing steels for linepipe applications, *Ironmaking and Steelmaking*, Vol. 32, №4, 2005, p. 325 – 330.
139. S.N. Prasad and D.S. Sarma, Influence of thermomechanical treatment on microstructure and mechanical properties of Nb bearing weather resistant steel, *Material Science and Engineering A*, Vol. 408, 2005, p. 53 – 63.
140. A. Bakkaloglu, Effect of processing parameters on microstructure and properties of an Nb microalloyed steel, *Material Letters*, Vol. 56, 2002, p. 200 – 209.
141. H.G. Hillenbrand, E. Amoris, K.A. Niederhoff, C. Perdrix, A. Streisselberger, U. Zeislmaier, Manufacturability of line pipe in grades up to X100 from TM processed plate, EUROPIPE, GmbH, www.europipe.de, 1995.

142. B. Hwang, S. Lee, Y.M. Kim, N.J. Kim and J.Y. Yoo, Correlation of rolling condition, microstructure and low temperature toughness of X70 pipeline steels, *Metallurgical and Materials Transactions A*, Vol. 36, July 2005, p. 1793 – 1805.
143. Z. Tang and W. Stumpf, The effect of microstructure and processing variables on the yield to ultimate tensile strength ratio in a Nb-Ti and a Nb-Ti-Mo line pipe steel, *Material Science and Engineering A*, Vol. 490, № 1-2, Aug. 2008, p. 391 - 402.
144. 42” Pipe mill brochure, British Steel North East Mills, Hartlepool, 1996.
145. H-G. Hillenbrand, C. Kalwa, A. Liessem, Technological solutions for ultra-high strength gas pipelines, *Proceedings of the 1st International conference on super-high strength steels*, 2-4 November 2005, Rome, Italy, www.europipe.com, 2008.
146. J. P. Ormandy, Plate to pipe tensile property variation in UOE processed line pipe steels, Thesis for the degree of Master of Philosophy, School of Metallurgy and Materials, University of Birmingham, UK, 2000.
147. N. Takahashi, A. Yamamoto, M. Miura, H. Makino, M. Hamada, I. Takeuchi, Fracture resistance against internal pressure on high strength over X80 line pipe, www.msm.cam.ac.uk/phase-trans/2005/link/67.pdf
148. D. Williams and C.B. Carter, *Transmission electron microscopy, II – Diffraction*, Plenum Press, New York, 1996.
149. B. Sundman, *Thermo-Calc. Users’ Guide*, Royal Institute of Technology, Stockholm, 1999.
150. C. Davis, M. Strangwood, D. Chakrabarti, Development of bimodal grain structures in Nb-microalloyed steels, *Microalloyed steels: Emerging technologies and application*, *Proceedings of the international conference on microalloyed steels*, 9 – 11 March, 2007, Kolkata, India, p. 96 – 106.
151. D. Chakrabarti, C. Davis and M. Strangwood, Characterization of bimodal grain structure and their dependence on inhomogeneous precipitate distribution during casting, *Materials Science Forum*, Vol. 500-501, 2005, p. 613 – 620.
152. M. Strangwood and C.L. Davis, Segregation behaviour in niobium-microalloyed steels, *Proceedings of the 2nd international conference on “Thermo-mechanical simulation and processing of steels”*, Ranchi, India, 2008, p. 453 – 463.
153. Hai Ni and Zhirui Wang, Effect of pre-strain and mean stress on cyclic plastic deformation response of iron-based alloys, *Material Science and Engineering A*, Vol. 314, 2001, p. 12 – 23.
154. D.G. Stalheim, K.R. Barnes, D.B. McCutcheon, Alloy designs for high strength oil and gas transmission linepipe steels, Presentation at the International Symposium on Microalloyed Steels for the Oil and Gas Industry, CBMM-TMS, Araxa, Brazil, 23-25 January 2006.

Results of the Dissertation were published in:

A.G. Kostryzhev, M. Strangwood and C.L. Davis, Influence of microalloying precipitates on Bauschinger effect during UOE forming of line-pipe steels, *Materials Technology: Advanced Performance Materials*, Vol. 22, № 3, 2007, p. 166 – 172.

A.G. Kostryzhev, M. Strangwood and C.L. Davis, Mechanical property development during UOE forming of large diameter line-pipe steels, *Proceedings of the 2nd international conference on “Thermo-mechanical simulation and processing of steels (SimPro’08)”*, 2008, p. 397 – 407.

A.G. Kostryzhev, M. Strangwood, and C.L. Davis, Bauschinger effect in Nb- and V-alloyed line-pipe steels, *Ironmaking and Steelmaking*, Vol. 36, № 3, 2009, p. 186 - 192.

and presented at the conferences:

“Microalloyed steels: production, properties, application”, 13 - 14 November, 2007, London, UK.

“Thermomechanical processing of steels”, 10 - 12 September, 2008, Padua, Italy.

“Thermo-mechanical simulation and processing of steel”, 9 – 11 December, 2008, Ranchi, India.